



HAL
open science

Magnetic Resonance Elastography and Supersonic Shear Imaging: simulation, experimental comparison and application to the characterization of the liver

Jinlong Yue

► **To cite this version:**

Jinlong Yue. Magnetic Resonance Elastography and Supersonic Shear Imaging: simulation, experimental comparison and application to the characterization of the liver. Biological Physics [physics.bio-ph]. Université Paris Saclay (COMUE), 2017. English. NNT: 2017SACLS483 . tel-01682936

HAL Id: tel-01682936

<https://theses.hal.science/tel-01682936>

Submitted on 12 Jan 2018

HAL is a multi-disciplinary open access archive for the deposit and dissemination of scientific research documents, whether they are published or not. The documents may come from teaching and research institutions in France or abroad, or from public or private research centers.

L'archive ouverte pluridisciplinaire **HAL**, est destinée au dépôt et à la diffusion de documents scientifiques de niveau recherche, publiés ou non, émanant des établissements d'enseignement et de recherche français ou étrangers, des laboratoires publics ou privés.

L'élastographie par résonance magnétique et l'élastographie ultrasonore par ondes de cisaillement supersonic: simulation, comparaison expérimentale et l'application pour la caractérisation du foie

Thèse de doctorat de l'Université Paris-Saclay
préparée à l'Université Paris-Sud

École doctorale n°575 Electrical, Optical, Bio-physics and Engineering
Spécialité de doctorat: Imagerie et physique médicale

Thèse présentée et soutenue à Orsay, 11/12/2017, par

M. Jinlong YUE

Composition du Jury :

M. Stefan Catheline Directeur de recherche, LabTAU	Président et Rapporteur
Mme. Meng Yin Associate Professor, Mayo Clinic	Rapporteur
Mme. Elisabeth Brusseau Chargé de recherche, CREATIS	Examineur
M. Xavier Maître Chargé de recherche, IR4M	Examineur
Mme. Claire Pellot-Barakat Chargé de recherche, IMIV	Examineur
Mme. Irène Buvat Directeur de recherche, IMIV	Directeur de thèse
Mme. Najat Salameh Assistant Professor, University of Basel	Invité

Titre : L'élastographie par résonance magnétique et l'élastographie ultrasonore par ondes de cisaillement supersonic: simulation, comparaison expérimentale et l'application pour la caractérisation du foie

Mots clés : élastographie, IRM, ultrason, simulation, reconstruction

Résumé : L'élastographie est une modalité d'imagerie médicale émergente qui permet de mesurer les propriétés mécaniques des tissus mous humains. Ces mesures peuvent servir de biomarqueurs pour l'amélioration de la prise en charge des maladies, du diagnostic précoce et de l'évaluation de la sévérité, au suivi de la réponse au traitement. Parmi les différentes approches de l'élastographie, l'élastographie par Résonance Magnétique (ERM) et l'élastographie ultrasonore par ondes de cisaillement (Supersonic Shear Imaging (SSI)) suscitent des intérêts particuliers. Ces deux modalités ont été largement étudiées pour des applications cliniques multiples. Toutefois, chaque modalité repose sur des conditions d'acquisition et de reconstruction différentes et caractérisées par leur propres limites qui peuvent induire des biais de mesure intra-et inter-modalité et donc entraver l'interchangeabilité des deux modalités pour des applications cliniques.

Dans un premier temps, ma thèse a porté sur l'identification des biais de mesure entre ERM et SSI. Grâce à une comparaison méthodologique approfondie des deux modalités, nous avons identifié les différentes caractéristiques de fréquence des ondes de cisaillement générées par les deux modalités et les contraintes spécifiques de reconstruction, en particulier en ERM, comme les principales sources de biais de mesure entre les deux modalités. Dans un deuxième temps, une étude de simulation a été effectuée afin de caractériser l'influence des conditions d'acquisition et de reconstruction sur l'exactitude et la précision des mesures d'ERM. Nous avons établi des abaci *in silico* pour identifier le nombre de voxels par longueur d'onde idéal (rapport λ/a) pour obtenir des mesures ERM exactes et précises. En outre,

nous avons montré que le rééchantillonnage pouvait s'avérer efficace afin de répondre aux critères de λ/a favorable lorsque le nombre de voxels par longueur d'onde initial était mal défini. Les résultats finaux, qui sont généralement calculés à partir des trois directions d'encodage, peuvent être améliorés grâce à des stratégies de pondération appropriées qui reposent sur le champ rotationnel du déplacement de l'onde de cisaillement. Pour la modalité SSI, nous avons utilisé le paramètre de qualité fourni par le fabricant afin d'éliminer raisonnablement des résultats peu fiables et améliorer encore la qualité des mesures.

Ensuite nous avons intégré les stratégies d'optimisation proposées dans chaque modalité pour effectuer des études de comparaison expérimentales impartiales entre ces deux modalités. Des études *in vitro* ont été effectuées sur des fantômes commerciaux calibrés et aussi des fantômes à la base de l'alcool polyvinylique. Des résultats expérimentaux confirment bien ceux de la simulation. Des mesures SSI et ERM sont en bon accord quand des biais reliés à la théorie, l'expérimentation et la reconstruction sont minimisés. Des études *in vivo* ont été ensuite effectuées sur le foie de deux volontaires sains. On a constaté que lorsque le foie est quasi-élastique, des mesures SSI et ERM avec la qualité optimisée concordent bien les uns et les autres, ils sont donc interchangeables. Dans le cas du tissu hépatique viscoélastique, des mesures SSI et ERM dépendent de la fréquence. Dans ce contexte, des mesures ERM et SSI pour la même fréquence spécifique sont nécessaires pour réaliser une comparaison impartiale entre des deux modalités.



Title : Magnetic Resonance Elastography and Supersonic Shear Imaging: simulation, experimental comparison and application to the characterization of the liver

Keywords : elastography, MRI, ultrasound, simulation, reconstruction

Abstract : Elastography is an emerging medical imaging modality which permits to measure the mechanical properties of human soft tissue. The measured mechanical properties can serve as potential biomarkers for improving the management of diseases, from early diagnosis, to severity evaluation and therapy response monitoring. Among different approaches, Magnetic Resonance Elastography (MRE) and Supersonic Shear Imaging (SSI) have shown particular interests. The two modalities have been widely investigated for multiple clinical applications. However, each modality is challenged by specific acquisition and reconstruction conditions which may induce intra- and inter-modality measurement biases and hence impede the interchangeability of the two modalities.

The first part of my thesis focused on identifying the measurement biases between MRE and SSI. Through a thorough methodological comparison study, we recognized different frequency characteristics of generated shear waves for the two modalities and modality specific reconstruction validity issues as the main sources for the measurement biases between the two modalities. Then through a dedicated simulation study, we established an *in silico* abaci to identify the favorable range of number of voxels per wavelength which leads to accurate and precise MRE. Moreover, resampling was proven effective to regulate poorly defined number of voxels per wavelength to the favorable range.

The overall outcome, which is usually computed from the three acquired motion-encoded directions, may further be improved by appropriate weighting strategies that are based on curl of shear displacement field. For SSI, we referred to the quality parameter provided by the manufacturer to reasonably eliminate unreliable results so as to further improve the measurement quality.

After establishing the potential measurement biases between MRE and SSI, we incorporated the proposed quality optimization strategies into both modalities in order to perform unbiased experimental comparison studies between the two modalities. First, *in vitro* studies were carried out on commercial calibrated phantoms as well as home-made polyvinyl alcohol phantoms. Experimental results corroborate well the simulation findings. MRE and SSI measurements agree well with each other when theory, experiment, and reconstruction biases are minimized. *In vivo* studies were then performed on the livers of two healthy volunteers. We found that when the liver is quasi-elastic, the quality-guided MRE and SSI measurements agree well with each other and hence are interchangeable. In case of viscoelastic liver tissue, both MRE and SSI measurements are frequency dependent. Thus frequency-specific measurements are essential for cross-validating the measurements of these two modalities.



Abstract

Elastography is an emerging medical imaging modality which permits to measure the mechanical properties of human soft tissue. The measured mechanical properties can serve as potential biomarkers for improving the management of diseases, from early diagnosis, to severity evaluation and therapy response monitoring. Among different approaches, Magnetic Resonance Elastography (MRE) and Supersonic Shear Imaging (SSI) have shown particular interests. The two modalities have been widely investigated for multiple clinical applications. However, each modality is challenged by specific acquisition and reconstruction conditions which may induce intra- and inter-modality measurement biases and hence impede the interchangeability of the two modalities.

The first part of my thesis focused on identifying the measurement biases between MRE and SSI. Through a thorough methodological comparison study, we recognized different frequency characteristics of generated shear waves for the two modalities and modality specific reconstruction validity issues as the main sources for the measurement biases between the two modalities. Then through a dedicated simulation study, we established an *in silico* abaci to identify the favorable range of number of voxels per wavelength which leads to accurate and precise MRE. Moreover, resampling was proven effective to regulate poorly defined number of voxels per wavelength to the favorable range. The overall outcome, which is usually computed from the three acquired motion-encoded directions, may further be improved by appropriate weighting strategies that are based on curl of shear displacement field. For SSI, we referred to the quality parameter provided by the manufacturer to reasonably eliminate unreliable results so as to further improve the measurement quality.

After establishing the potential measurement biases between MRE and SSI, we incorporated the proposed quality optimization strategies into both modalities in order to perform unbiased experimental comparison studies between the two modalities. First, *in vitro* studies were carried out on commercial calibrated phantoms as well as home-made polyvinyl alcohol phantoms. Experimental results corroborate well the simulation findings. MRE and SSI measurements agree well with each other when theory, experiment, and reconstruction biases are minimized. *In vivo* studies were then performed on the livers of two healthy volunteers. We found that when the liver is quasi-elastic, the quality-guided MRE and SSI measurements agree well with each other and hence are interchangeable. In case of viscoelastic liver tissue, both MRE and SSI measurements are frequency dependent. Thus frequency-specific measurements are essential for cross-validating the measurements of these two modalities.

Résumé de manuscrit en français

L'imagerie médicale est la pierre angulaire de la médecine moderne. Il est capable de révéler des pathologies anatomiques, fonctionnelles ou moléculaires qui sous-tendent une variété de maladies. Aujourd'hui, des technologies de l'imagerie médicale ont été largement appliquées dans la routine clinique afin d'aider les cliniciens à mieux prendre en charge des patients durant toute la procédure de soins, du diagnostic précoce des maladies, à la quantification de la gravité des maladies, puis à l'évaluation de la réponse au traitement. Actuellement, des modalités d'imagerie cliniques principales incluent: la Tomodensitométrie (TDM), l'Imagerie par Ultrason (US), l'Imagerie par Résonance Magnétique (IRM) et la Tomographie par Emission de Positrons (TEP). Toutes ces modalités peuvent fournir l'imagerie anatomique et fonctionnelle. En outre, l'IRM et TEP peuvent fournir l'imagerie moléculaire. En général, des altérations liées aux maladies apparaissent en premier lieu au niveau moléculaire et fonctionnel. Quand des changements anatomiques apparaissent, des maladies ont généralement atteint un stade avancé. Dans ce contexte, des informations obtenues de l'imagerie médicale susceptibles de révéler des altérations moléculaires ou fonctionnelles sont extrêmement importantes pour le pronostic des patients. De même, ces informations sont également utiles pour surveiller si le traitement est efficace.

Des propriétés mécaniques des tissus mous humaines peuvent fournir des informations importantes pour évaluer l'état du tissu. Des changements de ces propriétés mécaniques, qui souvent apparaissent avant des changements anatomiques apparents, sont en fait liés à l'altération de la composition du tissu, l'inflammation des tissus et la prolifération cellulaire etc. Par conséquent, ces propriétés mécaniques des tissus mous sont considérés comme des biomarqueurs potentiels pour la gestion des maladies. Depuis l'Antiquité, la rigidité des tissus mous a été exploitée comme une importante indication médicale par la pratique de palpation. De nos jours, avec l'aide d'imagerie médicale, palpation est par ailleurs effectuée par une méthode plus objective, moins dépendante de l'opérateur, qui est appelée l'Elastographie. De plus, l'élastographie permet de mesurer quantitativement des propriétés mécaniques régionaux qui sont inaccessibles par la palpation. Généralement, l'élastographie est composé de trois étapes élémentaires: l'excitation, l'acquisition et la reconstruction. Depuis la naissance de l'élastographie il y a trente ans, une évolution technique rapide a eu lieu dans les trois étapes élémentaires. Approches diverses ont été proposées. Parmi les différentes approches, l'Elastographie par Résonance Magnétique (ERM) et l'élastographie ultrasonore par ondes de cisaillement supersonic (Supersonic Shear Imaging (SSI)) ont présenté des perspectives particulières. ERM hérite de l'IRM

l'avantage de l'acquisition volumique 3D, qui permet de présenter la distribution des propriétés mécaniques tissulaire en 3D. SSI hérite de l'US l'avantage de haute résolution temporaire, qui permet de caractériser les propriétés mécaniques des tissus en temps réel. Leurs avantages complètent l'un et l'autre, par conséquent ils peuvent répondre aux besoins des cliniciens à différents stades de la gestion des maladies. Dans ce contexte, la combinaison des deux modalités peuvent aider les cliniciens à mieux prendre en charge des patients.

Jusqu'à maintenant, plein d'études ont été réalisées pour démontrer la faisabilité et la pertinence clinique de ERM et SSI dans une variété d'applications cliniques. Aujourd'hui, ils sont mis en œuvre dans la routine clinique pour la classification du stade de fibrose du foie et des tumeurs du sein. Toutefois, des questions concernant la validité de la mesure de chaque modalité et la validation croisée des mesures des deux modalités n'ont pas été pleinement prises en compte. En conséquence, désaccords entre des mesures inter-modalité et intra-modalité sont présents, qui empêchent l'interchangeabilité des deux modalités. Dans ce contexte, l'objectif de ma thèse est d'abord d'enquêter sur les sources de biais potentiels pour des désaccords entre des mesures inter-modalité et intra-modalité et proposer des stratégies correspondants pour les minimiser, par la suite valider ces stratégies proposés et réaliser des comparaisons impartiales entre ERM et SSI par des expériences *in vitro* et *in vivo* respectivement.

Ce rapport commence par l'état de lieu sur l'élastographie. Dans Chapitre 1, des principes physiques de base pour l'élastographie sont présentés dans un premier temps. Des hypothèses et des équations derrière l'élastographie statique et dynamique sont détaillés respectivement. L'avantage principal de l'élastographie dynamique par rapport à l'élastographie statique est que des tenseurs de contrainte et déformation sont non plus nécessaires pour obtenir des propriétés mécaniques quantitatives puisqu'ils sont remplacés par le champ de déplacement, qui est plus facilement accessible grâce à l'imagerie médicale. Par conséquent, des propriétés mécaniques quantitatives peuvent être déduites en résolvant des équations d'onde qui relient le champ de déplacement et des propriétés mécaniques. Et puis, un bref aperçu de l'évolution de l'élastographie par l'IRM et par l'US est donné. Pour l'élastographie par l'US, différentes approches se distinguent principalement par le caractéristique temporaire de l'excitation, qui varie du compression quasi statique, à l'excitation sinusoïdale stationnaire, à l'excitation impulsive. Des principes, avantages et limites de chaque approche sont présentés. Il existe aussi l'approche statique et dynamique pour ERM. Toutefois, l'approche dynamique est dominante à ce jour. Différentes approches dynamiques se distinguent principalement par des trois étapes essentielles de l'élastographie. Des principes, avantages et limites des différents dispositifs d'excitation, séquences d'acquisition et algorithmes de reconstruction sont présentés. Enfin, des applications cliniques potentielles pour ces deux modalités sont résumées en trois aspects: le diagnostic précoce des maladies, la quantification

de la gravité des maladies et l'évaluation de la réponse au traitement.

Dans Chapitre 2, des détails méthodologiques et l'implémentation expérimentale de ERM et SSI, qui sont au coeur du travail, sont présentés. Des acquisitions ERM sont effectuées sur un Philips 1.5 T MR Scanner (Achieva, Philips Healthcare, The Netherlands) et un Bruker 11.7 T MR scanner (BioSpec, Bruker, USA) tandis que des acquisitions SSI sont effectuées sur un Aixplorer système ultrasonore (Supersonic Imagine, Aix-en-Provence, France). Ces deux modalités diffèrent l'un et l'autre dans tous les trois étapes élémentaires (Table 1). Ces différences méthodologiques amènent des sources de biais pour des mesures des deux modalités. D'abord, des ondes de cisaillement générées pour ces deux modalités sont différentes en terme de caractéristique fréquentiel: l'onde mono-fréquentiel pour ERM tandis que l'onde avec une large bande de fréquence pour SSI. Différentes quantités physiques sont ainsi mesurées: la vitesse de phase pour ERM tandis que la vitesse de group pour SSI. Cette différence entraîne un biais de mesure théorique important entre ERM et SSI. Un milieu quasi-élastique, dans lequel la dispersion d'ondes de cisaillement entre des composantes avec différentes fréquences est négligeable, est donc nécessaire pour minimiser ce biais théorique. L'acquisition et la reconstruction de chaque modalité amènent des incertitudes spécifiques pour chaque modalité, qui influencent la validité de la mesure. Ces incertitudes forment un autre biais de mesure important entre des deux modalités. Du coup, des conditions d'acquisition et reconstruction ou des paramètres de qualité qui permettent de minimiser ces incertitudes sont cruciales pour une comparaison propre entre ces deux modalités. En outre, la vitesse de cisaillement est le paramètre de base estimé des deux modalités. Le module de cisaillement ou le module de Young sont ensuite dérivés de la vitesse de cisaillement en utilisant différents modèles de reconstruction, qui peut amener d'autres biais liés aux reconstruction modèles et l'effet d'échelle. Dans ce cadre, la vitesse de cisaillement doit être une estimation plus solide et aussi un paramètre de comparaison plus pertinent.

TABLE 1: Différences méthodologiques entre ERM and SSI

	ERM	SSI
Excitation	L'onde harmonique continue Mono-fréquence	L'onde transitoire Large bande de fréquence
Acquisition	3D volume Champs du déplacement tri-dimensionnel	2D image (ou 2D images successives) Champs du déplacement axial mono-dimensionnel
Reconstruction	Inversion locale de l'équation d'onde Modèle viscoélastique Vitesse de phase	Temps de vol Modèle élastique Vitesse de group

La reconstruction du ERM par l'inversion algébriques de l'équation de Helmholtz sur le champ rotationnel de l'onde de cisaillement peut théoriquement être impeccable. Toutefois, sa performance est contestée par des multiples paramètres expérimentaux, notamment la fréquence et l'amplitude des ondes mécaniques, la taille de voxel et le rapport signal sur bruit (RSB) de

l'acquisition. Dans Chapitre 3, nous avons étudié systématiquement l'influence conjointe des paramètres susmentionnés sur l'exactitude et la précision de ERM. Une source d'excitation ponctuelle a été simulée et des champs de déplacement réalistes (Figure 1) ont été analytiquement calculés en utilisant la fonction de Green élastique pour simuler des données ERM dans un milieu isotrope, homogène, linéaire élastique, et la moitié de l'espace infini.

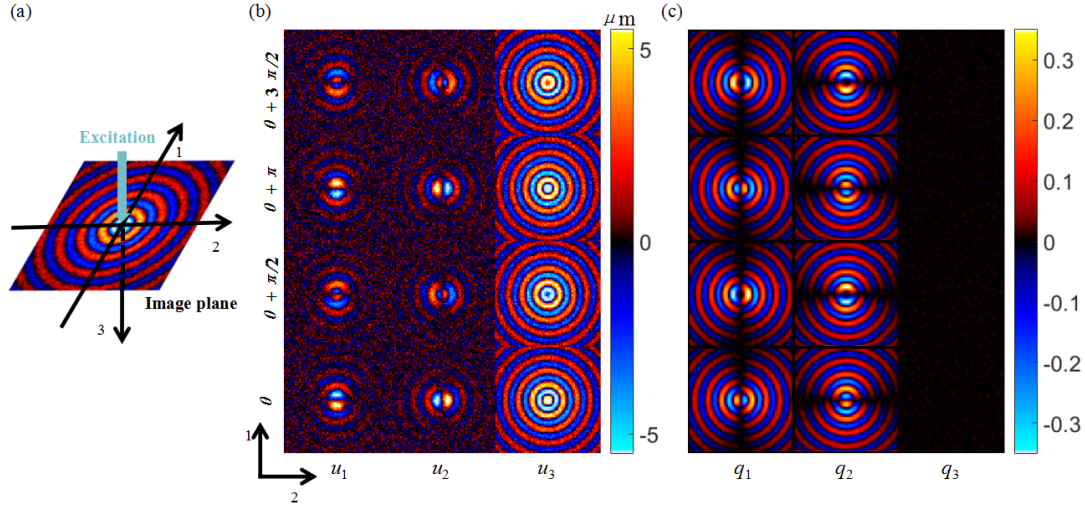


FIGURE 1: (a) Configuration de la source d'excitation simulée à incidence normale, (b) Le champ du déplacement calculé, \mathbf{u} , and (c) Le champ rotationnel calculé, \mathbf{q} , selon des trois directions d'encodage (colonnes) à quatre instants temporaires, $\theta + k\pi/2$, $k \in \{0, 1, 2, 3\}$, séparés uniformément sur une période d'excitation mécanique (rangs) pour $f = 200$ Hz et $\text{SNR} = 30$ à incidence normale.

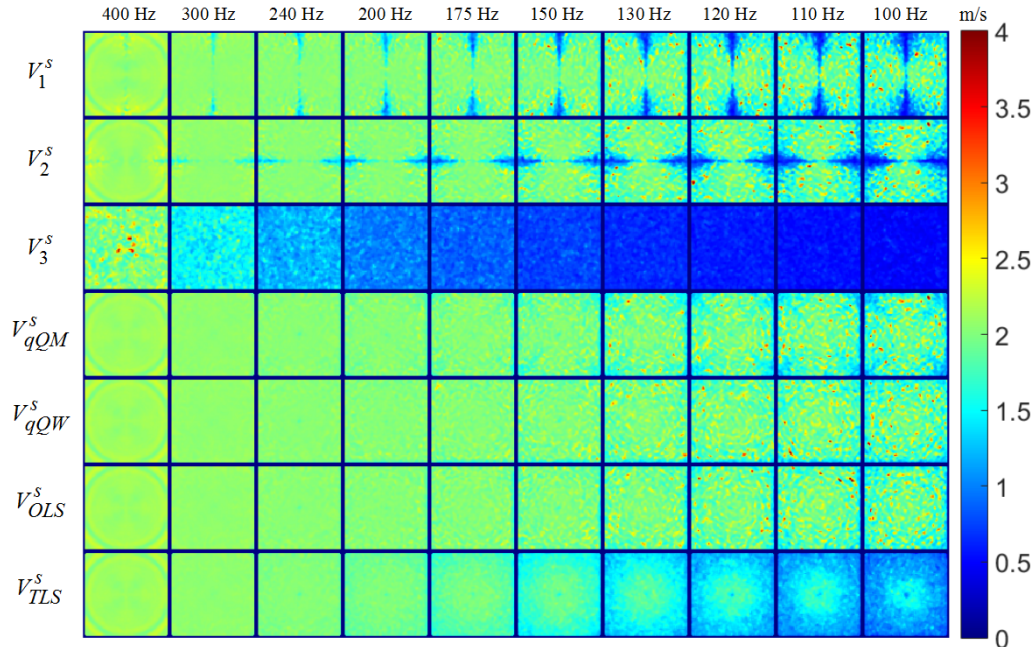


FIGURE 2: Cartes de vitesse individuelles ($V^s_i, i \in \{1, 2, 3\}$) et pondérées ($V^s_{qQM}, V^s_{qQW}, V^s_{OLS}, V^s_{TLS}$) (rangs) pour $f = 100 \sim 400$ Hz (colonnes) et $\text{SNR} = 30$ à incidence normale.

Nous avons proposé une méthode pour caractériser la propagation de l'incertitude au travers de la procédure de la reconstruction, et par conséquent une voxel-wise carte de qualité est obtenue pour caractériser la qualité des données. Différentes stratégies de pondération sur la qualité (qQM, qQW, OLS, TLS) sont évaluées sous des mêmes conditions d'acquisition et reconstruction. Ces stratégies de pondération sont démontrés effectives pour combiner la vitesse de cisaillement obtenues de différentes directions d'encodage et d'obtenir une estimation plus précise (Figure 2). Par contre, des stratégies basant sur la qualité du champ rotationnel de l'onde de cisaillement (qQM, qQW) sont plus appropriées par rapport aux stratégies basant sur des méthodes des moindres carrés (OLS, TLS) étant donné des différences potentielles en le RSB et la sensibilité d'encodage dans différentes directions d'encodage. En outre, on a proposé un nouveau critère MAPE (Moyenne de Absolute Pourcentage Erreur) pour évaluer simultanément l'exactitude et la précision de la reconstruction. En utilisant ce critère d'évaluation, nous avons montré que un échantillonnage spatial approprié (λ/a valeur approprié) des champs de déplacement discrets et bruités peut améliorer simultanément l'exactitude et la précision de la reconstruction (Figure 3). La gamme appropriée pour cet échantillonnage spatial peut être déduite de *in silico* abaci calculés avec des paramètres d'acquisition et des processus de reconstruction spécifiques à l'étude. De plus, nous avons démontré le rééchantillonnage comme une prétraitement efficace pour régler l'échantillonnage spatial mal défini à la gamme favorable.

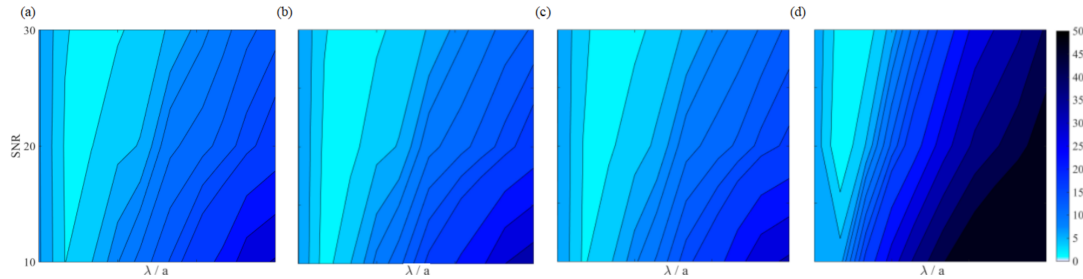


FIGURE 3: MAPEs de V^s_{qQM} (a), V^s_{qQW} (b), V^s_{OLS} (c) et V^s_{TLS} (d) à incidence normale en fonction de λ/a pour $SNR = \{30, 20, 10\}$.

Dans Chapitre 4, on a réalisé des expériences *in vitro* sur des fantômes pour l'objectif de, d'une part valider des conditions d'acquisition et reconstruction appropriées pour ERM proposés dans le Chapitre 3 ainsi que le paramètre de qualité pour SSI proposé par le système, d'autre part mener une comparaison impartiale entre ERM et SSI pour une validation croisée de leur mesures. D'abord, des mesures ont été faites sur une série de fantômes homogènes calibrés commerciaux (Model 039, CIRS, Norfolk, VA, USA). Chaque fantôme a été caractérisé par SSI sur un Aixplorer système ultrasonore avec trois sondes différentes (XC6-1 MHz, SL10-2 MHz et SL15-4MHz). Et puis, chaque fantôme a été caractérisé par ERM sur un Philips 1.5 T MR Scanner à cinq fréquences d'excitation différentes. En outre, des fantômes ont été caractérisés par l'élastographie transitoire sur un FibroScan 502 TOUCH système (Echosens, Paris, France) pour donner des valeurs de référence. En parallèle, des mesures ont été faites sur deux fantômes polyvinyl alcohol (PVA) faits à

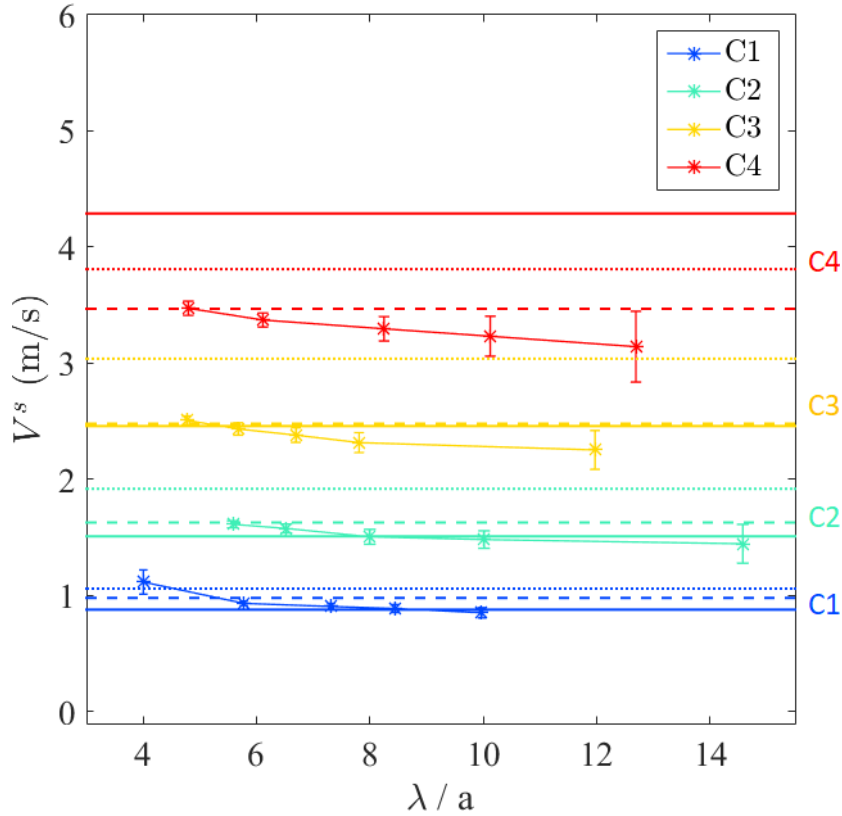


FIGURE 4: Valeurs moyennes et écart-types de V^s_{qQW} pour des phantoms C1-C4 sur des régions d'intérêts avec le même niveau de qualité 40 ± 4 en fonction de λ/a . Pour chaque fantôme, trois valeurs de référence ont été fournies. La ligne solide représente la mesure FibroScan; la ligne en dash représente la mesure SSI; la ligne en pointillé représente la mesure CIRS.

maison avec différentes densité massique. Pour chaque fantôme, des acquisitions SSI ont été réalisées sur le même Aixplorer système ultrasonore avec deux sondes différentes (SL10-2 MHz et SL15-4MHz); des acquisitions ERM à cinq fréquences d'excitation différentes ont été réalisées sur un Bruker 11.7 T MR scanner. Pour tous les deux types de fantômes, des stratégies proposées pour assurer la validité des mesures de ERM et SSI sont bien validées. Échantillonnage spatial approprié (λ/a environ $7 \sim 10$) pour ERM s'est avéré efficace pour améliorer l'exactitude et la précision de la reconstruction ERM au travers d'une large gamme de fréquence d'excitation: de dizaines de Hertz à milliers de Hertz, et aussi au travers des différents niveaux de résolution spatiale: de centaines de micromètres à plusieurs millimètres (Figure 4-5). L'efficacité de rééchantillonnage a été démontrée pour satisfaire des conditions d'acquisition appropriées. Pour SSI, le paramètre de qualité fourni par le système s'est avéré pertinent pour éliminer des mesures non fiables. En outre, des mesures entre des différents sondes ultrasonores sont en accord les uns et les autres, qui a montré que ces deux types de fantômes sont quasi-élastiques et donc la dispersion liée à la viscosité est négligeable pour des mesures SSI. Enfin, compte tenu de la minimisation des biais liés à la théorie, l'acquisition et la reconstruction, des mesurese de ERM et SSI concordent bien les uns et les autres (Figure 6-7).

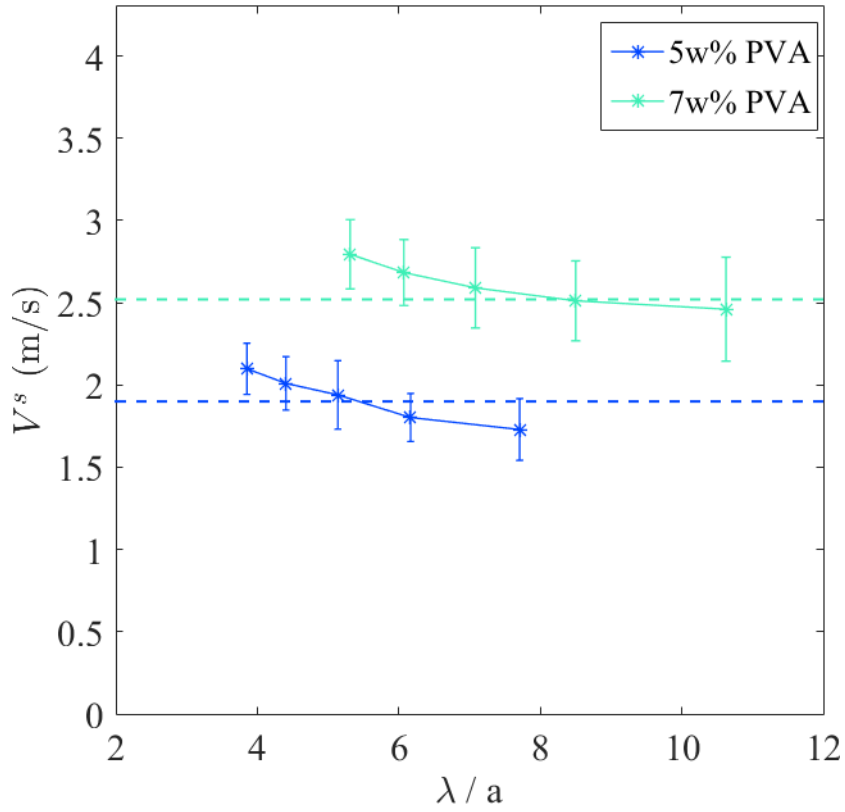


FIGURE 5: Valeurs moyennes et écart-types de V^s_{qQW} pour 5w% et 7w% PVA phantoms sur des régions d'intérêts avec le même niveau de qualité 40 ± 4 en fonction de λ/a . La ligne en dash représente la mesure SSI.

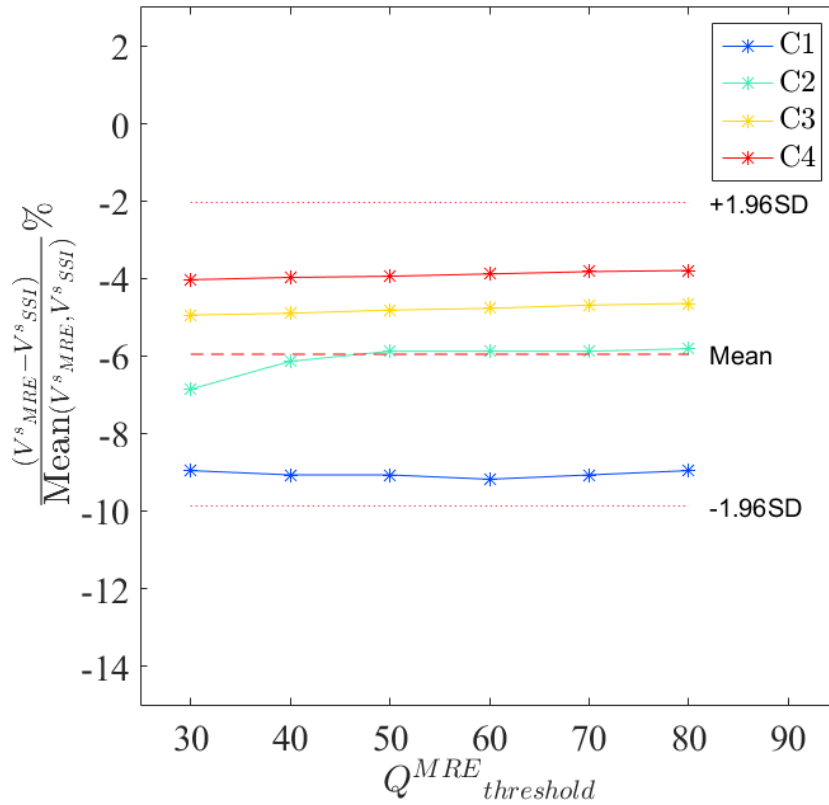


FIGURE 6: Bland et Altman type analyse entre des mesures SSI et des V^s_{qQW} valeurs obtenues de ERM avec rapports λ/a appropriés pour des fantômes calibrés C1-C4.

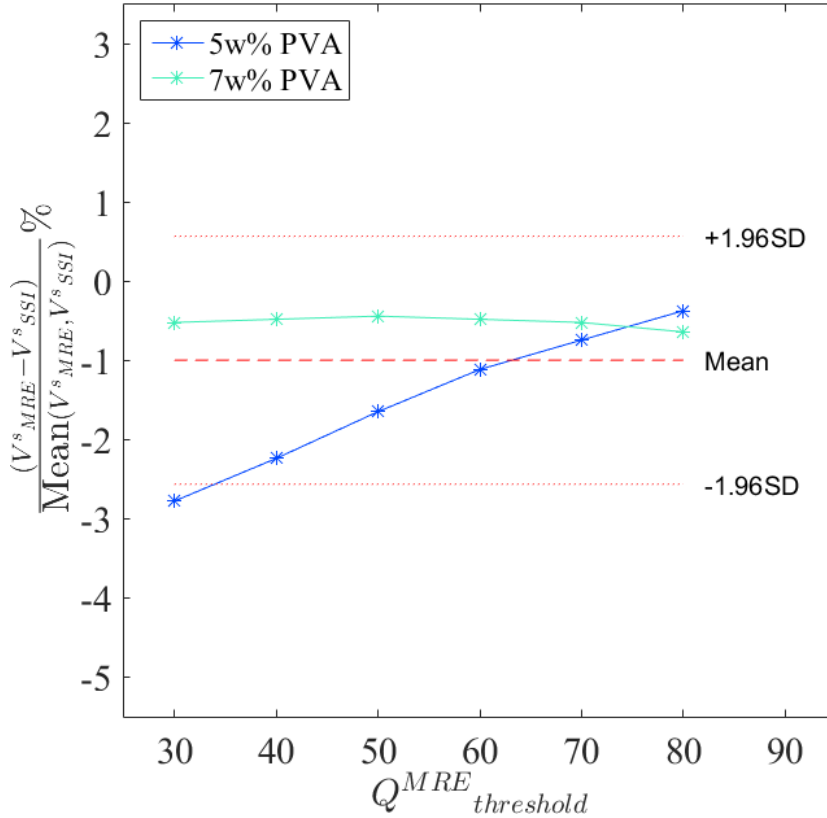


FIGURE 7: Bland et Altman type analyse entre des mesures SSI et des V^s_{qQW} valeurs obtenues de ERM avec rapports λ/a appropriés pour 5w% and 7w% PVA fantômes.

Dans Chapitre 5, on a réalisé *in vivo* des mesures SSI et ERM du foie sur deux volontaires sains en incorporant des stratégies d'optimisation pour des deux modalités. Des mesures SSI ont été réalisées sur un Aixplorer système avec deux sondes différents (XC6-1 MHz et SL10-2 MHz). Des mesures ERM ont été réalisées sur un Philips 1.5 T MR Scanner à une seule fréquence pour Volontaire 1 et à 5 fréquences pour Volontaire 2. Pour Volontaire 1 (Table 2), des mesures SSI entre des sondes différentes sont bien cohérentes qui démontrent que le foie de Volontaire 1 peut être considéré comme quasi-élastique. Du coup, le biais théorique entre ERM et SSI est négligeable. Dans ce contexte, des mesures ERM et SSI avec qualité optimisée concordent bien les uns et les autres. Pour Volontaire 2 (Table 3-4), des mesures SSI entre des sondes différentes et aussi des mesures ERM convergées pour différentes fréquences d'excitation diffèrent significativement. Du coup, la dispersion reliée à la viscosité du foie n'est plus négligeable. Dans ce contexte, des mesures ERM et SSI sont toutes fréquence dépendentes. Par conséquent, des mesures ERM et SSI pour la même fréquence spécifique sont nécessaires pour réaliser une comparaison impartiale entre des deux modalités dans un foie viscoélastique.

TABLE 2: SSI and MRE V^s and $|G^*|$ measurements for Volunteer 1

	SSI								MRE			
	Convex probe				Linear probe				70 Hz			
	V^s (m/s)		$ G^* $ (kPa)		V^s (m/s)		$ G^* $ (kPa)		V^s (m/s)		$ G^* $ (kPa)	
	MV	SD	MV	SD	MV	SD	MV	SD	MV	SD	MV	SD
Segment 4	1.46	0.06	2.14	0.18	1.44	0.17	2.12	0.51	1.48	0.23	2.23	0.47
Segment 6	1.50	0.06	2.27	0.18	1.53	0.11	2.33	0.32	1.49	0.19	2.30	0.48
Segment 8	1.62	0.12	2.32	0.42	1.63	0.23	2.73	0.86	1.49	0.18	2.05	0.44
Whole liver									1.48	0.20	2.19	0.47

TABLE 3: SSI and MRE V^s measurements for Volunteer 2

	SSI				MRE									
	Convex probe		Linear probe		40 Hz		65 Hz		70 Hz		85 Hz		105 Hz	
	MV	SD	MV	SD	MV	SD	MV	SD	MV	SD	MV	SD	MV	SD
	(m/s)		(m/s)		(m/s)		(m/s)		(m/s)		(m/s)		(m/s)	
Segment 4	1.71	0.10	2.09	0.43	0.76	0.06	1.37	0.15	1.47	0.22	1.60	0.12	2.26	0.38
Segment 6	1.69	0.09			0.76	0.08	1.26	0.12	1.43	0.08	1.77	0.18	2.09	0.51
Whole liver					0.75	0.07	1.35	0.13	1.47	0.10	1.69	0.18	2.07	0.48

TABLE 4: SSI and MRE $|G^*|$ measurements for Volunteer 2

	SSI				MRE									
	Convex probe		Linear probe		40 Hz		65 Hz		70 Hz		85 Hz		105 Hz	
	MV	SD	MV	SD	MV	SD	MV	SD	MV	SD	MV	SD	MV	SD
	(kPa)		(kPa)		(kPa)		(kPa)		(kPa)		(kPa)		(kPa)	
Segment 4	2.95	0.31	4.57	1.81	0.61	0.15	2.56	0.83	2.48	0.76	2.74	0.44	5.00	1.20
Segment 6	2.87	0.31			0.58	0.11	1.77	0.29	2.15	0.28	3.25	0.70	4.37	1.68
Whole liver					0.58	0.12	2.07	0.51	2.28	0.31	2.97	0.66	4.33	1.60

Acknowledgements

Many people contributed to this work in one way or another during this three-year adventure. I want to write down everybody's name, but unfortunately, I do not have the amount of paper that such a task would require. Hence, I would specially like to thank:

- The Chinese Scholarship Council, which financially supported me during three years through their PhD fellowship.
- My official PhD director, Irène Buvat, and two supervisors, Claire Pellot-Barakat and Xavier Maître for their unconditional support throughout this long but enriching process.
- All the members of IMIV and IR4M for their help and accompany during three years, especially Albine Pinseel, AIT AISSA Karima and also Jean-Christophe Ginefri, our representative in doctoral school, for their meticulous help and high efficiency in administrative affairs
- Marion Tardieu, Benoit Larrat, Hongchen Wang and Philippe Garteiser for their help and advice during my thesis
- Maud Creze and Linda Chami for their rich clinical experiences and precious help to the experimental part of my work.
- Meng Yin, Stefan Catheline for accepting to be the rapporteurs of this work, Elisabeth Brusseau, Najat Salameh for accepting to be the jury member.
- Last but not the least my family members and my girl friend, who always supported, encouraged me and firmly believed I was going to succeed despite the difficulties I encountered.

Contents

Abstract	ii
Résumé de manuscrit en français	iii
Acknowledgements	xii
General Introduction	1
1 Elastography: an emerging medical imaging modality	3
1.1 From palpation to Elastography	3
1.2 Underlying physical mechanisms for Elastography	4
1.2.1 Hooke's law	4
1.2.1.1 Generalized Hooke's law	4
1.2.1.2 Isotropic media	6
1.2.2 Mechanical wave equation	7
1.2.2.1 Elastic media	7
1.2.2.2 Helmholtz decomposition	7
1.2.2.3 Viscoelastic media	8
1.3 Ultrasound Elastography	9
1.3.1 Strain Elastography	9
1.3.2 Monochromatic Elastography	11
1.3.2.1 Sonoelastography	11
1.3.2.2 Vibro-acoustography	12
1.3.3 Transient Elastography	13
1.3.3.1 1D Transient Elastography	13
1.3.3.2 2D Transient Elastography	14
1.3.3.3 Acoustic Radiation Force Imaging (ARFI)	15
1.3.3.4 Supersonic Shear Imaging (SSI)	15
1.4 Magnetic Resonance Elastography	17
1.4.1 Quasi-static MRE	17
1.4.2 Dynamic MRE	17
1.4.2.1 Excitation equipments	18
1.4.2.2 Imaging sequences	20
1.4.2.3 Reconstruction methods	26
1.5 Potential clinical applications	27
1.5.1 Cancer diagnosis	27
1.5.2 Diffuse disease characterization	29
1.5.3 Therapy monitoring	30
1.6 Conclusions	30

2	Magnetic Resonance Elastography (MRE) and Supersonic Shear Wave Imaging (SSI): a methodological comparison	32
2.1	Introduction	32
2.2	External excitation	32
2.2.1	Guided compression wave excitation for MRE	32
2.2.2	Supersonic acoustic radiation force for SSI	35
2.2.3	Summary of the excitation step	37
2.3	Displacement field acquisition	37
2.3.1	Spin echo based MRE sequence	38
2.3.2	Ultrafast imaging and ultrasonic speckle interferometry for SSI	39
2.3.3	Summary of the acquisition step	40
2.4	Mechanical properties reconstruction	41
2.4.1	q-based model independent AIDE algorithm for MRE	41
2.4.2	Time of flight method for SSI	42
2.4.3	Summary of the reconstruction step	43
2.5	Discussions and Conclusions	44
3	Acquisition and reconstruction conditions <i>in silico</i> for accurate and precise Magnetic Resonance Elastography	46
3.1	Introduction	46
3.2	Methods	47
3.2.1	Analytic wave simulation	47
3.2.2	Simulated experimental conditions	48
3.2.3	Averaged shear velocity calculation	49
3.2.3.1	q-field quality parameter	50
3.2.3.2	q-field quality based methods	52
3.2.3.3	Least square based methods	52
3.2.4	Data analysis	53
3.3	Results and Discussions	54
3.3.1	Simulated wave patterns	54
3.3.2	Effects of averaging strategies on MRE accuracy and precision	55
3.3.3	Appropriate λ/a range for accurate and precise MRE	60
3.3.4	Effects of interpolation/decimation on regulating the λ/a ratio	62
3.3.5	Performance of the total q-field quality parameter Q^{MRE}_t on evaluating the reconstruction quality	63
3.4	Conclusions	64
4	In vitro SSI and MRE comparison study on phantoms	66
4.1	Introduction	66
4.2	In vitro phantom experiments	67
4.2.1	Commercial calibrated liver fibrosis phantoms	67
4.2.1.1	Phantom description	67
4.2.1.2	Experimental protocols	68
4.2.2	Home-made polyvinyl alcohol (PVA) phantoms	70
4.2.2.1	Phantom description	70

4.2.2.2	Experimental protocols	72
4.3	Computation of shear velocity mapping and data analysis . .	73
4.3.1	SSI post-processing	73
4.3.2	MRE reconstruction	74
4.4	Results and Discussions	75
4.4.1	Commercial calibrated liver fibrosis phantoms	75
4.4.1.1	SSI using different ultrasound probes	75
4.4.1.2	MRE for different excitation frequencies	79
4.4.1.3	SSI and MRE measurement comparison	83
4.4.2	PVA phantoms	85
4.4.2.1	SSI using different ultrasound probes	85
4.4.2.2	MRE for different excitation frequencies	89
4.4.2.3	SSI and MRE measurement comparison	92
4.5	Conclusions	93
5	In vivo SSI and MRE comparison study on liver	94
5.1	Introduction	94
5.2	Methods	95
5.2.1	Experimental protocols	95
5.2.1.1	SSI liver acquisition	95
5.2.1.2	MRE liver acquisition	96
5.2.2	Data analysis	97
5.2.2.1	SSI post-processing	97
5.2.2.2	MRE reconstruction	98
5.3	Results and Discussions	98
5.3.1	Volunteer 1	98
5.3.1.1	SSI liver measurements	98
5.3.1.2	MRE liver measurements	102
5.3.1.3	SSI and MRE measurement comparison	104
5.3.2	Volunteer 2	106
5.3.2.1	SSI liver measurements	106
5.3.2.2	MRE liver measurements	109
5.3.2.3	SSI and MRE measurement comparison	112
5.4	Conclusions	114
	Conclusions and perspectives	116
	Publication List	119
	Bibliography	120

General Introduction

Medical imaging is the cornerstone of modern medicine. It is able to reveal the anatomical, functional, or molecular alterations which underlie a variety of diseases. Nowadays, medical imaging technologies have been widely applied in clinical routine to help clinicians to better take charge of the patients during the whole care procedure, from early diagnosis to quantification of disease severity and evaluation of response to therapy. Currently, the main clinical imaging modalities include: Computer Tomography (CT), Ultrasound Imaging (US), Magnetic Resonance Imaging (MRI), and Positron Emission Tomography (PET). All these modalities can provide anatomical and functional imaging. In addition, MRI and PET can further provide molecular imaging. In general, disease related alterations first occur at molecular and functional levels. When the anatomical changes appear, diseases have usually already progressed to an advanced stage. In this context, imaging information which can reveal early molecular or functional alterations is extremely important for the prognostic of patients. Similarly, these information is also useful to monitor the effectiveness of the treatment plan.

Mechanical properties of human soft tissue can provide important information about tissue state. Their variations, which usually appear before apparent anatomical changes, are in fact related to tissue composition changes, inflammation effects, cell proliferation, etc. Therefore, they are considered to be appealing biomarkers for disease management. Since the ancient Egypt time, soft tissue rigidity has been exploited as an important medical indication through the practice of palpation. Nowadays, with the help of medical imaging technologies, palpation can alternatively be performed by a more objective, less operator dependent method, which is called Elastography. In addition, regional quantitative mechanical properties can be derived from Elastography. Generally, Elastography is composed of three elementary steps: external excitation to generate tissue deformation, displacement field acquisition, and reconstruction of mechanical parameters. Since the birth of Elastography thirty years ago (Krouskop, Dougherty, and Vinson, 1987), technical evolutions in all three elementary steps have taken place. A variety of approaches have been proposed. Amid the different approaches, Magnetic Resonance Elastography (MRE) and Ultrasound (US) based Supersonic Shear Imaging (SSI) have shown particular interests. MRE inherits the advantage of 3D volume acquisition of MRI, which permits to characterize the distribution of tissue mechanical properties along the three dimensions. SSI inherits the advantage of time efficiency of US, which permits to characterize the mechanical properties of tissue in real time. Their advantages compete with each other and hence they can satisfy the clinicians' needs for different

stages of disease management. Thus the combination of the two modalities can improve the clinical management of patients.

To this date, a large number of studies have been carried out to demonstrate the feasibility and clinical relevance of MRE and SSI in a variety of clinical applications. However, the issues concerning the measurement validity of each modality and the measurement cross-validation of the two modalities have not yet been fully addressed. As a consequence, intra-modality and inter-modality disagreements are present, which impede the interchangeability of the two modalities. In this context, the objective of my thesis was: 1) to investigate the potential bias sources leading to intra-modality / inter-modality disagreements and propose corresponding optimization strategies to minimize them; 2) to validate the proposed optimization strategies and cross-validate MRE and SSI measurements through *in vitro* and *in vivo* comparison studies.

This dissertation begins with a state of the art in elastography. In this chapter, the basic physical principles of elastography are first presented. Then a brief overview of the evolution of US and MRI-based elastography techniques is given. Finally, the potential clinical applications are summarized for both modalities.

In Chapter 2, the methodological details and the experimental implementation of MRE and SSI, which are the core of the work, are presented. The methodological differences between MRE and SSI and the resulting potential measurement bias sources occurring at each elastography elementary step are investigated. Strategies towards an unbiased comparison between MRE and SSI measurements are proposed.

In Chapter 3, a dedicated simulation study was carried out to investigate the appropriate acquisition and reconstruction conditions for accurate and precise MRE. During this study, we introduced a quality parameter for evaluating the reconstruction quality and *in silico* abaci for determining favorable acquisition conditions according to study-specific acquisition and reconstruction processes. In addition, the performance of different averaging strategies and the influence of data resampling were investigated.

Chapters 4 and 5 focus on the experimental validation of the optimization strategies proposed for MRE and SSI as well as on the experimental cross-validation of the quality-guided MRE and SSI measurements. In Chapter 4, two *in vitro* quality-guided MRE and SSI measurement comparison studies were carried out respectively on manufactured fibrosis-graded liver phantoms and home-made polyvinyl alcohol phantoms. In Chapter 5, the *in vivo* quality-guided MRE and SSI measurement comparison was performed on the livers of two healthy volunteers.

1 Elastography: an emerging medical imaging modality

1.1 From palpation to Elastography

Tactual palpation has been practiced in medicine since antiquity. Together with auscultation and tactile fremitus, palpation is still widely applied by clinicians. This practice allows clinicians to detect abnormalities in human soft tissues by sensing the changes of rigidity, which are generally correlated with pathological phenomena. For instance, scirrhous carcinoma of the breast are extremely hard nodules as a result of increased stromal density. However, the applications of palpation are limited in several aspects. First, palpation is operator dependent and the interpretation of the tissue rigidity is subjective, which make it difficult to standardize and normalize this practice; Second, palpation can only provide a global, qualitative estimation which does not satisfy the need of regional precise quantification for modern medicine; Finally, the application of palpation is limited to the tissues of superficial organs, such as breast, thyroid, and partially liver. In order to overcome these limitations, it has been proposed to replace the subjective manual palpation with an objective palpation performed using medical imaging technologies. This eventually emerged as the Elastography technology.

Elastography consists in visualizing and recording the tissue deformation induced by an external excitation using medical imaging technologies, then reconstructing the underlying mechanical properties of tissue from the measured deformation. In summary, Elastography is composed of three elementary steps: external excitation of the tissue, acquisition of the tissue deformation and reconstruction of the mechanical properties of tissue. Since the concept of Elastography was initialized more than twenty years ago, a variety of medical imaging modalities, such as ultrasound imaging, magnetic resonance imaging (MRI) as well as optical imaging, have been proposed to form imaging method specific Elastography. Among the different approaches, magnetic resonance elastography (MRE) and ultrasound elastography have shown particular perspectives for clinical applications. Nowadays, the two modalities are part of the imaging protocols in some clinical routines, for example staging liver fibrosis (Singh et al., 2016; Stebbing et al., 2010; Bavu et al., 2011).

1.2 Underlying physical mechanisms for Elastography

The essential parameter for characterizing soft tissues either by manual palpation or by Elastography is tissue elasticity. The tissue elasticity permits to relate the stress applied onto the tissue and the resulting strain of the tissue through the Hooke's law. In this way, the elasticity value can be deduced by resolving the Hooke's law upon proper joint assumptions and equations, which sets the reconstruction principle for Elastography. The Hooke's law is thus the fundamental element for understanding the basic physical mechanism supporting Elastography.

1.2.1 Hooke's law

The Hooke's law was originally stated by Robert Hooke to describe the first-order linear elastic behavior of springs, namely the force applied on the spring is proportional to the elongation of the spring. Afterwards, the Hooke's law was extended by physicists to describe the linear relationship between the applied stress, σ , and the resulting strain, ϵ , for elastic media under a small deformation.

$$\sigma = E \cdot \epsilon \quad (1.1)$$

with E as the Young's modulus. The original Hooke's law is in scalar format, which can be used to describe a simple traction or compression case. However, in real cases, the stress and strain may have multiple independent components, and so does the elasticity. Thus, the Hooke's law in tensor format is needed to generally describe this linear elastic behavior.

1.2.1.1 Generalized Hooke's law

In general, an arbitrary point, \mathbf{r} , of the continuum can be considered as an infinitesimal elementary volume. The stress has components on all the six sides of the elementary volume. On each side the stress can be resolved into components normal to the face and within it. This situation is illustrated in Fig (1.1) for the three visible facets. Thus, the exact form of the stress on the elementary volume should be a second order tensor, normally noted as σ_{ij} (equation (1.2)), which defines the stress acting on the plane normal to the axes i and being oriented along the direction j . The stress tensor components with repeating indices, e.g. σ_{11} , are denoted as normal stress, while the components with different indices are called shear stress. Consequently, this gives six shear and three normal stress components acting on the elementary volume. If the medium is in static equilibrium, the sum of all stress components acting on all the six sides is zero, inducing the symmetry of the stress tensor with $\sigma_{ij} = \sigma_{ji}$. Thus the stress tensor has six independent components.

$$\sigma_{ij} = \begin{bmatrix} \sigma_{11} & \sigma_{12} & \sigma_{13} \\ \sigma_{21} & \sigma_{22} & \sigma_{23} \\ \sigma_{31} & \sigma_{32} & \sigma_{33} \end{bmatrix} \quad (1.2)$$

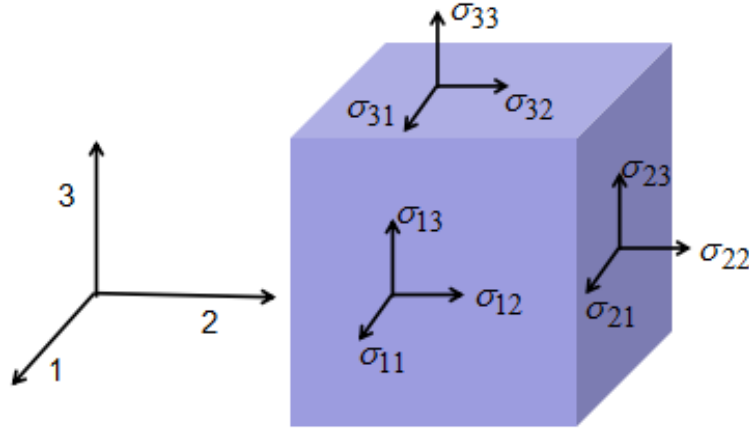


FIGURE 1.1: Illustration of the stress tensor components, σ_{ij} , on an elementary volume.

As mentioned above, each stress induces a strain, thus the exact form of the strain on the elementary volume should also be a second order tensor, normally noted as ϵ_{ij} (equation (1.3)). The components of the strain tensor with repeating indices are denoted as normal strain, all others as shear strain. Just as the stress tensor, the strain tensor has six independent components because of the static equilibrium, namely:

$$\epsilon_{ij} = \begin{bmatrix} \epsilon_{11} & \epsilon_{12} & \epsilon_{13} \\ \epsilon_{21} & \epsilon_{22} & \epsilon_{23} \\ \epsilon_{31} & \epsilon_{32} & \epsilon_{33} \end{bmatrix} \quad (1.3)$$

With the tensor definition of the stress and strain, the Hooke's law can be generalized along the tensor formalism (equation (1.4)) to describe the linear relationship between the stress and strain tensors under small strain level, where C_{ijkl} is introduced as the stiffness tensor.

$$\sigma_{ij} = C_{ijkl}\epsilon_{kl}, \text{ with } i, j, k, l \in \{1, 2, 3\} \quad (1.4)$$

The high order tensor format for Hooke's law leads to complicated relations, but it can be remarkably simplified by considering the symmetry of the tensors σ_{ij} , ϵ_{kl} and C_{ijkl} , and applying the Voigt notation to reduce the tensor order. Thus, equation (1.4) can be rewritten as a system of six linear equations:

$$\begin{bmatrix} \sigma_{11} \\ \sigma_{22} \\ \sigma_{33} \\ \sigma_{23} \\ \sigma_{13} \\ \sigma_{12} \end{bmatrix} = C_{IJ} \times \begin{bmatrix} \epsilon_{11} \\ \epsilon_{22} \\ \epsilon_{33} \\ \epsilon_{23} \\ \epsilon_{13} \\ \epsilon_{12} \end{bmatrix}, \text{ with } I, J \in \{1, 2, 3, 4, 5, 6\} \quad (1.5)$$

By simplification, the 4th order stiffness tensor, C_{ijkl} , with 81 components, is reduced to a 6×6 matrix, C_{IJ} , with 36 components. In addition, because of $C_{IJ} = C_{JI}$, the stiffness tensor has only 21 independent components.

1.2.1.2 Isotropic media

The composition of the 21 independent components for the stiffness tensor depends on the media's microscopical symmetry, which has in total 32 classes. For humane soft tissues, two symmetry classes are more often supposed, namely the isotropic class which is most widely used because of its simplicity, and the transverse isotropic class which is of particular interest for soft tissue with obvious fiber orientation, such as muscle and brain. In my thesis, we focus on the isotropic class. Assuming an isotropic elastic medium, C_{IJ} has only two independent components, called the Lamé parameters, λ and μ (the shear modulus). Equation (1.5) can then be explicitly written as:

$$\begin{bmatrix} \sigma_{11} \\ \sigma_{22} \\ \sigma_{33} \\ \sigma_{23} \\ \sigma_{13} \\ \sigma_{12} \end{bmatrix} = \begin{bmatrix} \lambda + 2\mu & \lambda & \lambda & 0 & 0 & 0 \\ \lambda & \lambda + 2\mu & \lambda & 0 & 0 & 0 \\ \lambda & \lambda & \lambda + 2\mu & 0 & 0 & 0 \\ 0 & 0 & 0 & 2\mu & 0 & 0 \\ 0 & 0 & 0 & 0 & 2\mu & 0 \\ 0 & 0 & 0 & 0 & 0 & 2\mu \end{bmatrix} \times \begin{bmatrix} \epsilon_{11} \\ \epsilon_{22} \\ \epsilon_{33} \\ \epsilon_{23} \\ \epsilon_{13} \\ \epsilon_{12} \end{bmatrix} \quad (1.6)$$

The equation (1.6) can be further simplified as:

$$\sigma_{ij} = \sum_l \lambda \epsilon_{ll} \delta_{ij} + 2\mu \epsilon_{ij} \quad (1.7)$$

where δ_{ij} is the Kronecker symbol ($\delta_{ij} = 1$ when $i = j$, 0 otherwise). With the two Lamé parameters, we can deduce three other elastic parameters as:

$$\begin{aligned} E &= \mu \frac{3\lambda + 2\mu}{\lambda + \mu}, \\ K &= \lambda + \frac{2\mu}{3}, \\ \nu &= \frac{\lambda}{2(\lambda + \mu)}. \end{aligned} \quad (1.8)$$

where K is the bulk modulus defined as the ratio of the infinitesimal pressure increase to the resulting relative decrease of the volume, ν is the Poisson's ratio defined as the signed ratio of transverse strain to axial strain.

Because soft tissue is mainly composed of water, it is hence quasi-incompressible. The compression modulus K can reach several GPa, which is far beyond the shear modulus, μ , normally in a range of tens of kPa. In this context, we have $K \gg \mu$, so that $K \approx \lambda$ and $\nu \approx 0.5$. The Young's modulus can thus be simplified as:

$$E = 3\mu \quad (1.9)$$

In summary, the generalized Hooke's law in equation (1.6) describes an equilibrium state of soft tissue under static excitation. It is the basic reconstruction principle for static Elastography. However, it is difficult to measure the tensor components using medical imaging technologies, especially the stress tensor. As a result, the static Elastography can only give qualitative information.

1.2.2 Mechanical wave equation

1.2.2.1 Elastic media

In a dynamic excitation mode, the perturbation state of soft tissue propagates in the form of a mechanical wave. The underlying mechanical wave equation can be developed by applying the Newton's second law to describe the perturbation state for each surface of an arbitrary elementary volume, \mathbf{r} :

$$\rho \frac{\partial u_i(\mathbf{r}, t)}{\partial t^2} = \sum Forces = \sum_j \frac{\partial \sigma_{ij}(\mathbf{r}, t)}{\partial r_j}, \quad i, j \in \{1, 2, 3\}. \quad (1.10)$$

where ρ is the density of soft tissue, $u_i(\mathbf{r}, t)$ represents the displacement field component for an arbitrary elementary volume \mathbf{r} , at time t , along direction i .

By substituting equation (1.7) into equation (1.10), we get the equation linking the Newton's second law and the Hooke's law as:

$$\rho \frac{\partial^2 u_i(\mathbf{r}, t)}{\partial t^2} = \sum_j \mu \frac{\partial^2 u_i(\mathbf{r}, t)}{\partial r_j^2} + \sum_j (\lambda + \mu) \frac{\partial u_j(\mathbf{r}, t)}{\partial r_j \partial r_i}. \quad (1.11)$$

Finally, the wave equation governing the displacement field, $\mathbf{u}(\mathbf{r}, t)$, in elastic, isotropic, and locally homogeneous media can be written as:

$$\rho \frac{\partial^2 \mathbf{u}(\mathbf{r}, t)}{\partial t^2} = \mu \nabla^2 \mathbf{u}(\mathbf{r}, t) + (\lambda + \mu) \nabla(\nabla \cdot \mathbf{u}(\mathbf{r}, t)). \quad (1.12)$$

1.2.2.2 Helmholtz decomposition

The mechanical wave propagation in soft tissue principally consists of three components: the compression wave, the shear wave, and the coupling term between the two previous components. Normally, the amplitude of the coupling term decreases much more rapidly with the distance to the excitation source than the other two components, and hence the coupling term is often negligible. Thus the displacement field \mathbf{u} is mainly composed of the compression wave component, \mathbf{u}_c , and the shear wave components, \mathbf{u}_s . The characteristics of the two waves are illustrated in Figure (1.2).

The compression wave is curl-free and the shear wave is divergence-free. According to the Helmholtz decomposition, equation (1.12) can be decomposed into two separate equations governing the compression wave and the shear wave respectively:

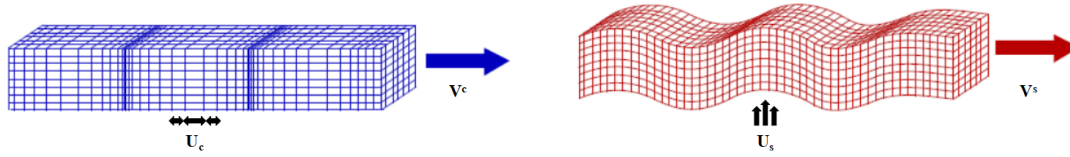


FIGURE 1.2: Illustration of the propagation characteristics of the compression wave component (left) and the shear wave component (right). For the compression wave, the media deformation (\mathbf{u}_c) is parallel to the wave propagation velocity (\mathbf{V}^c); For the shear wave, the media deformation (\mathbf{u}_s) is perpendicular to the wave propagation velocity (\mathbf{V}^s).

$$\begin{aligned}\frac{\partial \mathbf{u}_c}{\partial t^2} &= \frac{\lambda + 2\mu}{\rho} \nabla^2 \mathbf{u}_c, \\ \frac{\partial \mathbf{u}_s}{\partial t^2} &= \frac{\mu}{\rho} \nabla^2 \mathbf{u}_s,\end{aligned}\tag{1.13}$$

From equation (1.13), we deduce the compression wave velocity, V^c , and the shear wave velocity, V^s , as:

$$V^c = \sqrt{\frac{\lambda + 2\mu}{\rho}}, \quad V^s = \sqrt{\frac{\mu}{\rho}}.\tag{1.14}$$

For soft tissue, V^c is about 1500 m/s, similar to that of water. V^c varies little with the alterations of tissue. The V^s value of soft tissue is usually between 1 and 10 m/s. It varies with the alterations of tissue, which can provide good contrast for detecting tissue abnormalities. In this context, Elastography consists in exploiting the displacement field resulting from the shear wave component and then deducing the shear elastic moduli.

1.2.2.3 Viscoelastic media

Until now, we have only focused on elastic media. However, soft tissues are generally viscoelastic. For viscoelastic media, the stress tensor not only depends on the strain tensor but also depends on the temporal derivative of the strain tensor. Thus an extra viscosity tensor, η_{ijkl} , is needed to link the stress and strain tensor. The combination of the stiffness tensor and the viscosity tensor depends on the choice of the rheological models, which serve as modeling the mechanical behaviors of materials. The different rheological models are represented by mechanical analog models, with combinations (in series or in parallel) of dampers and springs. The Voigt model, which is represented as a damper and a spring placed in parallel, was usually chosen to rewrite the Hooke's law as:

$$\sigma_{ij}(t) = C_{ijkl} \epsilon_{kl}(t) + \eta_{ijkl} \frac{\partial \epsilon_{kl}}{\partial t}.\tag{1.15}$$

Then the wave equation for viscoelastic media can be written as follows:

$$\begin{aligned} \rho \frac{\partial^2 \mathbf{u}(\mathbf{r}, t)}{\partial t^2} = & \mu \nabla^2 \mathbf{u}(\mathbf{r}, t) + (\lambda + \mu) \nabla(\nabla \mathbf{u}(\mathbf{r}, t)) \\ & + \zeta \partial_t \nabla^2 \mathbf{u}(\mathbf{r}, t) + (\xi + \zeta) \partial_t \nabla(\nabla \mathbf{u}(\mathbf{r}, t)). \end{aligned} \quad (1.16)$$

Similar to equation (1.12), equation (1.16) can also go through the Helmholtz decomposition, so that the shear viscoelastic moduli can be deduced.

Equation (1.12) and (1.16) involve the calculation of both temporal and spatial derivatives of the displacement fields, which adds complexity to resolve the equation. For simplification, the Fourier transformation is applied on the displacement field in order to separate the spatial and time domain, leading to a time independent wave equation in frequency space as follows:

$$-\rho \omega^2 \mathbf{u}(\mathbf{r}, \omega) = \mu \nabla^2 \mathbf{u}(\mathbf{r}, \omega) + (\lambda + \mu) \nabla(\nabla \mathbf{u}(\mathbf{r}, \omega)). \quad (1.17)$$

$$\begin{aligned} -\rho \omega^2 \mathbf{u}(\mathbf{r}, \omega) = & \mu \nabla^2 \mathbf{u}(\mathbf{r}, \omega) + (\lambda + \mu) \nabla(\nabla \mathbf{u}(\mathbf{r}, \omega)) \\ & + j \omega_{exc} \zeta \nabla^2 \mathbf{u}(\mathbf{r}, \omega) + j \omega_{exc} (\xi + \zeta) \nabla(\nabla \mathbf{u}(\mathbf{r}, \omega)) \end{aligned} \quad (1.18)$$

In summary, equation (1.17) and (1.18) describe a perturbation state of soft tissue under dynamic excitation for elastic media and viscoelastic media respectively. They are the basic reconstruction principles for dynamic Elastography. The main advantage of the dynamic method compared to the static method lies in that the stress and strain tensors are no more necessary as they are replaced by the displacement field, which is more easily accessible through medical imaging systems. As a result, quantitative mechanical properties can be deduced.

1.3 Ultrasound Elastography

Since the concept of Ultrasound Elastography (UE) was introduced in the 1980s, a variety of UE technologies have been developed. These different variations are mainly distinguished by the temporal characteristic of the excitation mode, from quasi static compression to sinusoidal steady state motion, and then to impulsive motion. This section aims at giving a brief summary of the evolution of ultrasound based elastography technologies.

1.3.1 Strain Elastography

Ultrasound strain elastography was first of all introduced by Ophir *et al.* (Ophir *et al.*, 1991). This technology consists in measuring the axial strain induced in the tissue by applying an axial stress as illustrated in Figure (1.3

(a)-(b)). RF echo signals acquired before and after compression are cross-correlated to search the temporal delay maximizing the cross-correlation quality. The obtained temporal delay can be directly converted to axial displacement. Then the axial strain distribution can be obtained by differentiating the axial displacement spatially. The core principle of this technology is based on the scalar Hooke's Law (1.1) for which the stiffness of the tissue is inversely proportional to the strain. Thus, the strain image measured by strain elastography can give qualitative information on the tissue stiffness, namely the lower the strain, the higher the stiffness as illustrated in Figure (1.3 (c)).

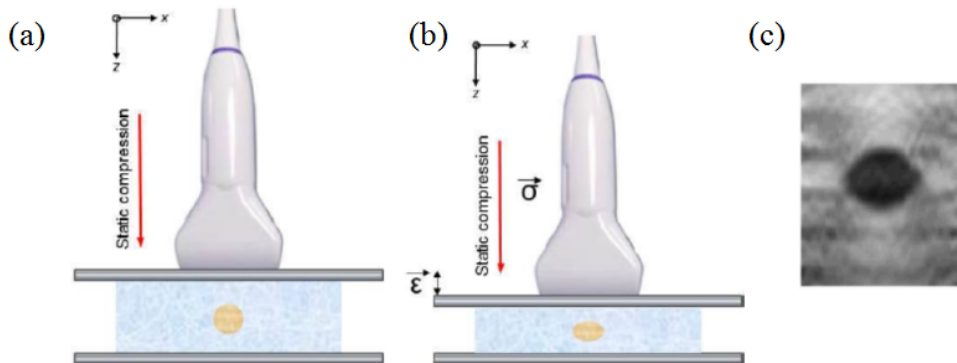


FIGURE 1.3: Static Elastography principle: an axial stress (σ) is applied on the medium to induce a deformation (ϵ). (a) medium before compression, (b) medium after compression, and (c) the corresponding strain image (zoomed around lesion) demonstrating a dark region of low strain and high stiffness (Latorre Ossa, 2012; Parker, Doyley, and Rubens, 2010).

Major engineering efforts have been made to improve the signal processing and the implementation of strain elastography (O'Donnell et al., 1994; Varghese and Ophir, 1997; Shiina et al., 2002; Hall, Zhu, and Spalding, 2003; Brusseau et al., 2008). Nowadays, strain elastography has been already installed in a number of ultrasound systems including Siemens, Hitachi, Ultrasonix etc. The advantage of the technology mainly lies in the simplicity and flexibility of using the ultrasound probe to produce localized compression near the region of interest in the breast and other superficial organs. However, this technology is challenged by the requirement to generate uniform stress over the whole region of interest in order to properly interpret the obtained strain image. It is also limited by the fact that only qualitative information can be deduced because the applied stress is not measurable. Moreover, it is difficult to compress deeper regions.

In order to overcome the limitations of ultrasound strain elastography, ultrasound dynamic elastography has been developed over the past decades. The dynamic approach can access quantitative information by exploiting the dynamic displacement field of the generated mechanical wave in the tissue. The different variations of ultrasound dynamic elastography are mainly distinguished by the frequency spectrum of the exploited mechanical wave, namely monochromatic wave and transient wave.

1.3.2 Monochromatic Elastography

Monochromatic elastography exploits an external continuous monochromatic source to excite the tissue. Then the characteristics of the generated mechanical wave is retrieved by ultrasound imaging.

1.3.2.1 Sonoelastography

Sonoelastography was inspired from Krouskop's work (Krouskop, Dougherty, and Vinson, 1987) and first developed by Lerner *et al.* (Lerner, Huang, and Parker, 1990). This technology consists in combining a low frequency external excitation (20 to 100 Hz) and ultrasound Doppler imaging to investigate the tissue elasticity. The principle of this approach lies in the fact that the frequency shift obtained by the Doppler effect is proportional to the amplitude of the displacements. It is believed that the measured amplitude of displacements is directly related to the tissue elasticity, namely the lower the amplitude, the stiffer the tissue. Nevertheless, this sonoelastography approach does not take into consideration the undesirable effects where the geometry and the heterogeneity of the medium infer wave reflections at the boundaries and where related interferences may lead to low wave amplitude or stationary waves. Moreover, this approach is still qualitative.

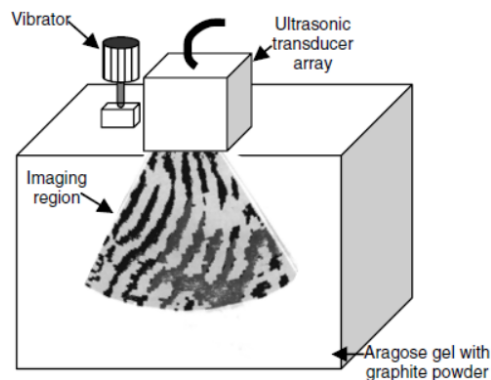


FIGURE 1.4: Illustration of the sonoelastography approach developed by Sato *et al.*, including external vibration and an imaging array with signal processing for deriving the phase of the vibration in tissue. The rate of change of phase can be estimated to yield tissue hardness (Sato *et al.*, 1985).

In order to overcome the limitations of the above first sonoelastography approach, Sato *et al.* (Sato *et al.*, 1985) developed a gradient based sonoelastography approach. This technology maps both the amplitude and the phase of the generated mechanical wave. Then the wave propagation velocity and dispersion properties can be derived by calculating the phase gradient and the amplitude gradient respectively (Figure (1.4)). The tissue elasticity can then be deduced using equation (1.9) and the right side of equation (1.14). The gradient based sonoelastography has the advantage of yielding quantitative tissue elasticity. However, the phase gradient approach requires an exact estimate of the wave propagation direction which may be biased by the conventional 2D ultrasound imaging.

1.3.2.2 Vibro-acoustography

The vibro-acoustography was first developed by M. Fatemi and J. Greenleaf (Fatemi and Greenleaf, 1999). Concretely, a confocal transducer produces two continuous ultrasound waves which have slight frequency difference (Δf) and intersect at the region of interest. The intersection of the two beams results in an oscillating radiation force with the frequency (Δf) over the region of interest, which emits an acoustic field in the surrounding medium. The generated sound waves are detected by a hydrophone tuned to the frequency (Δf) and filtered by a band-pass filter centered at the same frequency. Finally, the confocal transducer scans the whole transverse plane to form a 2D image (Figure (1.5)). This approach is mainly limited by a relative long acquisition time and a considerable energy deposition to the tissue under inspection. Moreover, the measured parameter is not directly related to the tissue viscoelastic properties, and it may also be biased by the imposed ARF and the geometry of the imaged object.

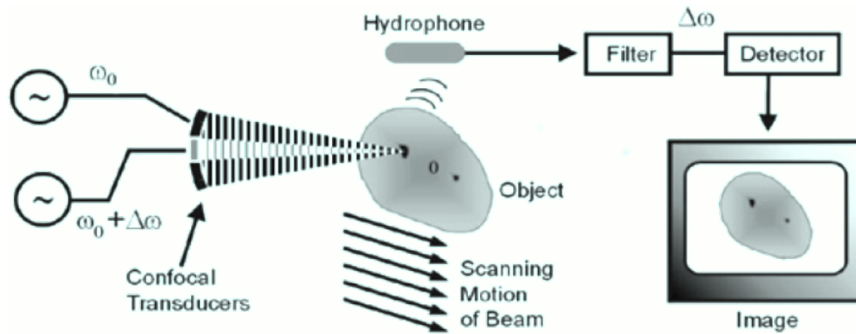


FIGURE 1.5: Illustration of the vibroacoustography approach developed by M. Fatemi and J. Greenleaf. Two ultrasonic beams with a slight frequency difference intersect at one point, resulting in a vibration of the object. A hydrophone then records the sound wave resulting from the vibration. The image is generated by scanning the whole transverse plane (Silva, 2003).

To simplify the instrumentation of the above approach, Chen *et al.* proposed an alternative approach to generate oscillating ARF, which consists in modulating the amplitude of a single incident ultrasound beam with the desired oscillating frequency for ARF (Chen, Fatemi, and Greenleaf, 2004). A cylindrical monochromatic shear wave is thus generated and propagates outwards from the focused beam axis. The phase of shear wave is measured at two different points along the propagation path and used to retrieve the shear wave speed (Figure 1.6). This process is repeated for a series of frequencies and the deduced shear wave speeds are fitted with the rheological Voigt model to inversely solve the tissue viscoelasticity.

In summary, ultrasound monochromatic approaches have the potential to map the tissue viscoelasticity. However, their application is mainly limited by the fact that it is impossible to separate the shear wave component from the compression wave component by using conventional 2D ultrasound imaging.

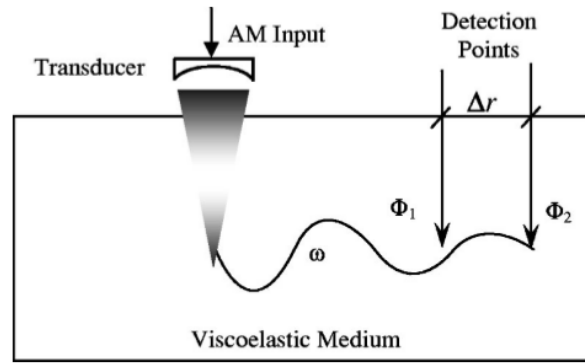


FIGURE 1.6: Illustration of the vibroacoustography approach proposed by Chen *et al.*. Amplitude-modulated focused ultrasonic beams are exerted, resulting in a monochromatic shear wave. The speed of the shear wave can be calculated from the phase values measured at two separate locations (Chen, Fatemi, and Greenleaf, 2004).

1.3.3 Transient Elastography

Transient elastography applies a transient (impulsive) excitation to the tissue. Thus a mechanical wave is generated and its displacement field is estimated by ultrasound imaging. Because the wave is transient and the compression wave component travels too fast to be captured by ultrasound imaging, the obtained displacement field mainly originates from the shear wave component.

1.3.3.1 1D Transient Elastography

1D impulse elastography was developed in the PhD thesis of S. Catheline (Catheline, 1998). This approach consists in impulsively exciting the media and then estimating the shear wave displacement in real time by ultrasound imaging along the trajectory (Figure 1.7 (a)). Concretely, a low frequency excitation (about 50 Hz) is performed by a circular piston (with a diameter ranging from 5 to 20 mm) integrated to the ultrasound probe. The generated shear wave displacement is then retrieved by cross-correlation of the RF echo signals obtained by an ultrasound probe more than 1,300 times (repetitions) per second (Gennisson, 2003). Finally, the shear wave velocity is deduced from a phase delay analysis of the measured displacement at central frequency 50 Hz (Figure 1.7 (b)). Assuming an isotropic and elastic medium, the Young's modulus of the medium can be deduced using the equation (1.9) and the right side of equation (1.14). Due to its effectiveness, this approach has been implemented in a stand-alone clinical device, the Fibroscan, manufactured by Echosense to characterize the stage of liver fibrosis by giving a global score based on the measured elasticity. However, this approach can only give a global elasticity estimation for the media under investigation, and hence it can not perform regional quantitative elasticity mapping.

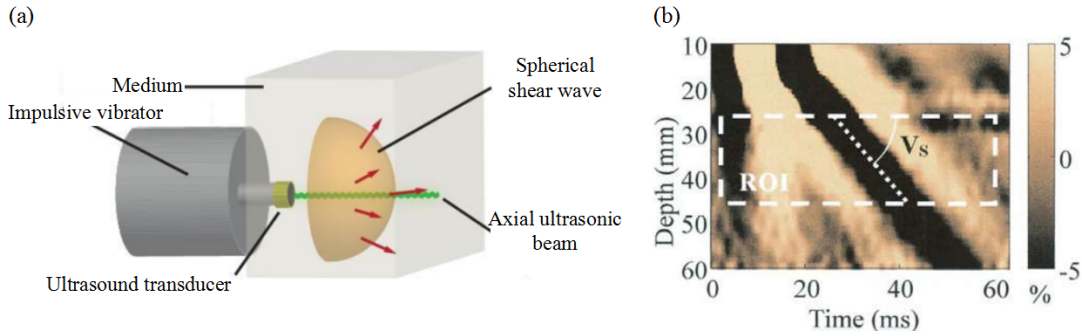


FIGURE 1.7: (a) Schematic representation of the 1D impulse elastography approach (Deffieux, 2008); (b) The speed of the shear wave can be deduced from a phase delay analysis of the measured displacement (Sandrin et al., 2003).

1.3.3.2 2D Transient Elastography

In order to overcome the limitations of 1D impulse elastography, a 2D impulse elastography method was developed in the thesis of Bercoff (Bercoff, 2004). This 2D approach consists in tracking the generated shear wave propagation by ultrasound imaging. The viscoelastic parameters can then be reconstructed through inversion of wave equation. The biggest challenge for tracking the shear wave propagation is the low frame rate (about 50 Hz) of conventional ultrasound imaging. To solve this issue, Bercoff *et al.* used ultra-rapid ultrasound imaging technology to increase the acquisition frame rate to more than 5000 Hz (Bercoff, Tanter, and Fink, 2004). The ultra-rapid ultrasound imaging technology will be detailed in Chapter 2. Similar to the 1D impulse approach, a vibrator is integrated to the ultrasound probe. The entire system is controlled by a computer (Figure 1.8).



FIGURE 1.8: The experimental set-up of the 2D impulse elastography approach developed by Bercoff *et al.* (Gennisson, 2003).

The shear wave displacement is also obtained using the cross-correlation method as done in the 1D impulse approach. Regarding the reconstruction, the out-of-plane component of the laplacien operator $\frac{\partial u_z}{\partial y^2}$ can not be obtained by the 2D ultrasound acquisition. The generated shear wave is transient and hence has a large spectral bandwidth. In this context, equation 1.18 should be rewritten as:

$$\mu^*(x, z) = -\rho \int_{\omega_0}^{\omega_1} \frac{\omega^2 u_z(x, z, \omega)}{\frac{\partial u_z(x, z, \omega)}{\partial x^2} + \frac{\partial u_z(x, z, \omega)}{\partial z^2}} d\omega \quad (1.19)$$

with $\omega \in \{\omega_0, \omega_1\}$ representing the spectral bandwidth where the displacement information exists, x, z representing the lateral and axial directions of ultrasound imaging. However, the reconstruction quality is very sensitive to noise for *in vivo* acquisitions, especially for the reconstruction of viscosity (Bercoff, 2004). Moreover, the implementation of the approach remains bulky and not very practical for *in vivo* experiments (Bercoff et al., 2003).

1.3.3.3 Acoustic Radiation Force Imaging (ARFI)

Acoustic Radiation Force Imaging was first developed by Nightingale *et al.* (Nightingale, Bentley, and Trahey, 2002). The ARFI approach uses the focused acoustic radiation force with short duration to excite the tissue. Then the temporal displacement profile in the excited region is recorded, allowing for a variety of parameters to be evaluated, including displacement at a given time after excitation, maximum displacement, time-to-peak displacement and time of recovery from peak displacement. These obtained parameters permit the retrieval of information regarding the elasticity and viscosity at the excitation region. The acoustic radiation forces are then focused successively at multiple locations and the obtained displacements are combined to form a 2D image (Figure 1.9). The main advantage of ARFI lies in the fact that the ultrasound probe serves at the same time as the excitation source and the acquisition device, making the entire system more compact. The main limitations of this approach lie in its qualitative measurement nature, the relative long acquisition time as well as the increase of tissue temperature due to multiple focus.

1.3.3.4 Supersonic Shear Imaging (SSI)

Supersonic Shear Imaging was also developed in Bercoff's thesis (Bercoff, 2004). This approach is in fact a further development of the 2D impulsive elastography that incorporates the idea of ARFI. The acoustic radiation force produced by the ultrasound probe replaces the external vibrator used in the 2D impulse approach, so that the entire system is more compact. Compared to the ARFI approach, ultrasound waves are focused successively at different depths of the media under investigation to create constructive spherical wave interferences which permit to enhance the amplitude and signal-to-noise ratio of the generated shear wave as well as to make the shear wave propagate further in the media. The general principle of SSI is illustrated in Figure (1.10). This approach has been implemented in a clinical imaging system, the Aixplorer, manufactured by Supersonic Imaging. This approach is the core ultrasound elastography modality used in my work. The methodological details will be described in Chapter 2.

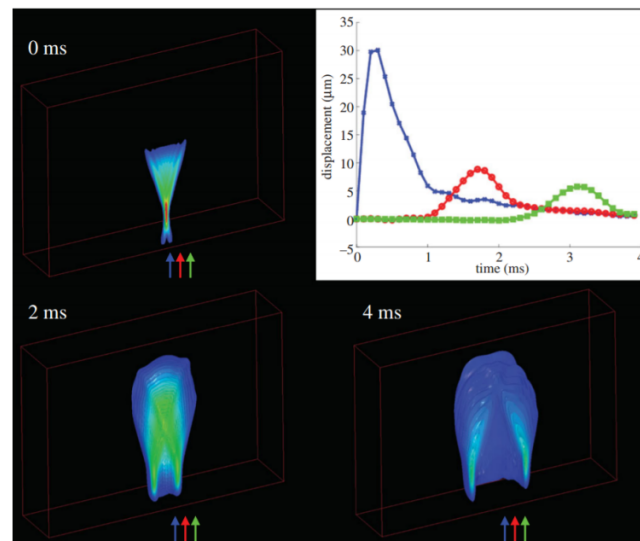


FIGURE 1.9: Illustration of the principle of the ARFI approach. The shear wave propagation is represented as isocontours of displacement at different times after impulsive (0 ms, 2 ms, 4 ms). The plot in the upper right shows the displacement-through-time profiles at the axial focal depth of the radiation force excitation at three different lateral positions (indicated by the arrows in the isocontour images). Blue, 0 mm; red, 1.5 mm; green, 3 mm (Palmeri and Nightingale, 2011).

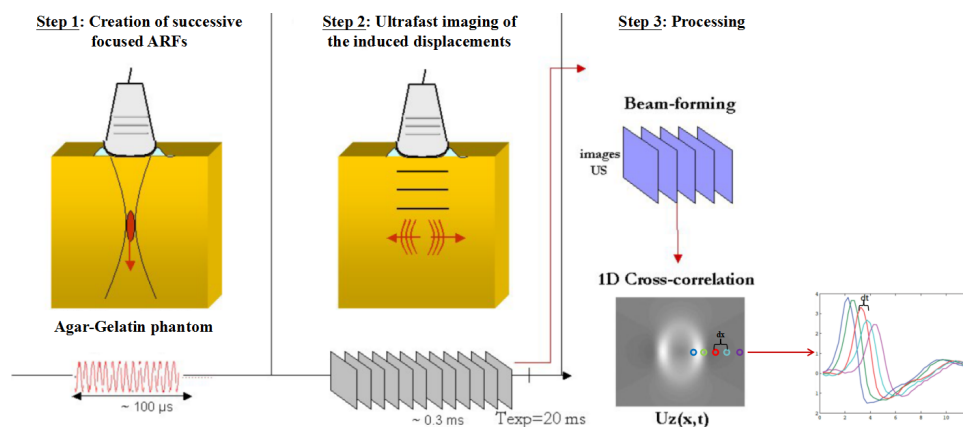


FIGURE 1.10: Illustration of the principle of the SSI approach. The ultrasound probe first acts as the distant source to induce shear waves in the medium. The probe then transfers to the reception mode to acquire the induced shear wave displacement using the ultrafast imaging method. Finally, the time of flight method is used to extract the elasticity values from the obtained displacement maps (Bercoff, 2004; Deffieux, 2008)

1.4 Magnetic Resonance Elastography

The concept of Magnetic Resonance Elastography (MRE) was born in the 1990s. The past two decades have seen a rapid evolution of MRE and a variety of approaches have been developed by different research groups to perform their proper MRE measurements. Like UE, there have been two main types of MRE approaches, namely static MRE and dynamic MRE. This section aims at giving a brief summary of existing MRE approaches used by other groups. The approach used in my work will then be detailed in Chapter 2.

1.4.1 Quasi-static MRE

In the beginning of MRE development, two main quasi-static approaches have been developed: namely the saturation tagging approach and the phase contrast approach. Fowlkes *et al* have proposed a saturation tagging approach to measure internal tissue strain by implementing the SPAtial Modulation of Magnetization (SPAMM) sequence (Fowlkes *et al.*, 1995). The SPAMM sequence can form rectangular grids of low (saturated) signal intensity over an entire imaging slice by selectively saturating the NMR signal in the tissue. Quasi-static compression after the saturation pulse and before the acquisition of MRI data will result in a geometric distortion of rectangular saturation grids. The tissue strain can then be deduced from the obtained distortion patterns. Plewes and colleagues have proposed a phase contrast approach to estimate the tissue strain by implementing additional motion encoding gradients (MEG) (Plewes *et al.*, 1995; Hardy *et al.*, 2005). The imaging sequence is synchronized with the external quasi-static compression. MEGs are applied respectively before and after compression. The principle of motion encoding using MR phase signal is identical to that of dynamic MRE approaches and will be detailed below. With the obtained tissue displacement information, the internal tissue strain can be deduced. Although encouraging results were obtained for quasi-static MRE approaches, they suffered from similar challenges and limitations as the ultrasound strain elastography did. As a result, the quasi-static MRE approaches have not been widely spread and accepted.

1.4.2 Dynamic MRE

Nowadays, most MRE approaches concentrate on the application of an external dynamic monochromatic excitation to excite the media under investigation. The quantitative mechanical properties can then be deduced by resolving appropriate wave equations. Different dynamic MRE approaches are mainly distinguished by the three following aspects: excitation equipments, imaging sequences, and reconstruction methods.

1.4.2.1 Excitation equipments

During twenty years of development, three categories of wave generation equipments have been developed for MRE (Tse et al., 2009; Mariappan, Glaser, and Ehman, 2010), namely piezoelectric transducer, electromagnetic transducer and passive wave generator.

Piezoelectric transducer

The piezoelectric transducer is placed directly in the magnet bore to induce the displacement into the regions of interest. In practice, the transducer is principally composed of non magnetic piezoelectric ceramics as in Figure 1.11. The piezoelectric stack is able to generate periodic oscillations when it is periodically polarized by the applied electrical field. Then a lever is used to amplify and transfer the oscillations generated by the piezoelectric stack to the point of excitation, which vibrates directly the regions of interest. The advantages of the piezoelectric material lie in its rapid response to the electrical stimulation, and the generated stable, well controlled oscillations. However, there are also several constraints with the piezoelectric transducer, including the low amplitude of the generated oscillation (smaller than a millimeter), the necessity of high tension electric field (about one hundred voltage) to polarize the material, and also the shielding equipments used to minimize the electromagnetic interference with the MR scanner (Tse et al., 2011; Uffmann et al., 2002). For *in vivo* applications, the active transducer is mainly limited by the oscillation amplitude level, which is insufficient to penetrate the cranial and thoracic barriers. In this context, the active transducer is adapted to human superficial tissues or organs, such as muscles and liver (Uffmann et al., 2004; Hirsch et al., 2014). Meanwhile the active transducer is also adapted for small animal imaging or *in vitro* tissue engineering (Salameh et al., 2009; Larrat et al., 2009; Chan et al., 2006; Othman et al., 2005).

Electromagnetic transducer

The electromagnetic transducer is also placed directly in the magnet bore against the regions of interest. It consists of a small coil with its axis perpendicular to the main magnetic field \vec{B}_0 (Rossman, Muthupillai, and Ehman, 1999). When a sinusoidal current goes through the coil, a magnetic field \vec{M} is generated and interacts with the main magnetic field \vec{B}_0 to result in a force \vec{N} , which is exerted on the regions of interest and induces periodic oscillations (Figure 1.12). The main advantage of the electromagnetic transducer is its capacity to modulate the oscillation amplitude by changing the coil size and the current intensity. This modulation procedure allows the electromagnetic transducer to obtain large oscillation amplitude (up to several millimeters) for high excitation frequencies (up to several hundred Hertz). However, as the oscillation amplitude level also depends on the orientation between the coil and the main magnetic field \vec{B}_0 , the position of the transducer is critical and limited (Braun, Braun, and Sack, 2003). Besides, as for the piezoelectric

transducer, the electromagnetic transducer is also capable of electromagnetically interfering with the MRI imager leading to artifacts (Tse et al., 2009).

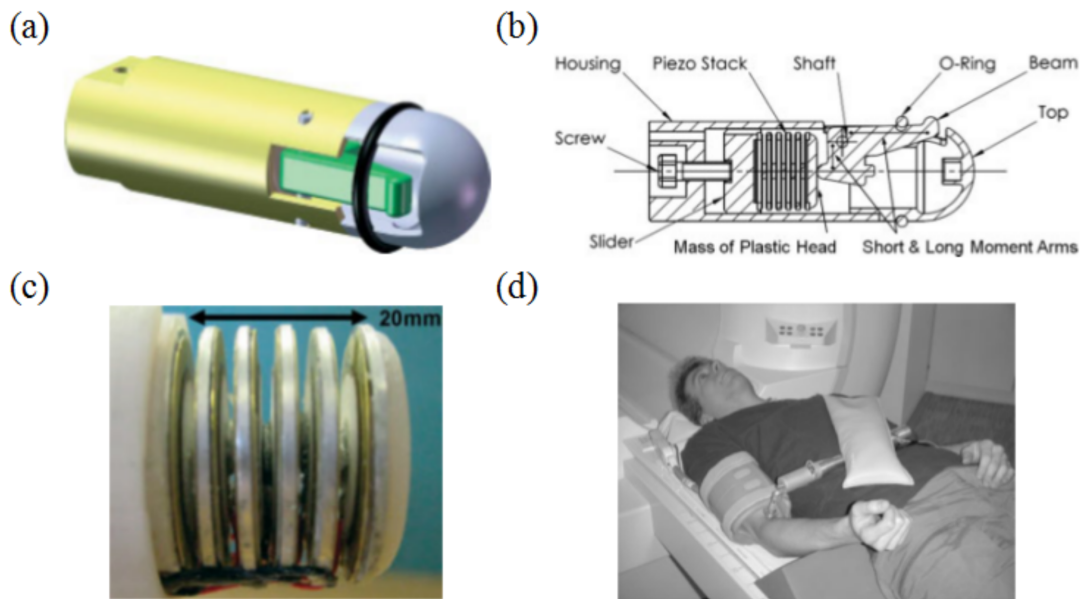


FIGURE 1.11: (a) 3D model of a piezoelectric transducer, (b) schematic cross-sectional view showing a piezoelectric stack actuating a beam-level to excite regions of interest and (c) the piezoelectric stack diagram (Tse et al., 2011). (d) position of a piezoelectric transducer for muscle MRE (Uffmann et al., 2002).

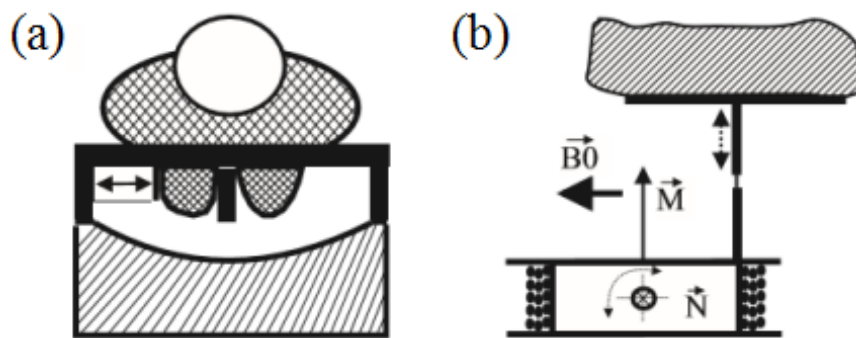


FIGURE 1.12: (a) Position of an electromagnetic transducer for breast MRE and (b) schematic cross-section seen from the top showing a small coil whose axis is perpendicular to the main magnetic field \vec{B}_0 . The magnetic moment \vec{M} produced by the coil interacts with \vec{B}_0 resulting in a force \vec{N} , which excites breast tissue (Sinkus et al., 2000).

Passive wave generator

The passive wave generator is composed of two parts: an active transducer placed outside the magnet bore for creating guided mechanical excitations, and a passive relay placed directly in the magnet bore against the regions of interest for transmitting the guided mechanical excitations into the regions of interest. In this category, a loudspeaker is usually used as the active

transducer. Because of the permanent magnet in the loudspeaker, it must be placed far enough from the imager to avoid the electromagnetic interference. To this day two main methods have been developed to connect the active transducer and the passive relay: either transmitting the generated acoustic pressure waves to a drum type passive generator through a pneumatic tube (Mariappan et al., 2009) (Figure 1.13(a)) or transmitting the vibration of the loudspeaker's membrane to a bar connected to the explored tissue (Asbach et al., 2008) (Figure 1.13(b)). The main advantage of the passive wave generator is that it completely avoids the electromagnetic interference with the imager. Besides, the drum type passive generator has the advantage of flexibly regulating the wave entry direction in order to better vibrate the regions of interest, although the amplitude of vibration may be attenuated by the tube. The solid connection between the membrane and the bar permits a lossless vibration transmission, but the bar lacks flexibility of regulation of the wave entry direction.

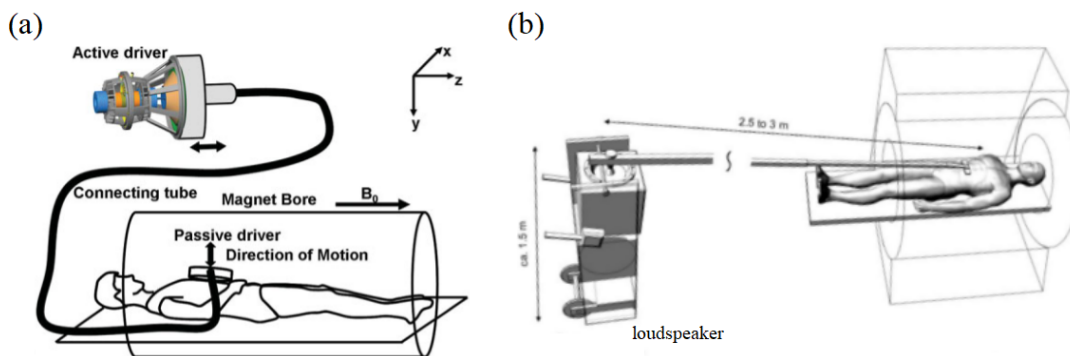


FIGURE 1.13: (a) Schematic of a drum type passive generator transmitting the acoustic pressure wave produced by the loudspeaker via a pneumatic tube (Mariappan et al., 2009); (b) schematic of a passive generator transmitting the vibration of the loudspeaker's membrane via a bar (Asbach et al., 2008).

1.4.2.2 Imaging sequences

Motion encoding using MR phase signal

The MR signal is a small electrical current induced in the receiver coil when the net magnetization tipped into the transverse plane recovers to the equilibrium state along the direction of the main static magnetic field (B_0). Frequency and phase encoding are applied to encode the localization of the signal by producing a K-space, which eventually goes through the Fourier transformation to get the final MR images. The obtained MR signal is a complex value composed of a magnitude part and a phase part. The magnitude part is proportional to the signal density resulting from different weighting mechanisms, such as T_1 , T_2 etc. The phase part is proportional to the cumulated magnetic field experienced by the spins, hence it is sensitive to their motions. In conventional anatomic MRI, the phase value is often discarded. It may be zeroed by optimizing the field homogeneity or eliminating motion-related artifacts in order to maximize the magnitude signal or not to distort

the anatomic images.

In contrast, when the motion of spins provides pertinent physiological informations, such as blood flow or soft tissue deformation under stress, the phase signal is a good candidate to encode these informations onto the signal. To record the motion information by accumulating the phase value, the motion encoding gradient (MEG), typically composed of two opposite gradient lobes with identical amplitude and duration as illustrated in Figure 1.14, needs to be additionally applied to make the conventional MRI sequence sensitive to the spin motion. The phase accumulation formula for spins at position \mathbf{r} during a period of t is given in equation (1.20), where γ , \mathbf{G}_{MEG} represent the gyromagnetic ratio of hydrogen nuclei and the amplitude of motion encoding gradient respectively. The principle of motion encoding is illustrated in Figure 1.14 by comparing the phase accumulation of static and mobile spins submitted to the same MEG. Static spins with fix position \mathbf{r}_0 are first dephased by the first gradient lobe (half of the bipolar gradient period T_{MEG}) then rephased by the second gradient lobe, resulting in a net phase accumulation of zero as demonstrated by equation (1.21). Mobile spins with original position \mathbf{r}_0 move at a constant speed v along the bipolar gradient direction, resulting in an unbalanced rephasing as demonstrated by equation (1.22).

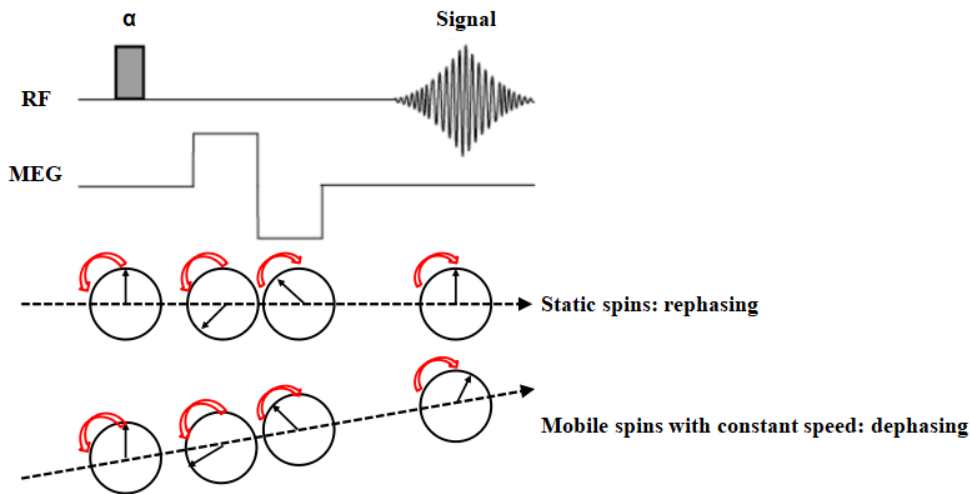


FIGURE 1.14: Evolution of phase accumulation for static spins and mobile spins during a gradient echo sequence with an additional bipolar gradient. Static spins refocus at the echo time, while mobile spins moving along the bipolar gradient direction have a non zero net dephasing at echo time.

$$\varphi(\mathbf{r}, t) = -\gamma \int_0^t \mathbf{G}_{MEG}(t) \cdot \mathbf{r} \cdot dt. \quad (1.20)$$

$$\begin{aligned}
 \varphi(\mathbf{r}, T_{MEG}) &= -\gamma \int_0^{T_{MEG}} \mathbf{G}_{MEG}(t) \cdot \mathbf{r}_0 \cdot dt \\
 &= -\gamma \cdot \mathbf{r}_0 \cdot G_{MEG} \int_0^{\frac{T_{MEG}}{2}} dt + \gamma \cdot \mathbf{r}_0 \cdot G_{MEG} \int_{\frac{T_{MEG}}{2}}^{T_{MEG}} dt \\
 &= 0.
 \end{aligned} \tag{1.21}$$

$$\begin{aligned}
 \varphi(\mathbf{r}, T_{MEG}) &= -\gamma \int_0^{T_{MEG}} \mathbf{G}_{MEG}(t) \cdot (\mathbf{r}_0 + \mathbf{v} \cdot t) \cdot dt \\
 &= -\gamma \int_0^{T_{MEG}} \mathbf{G}_{MEG}(t) \cdot \mathbf{r}_0 \cdot dt - \gamma \cdot \mathbf{G}_{MEG} \cdot \mathbf{v} \int_0^{\frac{T_{MEG}}{2}} t \cdot dt \\
 &\quad + \gamma \cdot \mathbf{G}_{MEG} \cdot \mathbf{v} \int_{\frac{T_{MEG}}{2}}^{T_{MEG}} t \cdot dt \\
 &= \gamma \cdot \mathbf{G}_{MEG} \cdot \mathbf{v} \cdot \frac{T_{MEG}^2}{4}.
 \end{aligned} \tag{1.22}$$

For MRE, an external harmonic excitation with angular frequency ω_{exc} is applied, which induces a periodic motion of the tissue spins, so that the position of spins with an original position \mathbf{r}_0 becomes:

$$\mathbf{r}(t) = \mathbf{r}_0 + \mathbf{A} \cos(\mathbf{k} \cdot \mathbf{r} - \omega_{exc} \cdot t + \theta). \tag{1.23}$$

with \mathbf{A} the displacement amplitude, \mathbf{k} the wave number and θ the initial phase offset. According to equation (1.20), the phase accumulation by applying N_{MEG} bipolar gradients can be written as:

$$\begin{aligned}
 \varphi(\mathbf{r}, N_{MEG} \cdot T_{MEG}, \theta) &= -\gamma \cdot \mathbf{r}_0 \cdot \int_0^{N \cdot T_{MEG}} \mathbf{G}_{MEG}(t) \cdot t dt \\
 &\quad - \gamma \cdot \mathbf{A} \int_0^{N \cdot T_{MEG}} \mathbf{G}_{MEG}(t) \cdot \cos(\mathbf{k} \cdot \mathbf{r} - \omega_{exc} \cdot t + \theta) \cdot dt
 \end{aligned} \tag{1.24}$$

From equation (1.21), the first term of equation (1.24) equals zero. The phase accumulation of the spins thus only depends on the spin motions along the bipolar gradient direction, namely the second term of equation (1.24). The sensitivity of the motion encoding depends on the number of bipolar gradients, N , the bipolar gradient duration, T_{MEG} , and also the bipolar gradient's shape.

Standard MRE sequences

Various standard MRI gradient echo or spin echo based sequences can be adapted to MRE simply by adding bipolar gradients.

Gradient echo based MRE sequence

The gradient echo based MRE sequence (Figure 1.15 (a)) was developed by researchers from the Mayo Clinic (Muthupillai et al., 1995). The trapezoidal bipolar gradients are synchronized with the external mechanical excitation and can be applied along each of the spatial encoding axis to encode the three-dimensional displacement field. Successive phase offset values (θ) between the mechanical excitation and the motion encoding gradients are imposed in order to acquire the displacement field at different instants of the mechanical excitation period. Considering trapezoidal bipolar gradients with the same duration as the period of the mechanical excitation ($T_{MEG} = T_{exc}$):

$$\mathbf{G}_{MEG}(t) = \begin{cases} \mathbf{A}_{MEG} & (n-1)T_{exc} < t < (2n-1)\frac{T_{exc}}{2} \\ -\mathbf{A}_{MEG} & (2n-1)\frac{T_{exc}}{2} < t < nT_{exc} \end{cases} \text{ with } n \in \{1, N\} \quad (1.25)$$

the phase accumulation formula can be written as:

$$\varphi(\mathbf{r}, N_{MEG} \cdot T_{MEG}, \theta) = \frac{2\gamma N_{MEG} T_{exc} \mathbf{A}_{MEG}}{\pi} \mathbf{A} \sin(\mathbf{k} \cdot \mathbf{r} + \theta). \quad (1.26)$$

The disadvantage of this sequence mainly lies in its sensitivity to the magnetic field inhomogeneity, which may introduce detrimental phase shifts contaminating the phase accumulation originating from spin motion. In order to cancel the above bias, a final phase difference image is often reconstructed from two phase images with opposite MEG polarities, which is at the cost of increasing acquisition time.

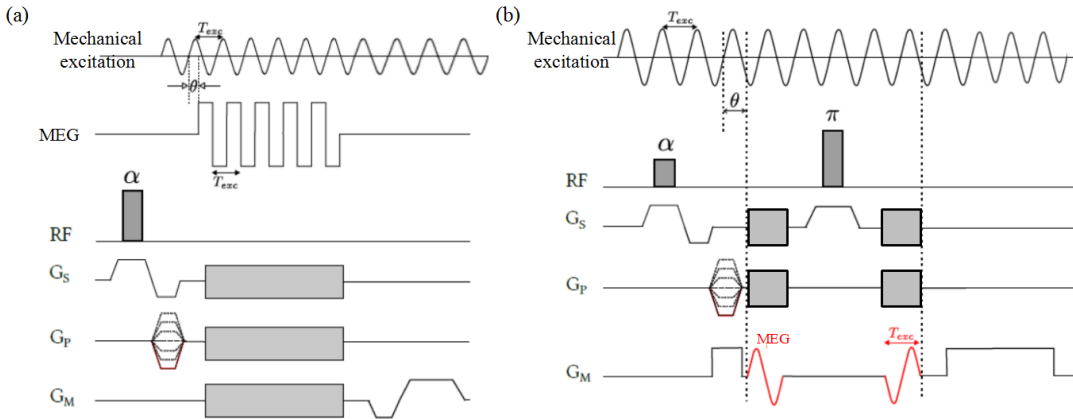


FIGURE 1.15: (a) Chronogram of the gradient echo based MRE sequence developed at Mayo Clinic (Muthupillai et al., 1995). The trapezoidal bipolar gradients are synchronized and applied along each of the encoding axis to encode the three-dimensional displacement field; (b) Chronogram of the spin echo based MRE sequence developed by Sinkus *et al.* (Sinkus et al., 2000). Two sinusoidal bipolar gradients with identical duration but opposite signs are synchronized and applied along each of the encoding axis to encode the three-dimensional displacement field.

Spin echo based MRE sequence

The spin echo based MRE sequence was developed by Sinkus *et al* (Sinkus et al., 2000). Two sinusoidal bipolar gradients with identical duration but

opposite signs are synchronized with the external mechanical excitation and applied on either side of the refocusing pulse (Figure 1.15 (b)) along each of the encoding axis to encode the three-dimensional displacement field. Along each encoding direction, the different instants of the excitation period are obtained by shifting the mechanical excitation from a phase offset θ with respect to the bipolar gradient. Considering sinusoidal bipolar gradients with the same duration as the period of the applied external excitation, namely $\mathbf{G}_{MEG}(t) = \mathbf{A}_{MEG} \cdot \cos(\omega_{exc} \cdot t)$, the phase accumulation formula can be written as:

$$\varphi(\mathbf{r}, 2 \cdot T_{MEG}, \theta) = \gamma T_{exc} \mathbf{A}_{MEG} \mathbf{A} \sin(\mathbf{k} \cdot \mathbf{r} + \theta). \quad (1.27)$$

The main advantage of the spin echo based MRE sequence lies in its relative immunity to the field inhomogeneity influence, which is due to the refocusing pulse. The main disadvantage of this sequence is the prolonged echo time TE and total acquisition time TA, which is governed by the refocusing pulse. The long TE value is especially critical for tissue with short transverse relaxation time T_2 , while the long TA is extremely challenging for *in vivo* applications. However, these challenges can be mediated by regulating the excitation frequency, the number of bipolar gradients and also the FOV size. The spin echo based MRE sequence was used for all MRE acquisitions performed during my work. The programming of this sequence was also one core part of my work. More details about the sequence will be presented in Chapter 2.

Accelerating MRE acquisitions

From the description of the two above standard MRE sequences, the long TE and TA imposed by the additional MEGs are the principal challenges for the application of MRE. The long TE may degrade the SNR especially for short T_2 tissues, the long TA may add discomfort for the patients or even forbid the exam in the case of acquisitions during breath-hold. In this context, multiple approaches have been proposed to accelerate the acquisition.

Echo planar based MRE sequence

Echo Planar Imaging (EPI) permits to accelerate the standard gradient echo or spin echo imaging sequences by acquiring the whole 2D k-space in a single RF excitation (single shot) or in a small number (multiple shots) RF excitations. This acceleration is obtained by continuously applying the alternative read gradient with an increment of the phase gradient. The EPI sequence has been adapted to the MRE sequence by adding bipolar gradients before the "zig-zag" traversal of k-space (Romano et al., 2014). An acceleration factor as high as 10 (Huwart et al., 2008b) can be achieved compared to the standard spin echo based MRE sequence. However, the sequence is susceptible to magnetic field inhomogeneities which may cause spatial distortions of the acquired images.

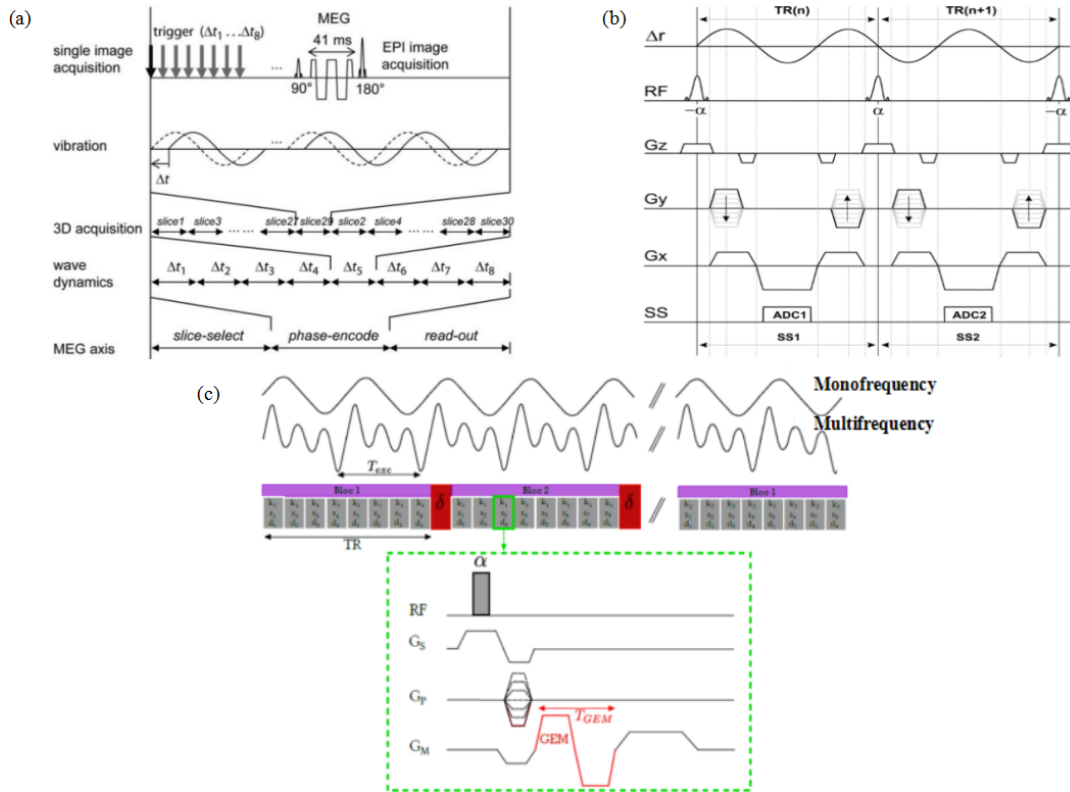


FIGURE 1.16: (a) Chronogram of the EPI based MRE sequence developed by Romano *et al.* (Romano *et al.*, 2014); (b) Chronogram of the bSSFP based MRE sequence developed by Bieri *et al.* (Bieri *et al.*, 2006); (c) Fractional encoding based MRE sequence developed by Garteiser *et al.* (Garteiser *et al.*, 2013).

Balanced Steady-state Free Precession based MRE sequence

Another sequence for reducing the acquisition time is the balanced Steady-state Free Precession (bSSFP) (Carr and Purcell, 1954). The bSSFP is a rapid gradient echo sequence. Its repetition time (TR) is far less than the transverse relaxation time (T2), which leads to equilibrium longitudinal and transversal magnetization states. The bSSFP sequence can be adapted for MRE by making use of the high sensitivity of the equilibrium state to alternating spin dephasing as shown in Figure 1.16 (b) (Bieri *et al.*, 2006). In contrast to conventional MRE, the bSSFP based MRE uses the inherently available read gradient as the motion encoding gradient, which avoids the additional bipolar gradient and thus improve the time efficiency. By tuning the TRs adapted to the external excitation frequency, an oscillating steady-state is produced that depends on the alternating motion induced phase offset. However, this approach is highly susceptible to magnetic field inhomogeneities which can induce additional phase shift and produce black bands on the image.

Fractional encoding MRE sequence

In contrast to the above standard accelerating schemes, the idea of fractional encoding, developed by Klatt *et al.* (Klatt *et al.*, 2007; Rump *et al.*, 2007), consists in using only one bipolar gradient with a frequency higher than that of the external excitation. Only a fraction of one vibration cycle is thus encoded

per TR so as to reduce the TE and TR. In this case, the phase accumulation formula can be written as:

$$\varphi(\mathbf{r}, \theta) = -\gamma T_{MEG} \mathbf{A}_{MEG} \mathbf{A} \frac{\cos(\theta + \pi q) \sin(\pi q)}{\pi(1 - q^2)}. \quad (1.28)$$

where $T_{MEG} < T_{exc}$, $q = \frac{T_{MEG}}{T_{exc}}$ and the phase accumulation reaches the maximum with $\theta = \pi(1 - q)$ and $q = 0.84$. Based on this principle, Garteiser *et al* (Garteiser *et al.*, 2013) has developed a gradient echo based fractional encoding MRE sequence as shown in Figure 1.16 (c). The sequence is divided into imaging blocks. Each block contains multiple shots, which have a duration of an integer number of vibration cycles. During each shot, a gradient echo based MRE sequence with fractional encoding is performed. Besides, this sequence also permits to encode a multi-frequency excitation in only one acquisition. The disadvantage of the sequence mainly lies in its reduced sensitivity for motion encoding, which might be critical for displacement fields with low amplitudes.

1.4.2.3 Reconstruction methods

Three main categories of reconstruction methods exist for MRE.

Local frequency estimation (LFE)

The first reconstruction algorithm to be developed for MRE is called local frequency estimation (LFE) (Manduca *et al.*, 1996). It was developed by researchers from the Mayo Clinic. LFE is an image processing method, which relies on a wavelet analysis of the displacement field to map the local wavelength, λ , in the medium. The associated shear stiffness, μ_{LFE} , is then deduced by inverting the right side of equation (1.14) under the assumption of no attenuation:

$$\mu_{LFE} = \rho \left(\frac{\omega_{exc} \lambda}{2\pi} \right)^2 \quad (1.29)$$

This algorithm allows the estimation of the shear stiffness from the displacement field acquired from one single encoding direction and at a single instant of the vibration cycle. However, the above 2D approach which favors the acquisition time, is inherently biased by the choice of the slice orientation with respect to the direction of the wave propagation (Manduca *et al.*, 2001; Zhang *et al.*, 2015). Moreover, this approach can not be extended to viscoelastic media.

Algebraic Inversion of the Differential Equation (AIDE)

This algorithm was also initially developed by researchers from the Mayo Clinic (Oliphant *et al.*, 2001). Following the Helmholtz decomposition of equation (1.18), AIDE inverts the Helmholtz equation governing the shear wave component for each voxel to compute the shear viscoelastic moduli, $\mu + j\omega_{exc}\zeta$. Provided the shear and compressional wave components are

separated, AIDE may theoretically be flawless upon proper joint assumptions and equation (Baghani, Salcudean, and Rohling, 2009). The compressional component can be suppressed by applying a spatial filter onto the original displacement field (Mariappan, Glaser, and Ehman, 2010), so that the shear viscoelastic moduli can be calculated using directly the displacement field (equation (1.30)). However, since residues remain, an alternative solution may be preferred through the application of the curl operator to completely remove the curl-free compression wave component (Sinkus et al., 2005), namely $\mathbf{q} = \nabla \times \mathbf{u}$. The shear viscoelastic moduli can then be deduced by inverting the \mathbf{q} -field based Helmholtz equation (equation (1.31)).

$$\mu_i + j\omega_{exc}\zeta_i = -\rho\omega_{exc}^2 \frac{u_i(\mathbf{r}, \omega_{exc})}{\nabla^2 u_i(\mathbf{r}, \omega_{exc})} \quad (1.30)$$

$$\mu_i + j\omega_{exc}\zeta_i = -\rho\omega_{exc}^2 \frac{q_i(\mathbf{r}, \omega_{exc})}{\nabla^2 q_i(\mathbf{r}, \omega_{exc})} \quad (1.31)$$

Three-Dimensional subzone-Based reconstruction algorithm

This algorithm was developed by researchers from Dartmouth College (Van Houten et al., 2001). This algorithm is a finite element based subzone technique which resolves the equation (1.18) in an iterative way. The imaged object is first meshed into a series of subzones. For each subzone, the equation (1.18) is resolved iteratively by updating the solution based on the differences between forward calculation of the displacement using the current solution and the measured displacement values. The algorithm does not require the differentiation of the measured displacement field, making it quite robust for low quality data. In addition, the algorithm can take the local inhomogeneity and the boundary conditions into account. In spite of these advantages, this approach is more time consuming than the others, which limits its application.

1.5 Potential clinical applications

Over the past twenty years, numerous studies have been carried out to prove the feasibility of elastography for characterizing tissue states or detecting tissue abnormalities for various organs, from superficial organs such as breast, thyroid, to more profound ones such as liver, prostate. The potential clinical applications of elastography can mainly be classified into three categories: cancer diagnosis, diffuse disease characterization, and therapy monitoring.

1.5.1 Cancer diagnosis

Because elastography permits to quantify regional mechanical properties of tissue, it has the potential to detect local tissue changes which can serve as additional information for cancer diagnosis. The most investigated organs

include breast, prostate, and thyroid.

Breast elastography has attracted a lot of attention since the very beginning of elastography technology, because breast, as a superficial organ, can be easily deformed by external excitation and breast cancer is one of the most prevalent female cancers all over the world. Many early freehand elastography systems have been developed for performing strain elastography of breast lesions and evaluating its clinical relevance (Doyley et al., 2001; Hiltawsky et al., 2001; Hall, Zhu, and Spalding, 2003). Currently, breast strain elastography has been commercially available from many manufacturers. Multiple clinical studies have shown the excellent sensitivity and specificity of strain elastography for differentiating breast carcinoma from benign lesions (Barr et al., 2012; Wojcinski et al., 2010; Itoh et al., 2006). An important feature for malignant lesions is that their sizes appear larger on the elastogram than on the B-mode. This may be due to the invasion nature of cancer tissue which is not obvious on B-mode. SSI can provide quantitative elasticity measurements for breast lesions. It has also been proven to improve the differentiation between benign and malignant lesions compared to B-mode ultrasound (Berg et al., 2012; Athanasiou et al., 2010). Moreover, both modalities are useful for confirming the cystic nature of the lesion (Cho et al., 2011; Barr and Lackey, 2011). MRE has also been exploited to improve breast tumor detection. Sinkus *et al* performed MRE of breast lesions to demonstrate that MRE could yield promising results for breast tumor detection (Sinkus et al., 2000). Afterwards a clinical study has proven that the combination of the BI-RADS categorization obtained via MR mammography with viscoelastic information deduced from MRE leads to a substantial rise in specificity for detecting malignant breast lesions (Sinkus et al., 2007).

Unlike breast elastography, which focuses on the differentiation of already detected lesions, prostate elastography was developed to identify suspicious target regions for biopsy and help decrease the rate of unnecessary biopsy. Strain elastography for prostate is performed using an inflatable balloon to improve the standardized compression level. Most studies report a significant improvement in prostate cancer identification by using strain elastography (Salomon et al., 2008; Brock et al., 2012). However, the improvement in sensitivity and specificity is still modest (Walz et al., 2011). Unlike strain elastography, SSI requires no compression on the rectal wall. SSI permits to achieve a negative predictive value for malignant lesions as high as 91% to avoid unnecessary biopsies in patients (Aboumarzouk et al., 2012). In addition, the ratio for the stiffness value between the nodule and the adjacent peripheral gland can provide more discriminatory values as it takes into account the increased stiffness of the peripheral zone from calcification and chronic prostatitis (Correas et al., 2011). MRE for prostate has also been of great interest for providing additional mechanical property information, which can be incorporated into multi-parametric prostate MRI in order to improve the prostate cancer detection accuracy. Several studies have been carried out to demonstrate the feasibility of MRE for prostate (Arani et al.,

2013; Sahebjavaher et al., 2015). However, vibration amplitude, repeatability and subject movement issues should be optimized before prostate MRE can be further investigated.

Thyroid elastography has only been exploited with ultrasound based elastography technologies. Both strain elastography and SSI have been proven an efficient tool for differentiating malignant lesions from benign ones (Lyshchik et al., 2005; Sebag et al., 2010), where malignant lesions are significantly stiffer than benign lesions, so that unnecessary biopsies can be avoided. However, most malignant follicular carcinomas are missed by elastography because they can be soft and difficult to differentiate from benign nodules (Bojunga et al., 2010). Finally, elastography might be useful in multinodular goitre to select nodules for fine needle aspiration biopsy, but there is no data available at present (Cosgrove et al., 2013).

1.5.2 Diffuse disease characterization

Diffuse disease often alters the mechanical properties of the tissue. The tissue characterization by elastography can thus provide useful information about this underlying alteration process. In this category, the most widespread application for elastography is liver fibrosis characterization. Nowadays, Transient Elastography (TE), performed using the FibroScan (Echosens, Paris, France), has become a mainstay for gastroenterologists to non-invasively characterize liver parenchymal stiffness in patients. Multiple clinical studies have shown that TE can assess the severity of liver fibrosis in patients with chronic viral hepatitis, provided that confounding factors are taken into account, so as to distinguish patients with absence and mild fibrosis from those with significant fibrosis and cirrhosis (Talwalkar et al., 2007; Liver, 2014; Chon et al., 2012). However, TE can only give a global estimation of liver stiffness and has no imaging component. Moreover, its application is challenged by perihepatic ascites (Parker, Doyley, and Rubens, 2010). To overcome the above limitations, SSI and MRE have been exploited to perform the regional quantification of liver stiffness (Bavu et al., 2011; Yin et al., 2007; Huwart et al., 2006). These two methods allow liver stiffness mapping in large and deep areas, avoiding the influence of ascites and also preventing biases due to fibrosis heterogeneities that are inherent to TE measurements. It has already been demonstrated that MRE and SSI can have similar or even better performance than TE for staging liver fibrosis (Ferraioli et al., 2012; Bohte et al., 2014).

Elastography can also be used to characterize musculoskeletal related diseases. For example, strain elastography can be used as a supplementary tool to conventional US scanning to increase the diagnostic confidence in diagnosing achilles tendinopathy (De Zordo et al., 2010; Klauser et al., 2013). MRE can also be used to examine the muscles in pathologies such as hemiplegia and disuse atrophy (Ringleb et al., 2007). In addition, MRE can also serve

as a prospective tool for characterizing subtle and diffuse tissue damage in neuroinflammatory diseases (Fehlner et al., 2015).

1.5.3 Therapy monitoring

The capacity of elastography for diagnosis due to the fact that tissue stiffness can serve as a potential biomarker for various diseases have been shown. In this context, elastography can also serve as a powerful tool to monitor the response to therapy of the same diseases, because the remission of these diseases are often accompanied with alterations of the underlying tissue stiffness.

In this category, the first proposed application was to use elastography to monitor high-intensity focused ultrasound (HIFU) treatments considering the intrinsic advantage that HIFU treatment and ultrasound imaging can be integrated into only one probe. Souchon *et al* have proven the ability of strain elastography for monitoring HIFU treatment of the prostate (Souchon et al., 2003; Curiel et al., 2005). During their *in vivo* studies, the HIFU lesions inside the prostate during and immediately after therapy were well visualized by strain elastography. Later, quantitative stiffness measurements by SSI have also demonstrated their usefulness to monitor the response of breast tumors under neo-adjuvant chemotherapy treatment (Latorre Ossa, 2012).

It has been shown that liver stiffness measured with MRE correlates with the fibrotic content of the liver (Venkatesh et al., 2011). Liver MRE may thus be able to monitor liver stiffness changes for patients under anti-fibrotic treatments. Venkatesh *et al* have demonstrated this perspective of liver MRE in assessment of treatment response and clinical follow-up of chronic liver diseases (Venkatesh, Yin, and Ehman, 2013). Besides, multiple *in vitro* or preclinical studies have demonstrated similar perspective of MRE for the thermal ablation therapies. This prospective is further enhanced by the fact that MRI has also the potential to guide these therapies, so that a synergy between the treatment guidance and treatment monitoring can be formed. Larrat *et al* have shown that MRE is a potential tool to monitor tissue stiffness changes for the rat brain between pre- and post-MRI-guided HIFU treatments (Larrat et al., 2009). Corbin *et al* have proven the ability of MRE to provide real-time elastograms to monitor the interventional MR applications (Corbin et al., 2015).

1.6 Conclusions

From early stages, elastography has kept holding the promise of objective, regional quantification of the mechanical properties of human tissues *in vivo*. The last two decades have seen rapid methodological developments of elastography, and over the past several years this technology has moved out of laboratory and into the hands of clinicians. The most rapidly adopted areas

include liver, breast, prostate, and thyroid. Numerous studies have demonstrated the various clinical perspectives of elastography, from early diagnostic to therapy follow-up. The wide area of application makes elastography a potential tool for clinicians to better take in charge their patients.

To this day, plenty of elastography approaches have been developed and different manufacturers have installed specific approaches in their imaging systems. Because different approaches may lead to different measurements due to methodological differences or method specific uncertainty issues, clinicians have to worry about the potential measurement discrepancies among the different systems and approaches. Thus the cross-validation of different elastography approaches should be an important issue to tackle before elastography can be widely accepted and applied by clinicians.

In my work, the comparison and cross-validation of two prospective approaches particularly widespread, namely MRE and SSI, are targeted. In Chapter 2, a methodological comparison between MRE and SSI is presented in order to infer potential measurement bias sources between the two approaches. Then, in Chapter 3, a simulation study is carried out to optimize the acquisition and reconstruction conditions for MRE so as to minimize the MRE specific measurement bias. Chapters 4 and 5 are dedicated to cross-validate the quality-guided measurements between MRE and SSI on tissue-mimicking phantoms and on the liver of healthy volunteers respectively.

2 Magnetic Resonance Elastography (MRE) and Supersonic Shear Wave Imaging (SSI): a methodological comparison

2.1 Introduction

Since the elastography concept was proposed by Ophir in 1991 (Ophir et al., 1991), a variety of technologies have been developed. Among different approaches, Magnetic Resonance Elastography and Supersonic Shear Wave Imaging have shown particular perspectives for clinical applications as described in Chapter 1. Potential applications of MRE and SSI overlap. Yet, each modality presents distinguished advantages demonstrating that MRE and SSI can be complementary and the combination of these two modalities can enforce the elastography technology in future clinical applications. For example, MRE can provide 3D regional information for preoperative planning while SSI can provide real time information for intra-operative monitoring. However, the two modalities differ from each other in all three elementary steps, namely excitation, acquisition and reconstruction. It is thus necessary to compare the methodologies of the two modalities in order to identify the potential measurement biases related to methodological differences. In this context, this chapter aims to give an overall presentation and comparison of the methodology of MRE and SSI. A step by step comparison is presented in this chapter according to the three elementary steps of elastography. The technological platforms used for the experimental comparison between MRE and SSI in Chapter 4 and 5 are also presented.

2.2 External excitation

For both modalities, a dynamic excitation is used to induce a displacement field in the object under investigation.

2.2.1 Guided compression wave excitation for MRE

In my work, I used the guided compression wave generation system developed in our laboratory (Maître et al., 2011). This wave generation system is mainly composed of two parts: the excitation package and the monitoring package. The excitation package (Figure 2.1) includes a function generator

(AFG 3021B, Tektronix, USA) to drive the excitation, an amplifier (P5000S, Yamaha, Japan) to amplify the analogue wave signal, a loudspeaker to transform the analogue signal into an acoustic pressure wave and at last a plastic tube and an appropriate acoustic adapter to transmit the pressure wave to the regions of interest. Both loudspeakers for low frequencies (PHL Audio 4530) and high frequencies (JBL 2446j) are included in order to cover a large excitation frequency range from 50-2000 Hz. The monitoring package (Figure 2.2) includes an oscilloscope (TDS 2014, Tektronix, USA) to control the output drive voltage and the synchronization between the wave generator and the MR scanner, and an optical measuring system (EVO-RM-8, FISO, Canada) to measure the wave pressure level exerted at the regions of interest.

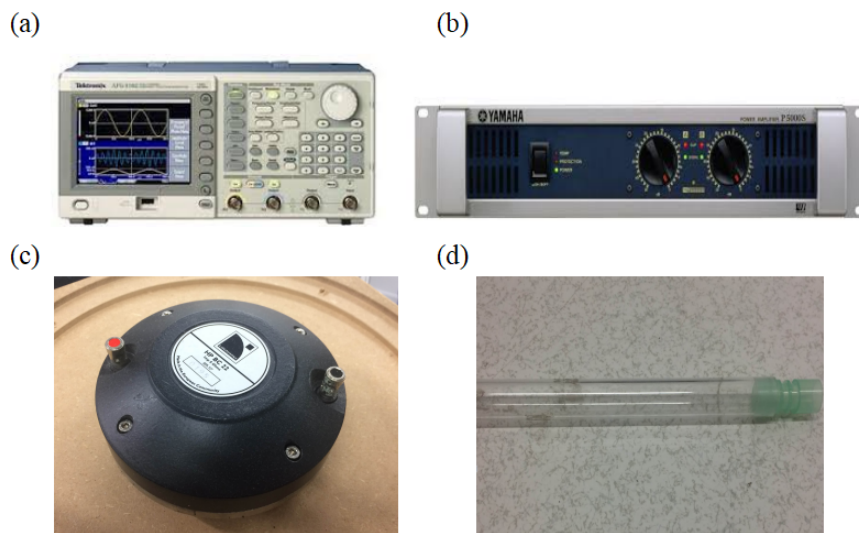


FIGURE 2.1: Excitation package of the wave generation system used during my thesis: (a) a function generator , (b) amplifier, (c) loudspeaker and (d) plastic tube and acoustic adapter.

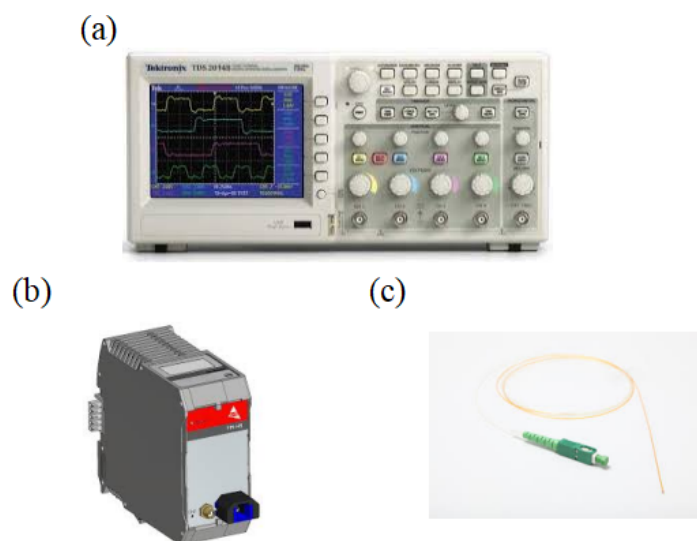


FIGURE 2.2: Monitoring package of the wave generation system used during my thesis:(a) oscilloscope, (b) optical measuring unit and (c) optical pressure sensor.

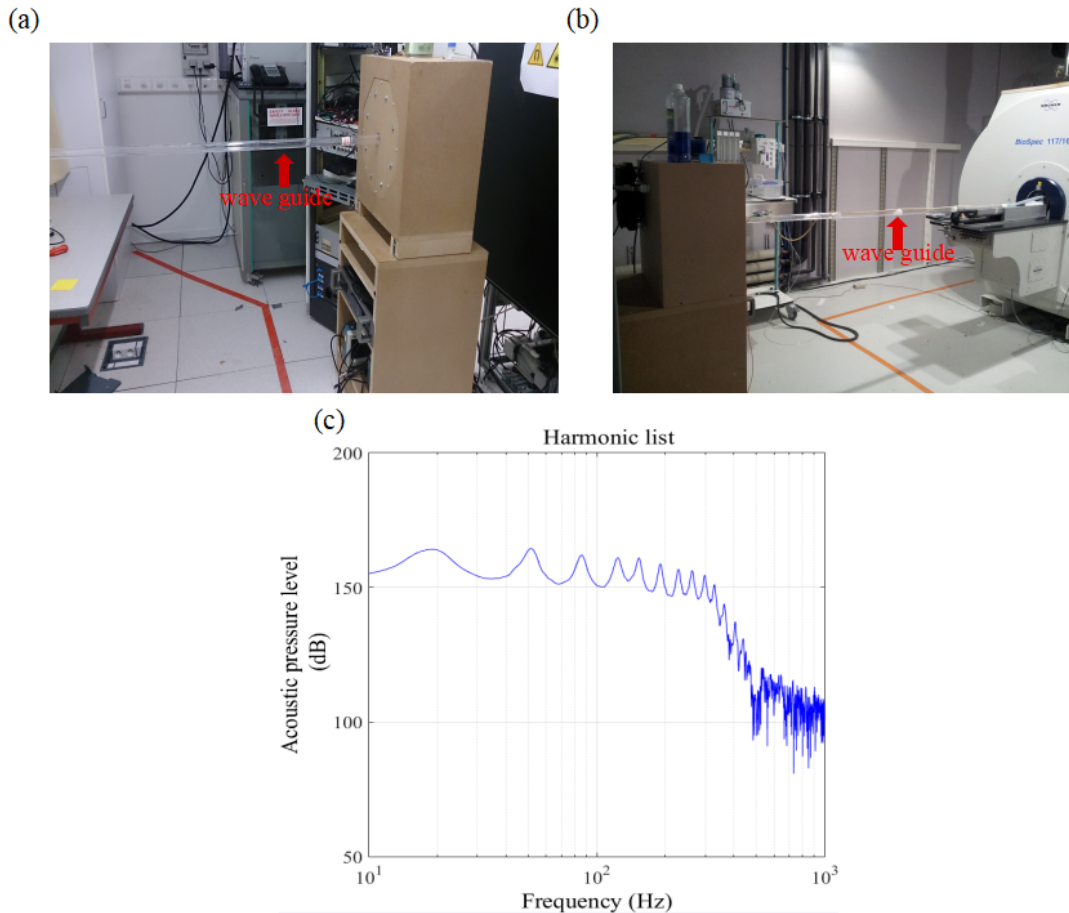


FIGURE 2.3: Installation of the excitation package for (a) Philips 1.5T MR scanner and (b) Bruker 11.7T MR scanner; (c) Resonance frequencies measured by the optical system for a low frequency loudspeaker used for the 1.5T MR scanner. The red arrows show the wave guides.

The main difference between our lab-made methods and methods from the literature lies in that the acoustic pressure wave is transmitted by a plastic tube and applied directly on the regions of interest without a passive relay. The main advantage of our wave generator resides in its flexibility to adjust the orientation of the entry wave and the size of the excitation source by choosing appropriate acoustic adapters at the end of the plastic tube. In addition, the optical monitoring system permits to identify the resonance frequencies of the plastic tube in order to guarantee a sufficient entry wave amplitude as well as to monitor the wave pressure level during acquisition. This wave generation system has been calibrated and optimized during Marion Tardieu's PhD (Tardieu, 2014). In my work, the wave generation system was implemented and adjusted using appropriate acoustic adapters for different MR scanners according to the experimental needs. For the Philips 1.5 T MR scanner (Achieva, Philips Healthcare, The Netherlands), both the excitation package and the monitoring package were placed in the technical room which is located behind the scanner room along the axis of the magnet. The wave guide passed through the penetration panel into the scanner room (Figure 2.3(a)). For the Bruker 11.7 T MR scanner (BioSpec, Bruker, USA),

the excitation package was placed in the scanner room across from the scanner (Figure 2.3(b)). The monitoring package was placed in the console room. Figure 2.3(c) presents an example of the frequency response measured by the optical system for a low frequency loudspeaker. The resonance frequencies are detected in order to be eventually used for MRE acquisition. The choice of the acoustic adapters will be presented in details in Chapters 4 and 5 according to different experimental needs.

2.2.2 Supersonic acoustic radiation force for SSI

Application of an acoustic radiation force (ARF) to create a mechanical vibration was first proposed by Sarvazyan *et al.* (Sarvazyan *et al.*, 1998) to assess the mechanical properties of soft tissues. The principle lies in the focusing of the ultrasonic beam at a given depth for a long enough time so as to push the soft tissue as illustrated in Figure 2.4(a). The response of the focusing zone was evaluated. Later Bercoff *et al.* proposed to combine the use of the ARF with Impulse Elastography to study the tissue response in regions surrounding the focusing zone (Bercoff, 2004). This combination permits to free the clinicians from the external vibrator, leading to better measurement flexibility and robustness. The focused ARF at arbitrary point \mathbf{r} and time t can be modeled as:

$$F(\mathbf{r}, t) = 2\alpha \frac{p^2(\mathbf{r})}{\rho c^2} \text{rect}_T(t) \quad (2.1)$$

where α is the tissue attenuation coefficient related to the central frequency of the emitted ultrasound, ρ is the tissue density, c is the ultrasound velocity in the tissue, and p is the pressure field in the focusing zone.

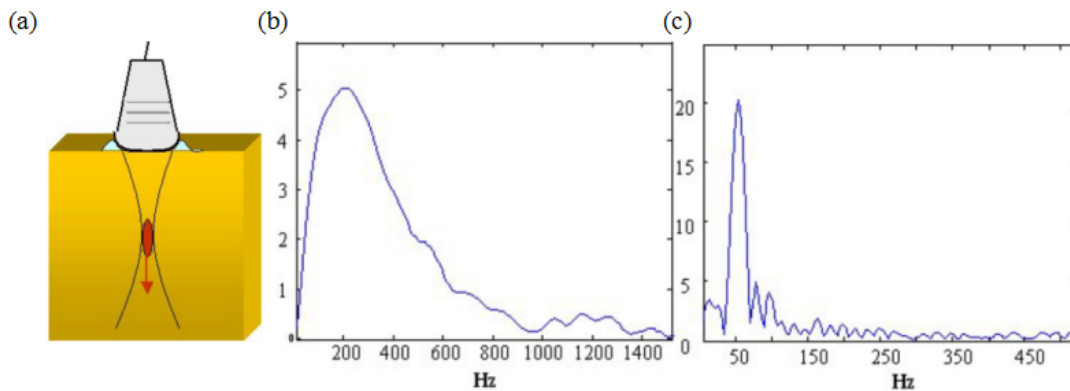


FIGURE 2.4: (a) Illustration of the generation of the ARF by focusing the ultrasonic beam and the generated shear wave spectral bandwidth for (b) a simple excitation with fixed amplitude and (c) an excitation with modulated amplitude (Bercoff, 2004).

The tissue response to the focused ARF can be well characterized by the Green's function (Aki and Richards, 2002). The propagation of shear waves in opposite directions were demonstrated both in simulations and experiments (Bercoff, 2004). The generated shear wave, induced by the extreme brief excitation time (typically about 100 μs), has a large spectral bandwidth

(Figure 2.4(b)) which depends on the tissue mechanical properties. To control the frequency spectrum and generate a mono-frequency shear wave, Bercoff *et al.* proposed to successively apply the focused ARF with a sinusoidal amplitude modulation at the focusing zone (Bercoff, 2004). The deposited energy can then be concentrated onto the specific frequency (Figure 2.4(c)), which is identical to the ARF amplitude modulation frequency.

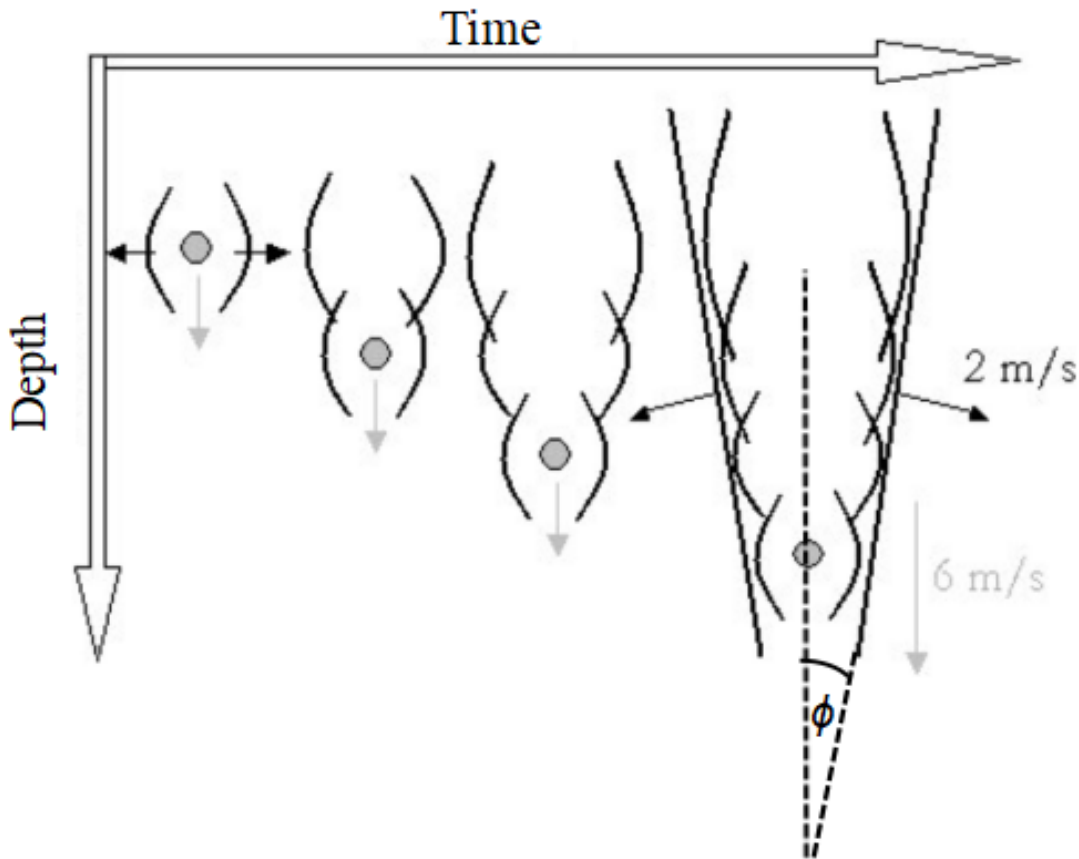


FIGURE 2.5: Principle of the supersonic mode for generating a conical shear wave front with a Mach number of 3 (Bercoff, 2004).

Although the focused ARF permits to generate shear waves in a precise location of the tissue, the amplitude of the shear wave is very low and even decreases significantly when it propagates away from the focusing zone, which limits the signal-to-noise ratio and thus challenges the reconstruction quality of the mechanical properties. Meanwhile, the exploitable region of interest is very limited due to the small size of the focusing zone. To overcome these limitations, subsequent translated focusing zones with the supersonic mode was proposed by Bercoff *et al.* to improve the total generated shear wave amplitude and also to enlarge the exploitable regions of interest with sufficient shear wave amplitude (Bercoff, 2004). The principle of the supersonic mode lies in successively focusing the ultrasonic beams at different depths with a corresponding source moving speed superior to the generated shear wave speed (Figure 2.5), so that the shear wave generated by each focusing zone constructively interferes to form a planar shear wave with higher spatial extension and amplitude. The supersonic mode is characterized by

the Mach number M , which is the ratio between the focusing source moving velocity and the generated shear wave speed. In Figure 2.5, it is observed that there exists an angle ϕ between the generated shear wave front and the axial direction. This inclination angle ϕ is related to the Mach number by the relationship $\phi = \tan^{-1}(1/M)$. When M equals ∞ , ϕ equals zero, and hence the shear wave front is exactly parallel to the axial direction. In real life, a finite Mach number is used, thus a conical shear wave front is observed which leads to measurement error. However, this measurement error is inferior to 5% and hence negligible when the Mach number is larger than 3 (Deffieux, 2008).

In my thesis, a clinical Aixplorer ultrasound system (Supersonic Imaging, Aix-en-Provence, France) was used. Three 2D ultrasound probes (Vermon, Tours, France) with different frequency bandwidths (XC 6-1 MHz, SL 10-2 MHz, SL 15-4 MHz) were respectively used to focus the ARF in the imaged objects. 'XC' represents single crystal curved probe, while 'SL' stands for super linear probe. There also exists a 3D probe (SLV 16-5 MHz). However, it in fact provides a series of 2D images instead of a true 3D imaging. We thus did not use this 3D probe in our work. In clinical mode, all the probes exert a focused ARF with a set amplitude, thus the generated shear wave always has a large frequency bandwidth.

2.2.3 Summary of the excitation step

Dynamic excitation is used for both MRE and SSI. Regarding the experimental setup, the excitation step of SSI is more compact and flexible because the excitation can be directly performed by the ultrasound probe. However, the excitation step of SSI is also more operator dependent due to the same reason. In contrast, the excitation package of MRE is more bulky, but it can be precisely pivoted and hence it is less operator dependent. Besides, the two modalities differ in the frequency characteristics of the generated shear waves. Mono-frequency shear waves are generated for MRE, while shear waves with large frequency bandwidths are induced for SSI. The fact that different types of shear waves are exploited by these two modalities is one important source to account for the potential discrepancies between MRE and SSI measurements.

2.3 Displacement field acquisition

The acquisition of the displacement field is the step where MRE and SSI differ the most significantly because of their differences in basic physics imaging principles. In general, MRE exploits the sensitivity of the MR phase signal to movement to encode the displacement field for a limited number of snapshots, typically 4, while SSI makes use of the high frame rate of ultrasound imaging to encode the displacement field along time, for typically thousands of snapshots.

2.3.1 Spin echo based MRE sequence

The spin echo sequence is adapted to the MRE sequence by adding additional bipolar gradients. The core part of this modification is to synchronize the bipolar gradients with the external excitation, first to make sure that during each dynamic acquisition, each line of the k-space encodes the information of the same vibration instant; and second to acquire different vibration instants by varying the phase offset between the bipolar gradient and the external excitation. To achieve the synchronization over the acquisition, excitation frequency specific time constraints were imposed for the MRE sequence as shown in Figure 2.6.

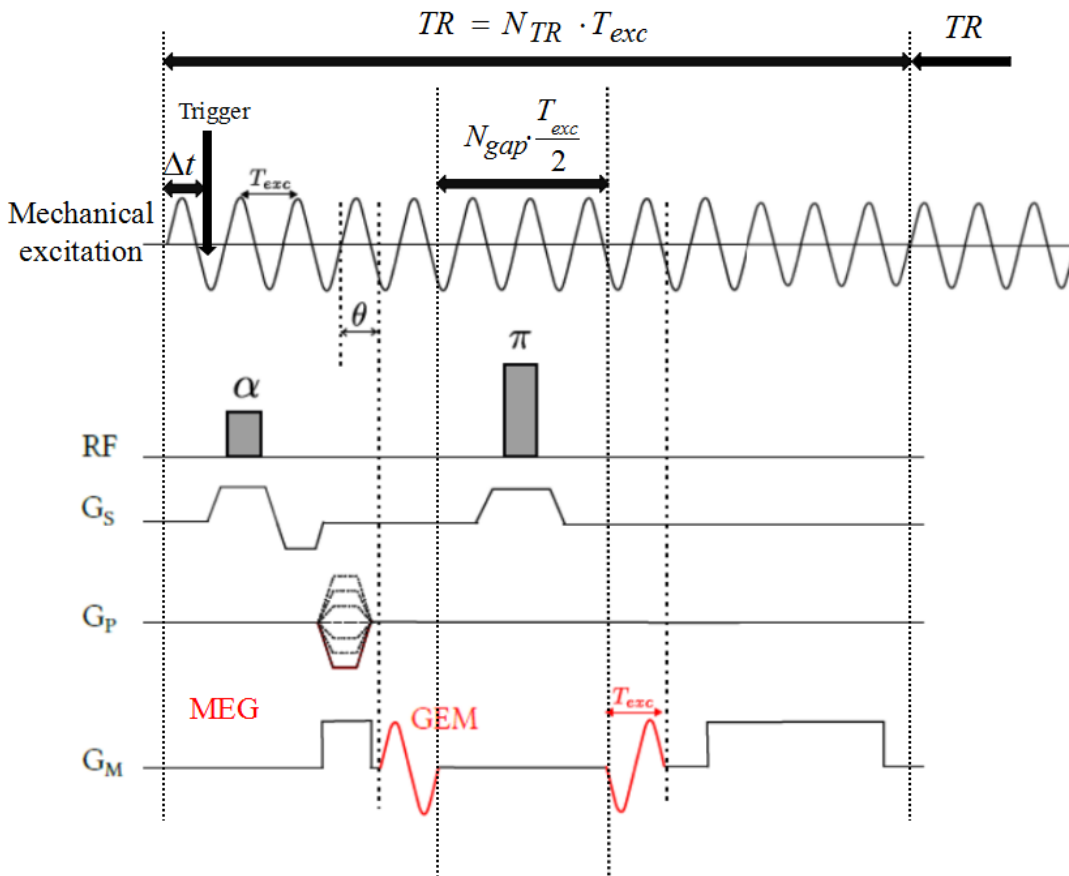


FIGURE 2.6: Chronogram of the spin echo based MRE sequence with the MRE specific time constraints.

First, the TR should be an integer fold (N_{TR}) of the excitation period (T_{exc}) to make sure that the bipolar gradient before the refocusing pulse always begins at the same vibration instant during each dynamic acquisition. Then the time interval between the bipolar gradients on either side of the refocusing pulse should be an integer fold (N_{gap}) of half the excitation period. The sign of the bipolar gradient after the refocusing pulse should be correspondingly adjusted to ensure the continuous phase accumulation. For example, in Figure 2.6, only one bipolar gradient was added on either side of the refocusing pulse. Because N_{gap} was set to 6, the sign of the second bipolar gradient had

to be set opposite to that of the first one to avoid phase cancellation and to guarantee phase accumulation. Finally, the phase offset between the bipolar gradient and the external excitation can be regulated by sweeping the position of the trigger generated by the MR system for the function generator. The time delay Δt between the excitation trigger and the imaging sequence depends on the number of dynamic instants (N_{dyn}) to acquire, and is an integer fold of $\frac{T_{exc}}{N_{dyn}}$. The bipolar gradients are successively applied along each of the field of view encoding axis to encode the three-dimensional displacement field. The displacement fields are deduced by inverting equation (1.27).

The spin echo based MRE sequence had already been installed on the Phillips 1.5 T MR scanner when I started my thesis, while, for the Bruker 11.7 T MR scanner, I worked with Benoit Larrat to program and install the spin echo based MRE sequence.

2.3.2 Ultrafast imaging and ultrasonic speckle interferometry for SSI

After generating the transit shear wave in the tissue, the ultrasound probe transfers to the reception mode for successively recording the Bmode images in order to track the shear wave propagation. The shear wave speed of soft tissue is usually between 1 and 10 m/s. Given a region of interest with a width of 4 cm, the shear wave generated in the middle of the region will take at most 20 ms to cross the whole region. In this case, a conventional ultrasound system with a frame rate of about 50 Hz (meaning each 20 ms to record a Bmode image) is not able to follow the shear wave front. To overcome the frame rate limit of conventional ultrasound imaging, the ultrafast imaging method using planar wave was proposed to record the shear wave propagation in real time (Sandrin et al., 2002). The ultrafast technique can achieve a frame rate of thousands of Hertz.

In contrast with the conventional method acquiring the Bmode image line by line, the ultrafast method emits only one planar wave into the media (Shattuck et al., 1984), then records and focuses the echo signals from the whole media (Figure 2.7). The ultrafast method permits a significant improvement of the frame rate and an important gain of acquisition time. However, this gain in time is at the cost of a degradation of the lateral spatial resolution and the image contrast (Bercoff, 2004). The lateral spatial resolution is slightly degraded and the image contrast is reduced by a factor of 2, because the focusing only appears in the reception step while it appears in both emission and reception steps for the conventional method. The above two degradation factors of the ultrafast method are in fact deleterious for Bmode images but do not affect significantly motion detection. Firstly, the generated shear wave often has a wavelength of about several centimeters, which is much higher than the lateral spatial resolution that lies within the range of a millimeter. The loss of lateral spatial resolution thus does not influence much the quality

of motion estimation. Secondly, the loss of contrast may be compensated by slightly sacrificing the frame rate to average the recorded echo signals.

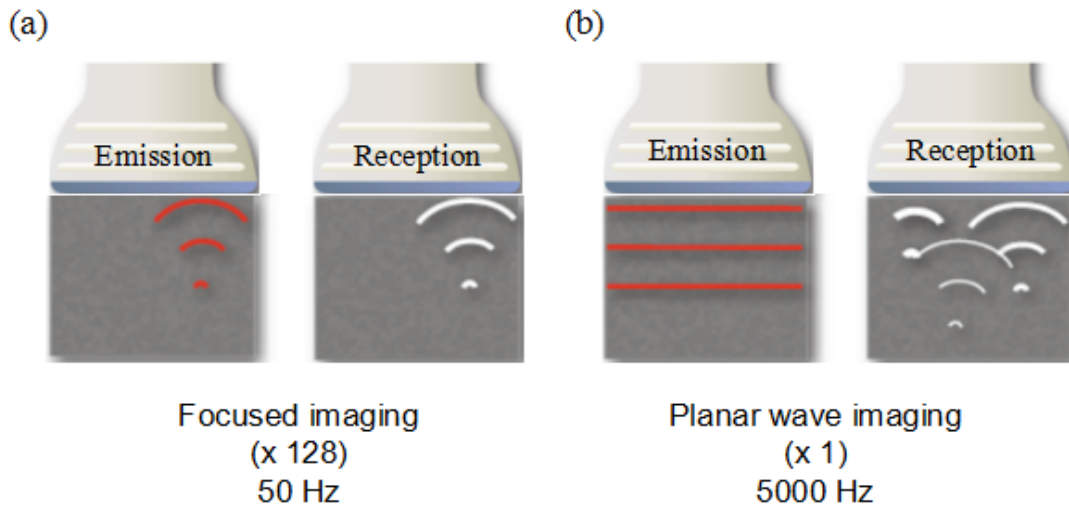


FIGURE 2.7: (a) Conventional imaging method focusing in both emission and reception steps; it needs to scan the focusing line across the whole volume to form a Bmode image yielding a low frame rate of about 50 Hz; (b) Planar wave imaging method focusing only during the reception step; it can achieve a frame rate of up to 5000 Hz (Deffieux, 2008).

With the acquired high frame rate Bmode images, the displacement field can be deduced by cross-correlating two successive Bmode images. In the clinical Aixplorer system, only 1-D displacement fields were recorded, namely the axial displacements, so this section focuses on the illustration of the axial displacement acquisition. The method used for deducing the axial displacement is called ultrasonic speckle interferometry (Walker et al., 1991). It is mainly composed of two steps: temporal splitting of the axial signal line for each Bmode image and cross-correlation of the RF signals from corresponding splitted windows.

First, each acquired axial line is splitted into a series of windows with an optimized window length of 8λ (Bercoff, 2004) and an overlapped percentage of 50% as illustrated in Figure 2.8 yellow region. Then the RF signals in corresponding axial windows from two successive Bmode images are cross-correlated to deduce the window specific temporal shift Δt maximizing the cross-correlation. Finally the axial displacement value U_z for a window (z, x) at time t is calculated as $\frac{c\Delta t}{2}$, with c corresponding to the ultrasound velocity in the tissue.

2.3.3 Summary of the acquisition step

MRE allows to acquire the three-dimensional displacement field, while SSI only allows to acquire 1-D displacement field. SSI benefits from a much

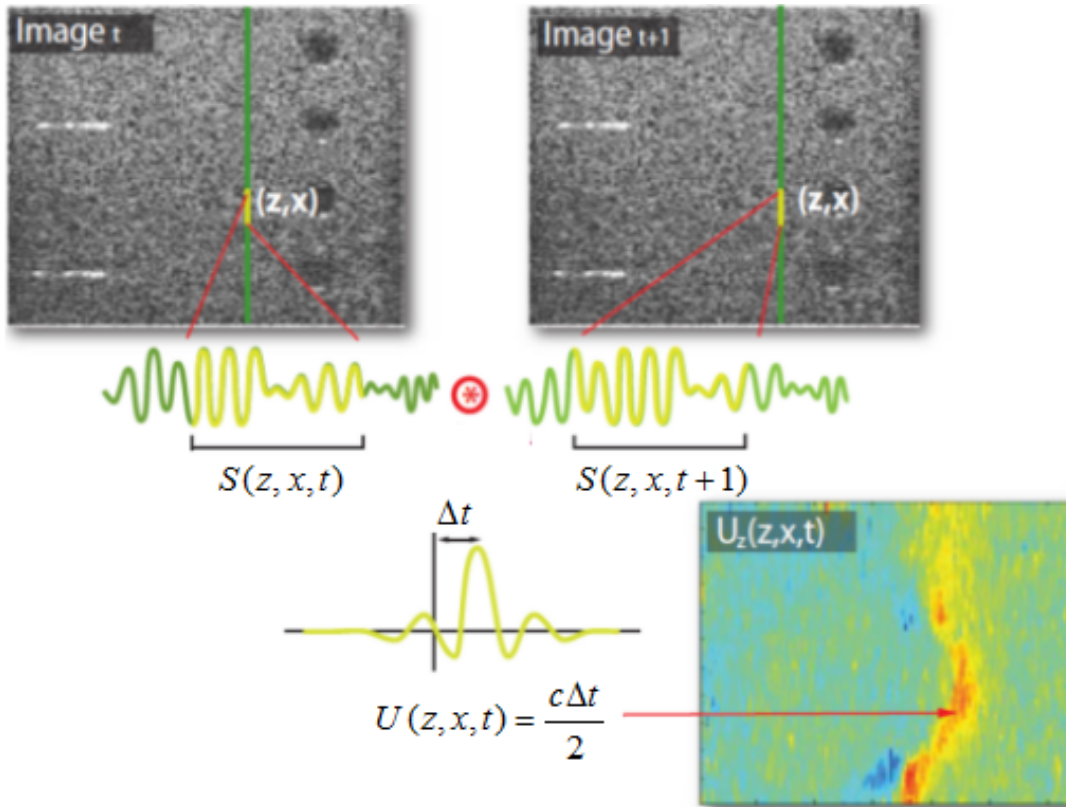


FIGURE 2.8: Calculation of the axial displacement by cross-correlating the RF signals (Deffieux, 2008). z, x represent respectively the axial and lateral direction.

higher time efficiency than MRE which requires long time acquisitions. Different acquisition features of MRE and SSI indicate their specific measurement uncertainty sources which may induce potential measurement discrepancies between MRE and SSI. The measurement uncertainty of the MR phase value influences the reconstruction validity of MRE while the cross-correlation quality between the displacement profiles of neighboring pixels influences the reconstruction validity of SSI.

2.4 Mechanical properties reconstruction

2.4.1 q-based model independent AIDE algorithm for MRE

The q-based AIDE approach based on Equation (1.31) as seen in Chapter 1 permits to deduce the shear viscoelastic moduli. It should be noted that the shear viscoelastic moduli obtained from equation (1.31) are model dependent, because the equation (1.17) has already incorporated the rheological Voigt model and hence equation (1.31) is also based on the rheological Voigt model. However, nowadays, there has not been a consensus on which model is the most appropriate for describing the tissue response under a mechanical excitation. In this context, we chose a model independent algorithm to reconstruct the mechanical properties. This algorithm has been used throughout

my thesis.

The model independent approach was developed by Ralph Sinkus' group in order to calculate the viscoelastic parameters without introducing rheological models (Sinkus et al., 2005). Without the rheological model assumption, the complex shear modulus can be written as:

$$G^*_i = -\rho\omega^2_{exc} \frac{q_i(\mathbf{r}, \omega_{exc})}{\nabla^2 q_i(\mathbf{r}, \omega_{exc})} \quad (2.2)$$

Because the local planar wave assumption used for the displacement field also holds for the q-field, each q-field component, q_i , can be written as:

$$q_i = |q_i| \cdot \exp^{k_i \cdot r_i} \quad (2.3)$$

where $k_i = \beta_i - j\alpha_i$ represents the complex wave number with $\beta_i = \frac{\omega_{exc}}{V^s_i}$, and α_i the attenuation parameter.

Equation (2.2) can then be rewritten as:

$$G^*_i = \frac{\rho\omega^2_{exc}}{k_i^2} = \frac{\rho\omega^2_{exc}}{(\beta_i - j\alpha_i)^2} \quad (2.4)$$

The shear dynamic modulus G_d and the shear loss modulus G_l can be deduced as:

$$G_{di} = \rho\omega^2_{exc} \frac{\beta_i^2 - \alpha_i^2}{(\beta_i^2 - \alpha_i^2)^2 + 4(\alpha_i\beta_i)^2}, \quad (2.5)$$

$$G_{li} = \rho\omega^2_{exc} \frac{2\alpha_i\beta_i}{(\beta_i^2 - \alpha_i^2)^2 + 4(\alpha_i\beta_i)^2}$$

In my thesis, we chose to principally exploit the shear velocity value V^s instead of the G_d and G_l modulus. This choice was motivated on the one hand by the investigation of the appropriate acquisition and reconstruction conditions for MRE through an *in silico* study with V^s as a robust physical reference mechanical property, on the other hand, to allow the comparison with the direct shear velocity measurement obtained from the SSI modality.

2.4.2 Time of flight method for SSI

The core idea of the time of flight approach consists in making full use of the high frame rate provided by the ultrafast technology in order to record the shear wave propagation in the imaged object in real time, which makes the tracking of the shear wave propagation possible. In this context, the time of flight dt of the shear wave front between two neighboring points with a distance dx can be estimated by intercorrelation of the acquired displacement profiles on these two points. Maximizing the intercorrelation function permits to obtain the time of flight. The shear velocity can then be deduced as $V^s = \frac{dx}{dt}$. The principle of the time of flight approach is illustrated in Figure

2.9. The main advantage of the time of flight approach is its low sensitivity to data noise because it does not require the calculation of spatial or temporal derivatives. The main disadvantage of the time of flight approach is its inability to access the shear viscous modulus.

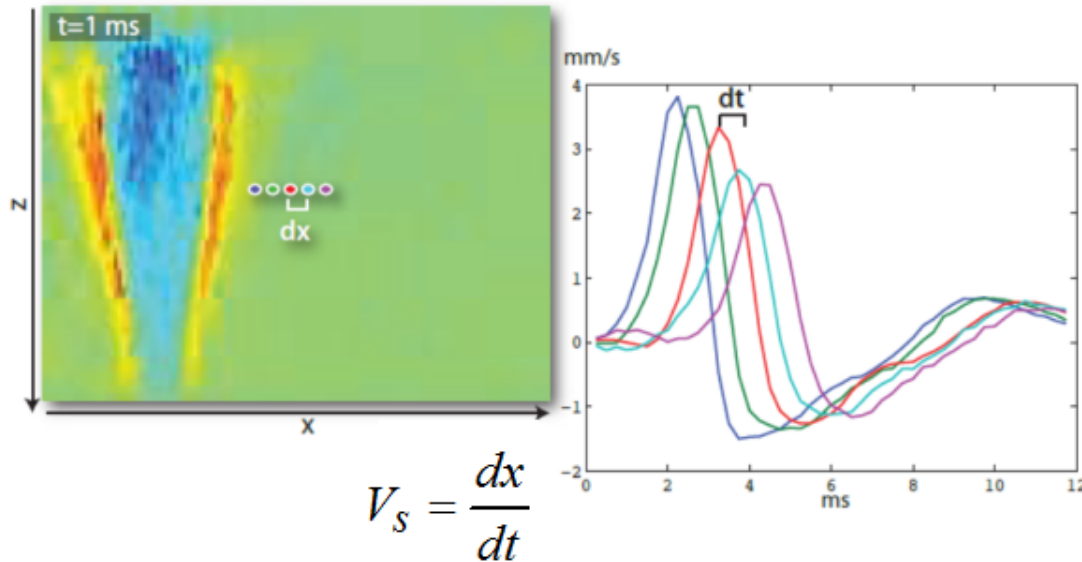


FIGURE 2.9: Principle of the time of flight approach (Deffieux, 2008). The flight time dt is estimated by intercorrelation of the displacement profiles of two neighboring points with distance dx . The shear velocity can then be deduced using $V^s = \frac{dx}{dt}$.

It should be noted that the measured shear velocity V^s is in fact a group velocity, because the generated shear wave has a large frequency bandwidth. In quasi-elastic media, all frequency components of the generated shear wave travel with the same phase velocity. In this case the measured shear group velocity equals the shear phase velocity and hence the shear elastic modulus (μ) can be deduced as ρV^{s2} . However, in viscoelastic media, shear wave dispersion exists between different frequency components. As a result, the measured group velocity no more equals the shear phase velocity and hence the shear elastic modulus can no longer be calculated using the relationship $\mu = \rho V^{s2}$.

The time of flight approach is the standard approach currently installed in the clinical Aixplorer system. Thus only the shear elastic information can be obtained. In my thesis, the measured shear velocity was principally exploited in order to investigate the influence of different probes on the shear velocity measurement, and to compare its value with the shear velocity measurement of MRE.

2.4.3 Summary of the reconstruction step

MRE and SSI greatly differ from each other in the reconstruction step. MRE makes full use of the acquired three-dimensional displacement field to locally invert the wave equation while SSI takes advantage of its high frame

rate to track the propagation of shear wave. Each modality has its own reconstruction validity issues which may again induce potential measurement discrepancies between MRE and SSI. Shear modulus or Young's modulus derived from the shear velocity may amplify the above measurement biases because of the squaring and scaling effects. Thus the shear velocity should be more appropriate comparison element between MRE and SSI.

2.5 Discussions and Conclusions

In this chapter, we have reviewed the possible methodological differences between MRE and SSI. The main differences between the two modalities in the respect to the three elementary steps of the elastography technology are summarized in Table 2.1. Based on the methodological differences between the two modalities, we infer that potential measurement biases between MRE and SSI mainly originate from two sources: the theoretical difference between their measurements and the reconstruction validity for each modality.

TABLE 2.1: Methodological differences between MRE and SSI

	MRE	SSI
Excitation	Continuous harmonic wave Mono-frequency	Transient wave Broad frequency bandwidth
Acquisition	3D volume Three-dimensional displacement field	2D image (or successive 2D images) One-dimensional axial displacement field
Reconstruction	Local inversion of wave equation Viscoelastic model Shear phase velocity	Time of flight Elastic model Shear group velocity

First, different frequency characteristics of generated shear waves for the two modalities may induce an important theoretical bias between their measurements. In a quasi-elastic medium, this theoretical bias may be negligible because the shear group velocity measured by SSI can be reasonably approximated as the shear phase velocity. In this case, it can be considered that SSI measures the same physical parameter as MRE. However, in a viscoelastic medium where there exists shear wave dispersion between different frequency components, this theoretical measurement bias can not be neglected. In addition, the frequency bandwidth of the generated shear waves depends on the emission frequency range of the ultrasound probe, which further complicates this theoretical bias. However, this feature can also serve as a qualitative indicator for evaluating the shear wave dispersion level in the medium under inspection. Concretely, if the measurements between probes with different emission frequency ranges agree well with each other, the medium can be considered quasi-elastic.

Second, the reconstruction validity of each modality plays an important role for the cross-validation of their measurements. This issue is more critical for MRE, because three order spatial derivatives are calculated, making the reconstruction very sensitive to noise. In addition, it should be noted that the

above two measurement biases can be amplified by the squaring and scaling effects when more complex moduli are compared. For example, under the same conditions, the measurement bias related to the shear elastic modulus is higher than that related to the shear velocity.

In conclusion, for a thorough cross-validation between MRE and SSI measurements, the above mentioned bias sources should be taken into consideration and minimized by optimizing the acquisition and reconstruction conditions as well as choosing an appropriate comparison metric. We stated that the shear velocity was the most appropriate metric for comparison between MRE and SSI. We used this parameter as the measurement comparison element in my thesis.

3 Acquisition and reconstruction conditions *in silico* for accurate and precise Magnetic Resonance Elastography

3.1 Introduction

As described in Chapter 1, the q-based AIDE method may theoretically be flawless upon proper joint assumptions and equation (Baghani, Salcudean, and Rohling, 2009). However, the performances of the q-based AIDE method are challenged by multiple experimental parameters, especially the frequency, f , and the amplitude, A , of the mechanical wave as well as the voxel size, a , and the signal-to-noise ratio, SNR, of the MRE acquisition. These parameters often have an entangled influence on the quality of the reconstruction, namely the accuracy and the precision of the computed viscoelastic moduli. Intuitively, appropriate sampling of the displacement field will be achieved when, first, for a given SNR, the number of voxels is adapted to the local shear wavelength, λ – the excitation frequency is accordingly selected – second, the local amplitude of the propagating wave actually emerges from the uncertainty of the displacement measurement, ΔA , which is determined by the effective SNR. In this respect, two more comprehensive parameters, λ/a and $A/\Delta A$ can serve as pertinent criteria to evaluate the reconstruction quality. Firstly, the quality of the reconstruction depends on the number of voxels per wavelength, λ/a , mainly because the acquired displacement fields are inevitably discrete and noisy. Papazoglou *et al.* have already reported the influence of the SNR on the choice of λ/a ratio while optimizing the MRE reconstruction outcomes (Papazoglou *et al.*, 2008). The simulations were carried out with a reconstruction method based on the displacement field \mathbf{u} which is nowadays less preferred compared to the q-field based reconstruction method. Besides the SNR influence was studied by adding white Gaussian noise to the displacement field which does not quite reproduce the physical process of data acquisition. Secondly, to cope with the three-dimensionality of the shear wave propagation in the living tissues, motion encoding is implemented along the three spatial directions and the three components of the displacement field are acquired. The three associated equations of motion can independently be inverted and shear viscoelastic moduli can be deduced. In the assumption of isotropy, the three computed moduli are expected to be similar and thus could be averaged

to get a more robust scalar value (Sinkus et al., 2007; Rouvière et al., 2011). However, in general, the components of the three-dimensional displacement field are different and, even for a fairly-well controlled SNR along each motion encoding direction, $i \in \{1, 2, 3\}$, the measured ratios $A_i/\Delta A_i$ may drastically differ. As a result, a mere average may jeopardize the estimation by incorporating poor quality data in the outcome. To mitigate this risk, some research groups have proposed various combination strategies to calculate a quality-weighted average of shear viscoelastic moduli, such as the q-field quality weighting (Arunachalam et al., 2016), the ordinary least square method (Oliphant et al., 2001), or the total least square method (Okamoto, Clayton, and Bayly, 2011). The aforementioned approaches have been independently undertaken. Here, they are challenged under the same controlled conditions for both data acquisition and reconstruction.

In this chapter, the aim was, on the one hand, to explore the influence of the λ/a ratio using a voxel-wise reconstruction quality criterion as well as to study the effect of interpolation or decimation on regulating this ratio, and on the other hand, to evaluate the effects of different averaging strategies and the quality parameters proposed in this chapter on the reconstruction quality. For that purpose, a fully-analytic model was used to simulate realistic mechanical spherical waves generated at the surface of a semi-infinite elastic medium by a point source allowing to obtain test MRE data sets in a defined elastic medium with arbitrary excitation frequency, excitation amplitude, voxel size, and signal-to-noise ratio. Noise was then added to the simulated complex MR signal in order to properly mimic the physical process of data acquisition.

3.2 Methods

3.2.1 Analytic wave simulation

The 3D displacement field, $u_i(\mathbf{r}, t)$, $i \in \{1, 2, 3\}$, as measured by MRE, may be analytically derived with the elastic Green function (Aki and Richards, 2002). Assuming an isotropic, homogeneous, linearly elastic, and half-space infinite media excited by a harmonic point source, the expression for the i^{th} component of the displacement field induced in the media, for an arbitrary point, \mathbf{r} , and time, t , is given by:

$$\begin{aligned}
 u_i(\mathbf{r}, t) = & \frac{A_{\text{exc}}}{2\pi\rho} (3\gamma_i\gamma_j - \delta_{ij}) \frac{1}{r^3} \int_{\frac{r}{Vc}}^{\frac{r}{Vs}} \tau \cos(\omega_{\text{exc}}(t - \tau)) H(t - \tau) d\tau \\
 & + \frac{A_{\text{exc}}}{2\pi\rho Vc^2} \gamma_i\gamma_j \frac{1}{r} \cos\left(\omega_{\text{exc}}\left(t - \frac{r}{Vc}\right)\right) H(t - \tau) \\
 & - \frac{A_{\text{exc}}}{2\pi\rho Vs^2} (3\gamma_i\gamma_j - \delta_{ij}) \frac{1}{r} \cos\left(\omega_{\text{exc}}\left(t - \frac{r}{Vs}\right)\right) H(t - \tau).
 \end{aligned} \tag{3.1}$$

where $r = |\mathbf{r}|$, $\gamma_i = \partial r / \partial x_i$ along the three spatial dimensions $i \in \{1, 2, 3\}$, δ_{ij} is the Kronecker symbol ($\delta_{ij} = 1$ when $i = j$, otherwise 0, where j is the excitation direction), H is the Heaviside step function ($H=1$ when $t \geq \tau$, otherwise 0), ρ is the mass density, ω_{exc} and A_{exc} stand for the angular frequency and the amplitude of the point source excitation, V^s and V^c represent the shear and compression wave velocities, respectively.

When the excitation stress is orthogonal to the surface of the medium and along the third spatial dimension $i = 3$, the analytic expression of the curl of shear displacement field, $\mathbf{q} = \nabla \times \mathbf{u}_s$, is:

$$q_1(\mathbf{r}, t) = \frac{A_{\text{exc}}\gamma_2}{2\pi\rho V^s{}^2} \sqrt{\frac{\omega_{\text{exc}}^2}{V^s{}^2} + \frac{1}{r^2}} \sin\left(\omega(t - r/V^s) + \arctan\left(\frac{-V^s}{\omega_{\text{exc}} \times r}\right)\right), \quad (3.2)$$

$$q_2(\mathbf{r}, t) = \frac{A_{\text{exc}}\gamma_1}{2\pi\rho V^s{}^2} \sqrt{\frac{\omega_{\text{exc}}^2}{V^s{}^2} + \frac{1}{r^2}} \sin\left(\omega(t - r/V^s) + \arctan\left(\frac{-V^s}{\omega_{\text{exc}} \times r}\right)\right), \quad (3.3)$$

$$q_3(\mathbf{r}, t) = 0. \quad (3.4)$$

To account for the embedded noise of the displacement field, we mimicked the MRE acquisition procedure. First, the simulated displacement field components were converted into noise-free recorded phase values, $\varphi_i(\mathbf{r}, t)$, of the simulated MR images for a three-dimensional motion-sensitized spin-echo-based MRE sequence according to equation (3.5) (Muthupillai et al., 1995).

$$\varphi_i(\mathbf{r}, t) = \gamma \frac{N}{2} T_{\text{exc}} \cdot G_{\text{MEG},i} \cdot u_i(\mathbf{r}, t), \quad (3.5)$$

where γ is the gyromagnetic ratio of hydrogen nuclei, N , the number of cycles of bipolar motion-encoding gradients with duration $T_{\text{exc}} = 2\pi/\omega_{\text{exc}}$ and amplitude $G_{\text{ME},i}$ along the three spatial dimensions, $i \in \{1, 2, 3\}$. The magnitude value of the simulated MR image was homogeneously set to 1. Second, a uniform white Gaussian noise with standard deviation σ was added to the real, I_{re} , and imaginary, I_{im} , parts of the simulated MR images, leading to the following noise-degraded phase values $\tilde{\varphi}_i(\mathbf{r}, t)$ and corresponding MRI magnitude SNR:

$$\tilde{\varphi}_i(\mathbf{r}, t) = \arctan\left(\frac{\tilde{I}_{\text{im}}}{\tilde{I}_{\text{re}}}\right), \quad \text{SNR} = \frac{1}{\sigma}. \quad (3.6)$$

Noise-degraded displacement fields were then deduced by inverting equation (3.5).

3.2.2 Simulated experimental conditions

The 3D wave propagation was simulated with Matlab (MathWorks, Natick, Massachusetts, USA) in an $(81 \times 81 \times 31)$ mm³ cuboid volume with compression wave velocity $V^c = 1500 \text{ m} \cdot \text{s}^{-1}$ and shear wave velocity $V^s =$

$2 \text{ m} \cdot \text{s}^{-1}$, as typically expected in soft tissues (Akhtar et al., 2011). As the pattern of the displacement field induced by a point source is rotationally-symmetric along the incidence axis, the outcomes of the reconstruction may differ with the relative orientation of the source incidence and the spatial and motion encoding axes. Hence, simulations were performed for two geometrical configurations: 1) when the incidence axis is aligned with the axis 3, i.e. when it is normal to the image plane (Figure 1 (a)); 2) when the incidence axis is at 30° with respect to the axis 3, i.e. when it is at oblique angle with the image plane (Figure 2 (a)). For each geometrical configuration, the excitation amplitude was the same at the center of the medium surface and a 1 mm isotropic voxel size was taken. The 3D displacement fields were generated at four time points equally spaced over one mechanical oscillation period. First, we explored ten λ/a ratios by varying fourfold the excitation frequency between $f = 100 \text{ Hz}$ and $f = 400 \text{ Hz}$ while maintaining the motion sensitivity of the sequence by increasing the number of cycles, N , of motion encoding gradients accordingly (see Equation 3.5). For each λ/a ratio, four levels of SNR (10, 20, 30, ∞) were simulated. Second, for $f = 100$ and 400 Hz , data were additionally either decimated or interpolated to achieve a λ/a ratio of 8.3.

3.2.3 Averaged shear velocity calculation

In Chapter 2, we have presented our reconstruction method and the general viscoelastic solution. In this chapter, as we assumed an isotropic, homogeneous and linearly-elastic medium, we obtain the simplified differential equations for the three components of the \mathbf{q} -field as:

$$-\rho\omega^2 q_i(\mathbf{r}, \omega) = \mu \nabla^2 q_i(\mathbf{r}, \omega), \text{ with } i \in \{1, 2, 3\}. \quad (3.7)$$

By substituting the relationship $V^s = \sqrt{\frac{\mu}{\rho}}$ into equation (3.7), we can then deduce the value of V^s along each motion-encoded direction as:

$$V_i^s(\mathbf{r}, \omega) = \frac{\omega}{\text{Re}\left(\sqrt{\frac{\nabla^2 q_i(\mathbf{r}, \omega)}{-q_i(\mathbf{r}, \omega)}}\right)}, \text{ with } i \in \{1, 2, 3\}. \quad (3.8)$$

In the isotropic assumption, the values of V_i^s along the three motion-encoded directions are expected to be identical. Thus it is reasonable to combine them to get a more robust velocity estimation. Four different averaging methods were implemented to combine the V_i^s along the three motion-encoded directions: two weighting methods based on the \mathbf{q} -field quality, namely the squared \mathbf{q} -field quality weighting method (qQW) and the maximum \mathbf{q} -field quality method (qQM); two least square methods, namely the ordinary least square method (OLS), and the total least square method (TLS).

3.2.3.1 q-field quality parameter

For the q-field quality weighting methods, we computed the 3D voxel-wise quality maps as the ratio between the amplitude of the curl of shear displacement field, $|\mathbf{q}|$, and the associated measurement uncertainty, $\Delta|\mathbf{q}|$. $\Delta|\mathbf{q}|$ was deduced from the measurement uncertainty of the displacement field amplitude, $\Delta|\mathbf{u}|$, by modeling the error propagation through polynomial fitting as follows.

A first order polynomial fitting with local kernel size $(3 \times 3 \times 3)$ was used to estimate the first order derivative of the complex displacement field \mathbf{u} . Thus, for each local point, we obtained the following overdetermined fitting system:

$$\begin{aligned} ax_1 + by_1 + cz_1 + d &= u_1 \\ ax_2 + by_2 + cz_2 + d &= u_2 \\ \dots & \\ ax_{27} + by_{27} + cz_{27} + d &= u_{27} \end{aligned} \quad (3.9)$$

where x_n , y_n and z_n are locally defined coordinates for u_n ($n = 1, 2, \dots, 27$) and $x_n, y_n, z_n \in \{-1, 0, 1\}$ which corresponds to the 1 mm isotropic voxel size. u_n features all the displacement measurements in the $(3 \times 3 \times 3)$ neighborhood of the targeted local point, so that a, b, c are the first order derivatives of the targeted local point along the three spatial dimensions.

Equation (3.9) could be written in the matrix form $\mathbf{AX} = \mathbf{B}$ as:

$$\begin{bmatrix} x_1 & y_1 & z_1 & 1 \\ x_2 & y_2 & z_2 & 1 \\ \vdots & \vdots & \ddots & \vdots \\ x_{27} & y_{27} & z_{27} & 1 \end{bmatrix} * \begin{bmatrix} a \\ b \\ c \\ d \end{bmatrix} = \begin{bmatrix} u_1 \\ u_2 \\ \vdots \\ u_{27} \end{bmatrix} \quad (3.10)$$

The parameters a, b, c, d were then solved using the least square method as:

$$\begin{aligned} a &= 0.0556 \sum_{n=1}^{27} x_n u_n, \\ b &= 0.0556 \sum_{n=1}^{27} y_n u_n, \\ c &= 0.0556 \sum_{n=1}^{27} z_n u_n. \end{aligned} \quad (3.11)$$

Equation (3.11) reveals that the uncertainty on a , b , and c originates from the uncertainty of u_n . Hence, according to the error propagation theory, the uncertainty on a , b , and c was expressed as:

$$\begin{aligned}
 \Delta a &= 0.0556 \sqrt{\sum_{n=1}^{27} x_n^2 \Delta u_n^2}, \\
 \Delta b &= 0.0556 \sqrt{\sum_{n=1}^{27} y_n^2 \Delta u_n^2}, \\
 \Delta c &= 0.0556 \sqrt{\sum_{n=1}^{27} z_n^2 \Delta u_n^2}.
 \end{aligned} \tag{3.12}$$

Because the SNR level is uniform across the simulated volume, the uncertainty of u_n should be uniform and equals to Δu_i defined along the encoding direction i , which is a function of the SNR and the number of displacement field samples, N_S , over one excitation period as in equation (3.13) (McGee et al., 2011; McGarry et al., 2011).

$$\begin{aligned}
 \Delta |u_i| &= \sqrt{\frac{2}{N_S}} \Delta u_i, \\
 \text{where } \Delta u_i &= \frac{2\Delta\tilde{\varphi}_i}{N\gamma T_{\text{exc}} G_{ME,i}}, \\
 \Delta\tilde{\varphi}_i &= \arctan\left(\frac{1}{SNR_i}\right), \quad SNR_i \neq \infty.
 \end{aligned} \tag{3.13}$$

However, a 3D Gaussian filter was applied to smooth the complex u -field before calculating the derivative, hence the value of Δu_n must be corrected accordingly. As the Gaussian filter corresponds to a convolution in the defined neighborhood, the measurement uncertainty for the smoothed u -field depends on the weighting matrix which is determined by the Gaussian filter parameters. Across our study, a kernel size $5 \times 5 \times 5$ and a standard deviation corresponding to 1 voxel were used for the Gaussian filter. Thus the corrected measurement uncertainty for the smoothed complex u -field was $0.15\Delta u_i$. Then the uncertainty on a , b , and c were deduced by implementing the corrected measurement uncertainty as:

$$\Delta a = \Delta b = \Delta c = 0.036\Delta u_i, \quad \text{with } i \in \{1, 2, 3\}. \tag{3.14}$$

Finally, according to the q -field definition, the uncertainty on q -field should be the root square of the uncertainties on two involved first order derivatives. Equation (3.14) reveals that all the first order derivatives have the same level of uncertainty in our simulation data, so $\Delta |q_i|$ was deduced as:

$$\Delta |q_i| = 0.051\Delta |u_i|. \tag{3.15}$$

The q-field quality parameter along each encoding direction Q_i and the total q-field quality parameter Q_t were deduced as:

$$\begin{aligned} Q^{MRE}_i &= |q_i|/\Delta|q_i|, \\ Q^{MRE}_t &= \sqrt{\sum_i (|q_i|/\Delta|q_i|)^2} \end{aligned} \quad (3.16)$$

3.2.3.2 q-field quality based methods

In the qQW method, the velocity V_{qQW}^s was deduced by weighting V_i^s with its corresponding squared q-field quality as:

$$V_{qQW}^s = \sum_i \frac{\left(\frac{|q_i|}{\Delta|q_i|}\right)^2 \times V_i^s}{\sum_i \left(\frac{|q_i|}{\Delta|q_i|}\right)^2}. \quad (3.17)$$

In the qQM method, the velocity V_{qQM}^s was deduced by the extraction of the V_i^s with the maximum q-field quality as:

$$V_{qQM}^s = V_i^s \Big|_{\max\left(\frac{|q_i|}{\Delta|q_i|}\right)}. \quad (3.18)$$

3.2.3.3 Least square based methods

In the OLS method, equation (3.7) could be rewritten as an overdetermined problem as shown in equation (3.19), where $\frac{-\omega^2}{V_i^{s,2}(\mathbf{r},\omega)}$ was the parameter to be fitted.

$$\frac{-\omega^2}{V_i^{s,2}(\mathbf{r},\omega)} q_i(\mathbf{r},\omega) = \nabla^2 q_i(\mathbf{r},\omega), \text{ with } i \in \{1, 2, 3\}. \quad (3.19)$$

The V_{OLS}^s was thus solved in a least-square sense as:

$$V_{OLS}^s = \frac{\omega}{\sqrt{\frac{\sum_i q_i(\mathbf{r},\omega) \nabla^2 q_i(\mathbf{r},\omega)}{\sum_i q_i(\mathbf{r},\omega) q_i(\mathbf{r},\omega)}}}. \quad (3.20)$$

In the total least square (TLS) method, the measurement uncertainty for both the q-field and the Laplacian of q-field were taken into consideration, so that equation (3.19) was rewritten as:

$$\frac{-\omega^2}{V_i^{s,2}(\mathbf{r},\omega)} (q_i(\mathbf{r},\omega) + E) = (\nabla^2 q_i(\mathbf{r},\omega) + F). \quad (3.21)$$

where E, F represent the error matrices for q_i and $\nabla^2 q_i$ respectively. V_{TLS}^s was then deduced by minimizing the norm of error matrices $\| [EF] \|$ (Okamoto, Clayton, and Bayly, 2011), using the singular value decomposition method (Golub and Van Loan, 1980).

$$V_{TLS}^s = V^s|_{\min\|EF\|}. \quad (3.22)$$

3.2.4 Data analysis

The first temporal harmonics, $u_i(\mathbf{r}, \omega)$, were calculated *via* a temporal Fourier transform of the simulated wave images at four phase offsets. A 3D Gaussian filter, with a kernel size of $5 \times 5 \times 5$ voxels and a standard deviation of 1 voxel, was applied to the complex \mathbf{u} -field. The first order derivatives of the \mathbf{u} -field and the second order derivatives of the \mathbf{q} -field were calculated by local polynomial fitting with respective kernel sizes $3 \times 3 \times 3$ and $5 \times 5 \times 5$. Equation (3.8) yields 3D maps of V_i^s along each motion-encoded direction. The voxels with a zero q_i field value were masked out to prevent any division by zero and the voxels with a tiny q_i field value were smoothed by the application of a median filter with a $3 \times 3 \times 3$ kernel onto the velocity maps. Three-dimensional maps of the averaged shear velocity were then calculated following the four weighting strategies. The reconstruction algorithm was implemented in a C++ based platform (Brun and Rademakers, 1997; Sinkus et al., 2005).

For individual V_i^s maps at normal incidence, regions of interest with identical volumes and levels of Q^{MRE}_i ($30 \pm 10\%$ for SNR 30 data, $20 \pm 10\%$ for SNR 20 data, $10 \pm 10\%$ for SNR 10 data) were selected, except for V_3^s maps for which regions of interest with identical levels of Q^{MRE}_i ($3 \pm 10\%$) were selected. The obtained masks were also applied for the corresponding V_i^s maps with SNR = ∞ . For averaged shear velocity maps at both normal and oblique incidences, regions of interest with identical volumes and levels of Q^{MRE}_t ($13 \pm 10\%$ for SNR 10 data, $26 \pm 10\%$ for SNR 20 data, $40 \pm 10\%$ for SNR 30 data) were selected. Mean values (MVs), standard deviations (SDs), and mean absolute percentage errors (MAPEs) were computed over these regions of interest as the main markers for data quality. MV and SD of V^s_i and the four averaged shear velocities were evaluated as a function of λ/a and SNR. MAPEs of the four averaged shear velocities were compared to determine the best strategy. For averaged shear velocity maps at normal incidence, regions of interest with identical volumes and levels of Q^{MRE}_t ($15, 20 \pm 10\%$ for SNR 10 data, $25, 30, 40 \pm 10\%$ for SNR 20 data, $50, 60, 70, 80, 90, 100 \pm 10\%$ for SNR 30 data) were selected. MAPEs computed over these regions of interest were evaluated as a function of λ/a to deduce *in silico* abaci. In addition, for SNR 30 data with $f = 100, 130, 240, 300, 400$ Hz, a $(10 \times 10 \times 20)$ mm³ cuboid volume region was selected in a quarter of the whole volume. V_{qQW}^s values calculated over these regions were plotted against the corresponding Q^{MRE}_t values. Finally, we compared the reconstruction quality of the four averaged shear velocities between the interpolated/decimated data sets and the original data sets. All the velocity analysis was conducted with Matlab (MathWorks, Natick, Massachusetts, USA).

3.3 Results and Discussions

3.3.1 Simulated wave patterns

Figure 3.1 represents the 3D dynamic \mathbf{u} -field (Figure 3.1(b)) and \mathbf{q} -field (Figure 3.1(c)) for $f = 200$ Hz and $\text{SNR} = 30$ at normal incidence. With respect to the two in-plane axes, the two fields are anti-symmetrical. They are 90° -rotated with respect to each other. Along the out-of-plane axis, \mathbf{u} -field is rotationally symmetrical and \mathbf{q} -field is zeroed. The four time points illustrate well the wave propagation over time. Thereafter, it is obvious that the data quality is governed by \mathbf{u} -field along the out-of-plane axis whereas it is governed by \mathbf{q} -field along the two in-plane axes. Figure 3.2 illustrates the 3D dynamic \mathbf{u} -field (Figure 3.2(b)) and \mathbf{q} -field (Figure 3.2(c)) for $f = 200$ Hz and $\text{SNR} = 30$ at oblique incidence. With respect to the horizontal in-plane axis, u_1 , q_2 , and q_3 are anti-symmetrical. Neither \mathbf{u} -field nor \mathbf{q} -field prevail significantly on data quality along specific spatial directions.

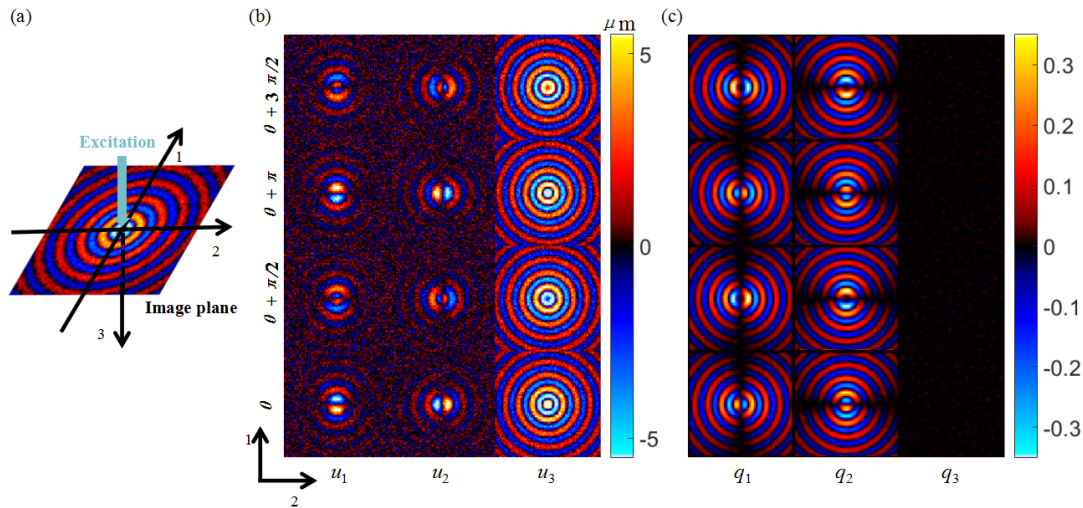


FIGURE 3.1: (a) Configuration of the simulated source excitation at normal incidence, (b) Computed displacement field, \mathbf{u} , and (c) Computed \mathbf{q} -field along the three motion encoding directions (columns) at four time points, $\theta + k\pi/2$, $k \in \{0, 1, 2, 3\}$, equally-spaced over one mechanical oscillation period (rows) for $f = 200$ Hz and $\text{SNR} = 30$ at normal incidence.

The simulated displacement field maps presented for normal and oblique incidences in Figures 3.1 and 3.2 exemplify how the spatial and motion encoding schemes determine the available field distribution and quality over the three spatial dimensions with respect to the excitation means. The \mathbf{u} -field distribution and quality illustrated in Figure 3.1(b) can simply be explained by the relative alignment of the propagation direction, here the wave incidence, with the out-of-plane encoding direction. The \mathbf{q} -field distribution and quality illustrated in Figure 3.1(b) can be well explained by equations (3.2) - (3.3). In Figure 3.2, the oblique incidence angle induces irregular patterns for both \mathbf{u} and \mathbf{q} -fields. In a mechanically-isotropic medium, as it is initially assumed in this study, the defined spatial reference frame is not an issue; data can be independently processed along each dimension to extract three

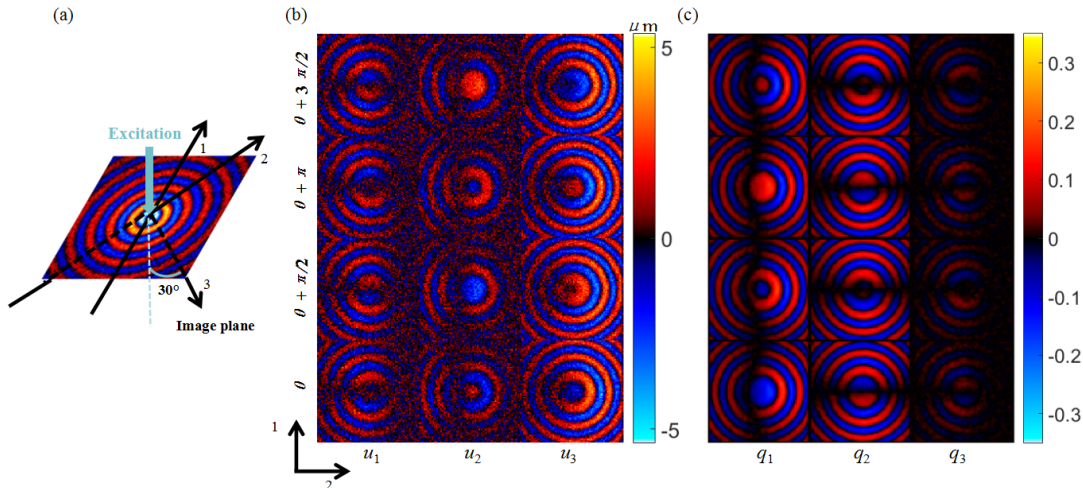


FIGURE 3.2: (a) Configuration of the simulated source excitation at oblique incidence, (b) Computed displacement field, \mathbf{u} , and (c) Computed \mathbf{q} -field along the three motion encoding directions (columns) at four time points, $\theta + k\pi/2$, $k \in \{0, 1, 2, 3\}$ equally-spaced over one mechanical oscillation period (rows) for $f = 200$ Hz and $\text{SNR} = 30$ at oblique incidence.

expectedly-identical velocity values from which an effective shear velocity can be deduced while minimizing the contamination of poor-quality data by using an appropriate combination strategy. In a mechanically-anisotropic medium, the three dimensions are not interchangeable any longer and thus the reference frame will be an important issue to tackle in order to condition the reconstruction quality.

3.3.2 Effects of averaging strategies on MRE accuracy and precision

Figure 3.3 and 3.4 summarize the individual V^s_i and the averaged shear velocity maps for $f = 100 - 400$ Hz and $\text{SNR} = 30$ at normal and oblique incidences respectively. In general, all types of shear velocities present a decreasing trend from high excitation frequency (low λ/a ratio) to low excitation frequency (high λ/a ratio). Moreover, the shear velocity estimation becomes more dispersed for high or low λ/a ratios. The discontinuity patterns on the V^s_i maps as well as the estimation quality difference between different V^s_i maps correspond well to the \mathbf{q} -field distribution patterns in Figure 3.1(c) and 3.2(c). The \mathbf{q} -field based averaging strategies effectively minimized the discontinuity patterns by combining good quality regions of individual V^s_i maps, so that more robust shear velocity estimation was obtained. The four types of averaged shear velocity maps are quite similar to each other, except for the V^s_{TLS} maps with lower excitation frequencies (higher λ/a ratios).

Figure 3.5 summarizes the V^s_1 and V^s_3 measurements as a function of λ/a and SNR at normal incidence. The accuracy and precision of V^s_1 outperform those of V^s_3 . For V^s_1 , the influence of the λ/a ratio on the reconstruction quality increases with the SNR level. For infinite SNR , the reconstruction accuracy and precision monotonously improve with λ/a , although the shear

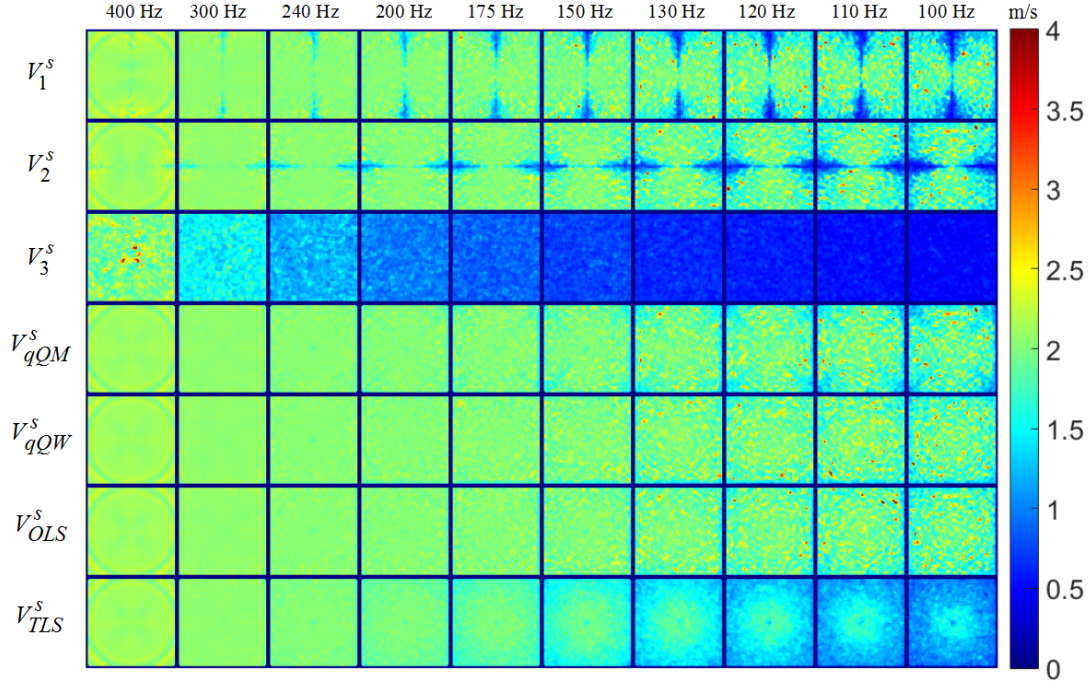


FIGURE 3.3: Individual V^s_i and averaged shear velocity maps (rows) for $f = 100 - 400$ Hz (columns) and $\text{SNR} = 30$ at normal incidence.

velocity is always overestimated. For a given finite SNR, both reconstruction accuracy and precision first improve with λ/a , then worsen for larger λ/a ratios. Hence, there exists a finite λ/a ratio that allows to simultaneously optimize the measurement accuracy and precision. The behavior of V^s_3 largely differs. For infinite SNR, q_3 equals zero, V^s_3 is not defined and set to zero (not shown in the figure). For any given finite SNR, V^s_3 follows the same trend: the reconstruction precision monotonously improves with λ/a but the reconstruction accuracy monotonously deteriorates with λ/a . V^s_2 , which is not presented here, exhibits the same characteristics as V^s_1 .

Figure 3.6 summarizes the four types of averaged shear velocity values as a function of λ/a and SNR at normal and oblique incidences. The first row in Figure 3.6 displays the averaged shear velocity values at normal incidence. For any averaging strategies, the reconstruction quality always improves with the SNR level. For any given finite SNR, the four averaged velocities follow similar trends with respect to λ/a as V^s_1 at normal incidence. The four averaged velocities show similar accuracy and precision for small λ/a ratios while discrepancies appear between V^s_{TLS} and the other three velocities at high λ/a ratios. For larger λ/a ratios, the precision of V^s_{TLS} is better than those of the other three averaged velocities. However, for the accuracy, it is just the opposite. This discrepancy is accentuated at low SNR level. The second row in Figure 3.6 displays the averaged shear velocity values at oblique incidence. The different averaging strategies have similar trends as those at normal incidence.

The general trend of all the measured shear velocities with respect to λ/a is due to the discrete and noisy displacement fields. Polynomial fitting was

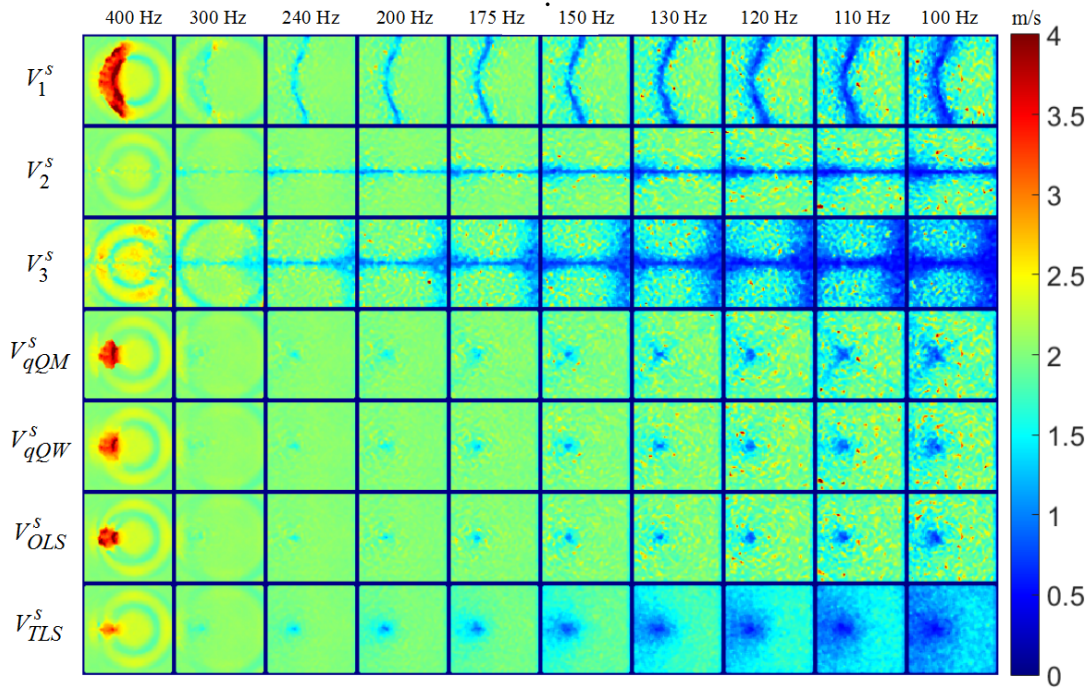


FIGURE 3.4: Individual V_i^s and averaged shear velocity maps (rows) for $f = 100 - 400$ Hz (columns) and $\text{SNR} = 30$ at oblique incidence.

used in our study to infer the derivatives. In principle, this approach can alleviate the noise amplification inherent to the finite difference method. However the fitting quality is degraded anyway by the discrete and noisy characteristics of the data. When data are noise-free, higher λ/a ratios yield more precisely-defined discrete displacement fields, hence higher fitting quality and more exact derivative estimations. In theory, at very large λ/a , the reconstruction error then tends to zero. For lower λ/a ratios, the polynomial fitting may introduce a bias as data sampling comes close to the Nyquist rate (Oliphant et al., 2001). When data are noise-contaminated, both the discrete displacement field and the noise influence the fitting quality and their respective effects compete with each other. As a result, the improvement on the estimation of the shear velocity at high λ/a ratio is impeded because the fitting becomes more sensitive to noise and less precise. In this noisy discrete context, there exists a finite optimal λ/a ratio to optimize the fitting quality and thus minimize the reconstruction error. However, the above analysis fails when the q-field only contains noise, which is the case for V_3^s of the normal incidence data. In this case, the deduced shear velocity does not carry any information on the wave propagation. The different behaviors of V_1^s, V_2^s and V_3^s also highlight the underlying need for the appropriate combining strategies, which can take the data quality along different encoding directions into consideration.

The influence of discrete and noisy data on the derivative estimations will be accentuated in realistic situations where the geometry and the heterogeneity of the medium cause wave reflections at the boundaries and where related interferences may lead to low wave amplitude or stationary waves (Oliphant

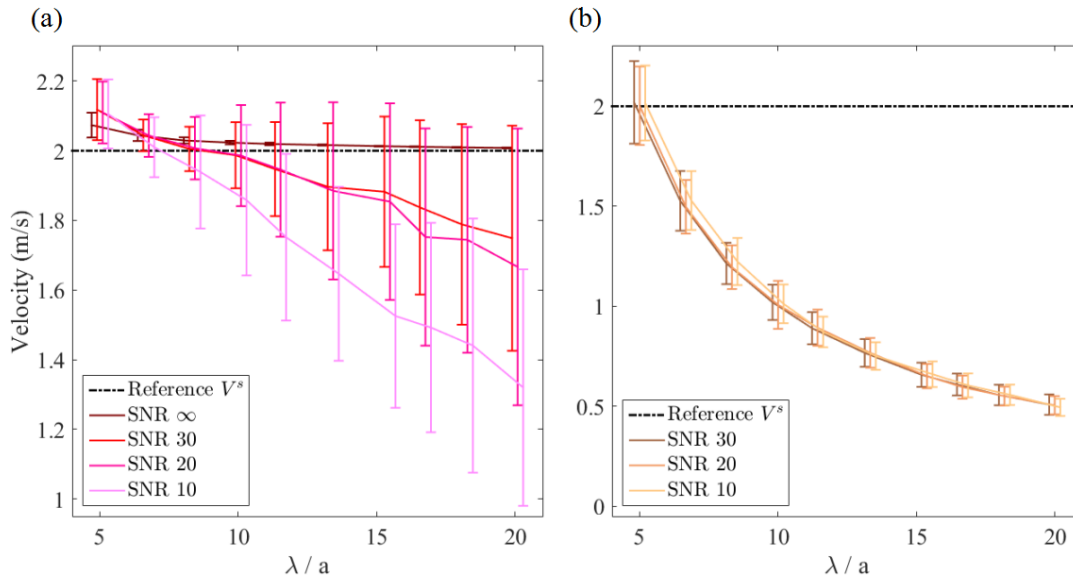


FIGURE 3.5: Mean value and standard deviations of V^s_1 (a) and V^s_3 (b) at normal incidence as a function of λ/a and SNR. For each λ/a ratio, the velocity values for different SNR levels were slightly shifted along the horizontal axis to improve the visibility.

et al., 2001). Some preprocessing approaches, such as spatio-temporal directional filter (Manduca et al., 2003) and physical boundary constraints (Garteiser et al., 2011) have been implemented to tackle the complex wave patterns. Other groups have proposed better controlled excitation modes to avoid the interference patterns (Corbin et al., 2015; Yasar, Royston, and Magin, 2013), yet they remain difficult to implement *in vivo*. It is indeed difficult to generalize these approaches for *in vivo* applications as the boundary conditions are specific to every organ. Thus organ-dedicated methodology studies should be carried out in the future (McGrath et al., 2016).

In this study, we compared four different averaging strategies: qQW, qQM, OLS and TLS. In general, these approaches can efficiently limit the contamination of poor quality data. They all present similar performance and lead to at least the same or even better reconstruction quality than the best shear velocity component. Nevertheless, the TLS method is largely outperformed by the three other ones and is more sensitive to data quality, especially for low SNR and high λ/a . In theory, the TLS method may provide better fitting outcomes than the OLS method when the independent and dependent variables of the overdetermined system are both noisy, which is just the case for MRE reconstruction. However, the performance of the TLS method largely depends on the relative noise level between independent and dependent variables (Okamoto, Clayton, and Bayly, 2011). In our study, the relative noise level is estimated by the ratio between the q-field and the Laplacian of the q-field for noise-free and noisy data. We obtained relative noise levels ranging from 2 (low λ/a and high SNR) to 112 (high λ/a and low SNR). The relative noise level may thus not be set appropriately for high λ/a and low SNR data due to the limited kernel size for Gaussian smoothing and local fitting. This

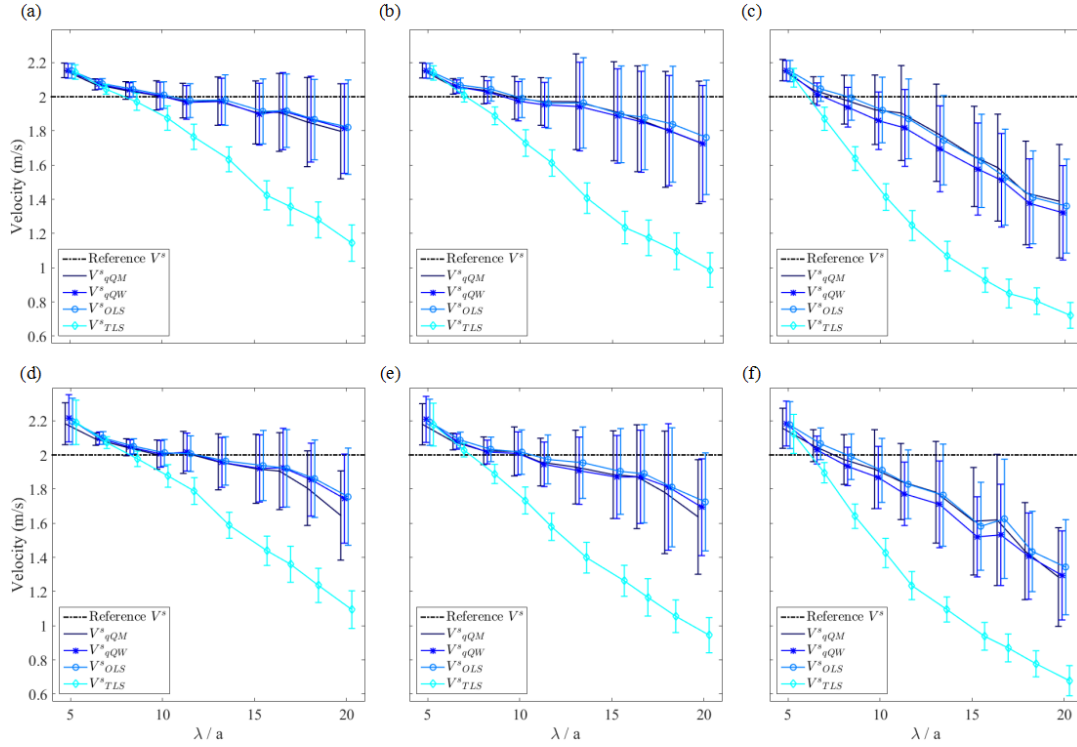


FIGURE 3.6: Mean values and standard deviations of V^s_{qQW} , V^s_{qQM} , V^s_{OLS} and V^s_{TLS} at normal incidence ((a),(b),(c)) and at oblique incidence ((d),(e),(f)) as a function of λ/a for SNR 30 ((a),(d)), 20 ((b),(e)), and 10 ((c),(f)). For each λ/a ratio, the velocity values for different averaging methods were slightly shifted along the horizontal axis to improve the visibility.

variation of relative noise level corresponds well to the discrepancy evolution observed between V^s_{OLS} and V^s_{TLS} in Figure 3.6. In general, the OLS method may be more relevant than the TLS method given the limited kernel size which is critical for the assumption of local mechanical homogeneity. However, for appropriately-conditioned or resampled data sets as shown in Table 1, the TLS method may be preferred to improve further the reconstruction results.

Equation (3.20) reveals that the OLS method intrinsically is a quality-weighted method for which the weighting metric is the amplitude of the q-field. In our study, weighting by the q-field amplitude is actually the same as weighting by the q-field quality because the SNR and the sensitivity of the measurement are expected to be independent of the direction of the applied motion encoding gradient, namely the method OLS is equivalent to the method qQW. However, more generally, the SNR and the sensitivity may differ with the gradient performances, such as slew rates and duty cycles, along the different encoding directions. These performance differences, for different encoding directions, may yield different TE/TR values, hence different SNR levels as well as different motion sensitizing levels, hence different Δq . Finally, concerning the estimated mechanical properties, the outcome values generally depend on the effectively-averaged physical quantity. However, for the

qQM and qQW methods, the corresponding appropriate λ/a conditions remain valid for any parameters to be extracted as q-field quality maps are computed independently of the physical quantity whereas, for least square methods, the appropriate λ/a conditions may be different for different extracted parameters as optimization is performed on the physical quantity itself.

3.3.3 Appropriate λ/a range for accurate and precise MRE

Figure 3.7 shows contour plots of the MAPE values for the four types of averaged shear velocity values as a function of λ/a and SNR at normal (first row) and oblique (second row) incidences. For a given SNR, MAPE values first decrease then increase with λ/a resulting in a minimum MAPE value when λ/a is around 6 – 9. When the SNR increases, the minimal MAPE values are achieved for slightly larger λ/a ratios. The λ/a range exhibiting the best compromise between accuracy and precision is similar for normal and oblique incidences.

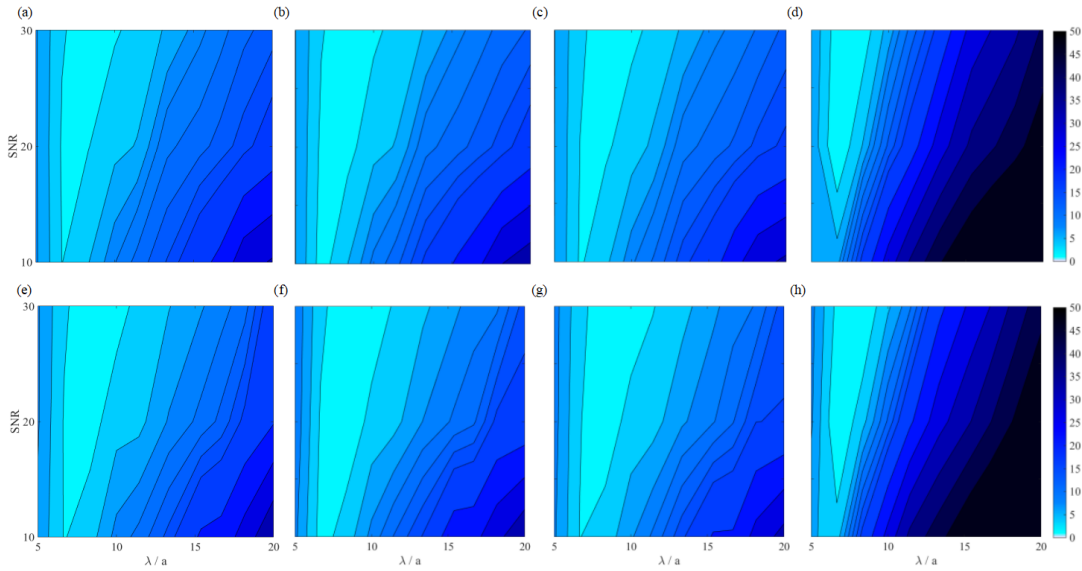


FIGURE 3.7: Mean absolute percentage errors of V^s_{qQM} ((a),(e)), V^s_{qQW} ((b),(f)), V^s_{OLS} ((c),(g)) and V^s_{TLS} ((d),(h)) at normal incidence ((a),(b),(c),(d)) and at oblique incidence ((e),(f),(g),(h)) as a function of λ/a for $\text{SNR} = \{30, 20, 10\}$.

Figure 3.8 presents the *in silico* abaci computed from the simulated data sets at normal incidence. Along each abacus, the MAPE values first decrease then increase with λ/a resulting in an appropriate λ/a range to minimize the MAPE values. This appropriate λ/a range only increase slightly when the abacus moves from low q-field quality regions to high q-field quality regions. For the q-field quality range 15 – 25, the appropriate λ/a range lies between 6 – 7. For the q-field quality range 25 – 100, the appropriate λ/a range lies between 7 – 10.

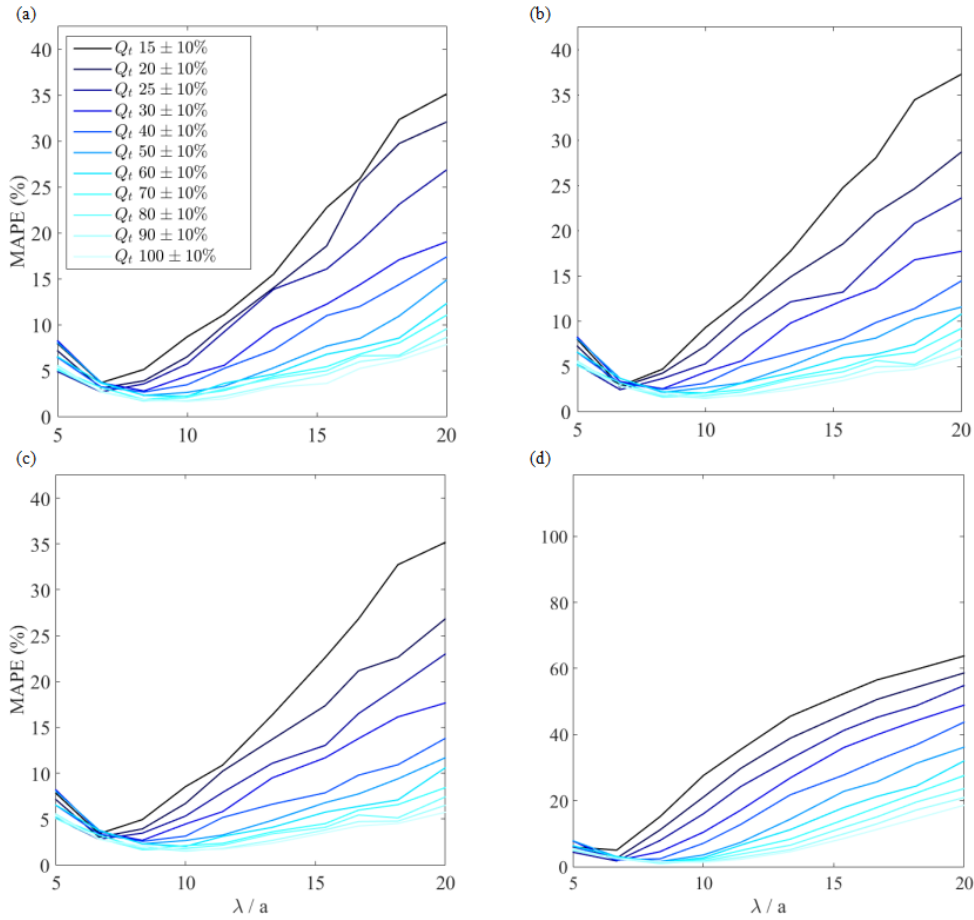


FIGURE 3.8: *In silico* abaci for predicting the appropriate λ/a range for V^s_{qQM} (a), V^s_{qQW} (b), V^s_{OLS} (c) and V^s_{TLS} (d) for given Q^{MRE}_t value.

On the basis of regional mean values of the elastic modulus, Papazoglou *et al.* assessed the accuracy of the MRE outcomes but not their precision (Papazoglou *et al.*, 2008). MAPE was used here as a criterion to determine the optimal λ/a ratio. The advantage of MAPE compared to the mean value lies in that it better represents voxel-wise reconstruction quality by taking the measurement precision into consideration. For example here, at normal incidence, for the V^s_{OLS} measurement, the optimal λ/a ratio for $SNR = 30$ would lie between 10 and 12 if only the velocity mean value was considered (Figure 3.6(a)). The resulting velocity estimation, though, would be much more dispersed, that is, considering the mechanically-homogeneous medium, much less precise compared to the estimation made with a λ/a ratio, optimized upon the MAPE, within 6 – 9 (Figure 3.7(c)). Therefore, MAPE is a more relevant criterion for optimizing q-based MRE. Figure 3.8 demonstrates that the appropriate λ/a range only varies slightly when the q-field quality is double or even triple, which is just in contrast with the linear increase found by Papazoglou *et al.* (Papazoglou *et al.*, 2008). This should be attributed to the higher robustness of the polynomial fitting method when calculating derivatives. This relative stability on favorable λ/a ranges can avoid challenging experimental conditions, such as extremely low excitation frequencies or extremely small voxel sizes.

In practice, the optimal λ/a ratio cannot be determined before the measurement and the reconstruction are performed. Yet, an appropriate λ/a range could be estimated by a rough estimation of the wavelength on acquired preliminary phase data. Besides, as illustrated on Figure 3.8, the appropriate λ/a range depends on the q-field quality, which is governed by the amplitude of the mechanical wave and the SNR of the MR measurement. This λ/a range could also be influenced by the kernel size used for smoothing or polynomial fitting, because the effective wavelength may change. In this context, the λ/a range corresponding to the best compromise is specific to the overall acquisition and reconstruction process that is implemented. It can be deduced from *in silico* abaci computed with the study-specific acquisition parameters and reconstruction processes.

3.3.4 Effects of interpolation/decimation on regulating the λ/a ratio

Finally, Table 3.1 summarizes the MVs and MAPEs of the four types of averaged shear velocities, computed from resampled data (interpolated or decimated) and corresponding original data sets at normal incidence. The estimation of the shear velocity from the interpolated or decimated data sets is more accurate and precise than from not optimally-conditioned data sets and the corresponding MAPEs are thus smaller, except for the V_{TLS}^s values of the interpolated data sets with $f = 400$ Hz and SNR = 10, 20. The outcomes with the interpolated data sets never really reach the same reconstruction quality as the targeted data sets with $\lambda/a = 8.3$, for which MAPEs remain minimal. In contrast, the outcomes with the decimated data sets are usually better than those of the targeted data sets. The overall gain in reconstruction quality is higher when the available SNR is higher.

In the course of MRE acquisitions, the implementation of required excitation frequencies and voxel sizes to produce data with appropriate λ/a ratios is not always achievable, owing to the limitations of SNR and acquisition time. Besides, mechanical properties, SNR, and shear wave amplitudes are generally not homogeneous across the targeted tissues and appropriate conditions may not be fulfilled everywhere at once. Thus appropriate preprocessing is necessary for acquired data with poorly-defined λ/a ratios. The results in Table 3.1 demonstrate that the decimation and interpolation procedures can be good options. They can effectively improve the polynomial fitting quality. Their performance, though, increases with the SNR level of the original data set; for high SNRs, MAPEs of resampled data can match and even outperform MAPEs of original data with appropriate λ/a ratios but smaller SNR. Such alternative may be helpful for choosing the appropriate acquisition voxel size when a trade off is to be made between λ/a and SNR. In a MRE isotropic acquisition, adapting the voxel size for appropriate λ/a ratios may induce an important SNR loss, which goes to the power of three. Thus it can be more relevant to favor enhanced SNR even if it implies non-optimal λ/a range,

TABLE 3.1: Mean values (MVs) and Mean absolute percentage errors (MAPEs) of V^s_{qQW} , V^s_{qQM} , V^s_{OLS} and V^s_{TLS} , computed from interpolated (red) or decimated (blue) and related original (black) data sets at normal incidence. All values are rounded to two decimals.

SNR	f (Hz)	λ/a	V^s_{qQM}		V^s_{qQW}		V^s_{OLS}		V^s_{TLS}	
			MV (m/s)	MAPE (%)	MV (m/s)	MAPE (%)	MV (m/s)	MAPE (%)	MV (m/s)	MAPE (%)
30	400	5.0	2.15	7.72	2.15	7.58	2.15	7.57	2.14	7.22
	400	8.3	2.04	3.25	2.04	3.01	2.05	3.30	1.95	3.08
	240	8.3	2.04	2.60	2.04	2.38	2.04	2.54	1.97	2.20
	100	8.3	2.00	1.07	2.02	1.13	2.02	1.16	1.99	0.98
	100	20.0	1.80	14.13	1.81	13.28	1.82	13.62	1.14	42.79
20	400	5.0	2.15	7.72	2.15	7.60	2.15	7.54	2.14	6.95
	400	8.3	2.03	4.00	2.01	3.45	2.04	3.96	1.86	7.26
	240	8.3	2.04	3.43	2.03	2.82	2.04	3.20	1.89	5.61
	100	8.3	2.03	1.74	2.04	2.12	2.04	2.13	2.02	1.41
	100	20.0	1.73	19.13	1.73	19.13	1.76	17.71	0.99	50.67
10	400	5.0	2.16	7.80	2.15	7.61	2.15	7.51	2.11	5.60
	400	8.3	1.95	6.91	1.90	7.15	1.95	6.53	1.60	19.89
	240	8.3	1.98	5.40	1.94	5.44	1.99	5.01	1.64	18.08
	100	8.3	2.03	2.73	2.03	2.54	2.04	2.73	1.97	1.99
	100	20.0	1.39	32.47	1.32	34.88	1.36	32.85	0.72	63.94

Red rows correspond to data which have been interpolated from $(1 \times 1 \times 1) \text{ mm}^3$ to $(0.6 \times 0.6 \times 0.6) \text{ mm}^3$, blue rows correspond to data which have been decimated from voxel size $(1 \times 1 \times 1) \text{ mm}^3$ to $(2.4 \times 2.4 \times 2.4) \text{ mm}^3$.

and then properly resample the data afterwards for achieving appropriate λ/a ratios. Multiple resampling could eventually be implemented to cope with heterogeneous media with multiple appropriate λ/a conditions, which could be independently and regionally fulfilled before reconstruction and final common resampling for a global recombination. Alternatively, multiple frequency MRE could be implemented to acquire several λ/a conditions at once. Moreover, MRE in realistic viscoelastic media should fulfill similar appropriate conditions as λ/a is not affected by added viscosity for which only the wave amplitude is damped.

3.3.5 Performance of the total q-field quality parameter Q^{MRE}_t on evaluating the reconstruction quality

Figure 3.9 presents the voxel-wise velocity-quality parameter clusters for the four types of quality weighted shear velocities reconstructed with different λ/a conditions. It is shown that the proposed Q^{MRE}_t can well characterize the reconstruction quality. Both the measurement accuracy and precision improve with Q^{MRE}_t . For different weighting strategies and λ/a conditions, obtained shear velocity values always converge as long as Q^{MRE}_t is high enough. However, the converged shear velocity values for higher λ/a conditions ($f = 300, 400 \text{ Hz}$) are overestimated against the reference value. This

overestimation is due to the fact that the influence of the discrete displacement field is dominant against the noise influence when Q^{MRE}_t is extremely high. Although high Q^{MRE}_t values can always lead to valid shear velocity values, in real practice Q^{MRE}_t is often limited by the wave amplitude level and SNR level. In this context, both Q^{MRE}_t and λ/a conditions should be optimized in order to obtain accurate and precise reconstruction results more efficiently. As shown in Figure 3.9, for achieving similar reconstruction quality, appropriate λ/a conditions can alleviate the demand for high Q^{MRE}_t levels.

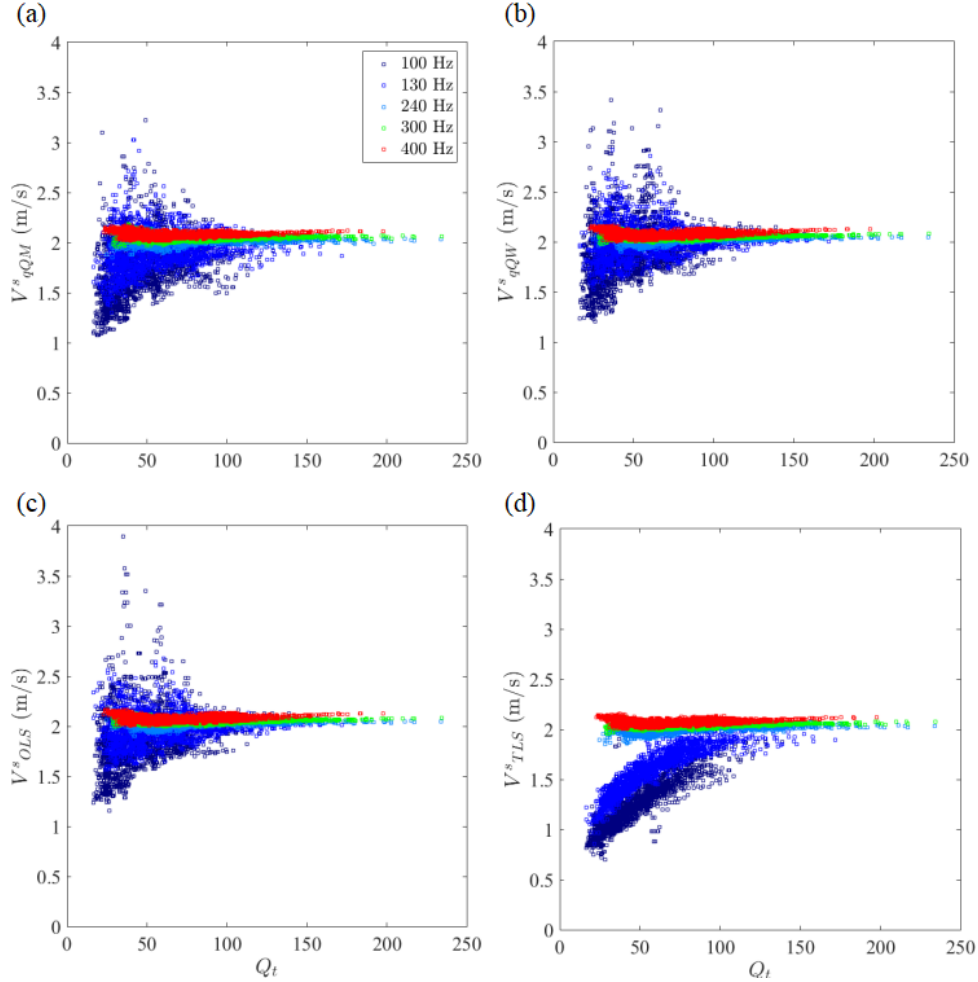


FIGURE 3.9: Voxel-wise V^s_{qQM} (a), V^s_{qQW} (b), V^s_{OLS} (c) and V^s_{TLS} (d) values as a function of the corresponding Q^{MRE}_t values over a $(10 \times 10 \times 20)$ mm³ cuboid volume region for SNR 30 data with $f = 100, 130, 240, 300, 400$ Hz.

3.4 Conclusions

In this chapter, we have designed a simulation study to investigate the performance of a q-based AIDE method to process discrete and noisy displacement fields. First, we have demonstrated that the quality weighting strategies based on the q-field, the curl of the displacement field \mathbf{u} , and the least

square methods can be effective to combine the shear velocity measurements along different encoding directions and obtain a more accurate and precise estimation. However, q-field quality based methods are more generally appropriate than least square methods given the potential differences in SNR levels and motion sensitizing levels in the different encoding directions. Second, we demonstrated that the MAPE value could be a pertinent criterion for determining the appropriate range for the ratio between the wavelength and the voxel size, λ/a , to optimize the MRE reconstruction accuracy and precision. This λ/a depends on the overall acquisition and reconstruction methods and thus can be guided using *in silico* abaci computed with the study-specific acquisition parameters and reconstruction processes. It has also been proven that decimation and interpolation can be effective preprocessing steps to adjust the originally poorly defined λ/a ratio to the appropriate range. Finally, the q-field quality parameter Q^{MRE}_t has been demonstrated effective to evaluate the voxel-wise reconstruction quality for different quality weighting strategies. Q^{MRE}_t and λ/a should be optimized together in order to obtain accurate and precise reconstruction results more efficiently.

4 In vitro SSI and MRE comparison study on phantoms

4.1 Introduction

In Chapter 2, we have presented in details the methodological differences between SSI and MRE in the three elementary steps of the elastography technology process, namely excitation, acquisition and reconstruction, which could lead to variations in the estimation results. These potential measurement biases impede the free choice of clinicians between SSI and MRE according to their needs without worrying about measurement consistency. The interchangeability and cooperation between the two modalities are thus challenged. Therefore, as already pointed out in Chapter 1 it should be meaningful to compare the two modalities in order to cross-validate their measurements. According to our knowledge, there have been several studies dedicated to the cross-validation of SSI and MRE measurements. Yoon *et al.* have compared the measurements of SSI and MRE *in vivo* on patients with different fibrosis stages (Yoon et al., 2013). They found a moderate correlation between the liver stiffness measurements obtained with the two modalities, but no agreement. The SSI measurements were significantly higher than those of MRE. Xie *et al.* carried out an *in vitro* comparison study on commercial calibrated quasi-elastic phantoms between MRE and Ultrasound Shear Wave Elastography (USWE) which is similar to SSI, but without the supersonic mode (Xie et al., 2012). They also observed an overestimation of the USWE measurements against the MRE measurements. Urban *et al.* have compared USWE and MRE measurements over a wide frequency range (60-600 Hz) on commercial viscoelastic phantoms (Urban, Chen, and Ehman, 2017). They found good agreement between the two modalities at low frequency range 60-200 Hz. However, the deviation between the two modalities increases at 300 Hz and above where the USWE measurements are overestimated against the MRE measurements.

The measurement disagreements found in the first two studies could be explained by the methodological differences between the two modalities. First, the reported studies did not take into consideration the potential influence of the reconstruction validity of each modality for the comparison. Second, comparing measurements in terms of Young's modulus might not be the most pertinent choice. Different reconstruction models were used for the two modalities. The Young's modulus measured by the two modalities may thus not represent the same physical parameter. In addition, the Young's modulus was obtained through the relationship $E = 3\rho V^{s2}$, which may boost the

apparent measurement discrepancy because of the squaring and scaling effects. Third, SSI measures the shear group velocity, which, in a viscoelastic medium, differs from the shear phase velocity measured in MRE and thus brings an important theoretical bias for the comparison. For the third study carried out by Urban *et al.*, they compared the frequency-specific shear phase velocity measurements between USWE and MRE and hence avoided the theoretical bias due to viscoelastic media as well as the measurement discrepancy because of the squaring and scaling effects. However, validity issues on USWE and MRE were not taken into consideration either in this study. The shear phase velocity was not available on the clinical Aixplorer system during my thesis. We thus propose to compare the quality-guided MRE and SSI shear velocity measurements using a quasi-elastic medium in order to minimize the theoretical bias between the shear group velocity measured by SSI and the shear phase velocity measured by MRE.

In this chapter, we first describe the validation of the SSI quality parameter provided by the Aixplorer system as well as the acquisition and reconstruction conditions for accurate and precise MRE derived from Chapter 3 on commercial homogeneous, quasi-elastic and calibrated phantoms (Model 039, CIRS, Norfolk, VA, USA). Then we report the cross-validation of the quality-guided SSI and MRE measurements on these phantoms. Normally, the reference values provided by CIRS should be used to validate the SSI and MRE measurements. However, reference values are highly dependent on the calibration method (Oudry *et al.*, 2014). The method used by CIRS to obtain the reference measurements for the calibrated phantoms might not be the most pertinent for comparison with *in vitro* elastography imaging technologies. Xie *et al.* have presented the inconsistency between the reference values provided by CIRS and USWE, MRE measurements (Xie *et al.*, 2012). In this context, we used the well validated Transient Elastography (Fibroscan, Echo-sense, France) technology to additionally characterize the calibrated phantoms and used the obtained measurements as "third-party" reference values. The same validation and comparison study was also carried out on homemade polyvinyl alcohol (PVA) phantoms. This study aimed at, on the one hand, validating the favorable acquisition and reconstruction conditions for high frequency MRE as well as cross-validating the corresponding quality-guided measurements with those of SSI, on the other hand, validating our PVA phantom fabrication procedure.

4.2 In vitro phantom experiments

4.2.1 Commercial calibrated liver fibrosis phantoms

4.2.1.1 Phantom description

The batch of calibrated phantoms (Model 039, CIRS, Norfolk, VA, USA) consists of four cylindrical homogeneous phantoms (Figure 4.1). They often serve as the standard reference tool for determining sources of variation in

shear wave elastography measurements (Oudry et al., 2014). Each phantom was filled with a Zerdine solid elastic hydrogel with apparently different values of Young's modulus (3.5, 11.4, 28.6, and 44.4 kPa), a tissue-average speed of sound of 1540m/s, a density of 1030 Kg/m³, a Poisson's ratio of 0.5 and speckle contrast levels matching that of a healthy liver. Each phantom was covered by a Saran Laminate membrane on the surface and protected by a plastic container. The different Young's modulus values of the four phantoms correspond to various stages of liver fibrosis from 3.5 kPa representing the elasticity of healthy tissue to 44.4 kPa corresponding to the elasticity of tissue with stage-four liver fibrosis. For simplification purpose in the following text, the four phantoms are named C1, C2, C3 and C4 in the order of increasing elasticity values.



FIGURE 4.1: Four calibrated phantoms C1-C4 with corresponding Young's modulus 3.5, 11.4, 28.6, and 44.4 kPa

4.2.1.2 Experimental protocols

SSI

The SSI acquisitions were carried out on an Aixplorer ultrasound system (Supersonic Imagine, Aix-en-Provence, France) at hospital Pitié Salpêtrière, France. The phantoms were characterized by the probes XC6-1 MHz, SL10-2 MHz and SL15-4 MHz respectively. The pixel size of the obtained shear velocity maps depended on the probe. It was $0.8 \times 0.6 \text{ mm}^2$ for the XC6-1 MHz probe, $0.35 \times 0.20 \text{ mm}^2$ for the SL10-2 MHz probe and $0.21 \times 0.20 \text{ mm}^2$ for the SL15-4 MHz probe. Comparable 2D insonification windows were placed in the center of each phantom. An artificial arm was used to hold the probes steadily on the surface of the phantoms to minimize the operator dependent influence.

TE

The TE acquisitions were carried out on a FibroScan 502 TOUCH system (Echosens, Paris, France) at hospital Pitié Salpêtrière, France. The phantoms were characterized by the probe M (3.5 MHz) at an excitation frequency of 50 Hz. For each phantom, ten valid measurements were acquired. The median of the ten valid measurements was taken as the final estimation.

MRE

The MRE acquisitions were carried out on a Philips 1.5 T MR Scanner (Achieva, Philips Healthcare, The Netherlands) at SHFJ, France. The phantoms were placed horizontally into a commercial knee coil (Philips Healthcare, The Netherlands). The wave generation system introduced in Chapter 2 was implemented to provide the external harmonic excitation. A home-made cylindrical wood block with an acoustic adapter inserted in the center was additionally used here to connect the wave guide with the surface of the calibrated phantoms in order to achieve a point source excitation. The experimental installation is shown in Figure 4.2.



FIGURE 4.2: MRE experimental installation for the calibrated phantoms. A home-made cylindrical wood block with an acoustic adapter inserted in the center (a) was used to induce a point source excitation (b) and a knee coil (c) was used for signal reception.

Then each phantom was imaged and mechanically characterized at five different excitation frequencies using the spin-echo based MRE sequence. Imaging was performed on the axial plane relative to the bore of the MR scanner, which produced axial cross sections of the cylindrical phantoms. For each phantom, excitation frequencies were chosen so as to cover a corresponding λ/a range of 4-15, which was estimated by a manual estimation of the wavelength on the acquired phase images. For different frequency acquisitions of each phantom, the number of MEG, N_{MEG} , was adjusted according to the applied excitation frequency, f_{exc} , to make sure that the applied TE/TR values were appropriate for enough signal reception on the one hand, were also similar among different frequency acquisitions on the other hand. The amplitude of MEG, G_{MEG} , was $21 \text{ mT} \cdot \text{m}^{-1}$. MEG was applied successively

along the three spatial encoding directions M (y axis of the imager), P (x axis of the imager) and S (z axis of the imager) to encode the three-dimensional displacement field. Along each encoding direction, four different instants of the vibration cycle were acquired. The MRE sequence parameters are detailed in Table 4.1. In addition, the data set for phantom C1 with $f = 137$ Hz was interpolated to achieve a λ/a ratio of 8.

TABLE 4.1: MRE sequence parameters for the calibrated phantoms

	a (mm)	FOV (mm ³)	f_{exc} (Hz)	TE/TR (ms/ms)	N_{MEG}	TA
C1	1.75	$112 \times 112 \times 40.25$	55	45/1254	1	16 min 15 s
			65	38/1415	1	18 min 19 s
			75	33/1227	1	15 min 53 s
			95	37/1210	2	15 min 40 s
			137	36/1175	3	15 min 12 s
C2	1.25	$120 \times 120 \times 30$	90	33/1067	1	20 min 39 s
			131	34/1099	2	21 min 15 s
			164	37/1170	3	22 min 38 s
			201	35/1076	4	20 min 48 s
			235	36/1122	5	21 min 42 s
C3	1.5	$120 \times 120 \times 37.5$	137	36/1277	3	20 min 37 s
			210	40/1309	5	21 min 9 s
			245	39/1225	5	19 min 47 s
			289	40/1210	7	19 min 32 s
			344	36/1162	7	18 min 45 s
C4	2	$128 \times 128 \times 46$	130	38/1239	3	16 min
			163	40/1128	4	14 min 36 s
			200	40/1151	5	14 min 54 s
			270	41/1191	7	15 min 24 s
			344	41/1136	9	14 min 42 s

4.2.2 Home-made polyvinyl alcohol (PVA) phantoms

4.2.2.1 Phantom description

I collaborated with Julea Felicia, who is a PhD candidate in the Laboratory IR4M, to fabricate the homogeneous PVA phantoms. The basic ingredients for the PVA phantoms include the PVA powder (SigmaAldrich, St Louis, USA), the vegetable coal powder (VWR International, Le Périgares, FRANCE) and the distilled water. We fabricated two series of phantom samples with different PVA mass concentration, namely 5w% PVA and 7w% PVA. The exact compositions for the two series of phantom samples are listed on Table 4.2.

First, the PVA powder was diluted in distilled water at 95° C with a magnetic agitator mixing them homogeneously (Figure 4.3 (a)). When the solution became translucent, the vegetable coal powder was added into the solution, which served as scattering particles for ultrasound imaging.

TABLE 4.2: Composition of the 5w% and 7w% PVA phantoms

	PVA (g)	Vegetable coal (g)	Distilled water (ml)
5w% PVA	12.5	1.25	236.25
7w% PVA	17.5	1.25	231.25

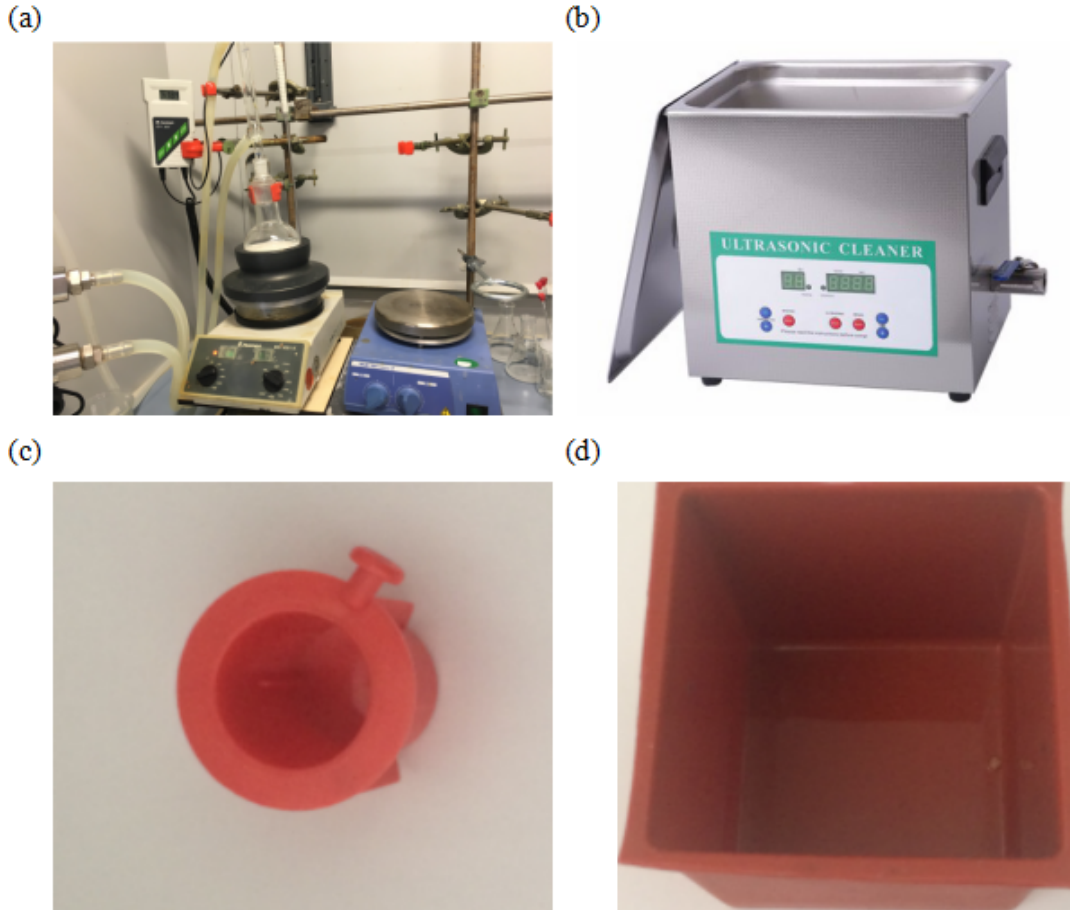


FIGURE 4.3: Home-made PVA phantom fabrication: (a) solution preparation system; (b) ultrasonic degassing equipment; (c) plastic plug used for preparing the samples for MRE measurements; (d) cubic silicon mold used for preparing the samples for SSI measurements.

Next the solution was degassed by an ultrasonic degassing equipment (Figure 4.3 (b)) to prevent cavitation effects for both MRE and SSI. After the degassing, the solution was respectively poured into a plastic plug with a diameter 20 mm (Figure 4.3 (c)) and a $5 \times 5 \times 5 \text{ cm}^3$ cubic silicon mold (Figure 4.3 (d)). Finally, the phantom samples underwent three thaw/freeze cycles (i.e. -20° C during 12 hours followed by 20° C during the next 12 hours) to reach the desirable rigidity and then they were kept in the distilled water at 5° C in the refrigerator. The two different geometries and volumes of phantom samples were chosen here to satisfy both the MRE and SSI measurement needs. The phantom samples prepared in the plastic plugs were suitable for the experimental installation on the Bruker 11.7 T MR scanner,

while the phantom samples prepared in the silicon molds were suitable for the SSI measurements.

4.2.2.2 Experimental protocols

SSI

The PVA phantoms were measured on the same Aixplorer system as the calibrated phantoms with the SL10-2 MHz and SL15-4 MHz probes respectively. The focal zone of the XC6-1 MHz probe was too deep to adapt to the size of the PVA phantoms. The pixel size of the obtained shear velocity maps was $0.35 \times 0.20 \text{ mm}^2$ for the SL10-2 MHz probe and $0.21 \times 0.20 \text{ mm}^2$ for the SL15-4 MHz probe. The acquisition protocol was identical to that of the calibrated phantoms.

MRE

The MRE acquisitions were carried out on a Bruker 11.7 T MR scanner (BioSpec, Bruker, USA) at NeuroSpin, France. The phantoms were placed into a plastic tube (Figure 4.4 (a)), which in turn was inserted into a T/R volume coil (Bruker, USA) (Figure 4.4 (b)). The wave generation system introduced in Chapter 2 was implemented to provide the external harmonic excitation. A micropipette was additionally used here to connect the wave guide with the surface of the PVA phantoms in order to realize a point source excitation. The whole experimental installation is shown in Figure 4.4.

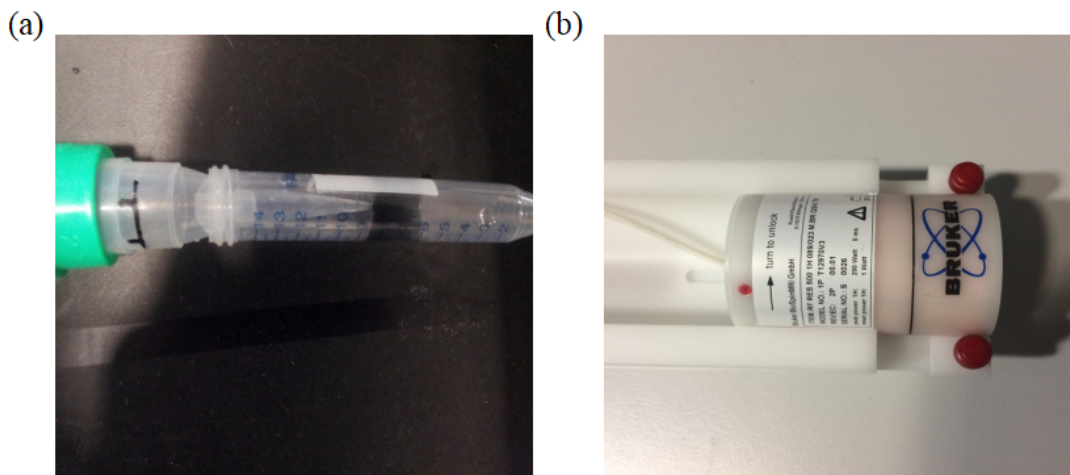


FIGURE 4.4: The MRE experimental installation for the PVA phantoms using a point source (a) for external excitation and a volume coil (b) for signal reception.

Each phantom was imaged and mechanically characterized at five excitation frequencies using the spin-echo based MRE sequence. Imaging was performed on the axial plane relative to the bore of the MR scanner, which produced axial cross sections of the cylindrical phantoms. The excitation frequencies were chosen to cover a corresponding λ/a range 4 – 12. As for the calibrated phantoms, wavelength was manually estimated on the acquired

phase images. For different frequency acquisitions of each phantom, the number of MEG, N_{MEG} , was chosen to maximize the data quality of the acquired phase images, namely the ratio between the accumulated phase value and the associated phase measurement uncertainty. These frequency specific N_{MEG} values also allowed to ensure that the applied TE/TR values were similar among different frequency acquisitions. The amplitude of MEG, G_{MEG} , was $577.2 \text{ mT} \cdot \text{m}^{-1}$. MEG was applied successively, along the three encoding directions M (x axis of the imager), P (y axis of the imager) et S (z axis of the imager) to encode the three-dimensional displacement field. The MRE sequence parameters are detailed in Table 4.3.

TABLE 4.3: MRE sequence parameters for the PVA phantoms

	a (mm)	FOV (mm ³)	f_{exc} (Hz)	TE/TR (ms/ms)	N_{MEG}	TA
PVA phantoms	0.3	$21 \times 21 \times 6$	800	29.4/1025	18	14 min 21 s
			1000	28.5/1020	22	14 min 15 s
			1200	27.9/1000	26	14 min
			1400	27.9/1000	30	14 min
			1600	27.5/1000	34	14 min

4.3 Computation of shear velocity mapping and data analysis

4.3.1 SSI post-processing

The obtained Dicom images were processed by the dedicated Matlab function (provided by Supersonic Imagine) that we adapted for our specific study to extract the embedded shear velocity (V^s) maps together with the corresponding quality maps. For each individual measurement, two types of regions of interest were generated. First, the quality parameters on each quality map were sorted in ascending order and divided into ten equal sub-populations (SP1, SP2,...,SP9, SP10), so that each sub-population represented 10% of the total quality parameter population as shown in Figure 4.5. The lower limit of each sub-population was defined as the quality quantile (LQ₁, LQ₂,...,LQ₉, LQ₁₀) for this sub-population. SP1 contained pixels with the lowest 10% quality parameters while SP10 contained pixels with the highest 10% quality parameters. Ten regions of interest were thus generated for each obtained shear velocity map. MVs and SDs of V^s values were computed over those regions of interest. Then we plotted those MVs and SDs as a function of the corresponding sub-populations. The evolution of quality quantiles of these sub-populations were also plotted. From these obtained quality evolution plots, an empirical quality parameter threshold, $Q^{SSI}_{threshold}$, was deduced for the calibrated and PVA phantoms. Second, region containing pixels with data quality superior to $Q^{SSI}_{threshold}$ was generated for each shear velocity map. MVs and SDs of V^s values calculated over these regions were

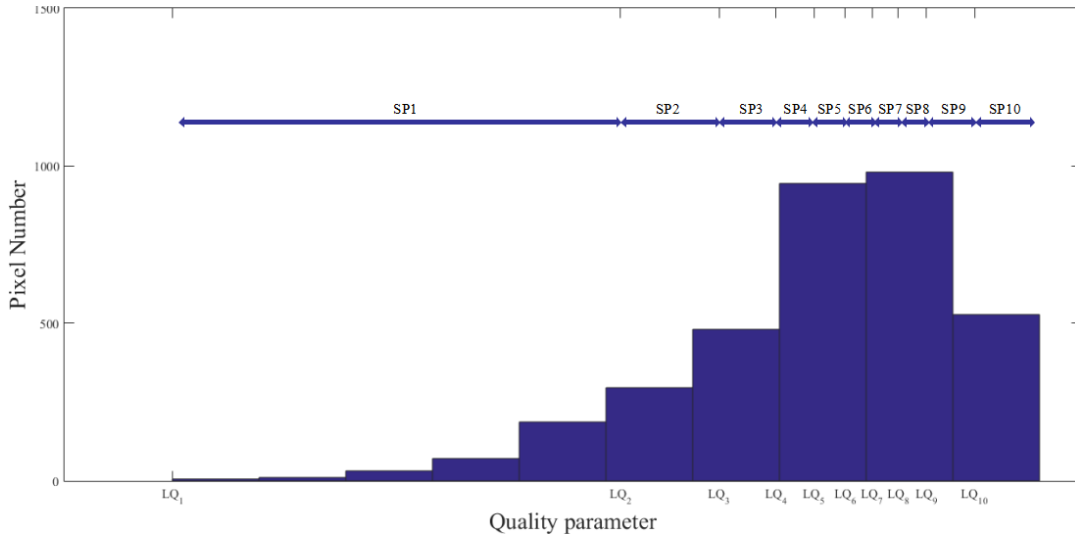


FIGURE 4.5: Quality parameter distribution for the C1 phantom measurement obtained with the XC6-1 MHz probe. SP_i , LQ_i ($i \in 1 \sim 10$) respectively represent the ten equal sub-populations of the whole quality parameter population and the corresponding lower limits.

used for the comparison among different ultrasound probes. For each phantom, the mean value of different probe measurements was used for the comparison with the corresponding MRE measurement. All the velocity analysis was conducted with Matlab (MathWorks, Natick, Massachusetts, USA).

4.3.2 MRE reconstruction

All the acquired MRE data sets were reconstructed using the q-based AIDE method described in Chapter 2. The qQW method detailed in Chapter 3 was used to combine the V^s_i values along the three motion-encoded directions to obtain the quality weighted shear velocity (V^s) maps accompanied with the associated q-field quality (Q^{MRE}_t) maps. For each data set, three types of regions of interest were generated. First, regions of interest with identical levels of Q^{MRE}_t ($40 \pm 10\%$) and volumes as studied in Chapter 3 were selected on all the obtained shear velocity maps except for that of the interpolated data set. MVs and SDs were computed over these regions of interest. For each phantom, the obtained MVs and SDs of shear velocity was evaluated as a function of λ/a in order to validate the favorable λ/a range deduced from Chapter 3. Second, for all the obtained V^s maps, V^s values were plotted against the corresponding Q^{MRE}_t values. Finally, a series of regions with increasing quality threshold ($Q^{MRE}_{threshold}$) values (30, 40, 50, 60, 70, 80) were selected on the shear velocity maps with favorable λ/a values which were manually estimated on the acquired phase images. MVs were computed over these regions and then compared with the SSI measurements. All the velocity analysis was conducted with Matlab (MathWorks, Natick, Massachusetts, USA).

4.4 Results and Discussions

4.4.1 Commercial calibrated liver fibrosis phantoms

4.4.1.1 SSI using different ultrasound probes

Figure 4.6 presents the Dicom images of the SSI measurements obtained with different probes for the calibrated phantom C4. Both the Bmode images and the elasticity maps are homogeneous. The Q-boxes representing the positions of the chosen regions of interest and the calculated result statistics in these regions show that the measurements obtained with the three probes agree well with each other.

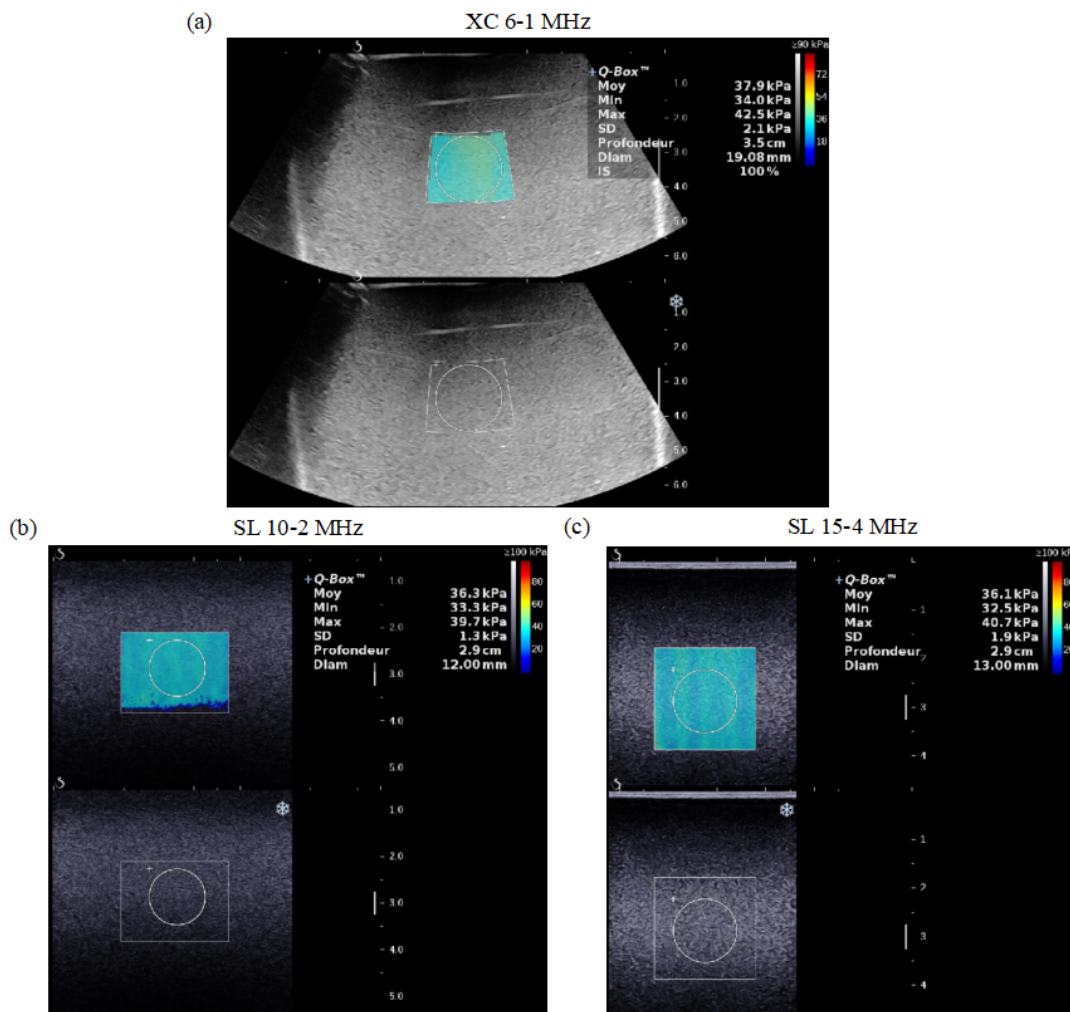


FIGURE 4.6: SSI images obtained with three different probes for the phantom C4.

Figure 4.7 and 4.8 display the velocity maps and the associated quality maps extracted from the corresponding Dicom images obtained with different probes for all the calibrated phantoms. It is shown that all the probes characterize well the shear velocity contrast across the four calibrated phantoms. For each phantom, the shear velocity maps obtained with different probes are similar to each other. The zero velocity and quality parameter values for the XC6-1

MHz probe were produced by the regridding of the trapezoid insonification windows. The zeroed velocity values for the SL15-4 MHz probe were due to the application of a quality parameter threshold of about 0.5 by the Aixplorer system to eliminate the pixels with insufficient data quality. In addition, the degradation of the quality parameters for the probe SL15-4 MHz in deeper regions are considered with the depth limitation when using the high frequency probe.

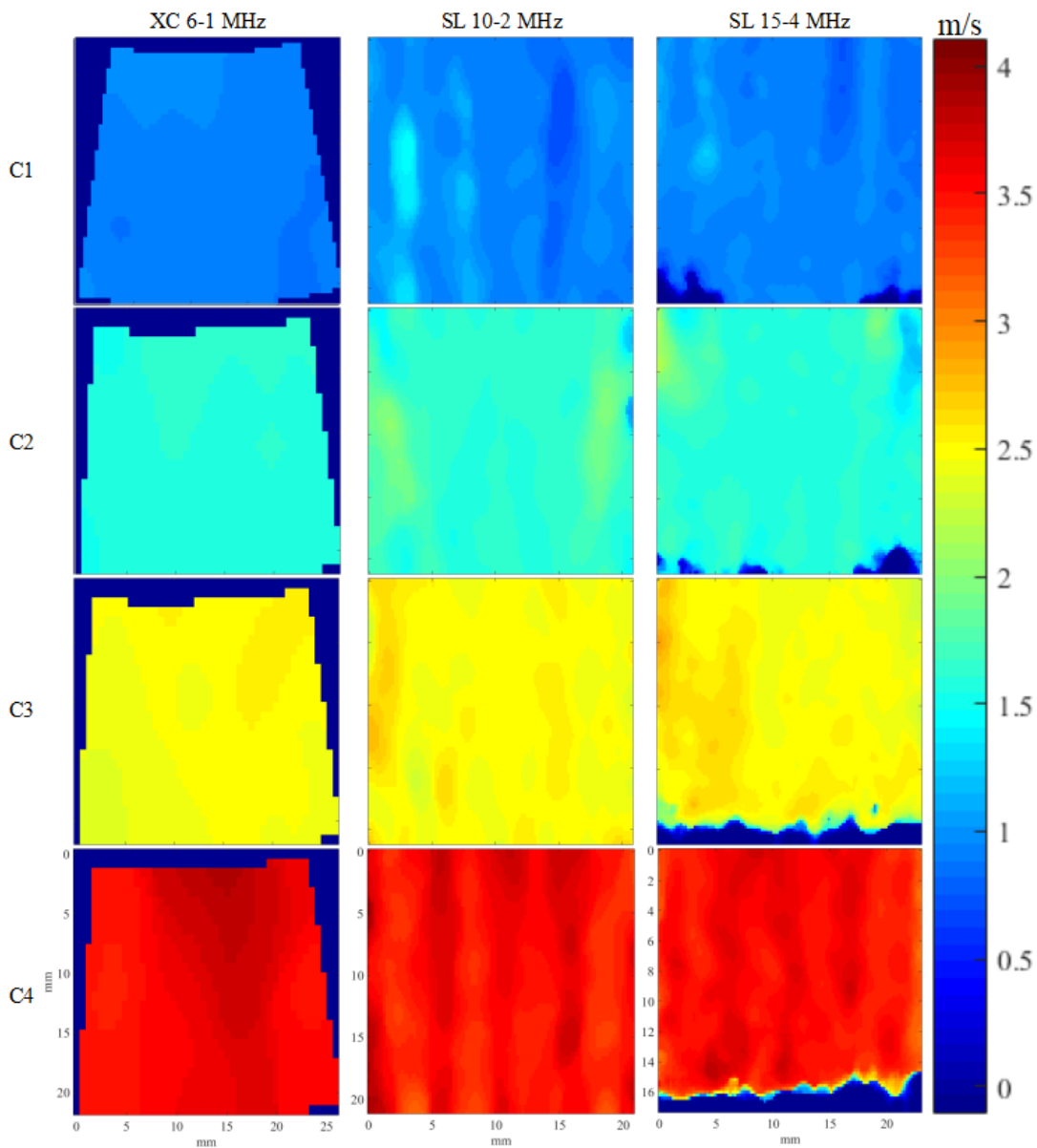


FIGURE 4.7: Shear velocity maps obtained with three different probes for the phantoms C1-C4.

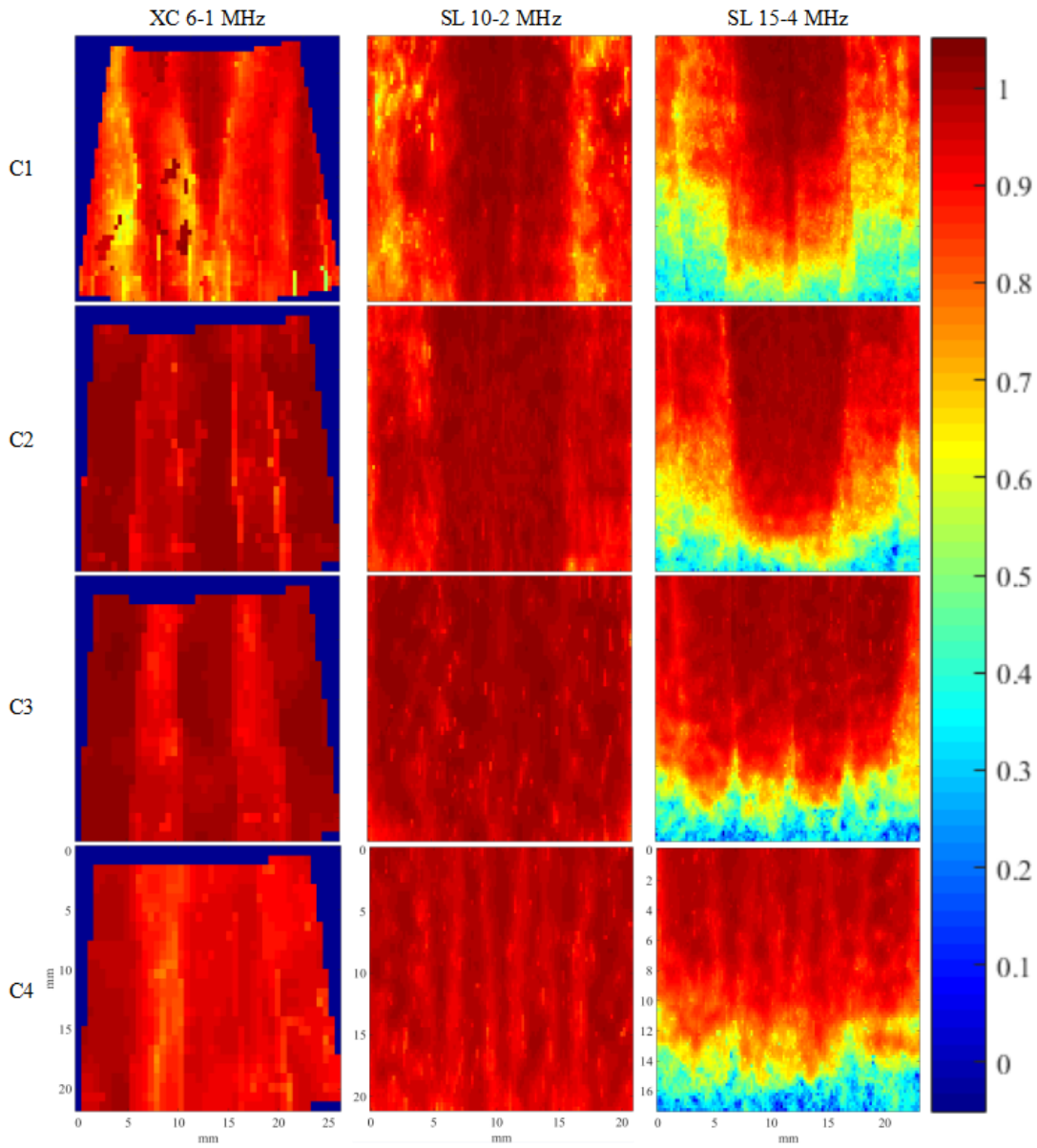


FIGURE 4.8: Quality maps obtained with three different probes for the phantoms C1-C4.

Figure 4.9 presents the $MV \pm SD$ of shear velocity values and the quality quantiles for different sub-population regions obtained with different probes for all the calibrated phantoms. It is shown that quality parameters can well characterize the SSI measurement validity. An empirical quality threshold of 0.7 seems to be pertinent to ensure the validity of the SSI measurements.

Besides, we also observed that SSI could always generate shear velocity maps with high quality as long as the depth of the insonification window was adapted to the frequency bandwidth of the chosen probe. The common clinical routine is to place regions of interest in the middle of the insonification window. This seems to be an appropriate practice given that the quality parameter is usually optimal in the center. For example, the mean elasticity values measured in the Q-boxs in Figure 4.6 agree well with the valid shear velocity values observed in Figure 4.9.

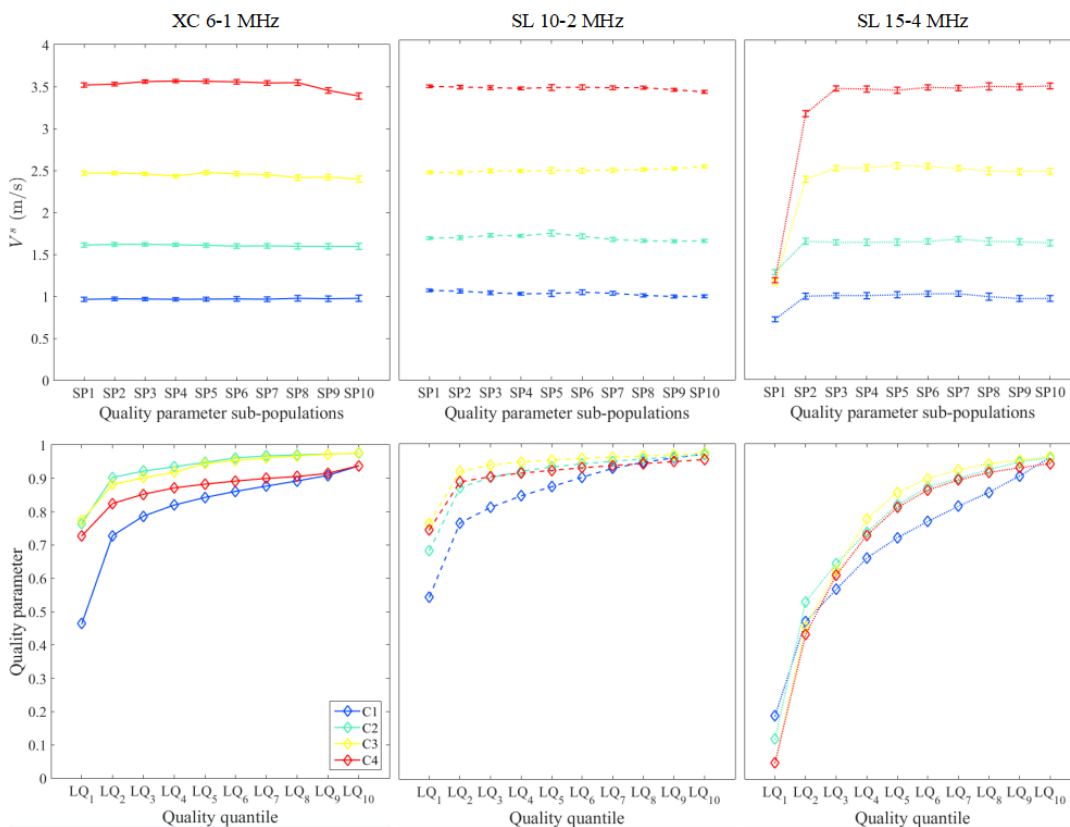


FIGURE 4.9: The first row represents $MV \pm SD$ of shear velocity values for different sub-population regions obtained with three different probes for the phantoms C1-C4; The second row represents the quality quantiles of these regions.

Figure 4.10 compares shear velocity measurements with different probes for all the calibrated phantoms over the regions of interest with the quality parameter higher than 0.7. Excellent measurement agreements between different probes were found for all the calibrated phantoms. This demonstrates the quasi-elastic nature of the calibrate phantoms. Hence, the shear wave dispersion due to viscosity should be negligible. The shear group velocity measured by SSI can thus be reasonably approximated as the shear phase velocity, which allows to minimize the theoretical bias between SSI and MRE measurements.

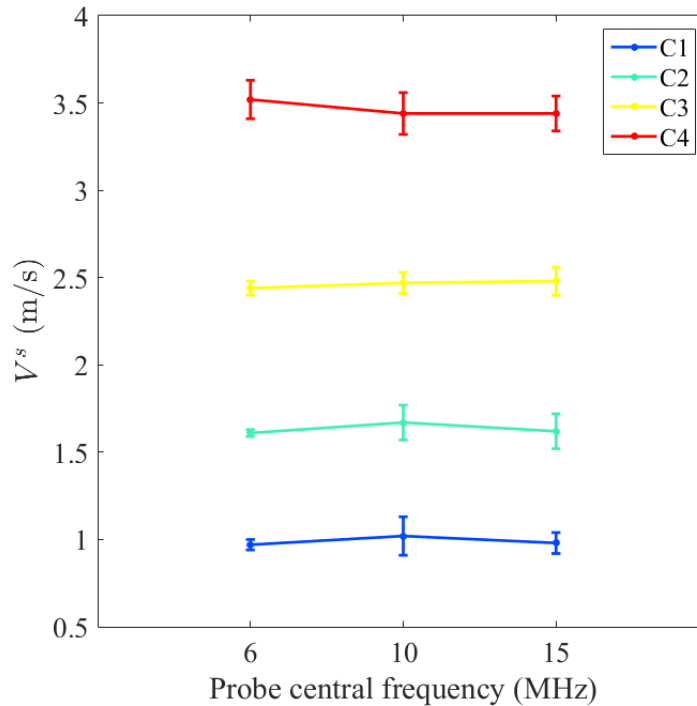


FIGURE 4.10: $MV \pm SD$ of shear velocity values for the phantoms C1-C4 measured with different probes over the regions of interest with the quality parameter higher than 0.7.

4.4.1.2 MRE for different excitation frequencies

Figure 4.11 presents the acquired MR phase images and the computed q-field of the calibrated phantom C4 along three orthogonal encoding directions for a series of excitation frequencies. In general, the wave patterns on both phase images and q-field correspond well to those of the normal incidence data sets observed in the simulation study in Chapter 3. With respect to the two in-plane axes, namely the encoding direction x and y, the wave patterns on both phase images and q-field are anti-symmetrical. Along the out-of-plane axis, namely the encoding direction z, the wave patterns on the phase images are rotationally symmetrical. However, the q-field along the out-of-plane axis is no more zero. Besides, neither phase nor q-field images prevail significantly on the data quality along specific encoding directions. The reasons for the wave pattern differences between the experimental and simulated data

sets can be twofold. First, the phantom has physical boundary and hence there exists wave reflection from the boundary; Second, the phantom container was badly decoupled from the wave guide, hence the vibration of the phantom container plays as an additional excitation source.

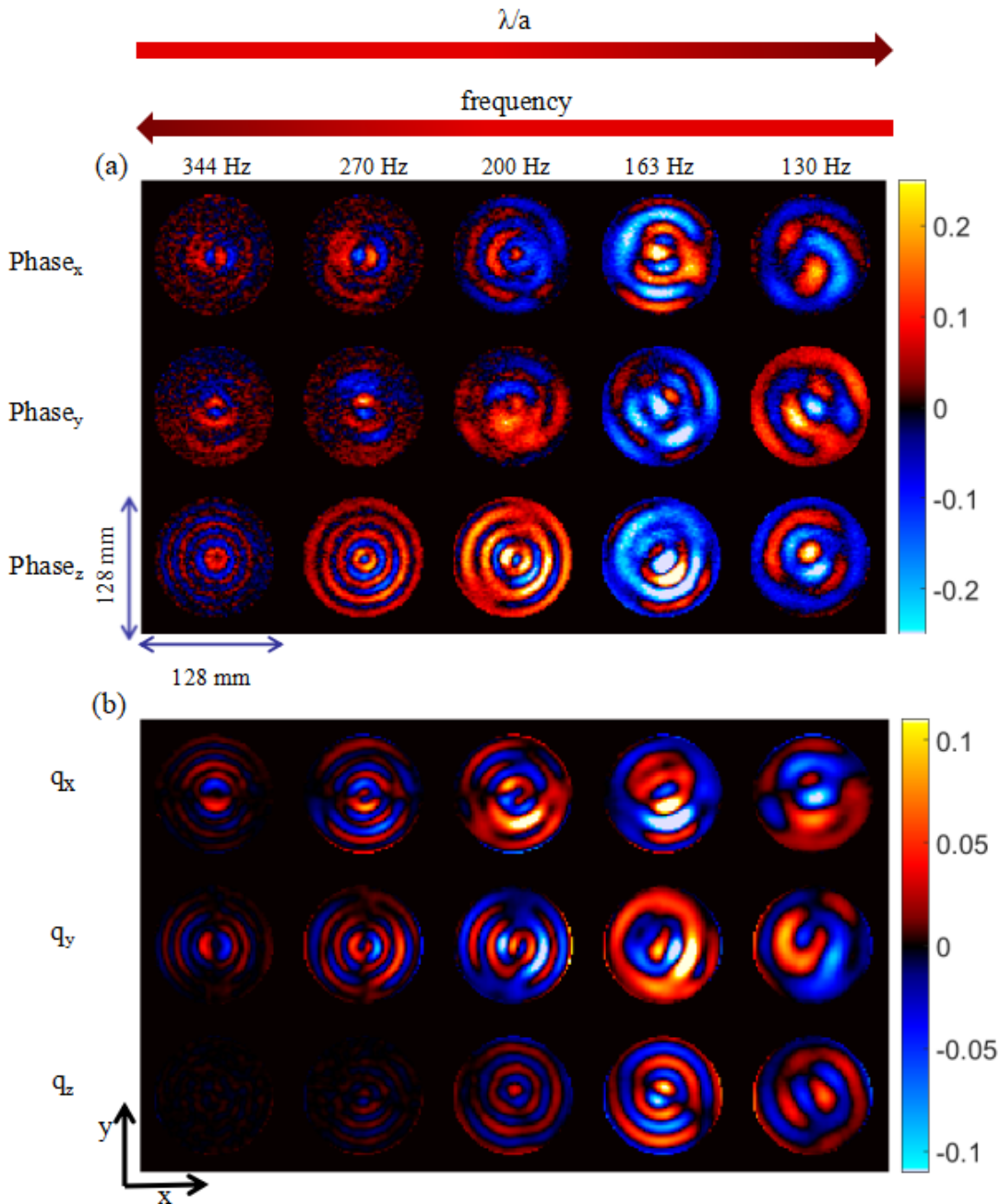


FIGURE 4.11: (a) Acquired MR phase images and (b) Computed q-field of the phantom C4 along three orthogonal encoding directions at one time point for $f = 344, 270, 200, 163, 130$ Hz.

These wave pattern differences are more significant for the low excitation frequency data sets. Because point source induced wave amplitude attenuated more slowly at low excitation frequencies and hence higher reflection wave amplitude from the boundary; meanwhile, the container's vibration is more important at low excitation frequencies. In spite of the above boundary issues, the wave interference does not disrupt the wavelength evolution trend as a function of the excitation frequency.

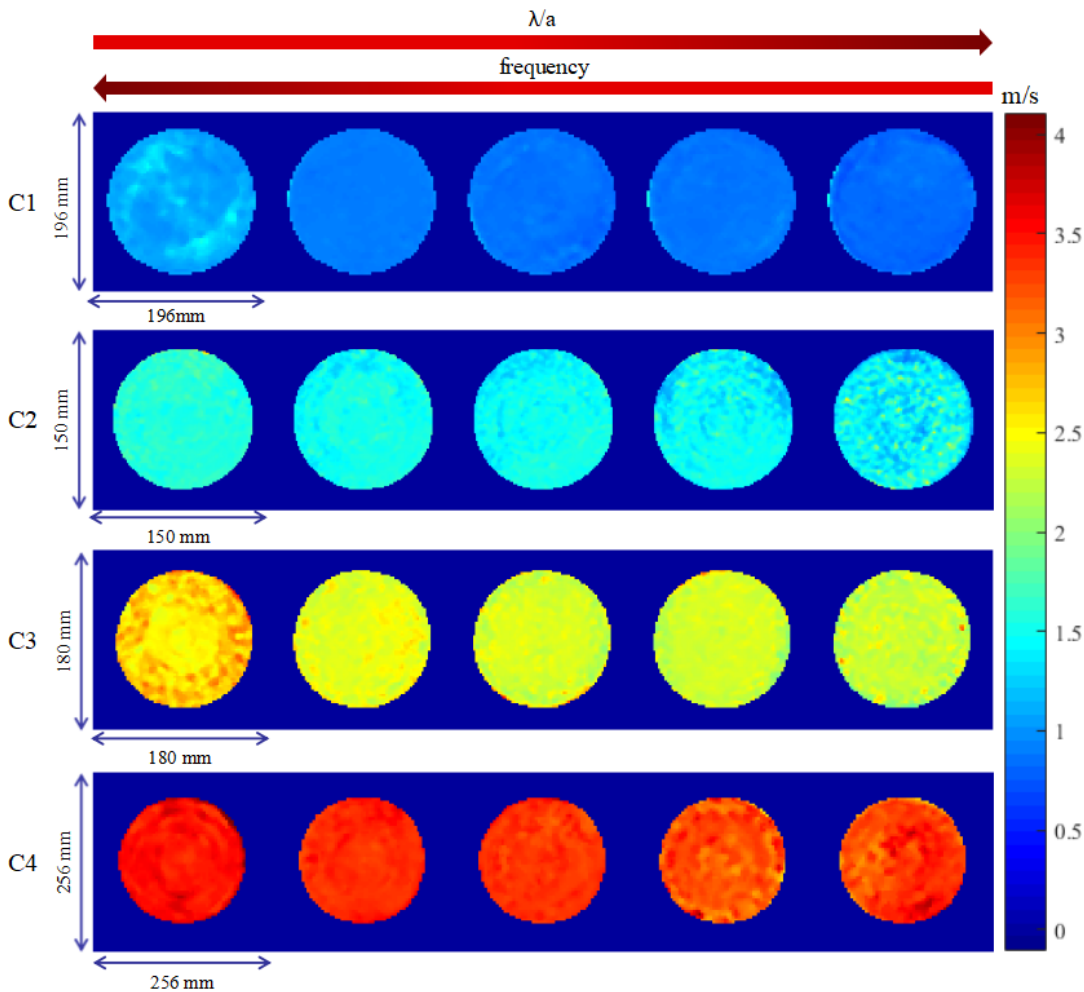


FIGURE 4.12: V^s maps of the phantoms C1-C4 (from up to down) for high excitation frequency to low excitation frequency (from left to right).

Figure 4.12 displays the V^s maps of all the calibrated phantoms for different excitation frequencies. The overall shear velocity contrast is significant across the four calibrated phantoms, which is insensitive to the excitation frequency. However, the accuracy and precision of regional shear velocity quantification for each phantom depend on the excitation frequency, more exactly the λ/a ratio. For each phantom, the shear velocity estimation presents a similar decreasing trend from high excitation frequency (low λ/a ratio) to low excitation frequency (high λ/a ratio). Moreover, the shear velocity estimation seems to be more dispersed for extremely high or low λ/a ratios.

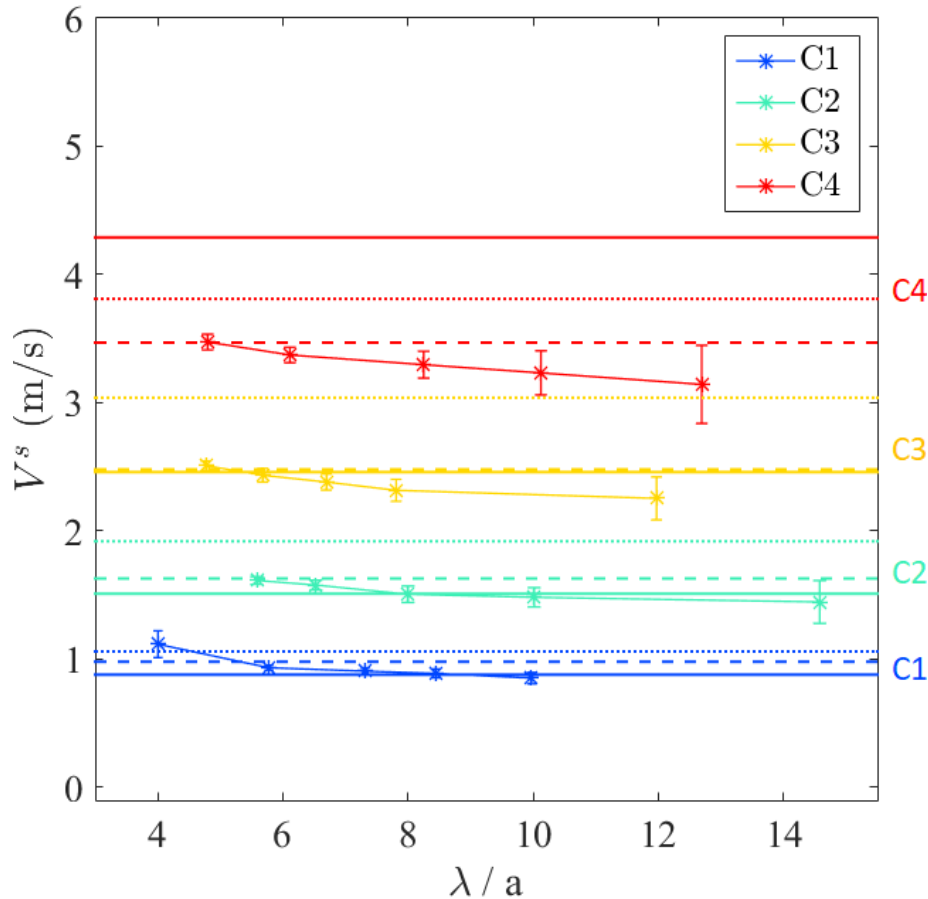


FIGURE 4.13: $MV \pm SD$ of V^s for the phantoms C1-C4 over the regions of interest with identical Q^{MRE}_t level of $40 \pm 10\%$ as a function of λ/a . For each phantom, three reference values were provided. The solid line represents the FibroScan measurement; the dashed line represents the SSI measurement; the dotted line represents the CIRS measurement.

Figure 4.13 summaries $MV \pm SD$ of V^s values as a function of λ/a for all the calibrated phantoms. For each phantom, the general trend for the shear velocity estimation corroborates well the simulation results. The mean values decrease with the λ/a values. The standard deviation values may not perfectly reproduce the same trend as the simulation results for all the phantoms. However, they always tend to degrade for larger λ/a ratios. Shear velocity measurements provided by CIRS and TE were proposed as the reference values to further evaluate the MRE measurement accuracy and precision. The two types of reference values correlate well with each other, but they do not agree with each other. There exists a systematic overestimation of CIRS measurements against TE measurements for the phantoms C1-C3. However, this trend was inverted for the stiffest phantom C4. Xie *et al.* have reported similar relationships between CIRS and TE measurements (Xie *et al.*, 2012).

The CIRS measurements are also largely superior to the MRE measurements. Because we do not know exactly which method was used by CIRS to obtain

their measurements, it is impossible to analyze the underlying reasons for the observed measurement bias. The CIRS measurements were thus not used to evaluate the MRE measurement quality. In contrast, the TE measurements lie in the same range with the MRE measurements, except for the phantom C4. Besides, there have already been several dedicated studies to demonstrate the good agreement between MRE and TE measurements (Oudry et al., 2009a, Oudry et al., 2009b, Bensamoun et al., 2008). The TE measurements were thus used as reference values to evaluate the MRE measurement quality. For phantoms C1-C2, it is obvious that the MRE measurement quality first improves with λ/a , then worsen for larger λ/a ratios resulting in an appropriate λ/a range around 7 – 10. This appropriate λ/a range corresponds well to the abaci obtained in the simulation study. For phantom C3, the appropriate λ/a range is slightly shifted towards 5 – 7, while for phantom C4, there does not exist any more appropriate λ/a range because the TE measurement is largely superior to the MRE measurements. The inconsistent observations for phantoms C3-C4 are mainly due to the coupling effect in the near field, which in fact leads to an overestimation for the TE measurements (Oudry et al., 2009b). Oudry *et al.* have reported that a measurement depth superior to $3/4 \lambda$, which is proportional to the expected shear velocity value, was needed to avoid the coupling effect in the near field. The measurement depth of the M probe is 25 – 55 mm. This measurement depth is sufficient for soft phantoms C1-C2 that have λ values around 18 – 30 mm at 50 Hz (the central excitation frequency for TE), but not enough for the stiffer phantoms C3-C4 whose λ values are around 50 – 70 mm at 50 Hz.

Figure 4.14 presents the voxel-wise velocity-quality parameter clusters for all the reconstructed data sets. For all the phantoms, we observed similar velocity-quality parameter evolution trend as shown in 3.3.5. This good correspondence with the simulation results validated the effectiveness of the proposed quality parameter Q^{MRE}_t for real experimental data. For all the phantoms, the converged shear velocity values for different frequency data sets are close to each other. This demonstrated again the quasi-elastic nature of these phantoms. The slightly higher converged shear velocity values for higher frequency data sets are mainly due to the lower λ/a conditions as illustrated in Chapter 3. The different converged values between original and interpolated data sets (Figure 4.14 (a)-(b)) further confirmed this explanation. Meanwhile, the improved reconstruction quality for the interpolated data set validated the performance of resampling for real experimental data.

4.4.1.3 SSI and MRE measurement comparison

Figure 4.15 presents a Bland-Altman like analysis between MRE and SSI measurements for all the calibrated phantoms. For each phantom, the MRE measurement with appropriate λ/a ratio was used, namely the 65 Hz ($\lambda/a = 8.4$) data set for C1, the 164 Hz ($\lambda/a = 8$) data set for C2, the 210 Hz ($\lambda/a = 6.8$) data set for C3 and the 200 Hz ($\lambda/a = 8.3$) data set for C4. In general, the SSI measurements are overestimated compared to the MRE measurements. The

measurement discrepancy between the two methods decreases with the stiffness of the phantoms as well as the quality threshold value used to generate MRE mask regions.

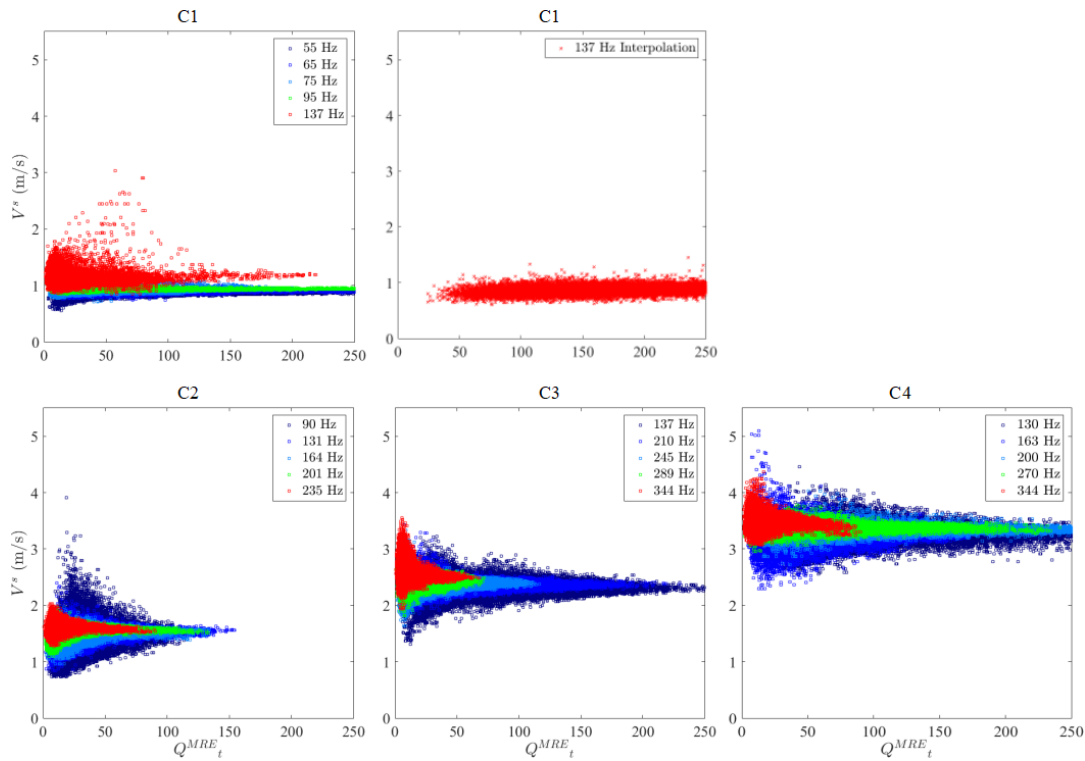


FIGURE 4.14: Voxel-wise V^s as a function of the corresponding Q^{MRE}_t values over the whole phantom volume region for all the reconstructed data sets.

Although the measurements between MRE and SSI are not perfectly consistent, there is a good agreement between the two methods in terms of relative mean difference (less than 10%) that should be emphasized. This discrepancy level is smaller than that reported by Oudry *et al.* (Oudry *et al.*, 2009b). In their study, they found an overall averaged difference of 23 % for the shear modulus measured by MRE and Fibroscan, which corresponds to an averaged difference of about 11 % for the shear velocity measurement. In addition, if we used higher quality thresholds for MRE measurements, the discrepancy between MRE and SSI could be further reduced to less than 5 %. The improved agreement in our comparison study is owing to: 1) the quality-guided MRE measurements with appropriate acquisition and reconstruction conditions and the empirically chosen quality parameter threshold for the SSI measurements; 2) the negligible coupling effect and viscosity related shear wave dispersion. Considering the measurement precision and reproducibility issue for each modality, the measurement discrepancy observed in our study can be considered as negligible and thus the quality-guided MRE and SSI measurements can be considered to be equivalent.

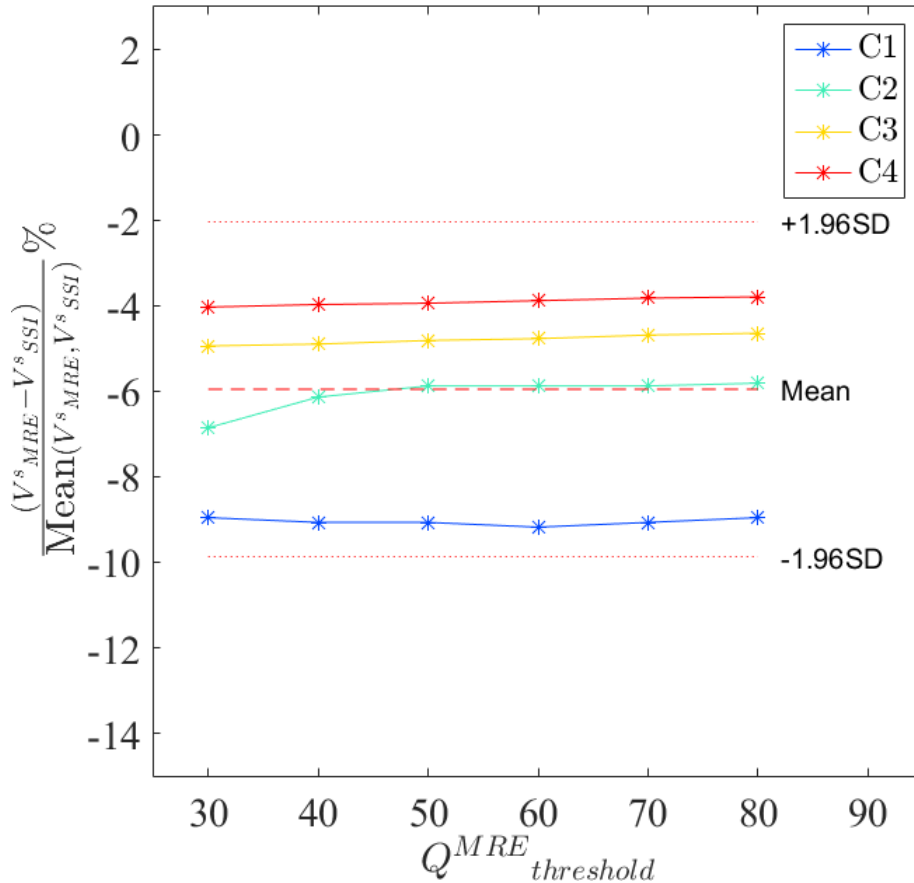


FIGURE 4.15: Bland and Altman like analysis between SSI V^s measurements and those of MRE with appropriate λ/a ratios for the calibrated phantoms C1-C4.

4.4.2 PVA phantoms

4.4.2.1 SSI using different ultrasound probes

Figure 4.16 presents the Dicom images of SSI measurements obtained with different probes for the 5w% and 7w% PVA phantoms. The Bmode images and the superimposed elasticity maps are quite homogeneous, which demonstrates a good dissolution and uniform mixture of the PVA powder in the distilled water. White lines were observed for the 5w% PVA phantom, which was mainly due to the deposition of vegetable coal particles (Figure 4.16). For the 7w% PVA phantom, we reduced the ultrasound penetration level, so the white lines were not observed.

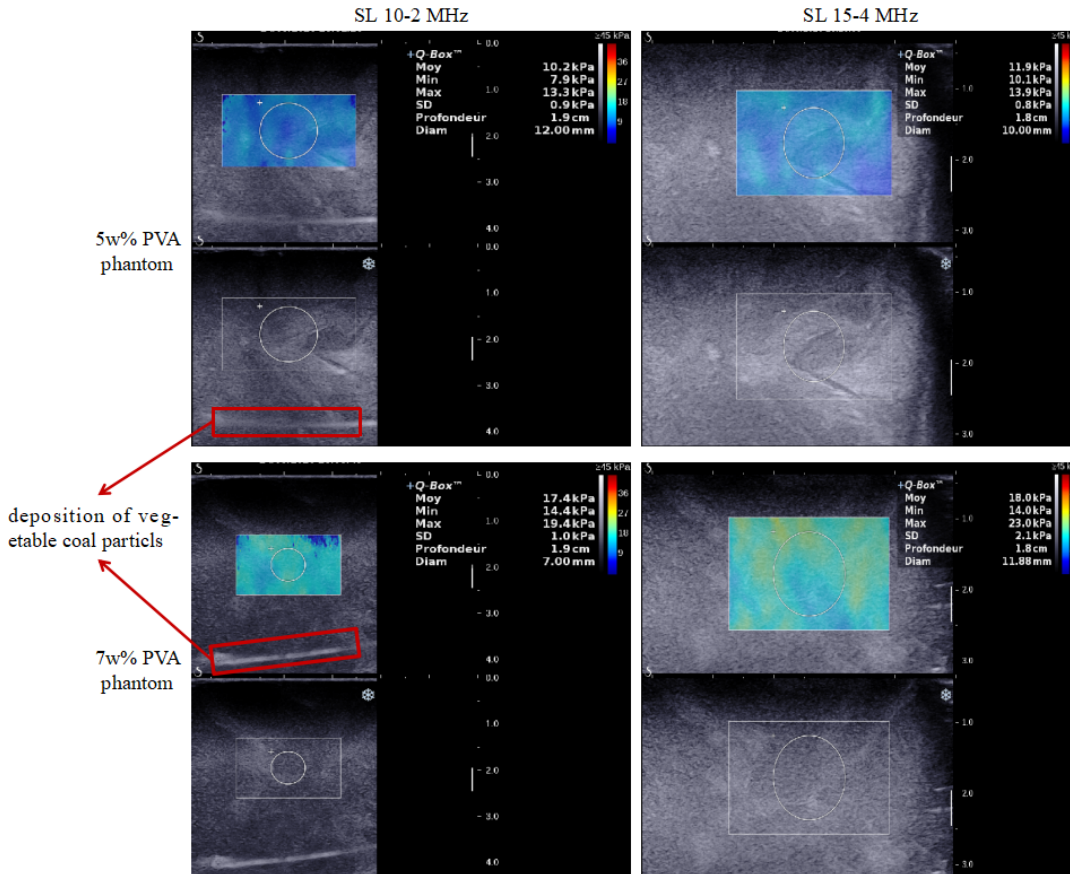


FIGURE 4.16: SSI images obtained with two different probes for 5w% and 7w% PVA phantoms.

Figure 4.17 displays the shear velocity maps and the quality maps extracted from the corresponding Dicom images. In general, high quality shear velocity maps were generated in the whole insonification windows. However, the distribution of the quality parameters was not as homogeneous as that of the calibrated phantoms. This was mainly due to the slight local inhomogeneities within the PVA phantoms, which show as small white fissures on the Bmode images (Figure 4.16). The local inhomogeneities were principally caused by the imperfection of the fabrication procedure. They could induce complex wave interferences and distortions, which may degrade the reconstruction algorithm. However, the quality analysis in Figure 4.18 presents that shear velocity values are still quite stable, not biased by the above local inhomogeneity issue. Similar to the calibrated phantoms, an empirical quality parameter threshold of 0.7 seems to be pertinent to ensure the validity of the SSI measurements for the PVA phantoms.

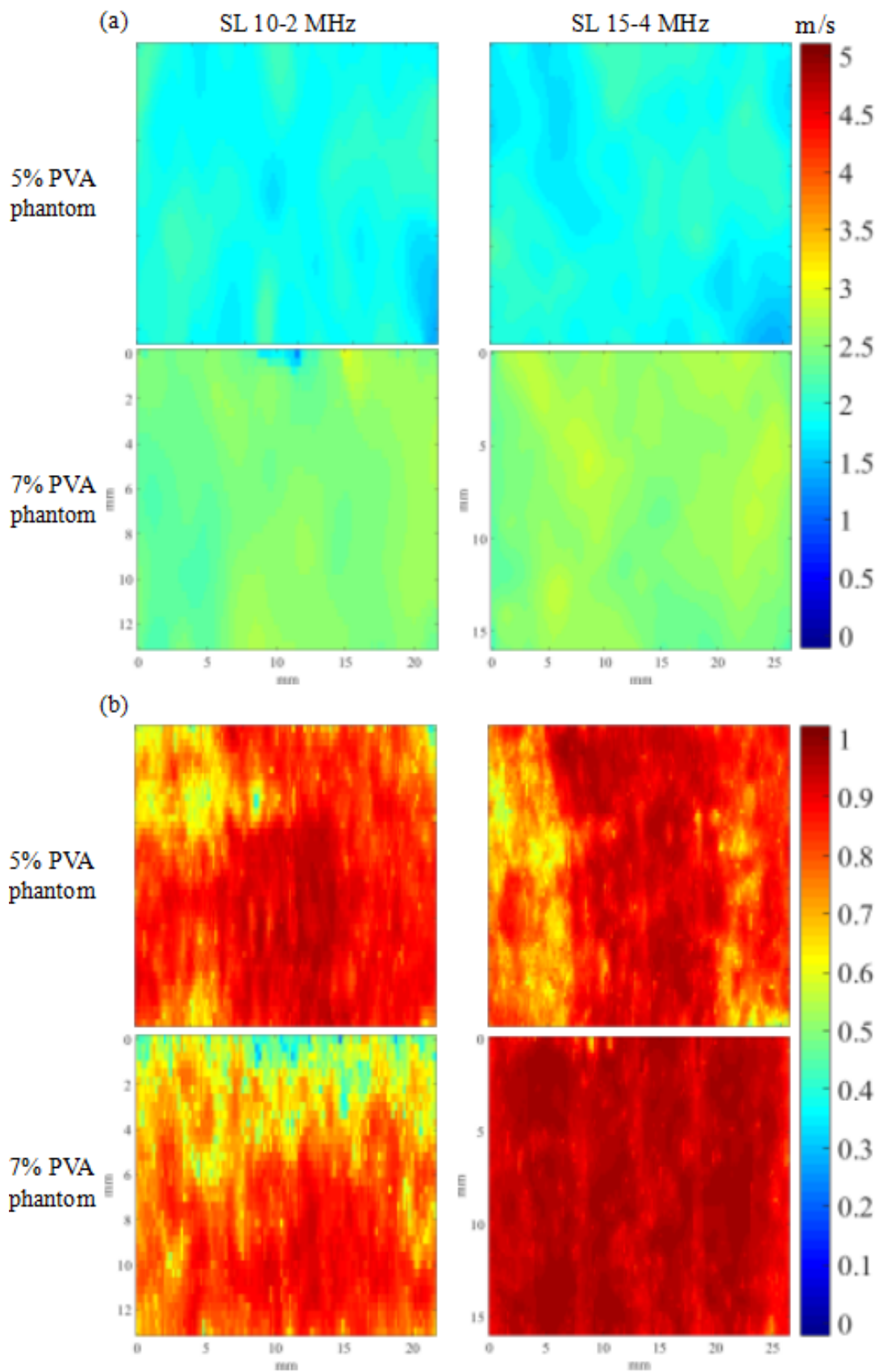


FIGURE 4.17: Shear velocity maps (a) and associated quality maps (b) obtained with two different probes for 5w% and 7w% PVA phantoms.

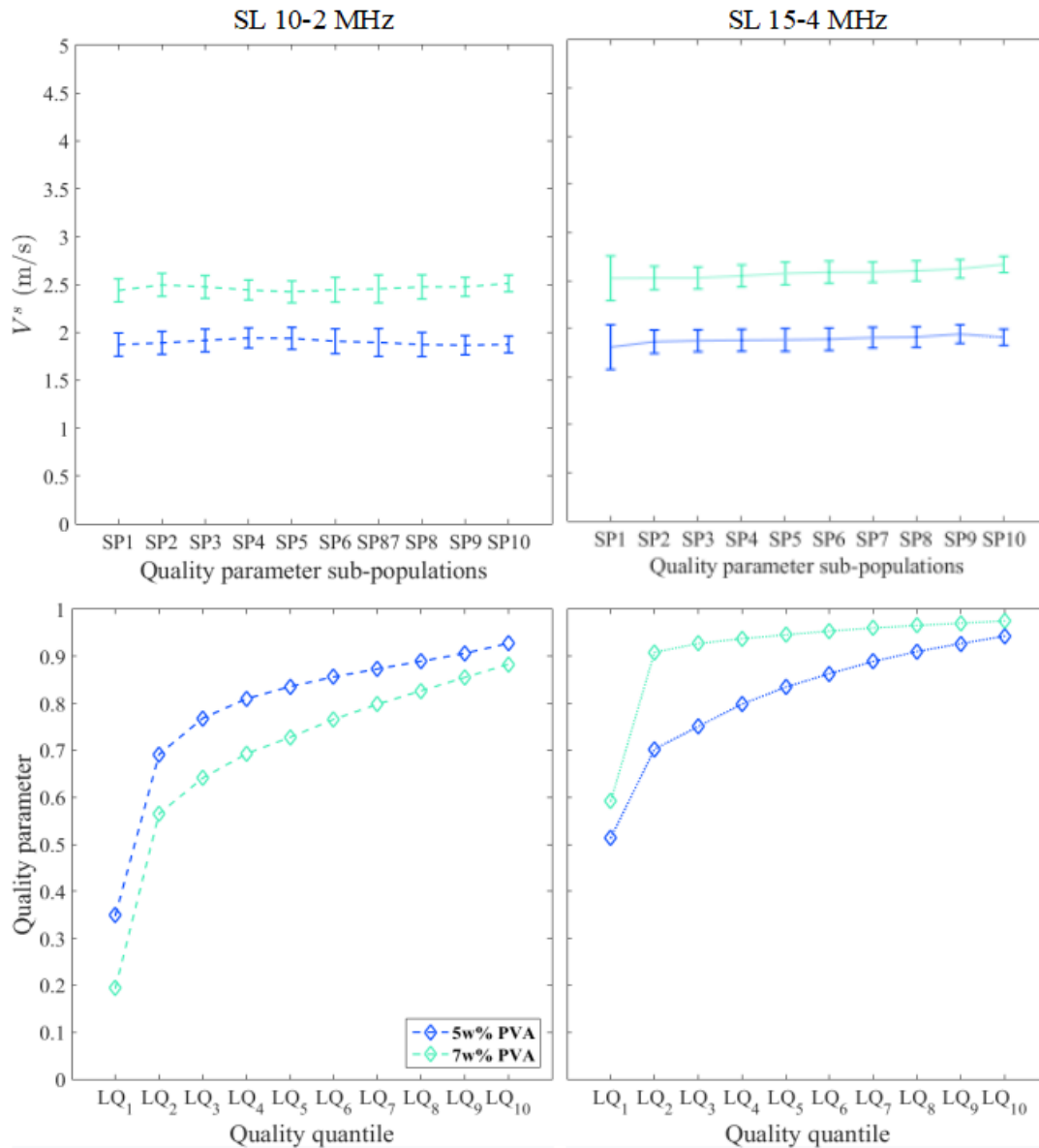


FIGURE 4.18: The first row represents $MV \pm SD$ of shear velocity values for different sub-population regions obtained with two different probes for 5w% and 7w% PVA phantoms; The second row represents the quality quantiles of these regions.

Figure 4.19 compares shear velocity measurements with different probes for the two PVA phantoms over the regions of interest with the quality parameter higher than 0.7. Excellent measurement agreements between different probes were found for both phantoms. This demonstrates the quasi-elastic nature of the home-made PVA phantoms. Hence, the shear wave dispersion due to viscosity should be negligible. The shear group velocity measured by SSI can thus be reasonably approximated as the shear phase velocity. This allows to minimize the theoretical bias between the shear phase velocity measured with MRE and the shear group velocity measured with SSI.

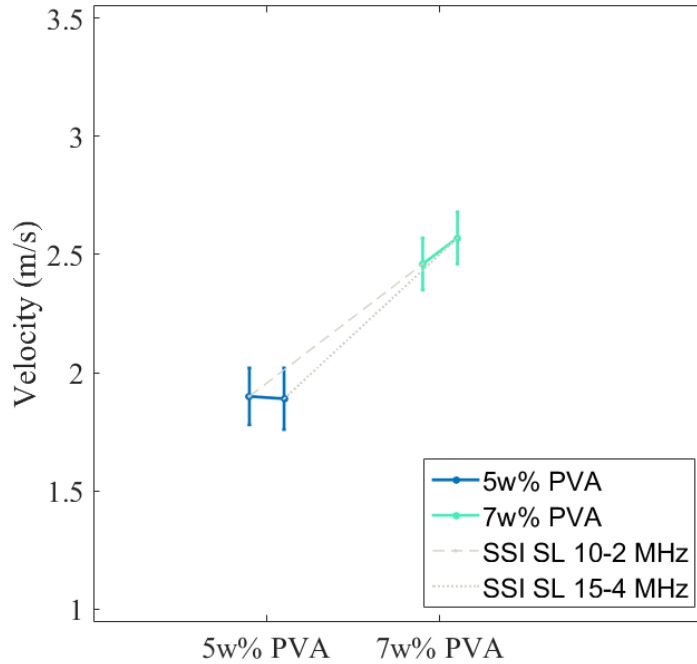


FIGURE 4.19: $MV \pm SD$ of shear velocity values for 5w% and 7w% PVA phantoms measured with different probes over the regions of interest with the quality parameter higher than 0.7.

4.4.2.2 MRE for different excitation frequencies

Figure 4.20 presents the acquired MR phase images and the computed q -field of the 5w% PVA phantom along three orthogonal encoding directions for a series of excitation frequencies. In general, the wave patterns on both phase images and q -field correspond well to those observed in the simulation study. Although we used higher excitation frequencies than those used for the calibrated phantoms, smaller sample sizes of PVA phantoms as well as the potential coupling between the plastic tube wall and the excitation source led to boundary issues similar to those observed on calibrated phantoms and discussed in section 4.4.1.2.

Figure 4.21 displays the V^s maps of both PVA phantoms for different excitation frequencies. As for the calibrated phantoms, the overall shear velocity contrast between the two PVA phantoms is significant no matter what the excitation frequency is, but the regional shear velocity quantification for each phantom depends on the λ/a ratio. Figure 4.22 summaries $MV \pm SD$ of V^s values as a function of λ/a for both PVA phantoms. For both phantoms, the mean values decrease with λ/a ratios. The measurement precision does not vary significantly across excitation frequencies as for the simulation datasets or the calibrated phantoms. This is mainly due to the local inhomogeneities of the PVA phantoms, which in fact conceals the λ/a dependent measurement precision trend. However, it is clearly shown that the shear velocity estimation is more closer to the SSI measurements when λ/a is around 7. This λ/a value corroborates well the appropriate λ/a range deduced from the simulation results.

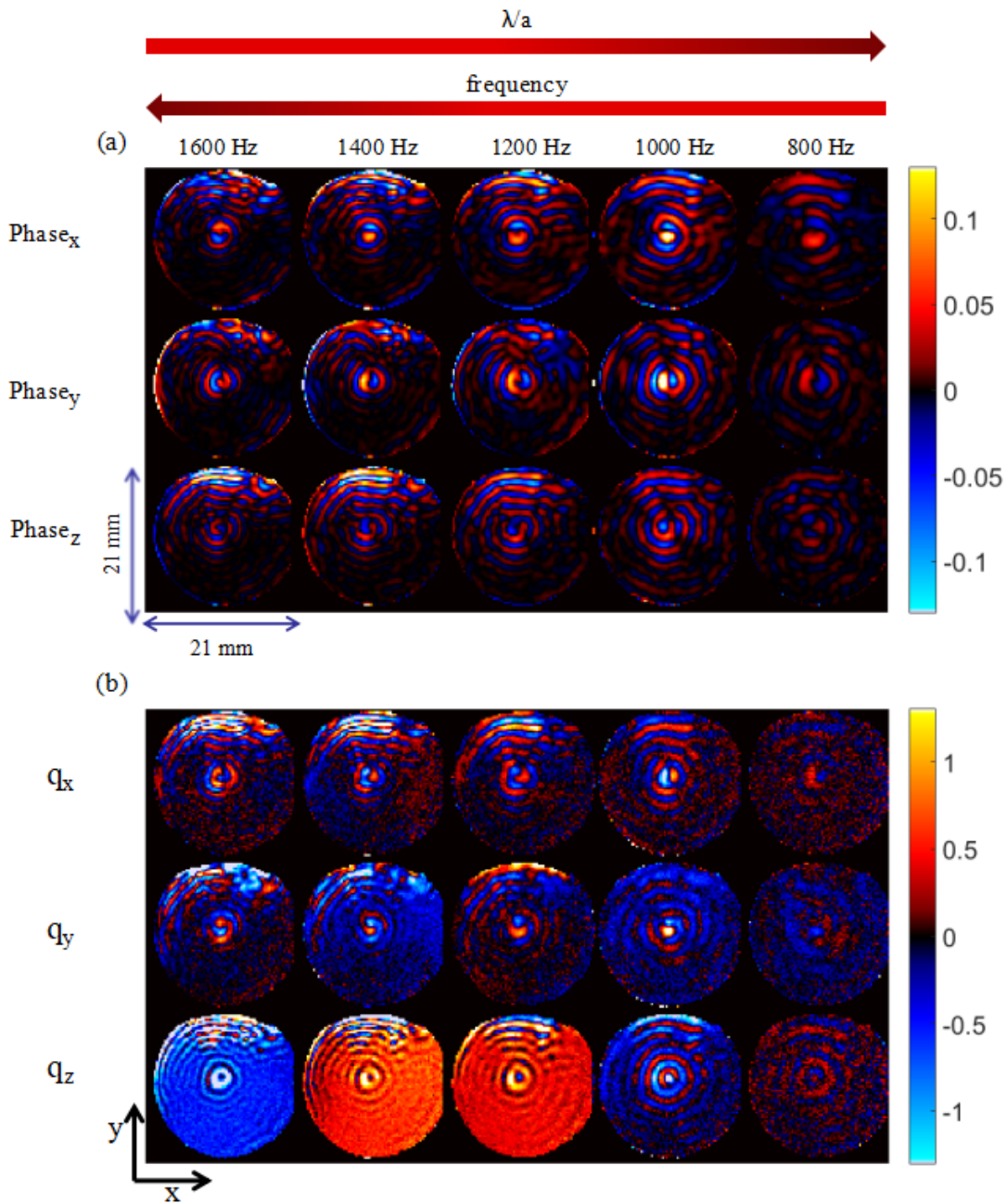


FIGURE 4.20: (a) Acquired MR phase images and (b) Computed q -field of the 5w% PVA phantom along three orthogonal encoding directions at one time point for $f = 1600, 1400, 1200, 1000, 800\text{Hz}$.

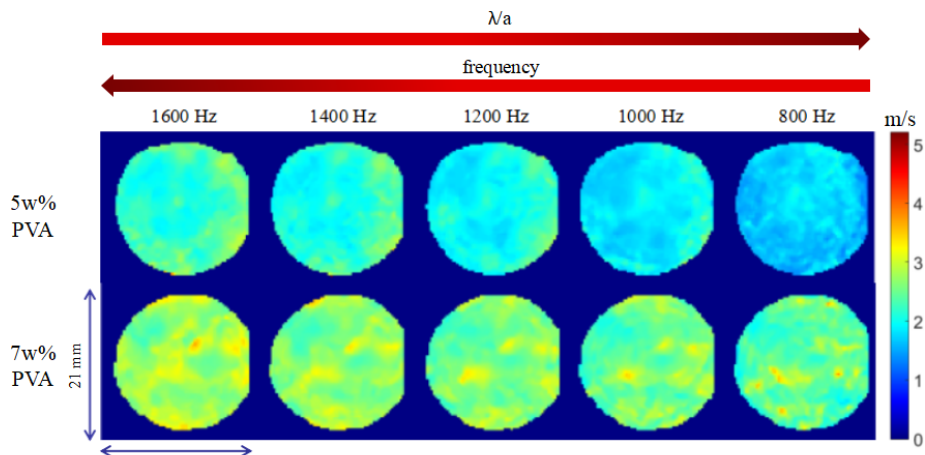


FIGURE 4.21: V^s maps of the 5w% and 7w% PVA phantoms for $f = 1600, 1400, 1200, 1000, 800\text{Hz}$.

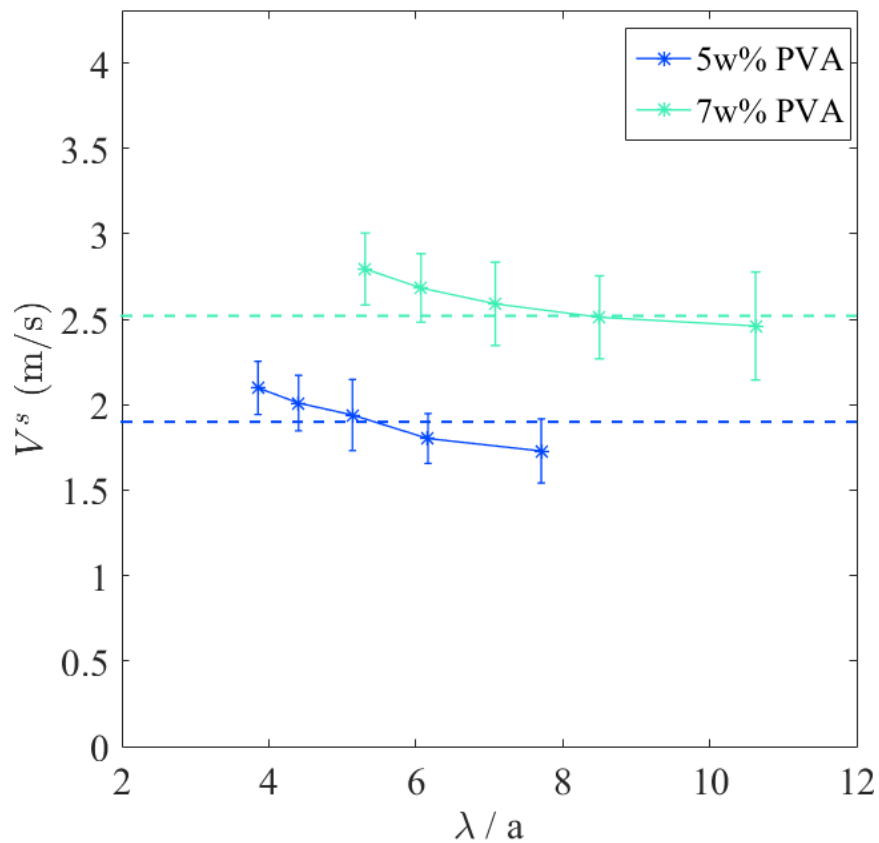


FIGURE 4.22: $MV \pm SD$ of V^s for 5w% and 7w% PVA phantoms over the regions of interest with identical Q^{MRE}_t level of $40 \pm 10\%$ as a function of λ/a . The dashed lines represent the SSI measurements for both phantoms.

4.4.2.3 SSI and MRE measurement comparison

Figure 4.23 presents a Bland-Altman like analysis between MRE and SSI measurements for the PVA phantoms. For each phantom, the MRE measurement with appropriate λ/a ratio was used, namely the 1000 Hz data sets for both phantoms. In general, the SSI measurements are higher than the MRE measurements. The measurement discrepancy between the two modalities decreases as the phantom stiffness increases as well as the quality threshold value used to generate MRE mask regions. An overall averaged difference of about 1-3 % was found, which is significantly lower than that for the calibrated phantoms. This improved agreement can be mainly attributed to the overall higher q-field quality of the MRE acquisitions of the PVA phantoms. The good agreement between the two modalities on the PVA phantoms demonstrates that, on the one hand, the quality-guided MRE and SSI measurements are interchangeable, and on the other hand, the polyvinyl alcohol is a good candidate for fabricating elastography phantoms aimed at comparing the measurement performances between MRE and SSI.

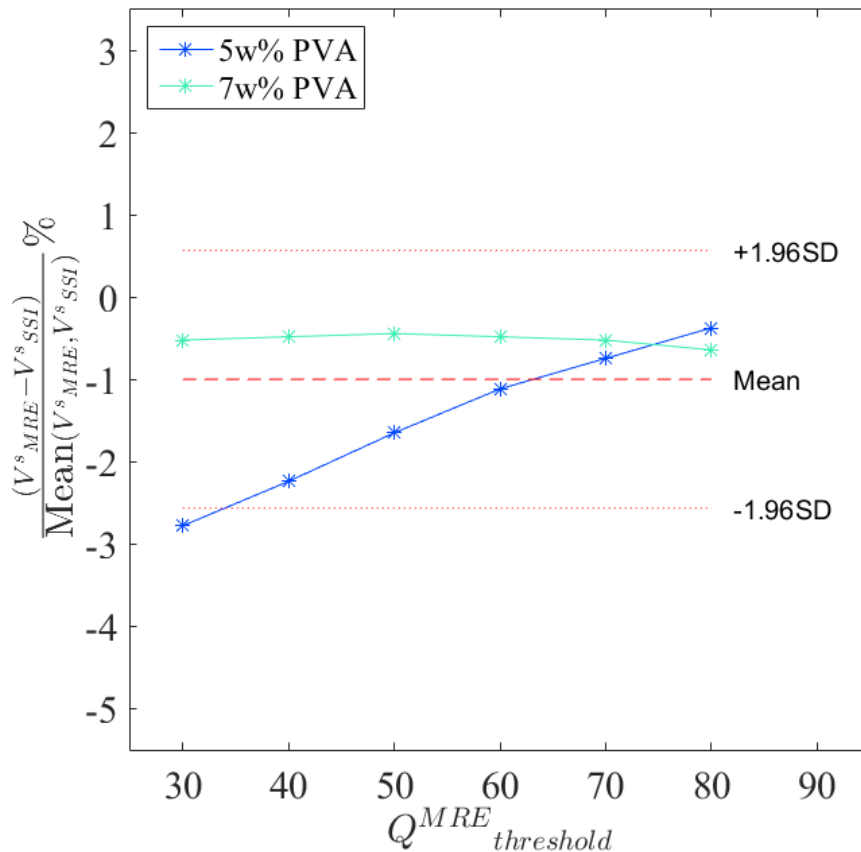


FIGURE 4.23: Bland and Altman like analysis between SSI V^s measurements and those of MRE with appropriate λ/a ratios for 5w% and 7w% PVA phantoms.

4.5 Conclusions

In this chapter, we have carried out a quality-guided comparison study between MRE and SSI measurements on commercial calibrated phantoms and home-made PVA phantoms respectively. First, we demonstrated that SSI measurement comparison between different ultrasound probes had the potential to qualitatively evaluate the shear wave dispersion level of the media under investigation due to viscosity. Using this method, the commercial calibrated phantoms and the PVA phantoms were both proven to be quasi-elastic media and hence adapted for cross-validating MRE and SSI measurements. Second, the MRE measurements on the two types of phantoms validated the favorable MRE acquisition and reconstruction conditions found from the simulation study in a wide frequency range. Finally, we demonstrated that the quality-guided shear velocity measurements of the two modalities on quasi-elastic media agreed well with each other and hence were interchangeable. Besides, our PVA phantom fabrication procedure was well validated. It can serve as a basis for further fabrication of viscoelastic and heterogeneous PVA phantoms.

5 In vivo SSI and MRE comparison study on liver

5.1 Introduction

The characterization of liver fibrosis is one of the most widespread applications of elastography. TE, SSI and MRE have all been investigated in large cohorts of patients with chronic liver diseases to demonstrate their ability to distinguish patients with no/mild fibrosis from those with significant fibrosis or cirrhosis (Talwalkar et al., 2007; Bavu et al., 2011; Huwart et al., 2007; Yin et al., 2015). TE, performed using the FibroScan (Echosens, Paris, France), has become a mainstay for gastroenterologists to non-invasively characterize liver parenchymal stiffness in patients. However, thanks to their capacity to regionally quantify liver stiffness (unlike TE that only provides a global liver stiffness measurement), MRE and SSI have shown particular interests for liver fibrosis characterization. One important advantage of regional quantification lies in the fact that it allows to characterize the liver stiffness in more homogeneous regions with less vessel artifacts. Besides, MRE and SSI can have similar or even better technical success rates and diagnostic performances than TE for the staging of liver fibrosis (Leung et al., 2013; Bohte et al., 2014; Yin and Venkatesh, 2017). Although all three modalities can produce high performance cut-off values of liver stiffness for effectively staging fibrosis, these cut-off values are usually not consistent because of the existing inter-modality and even intra-modality measurement discrepancy. First, the three modalities exploit the shear waves with different frequency characteristics and hence measure different mechanical properties which may produce important theoretical biases between modalities especially in viscoelastic media (Yoon et al., 2013; Deffieux et al., 2015; Tang et al., 2015). Second, the measurements obtained with a same modality may not be consistent across different studies because of operator dependence (particularly for ultrasound elastography), different acquisition and reconstruction procedures and also different patient populations. The Ultrasound Modality Committee formed in 2012 under the frame of Quantitative Imaging Biomarkers Alliance (QIBA) performed an interlaboratory study of shear-wave speed estimation on phantoms (Hall et al., 2013). The study revealed significant differences in shear-wave speed estimates related to depth of measurements and between systems. The same significant intra-modality difference exist for MRE. *Huwart et al* have deduced an optimal cut-off value of 3.1 kPa from MRE for distinguishing moderate and severe fibrosis (Huwart et al., 2008a) while *Yin et al* have found an optimal cut-off value of 6.7 kPa using MRE for the same purpose (Yin et al., 2007). These inter- and intra-modality differences impede

the standardization of elastography techniques for liver fibrosis characterization. Thus it is important to identify the potential underlying reasons for these liver stiffness measurement discrepancies and then minimize their influences in order to cross-validate different modalities. In this chapter, we focus on the cross-validation of liver stiffness measurements using SSI and MRE.

In our study, we only considered healthy volunteers. The influence of different aetiologies of liver disease is thus negligible. In this context, the intra- and inter-modality measurement discrepancies for MRE and SSI liver stiffness measurements are mainly due to the theoretical discrepancy and modality specific validity issues as described in Chapter 2. To address the above issues, we carried out an *in vivo* comparison study between quality-guided MRE and SSI liver stiffness measurements. The appropriate acquisition and reconstruction conditions for MRE and SSI established in Chapter 3 and 4 were incorporated in this comparison study. To implement these optimization strategies, common hypotheses about healthy liver behavior were made, namely those of isotropic, homogeneous and quasi-elastic tissues.

5.2 Methods

5.2.1 Experimental protocols

Two healthy volunteers were enrolled for MRE and SSI liver measurements. The basic physiological informations for the two volunteers are listed in Table 5.1. All the acquisitions were performed at fasting stage.

TABLE 5.1: Volunteers' characteristics

	Volunteer 1	Volunteer 2
Gender	Male	Male
Age (yrs)	41	28
Body Mass Index (BMI)	21	25
Skin-to-(right)-Liver-surface Thickness (SLT) (mm)*	13	20

*SLT was measured by the radiologist on the B-mode ultrasound. SLT values were classified as normal (SLT <18 mm) or elevated (SLT ≥18 mm) (Chami et al., 2016)

5.2.1.1 SSI liver acquisition

The SSI acquisitions were carried out by an experienced radiologist (Maud CREZE) on an Aixplorer ultrasound system (Supersonic Imagine, Aix-en-Provence, France) at hospital Kremlin-Bicêtre, France. SSI exploration of the liver is usually performed using the abdominal probe (XC6-1 MHz). However, some studies reported measurement failures using the convex probes due to unfavorable clinical conditions (such as high BMI and SLT values) resulting in poor filling of elasticity maps (Varbobitis et al., 2016; Huang et al., 2014). In this context, besides the convex probe, we additionally used the

linear high frequency probe (SL10-2 MHz) to characterize the liver in our study. The measurements by the two different probes also permits to evaluate the frequency dependence of the SSI measurements and hence to verify the hypothesis of quasi-elastic medium for the liver. Different liver segments were probed for the two volunteers (Table 5.2) because the regions that were easily accessible for the 2 volunteers were different. For each segment, three successive measurements (M1,M2,M3) were performed with both probes except for the segment 5 of Volunteer 2 which could only be measured by the abdominal curved probe.

TABLE 5.2: SSI liver acquisition parameters for the two volunteers

	Probe central frequency (MHz)	Pixel Size (mm ²)	Liver segments
Volunteer 1	6	0.35 × 0.2	4,6,8
	10	0.6 × 0.6	4,6,8
Volunteer 2	6	0.35 × 0.2	4,5
	10	0.6 × 0.6	4*

*The SSI measurements for segment 5 with the linear probe had poor filling of elasticity maps. Thus they are considered as measurement failures.

5.2.1.2 MRE liver acquisition

The MRE acquisitions were carried out on a Philips 1.5 T MR Scanner (Achieva, Philips Healthcare, The Netherlands) at SHFJ, France. The volunteers laid in the supine position with feet first. A commercial torso cardiac coil (Philips Healthcare, The Netherlands) was used to receive the MR signal (Figure 5.1 (a)). The wave generation system introduced in Chapter 2 was implemented to provide the external harmonic excitation. An elastomer was additionally used here to connect the wave guide with the surface of the skin in order to realize a point source like excitation (Figure 5.1 (b)). The wave guide and elastomer were fixed by a strap at the edge of the right chest diaphragm. The vibration penetrated into the liver from the lower liver segments as they were pressed out of the protection of the chest diaphragm during breath-holds in full inspiration (Figure 5.1 (c)).

For both volunteers, the liver was imaged and mechanically characterized using the spin-echo based MRE sequence. Imaging was performed on the axial plane relative to the bore of the MR scanner, which produced axial cross sections of liver. Saturation bands were applied on the left and right sides of the imaged liver sections in order to reduce the total acquisition time. Because of complex *in vivo* conditions, it was difficult to manually evaluate the wave length from the acquired phase images of liver. We used the SSI shear velocity measurements as a reference to choose the excitation frequencies that satisfied appropriate λ/a conditions. For Volunteer 1, an excitation frequency of 70 Hz was chosen in order to achieve a corresponding λ/a about 7. For Volunteer 2, five different excitation frequencies were used to cover a corresponding λ/a range of 5~14. MEG was applied successively along the three

spatial encoding directions M (axis y of imager), P (axis x of imager) and S (axis z of imager) to encode the three-dimensional displacement fields. For each frequency acquisition, the volunteer was asked to perform 12 successive breath-holds in full inspiration in order to obtain the four (temporal) phases in each of the three encoding directions. The MRE sequence parameters are detailed in Table 5.3

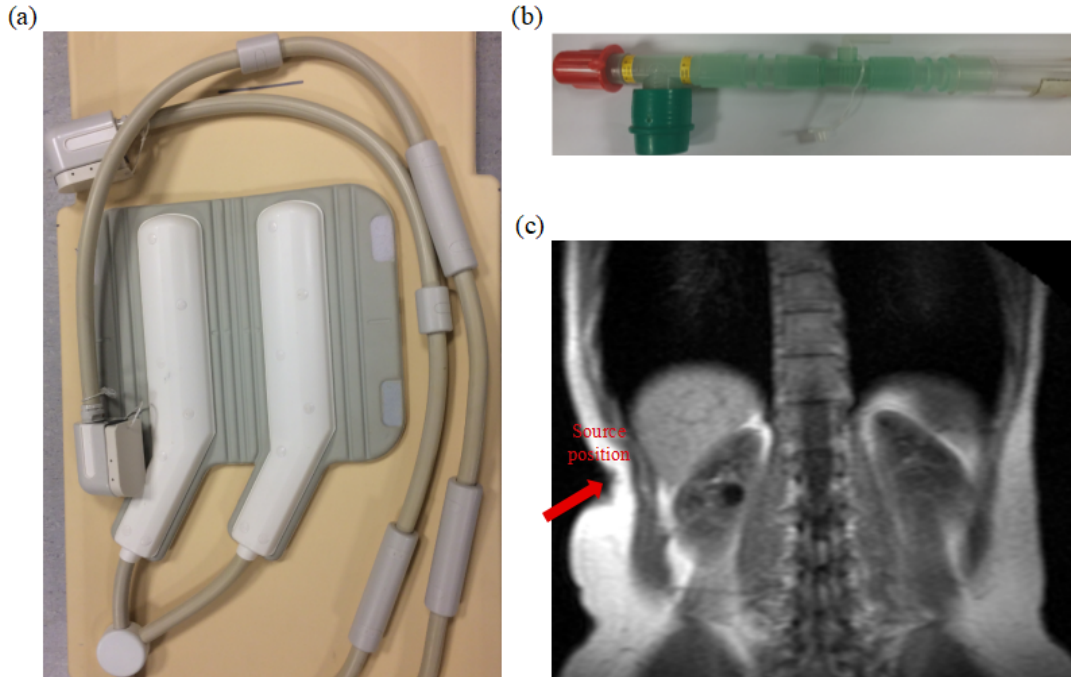


FIGURE 5.1: MRE experimental installation for the liver. A torso cardiac coil (a) was used for signal reception, an elastomer (b) was used to induce a point source like excitation into the lower liver segments (c), the red arrow shows the source position.

TABLE 5.3: MRE sequence parameters for the two volunteers

	a (mm)	FOV (mm ³)	f_{exc} (Hz)	TE/TR (ms/ms)	N_{MEG}	Breath-hold (s)	TA
Volunteer 1	3	240 × 240 × 36	70	33/640	1	31	6 min 3 s
Volunteer 2		240 × 240 × 24	40	87/1000	2	46	9 min 15 s
		240 × 240 × 30	65	54/769	2	36	7 min 7 s
		240 × 240 × 30	70	50/714	2	34	6 min 43 s
		240 × 240 × 30	85	41/588	2	28	5 min 33 s
		240 × 240 × 30	105	33/686	2	33	6 min 27 s

5.2.2 Data analysis

5.2.2.1 SSI post-processing

Shear velocity maps together with the associated quality maps were extracted from the obtained Dicom images using the dedicated Matlab function (provided by Supersonic Imagine) that we adapted for our specific study. First,

we carried out the quality analysis for each individual measurement as described in 4.3.1 in order to deduce an empirical quality parameter threshold, $Q^{SSI}_{threshold}$. Second, a circular region of interest was selected in the middle of the insonification window for each individual measurement, avoiding big vessels and artifacts. Pixels with a quality parameter inferior to the deduced $Q^{SSI}_{threshold}$ value were excluded from the selected regions. MVs and SDs of the shear velocity (V^s) and shear modulus (G) values were calculated over these circular regions. For each combination of liver segment and ultrasound probe (Table 5.2), three successive measurements (M1,M2,M3) were performed and hence three MVs and SDs of V^s and G were obtained. The variability for MVs of M1,M2 and M3 was expressed using a coefficient of variation (CV) where CV was calculated as $CV = (\text{standard deviation of three MVs} / \text{mean value of three MVs}) \times 100\%$. The mean values of the three successive MVs and SDs were used as the representative measurements for each combination of liver segment and ultrasound probe and ultimately compared with the corresponding MRE measurements.

5.2.2.2 MRE reconstruction

All the acquired MRE data sets were reconstructed using the q-based AIDE method detailed in Chapter 2. The qQW method detailed in Chapter 3 was used to combine the V^s_i values along the three motion-encoded directions to obtain the quality weighted shear velocity (V^s) maps accompanied with the associated q-field quality (Q^{MRE}_t) maps. In addition, the magnitude of shear complex modulus ($|G^*|$) maps were also calculated using the qQW method. For each data set, two types of regions of interest, avoiding big vessels and liver boundaries, were generated with the help of an experienced radiologist. First, regions of interest were placed on the liver segments corresponding to those used for the SSI measurements, which are defined as ROI_{seg4} , ROI_{seg5} , etc. Second, regions of interest were generated over the whole acquired liver volume, which are defined as ROI_{liver} . For each data set, V^s values over the ROI_{liver} were divided into ten equal sub-populations and plotted against the corresponding quantity quantiles as described in 4.3.1 in order to deduce an empirical quality parameter threshold, $Q^{MRE}_{threshold}$, for guaranteeing the convergence of measurements. For all the ROIs obtained for each data set, voxels with a quality parameter inferior to $Q^{MRE}_{threshold}$ were excluded for the computation of MVs and SDs of V^s and G^* values.

5.3 Results and Discussions

5.3.1 Volunteer 1

5.3.1.1 SSI liver measurements

Figure 5.2 presents the SSI acquired images. Figure 5.3 shows the extracted shear velocity maps together with the corresponding quality maps of the SSI

measurements obtained with the two probes for Volunteer 1. As can be observed, the shear velocity maps obtained with the XC6-1 probe are more homogeneous than those obtained with the SL10-2 probe. Segment 4 has a better quality parameter distribution than the others.

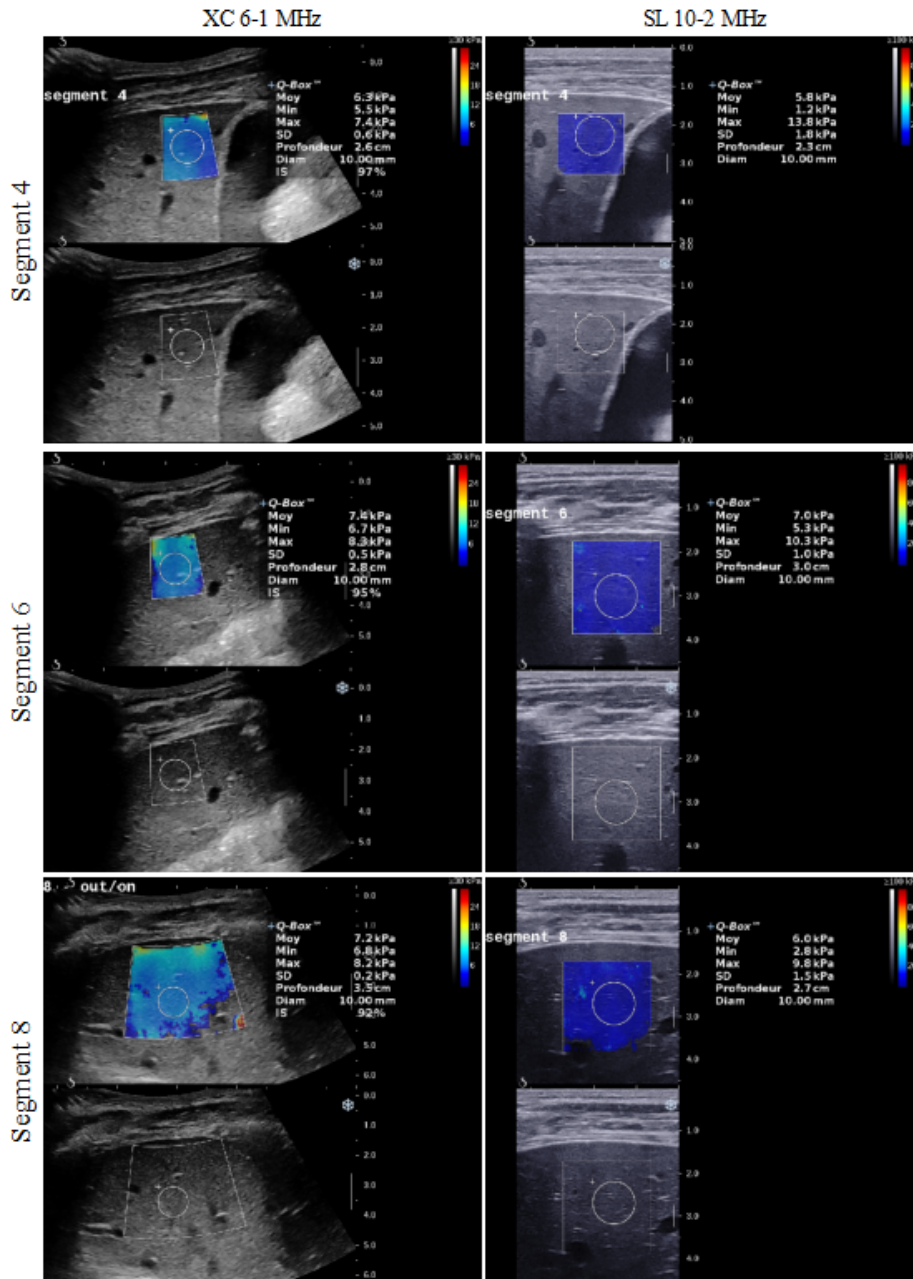


FIGURE 5.2: SSI images for one of the three successive measurements for each segment obtained with the abdominal probe (left column) and the linear probe (right column) for Volunteer 1.

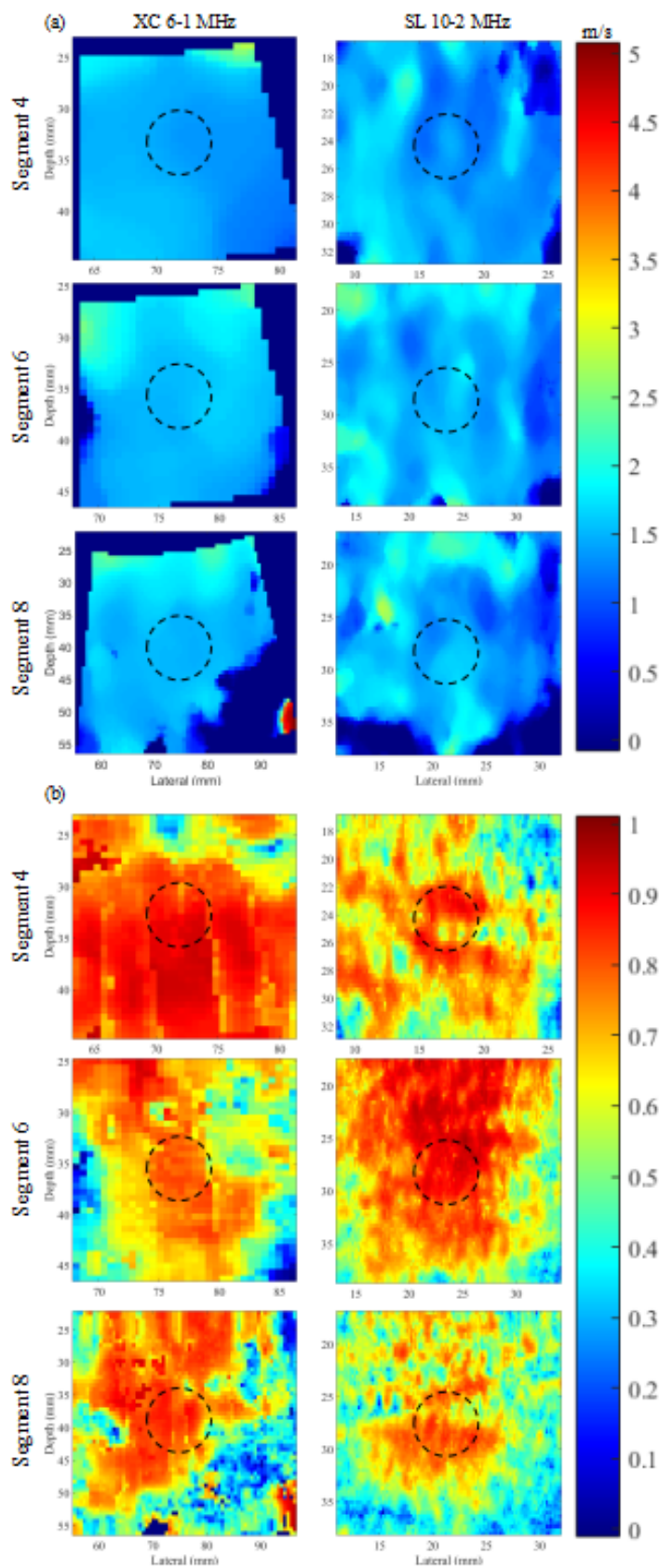


FIGURE 5.3: Extracted shear velocity images (a) together with the associated quality maps (b) for one of the three successive measurements for each segment obtained with the abdominal probe (left column) and linear probe (right column) for Volunteer 1. The dotted black circles represent the regions of interest used for calculating MVs and SDs.

Figure 5.4 presents the $MV \pm SD$ of shear velocity values (top row) and the quality quantiles (bottom row) for different sub-population regions of segment 4 obtained with the XC6-1 probe (left column) and SL10-2 probe (right column) for Volunteer 1. As shown in Chapter 4, the quality parameters can well characterize the SSI measurement validity. The measurement precision improves with the quality parameter. A $Q^{SSI}_{threshold}$ value of 0.7 as found in Chapter 4 seems to be pertinent to ensure the validity of the SSI measurements. The three successive measurements (M1,M2,M3) for each segment and probe are close to each other in accuracy, but vary in precision. For M1 (red) and M3 (blue) of the SL10-2 probe, the MVs increase for higher quality regions and hence the accuracy degrades. This could be operator dependent, because the operator needed to compress more the skin with the SL10-2 probe in order to obtain good filling of elasticity maps. This probably resulted in the hardening of the liver. The overall measurement accuracy, precision and repeatability of the XC6-1 probe appears to be better than those of the SL10-2 probe.

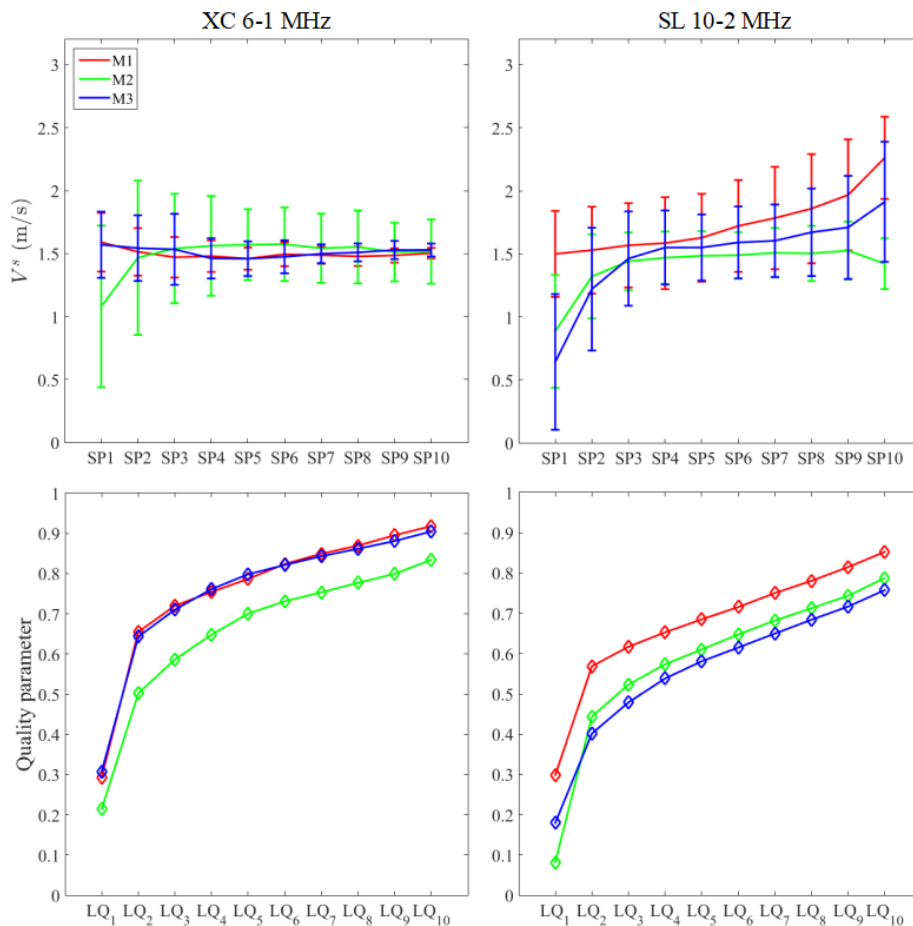


FIGURE 5.4: The first row represents the $MV \pm SD$ of shear velocity values for different sub-population regions of segment 4 obtained with the abdominal probe (left column) and the linear probe (right column) for Volunteer 1; The second row represents the quality quantiles of these regions.

Table 5.4 summarizes the successive SSI V^s measurements over different regions of interest with two different probes for Volunteer 1. The CV values for MVs between successive SSI measurements are always inferior to 30%, which is the common clinical criteria to evaluate if the SSI measurements are valuable (Yoon et al., 2013). This demonstrates the good reproducibility of SSI measurements. The standard deviations obtained with the SL10-2 probe tend to be higher than those of the XC6-1 probe. This is mainly due to the fact that the shear velocity maps obtained by the SL10-2 probe have higher spatial resolutions and hence reveal more details or noise, particularly in homogeneous tissue as pointed out by Chami et al (Chami et al., 2016).

TABLE 5.4: Reproducibility of SSI V^s measurements for Volunteer 1

		Probe XC6-1 MHz				Probe SL10-2 MHz			
		M1	M2	M3	CV	M1	M2	M3	CV
		(m/s)	(m/s)	(m/s)	(%)	(m/s)	(m/s)	(m/s)	(%)
Segment 4	MV	1.47	1.45	1.47	0.68	1.54	1.36	1.43	6.25
	SD	0.06	0.06	0.06		0.25	0.15	0.11	
Segment 6	MV	1.58	1.48	1.44	4.67	1.56	1.52	1.50	1.96
	SD	0.05	0.06	0.07		0.11	0.08	0.13	
Segment 8	MV	1.53	1.58	1.76	7.41	1.78	1.50	1.61	8.59
	SD	0.13	0.08	0.16		0.25	0.15	0.11	

5.3.1.2 MRE liver measurements

Figure 5.5 presents the acquired MR phase images and the computed q-field for Volunteer 1 along three orthogonal encoding directions using the excitation frequency of 70 Hz. The wave propagation in the liver is still observed, however the wave patterns are not at all regular as those shown in Chapters 3 and 4. The complex *in vivo* conditions are responsible for these wave pattern disturbances. First, the liver geometry is not symmetric and the source position (as shown in Figure 5.5) is oblique to the imaging planes. Second, the size of the liver planes we imaged is not large enough compared to the wave length under the current excitation frequency, which makes it difficult to identify a whole wave length in the obtained images. The limited size also leads to high wave reflection from the boundary which causes wave interferences and hence perturbs the wave propagation patterns. Third, the vessels in the liver can locally distort the wave propagation and hence they are also an important source of these wave pattern disturbances.

Figure 5.6 presents the obtained shear velocity and magnitude of shear complex modulus maps together with the associated quality map. The quality parameter distribution is coherent with the source position: the up left boundary of the liver which is close to the source has higher quality parameters than the far away regions. However the wave reflection may produce other high quality regions such as the down left corner of the liver as shown in the quality map. The V^s map appears smoother than the $|G^*|$ map. Figure 5.7 represents the quality analysis of the V^s and $|G^*|$ values over the $\text{ROI}_{\text{liver}}$

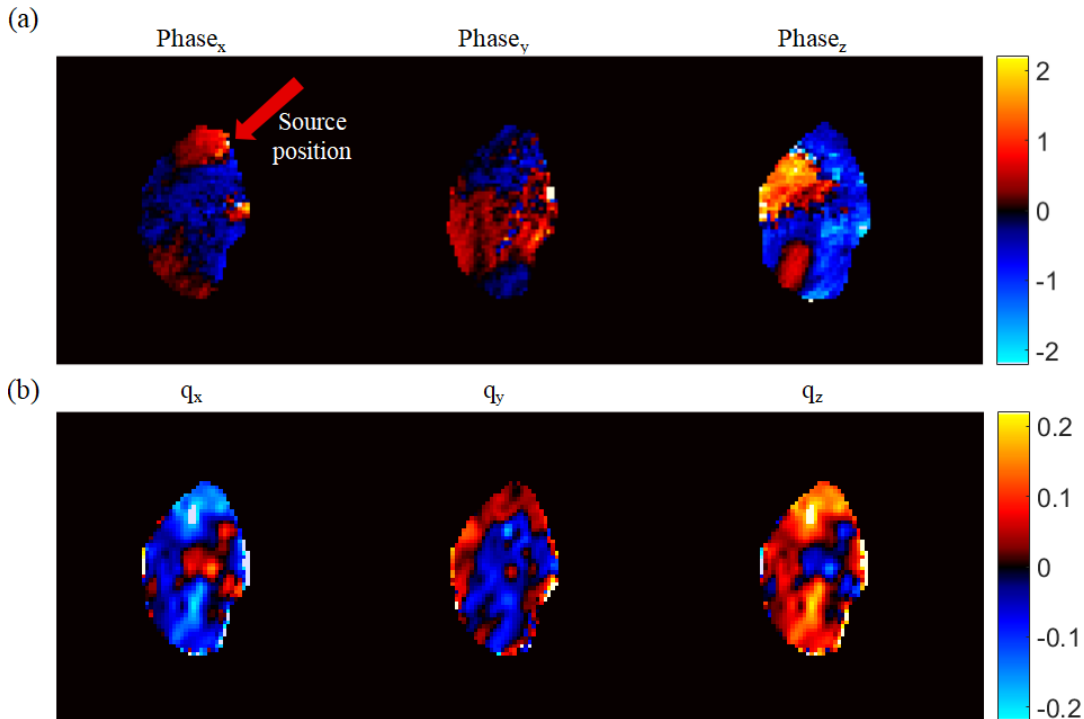


FIGURE 5.5: (a) Acquired MR phase images and (b) Computed q -field along three encoding directions at one time point for Volunteer 1.

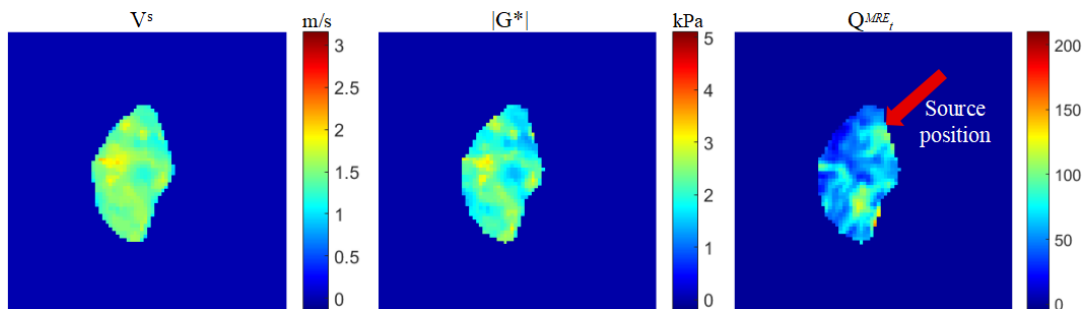


FIGURE 5.6: V^s , $|G^*|$ and associated Q^{MRE}_t maps for Volunteer 1.

of Volunteer 1. The voxel-wise V^s -quality parameter and $|G^*|$ -quality parameter clusters (Figure 5.7 (a)-(b)) show that the measurement precision improves with the Q^{MRE}_t values. Both V^s and $|G^*|$ values tend to converge when Q^{MRE}_t is high enough. Figure 5.7 (c)-(e) illustrate further the evolution of the V^s and $|G^*|$ measurements with the increasing Q^{MRE}_t intervals. It seems that the V^s measurements reach a stable level in both accuracy and precision when Q^{MRE}_t is superior to 60 as indicated in Figure 5.7 (c) and (e). Thus 60 was selected as an empirical $Q^{MRE}_{threshold}$ for the computation of MVs and SDs of the V^s measurements. The $Q^{MRE}_{threshold}$ necessary for the $|G^*|$ measurements to converge was not as evident as that of the V^s measurements. This is due to the fact that $|G^*|$ depends at the same time on the real and imaginary parts of the complex wave number as shown in Chapter 2. The real part of the complex wave number is related to V^s and hence its measurement quality is equal to that of V^s . The imaginary part of the complex wave number reflects the attenuation occurring in the tissue. Although

the viscosity related attenuation can be negligible under the assumption of quasi-elastic media, the attenuation always exists due to the fact that it is difficult to have an ideal local planar wave. However, since the real part is usually largely superior to the imaginary part in normal soft tissue, the measurement quality of $|G^*|$ can be thought to be dominated by that of the real part, namely the measurement quality of V^s . In this context, the same quality threshold of 60 was also applied for the computation of MVs and SDs of the $|G^*|$ measurements.

5.3.1.3 SSI and MRE measurement comparison

Table 5.5 summarizes the MRE and SSI measurements over different regions of interest for Volunteer 1. The SSI measurements of different probes agree well with each other regarding to the mean values except for the $|G^*|$ measurements for the segment 8. This good agreement indicates that the liver of Volunteer 1 can be considered quasi-elastic. The significant discrepancy between the $|G^*|$ measurements for the segment 8 with different probes is probably due to the squaring effect as pointed out in Chapter 2. Normally, healthy liver is considered to be homogeneous and hence the measurements for different segments should be similar between each other. Here, we found the measurements of segment 8 to be higher than those of segments 4 and 6. The main reason for this discrepancy may lie in the fact that the insonification windows placed on segment 8 contain more vascularized regions than those placed on the other segments as shown in the Bmode images of Figure 5.2. The shear wave propagation is thus more easily perturbed leading to the radiologist exerting more pressure on the probe in order to obtain stable images. As a result, the liver may become stiffened.

For MRE measurements, the V^s values calculated on different liver regions are highly consistent, which confirmed the hypothesis of liver homogeneity. In addition, this good measurement agreement across different liver regions also demonstrates the effectiveness of the proposed $Q^{MRE}_{threshold}$ value to guarantee the MRE measurement validity. The consistency of $|G^*|$ measurements between different liver regions is less pronounced than that of V^s measurements because the squaring effect amplifies the $|G^*|$ measurement discrepancy between different regions. We took the mean value of the SSI measurements for segment 4 obtained with the abdominal probe as the final SSI measurement for Volunteer 1, namely $V^s = 1.46$ m/s, $|G^*| = 2.14$ kPa, as this combination of segment and probe produces the best measurement reproducibility and the least spatial variability as shown in Table 5.4. For MRE, we took the MVs of V^s and $|G^*|$ calculated over the ROI_{liver} to compare with the corresponding SSI measurements. The measurement discrepancy between the two modalities is less than 2% for V^s measurements and less than 5% for $|G^*|$ measurements. Considering the measurement precision and reproducibility issue for each modality, this measurement discrepancy can be considered as negligible and thus the quality-guided liver MRE and SSI measurements can be considered to be equivalent for Volunteer 1.

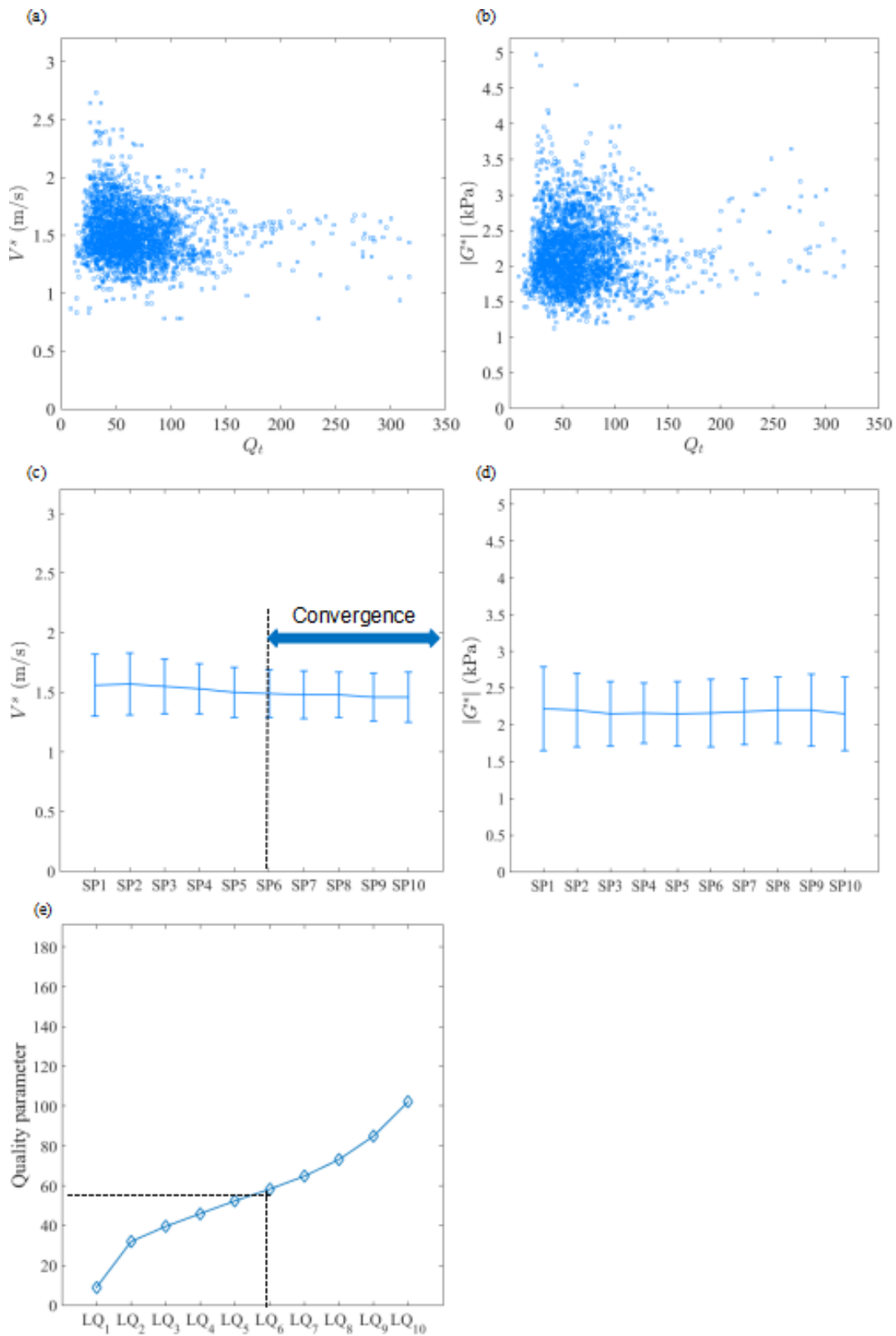


FIGURE 5.7: (a), (b) Voxel-wise V^s and $|G^*|$ values over $\text{ROI}_{\text{liver}}$ as a function of the corresponding quality parameters for Volunteer 1; (c), (d) $\text{MV} \pm \text{SD}$ of V^s and $|G^*|$ values calculated over different sub-population regions of $\text{ROI}_{\text{liver}}$; (e) Quality quantiles of these sub-population regions.

TABLE 5.5: SSI and MRE V^s and $|G^*|$ measurements for Volunteer 1

	SSI								MRE			
	Convex probe				Linear probe				70 Hz			
	V^s (m/s)		$ G^* $ (kPa)		V^s (m/s)		$ G^* $ (kPa)		V^s (m/s)		$ G^* $ (kPa)	
	MV	SD	MV	SD	MV	SD	MV	SD	MV	SD	MV	SD
Segment 4	1.46	0.06	2.14	0.18	1.44	0.17	2.12	0.51	1.48	0.23	2.23	0.47
Segment 6	1.50	0.06	2.27	0.18	1.53	0.11	2.33	0.32	1.49	0.19	2.30	0.48
Segment 8	1.62	0.12	2.32	0.42	1.63	0.23	2.73	0.86	1.49	0.18	2.05	0.44
Whole liver									1.48	0.20	2.19	0.47

5.3.2 Volunteer 2

5.3.2.1 SSI liver measurements

Figure 5.8 and 5.9 present the SSI acquired images and extracted shear velocity/quality maps obtained with the two probes for Volunteer 2. As for Volunteer 1, the shear velocity maps obtained with the XC6-1 probe are more homogeneous than those obtained with the SL10-2 probe. Segment 4 also has a better quality parameter distribution than segment 5. The segment 5 was not successfully characterized by the SL10-2 probe probably because the SLT was too high (about 20 mm) to allow a sufficient penetration of the ultrasound beams and provide a properly color-coded elastogram. Figure 5.10 presents the $MV \pm SD$ of shear velocity values and the quality quantiles for different sub-population regions of segment 4 obtained with different probes for Volunteer 2. We observe similar evolution trend as Volunteer 1 between shear velocity values and the corresponding quality parameters. In general, the measurement precision improves with the quality parameter as expected. A $Q^{SSI}_{threshold}$ value of 0.7 is also found to be sufficient to ensure the validity of the SSI measurements. The overall measurement accuracy, precision and reproducibility for both probes are not as good as those of Volunteer 1 because of the higher SLT value. Table 5.4 summarizes the successive SSI V^s measurements over different regions of interest with two different probes for Volunteer 2. The CV values for MVs between successive SSI measurements are always largely inferior to 30% demonstrating the good reproducibility of SSI measurements. The spatial variability is also much higher for the SL10-2 probe as found for Volunteer 1.

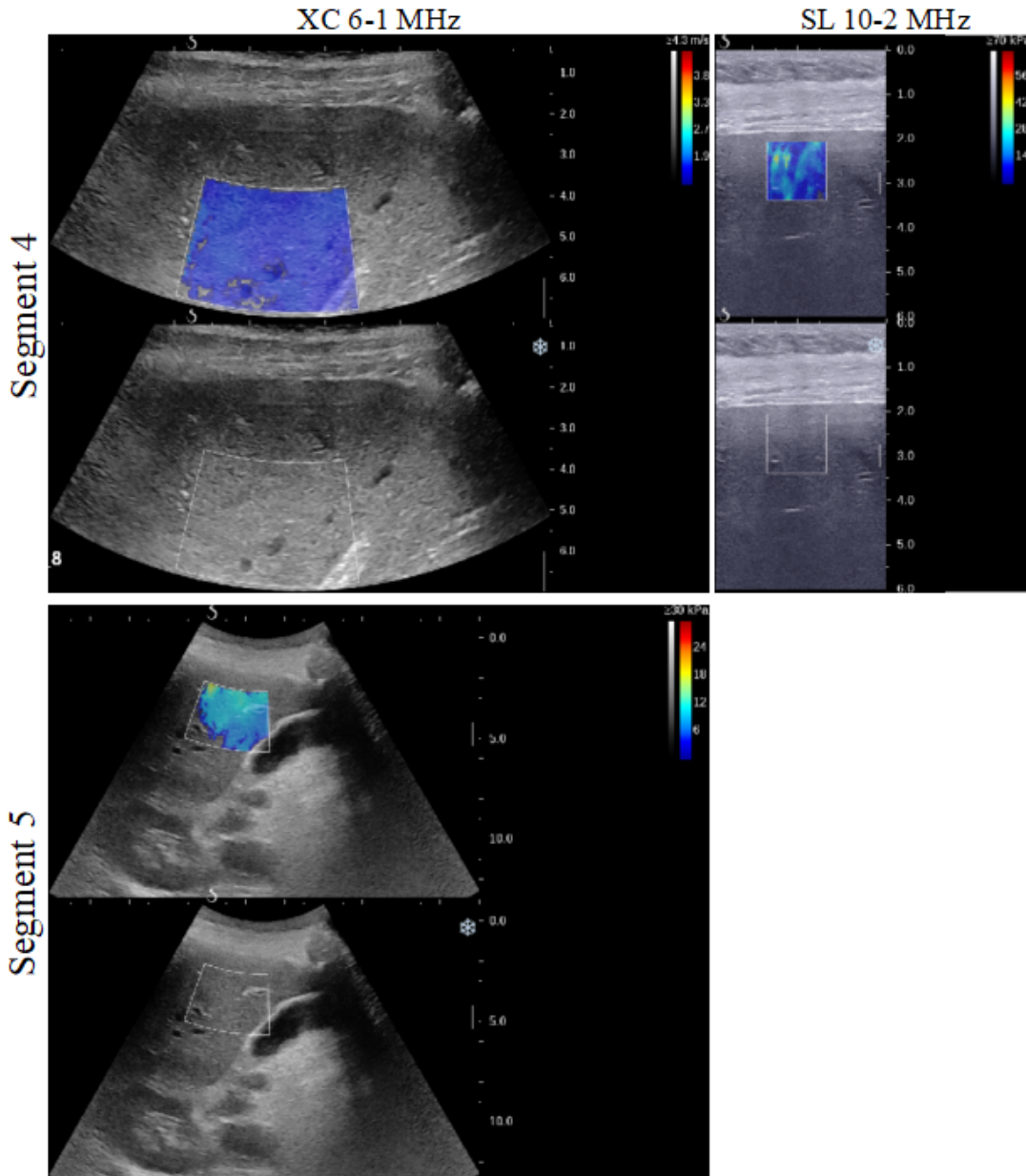


FIGURE 5.8: SSI images for one of the three successive measurements for each segment obtained with the abdominal probe (left column) and the linear probe (right column) for Volunteer 2.

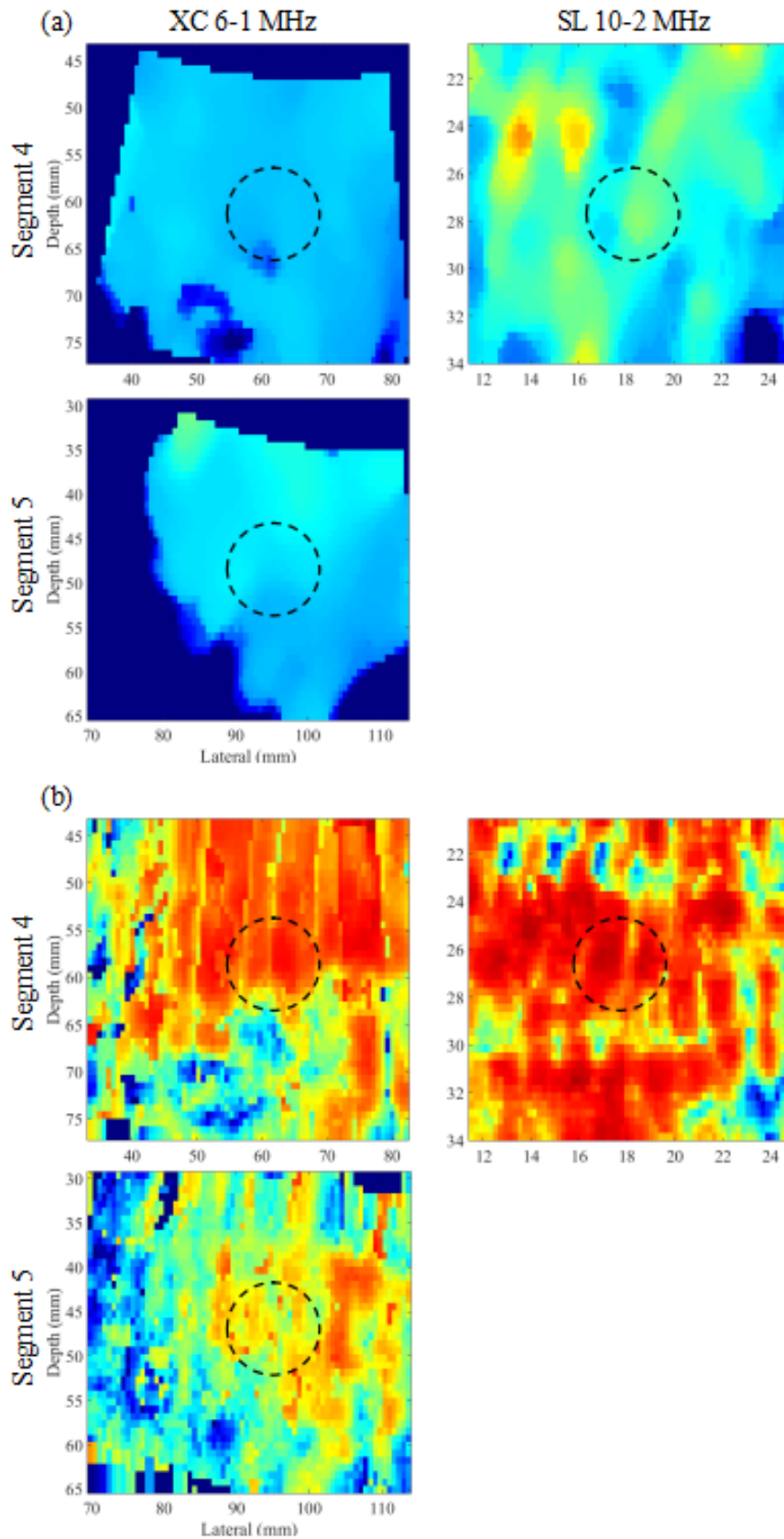


FIGURE 5.9: Extracted shear velocity images (a) together with the associated quality maps (b) for one of the three successive measurements for each segment obtained with the abdominal probe (left column) and linear probe (right column) for Volunteer 2. The dotted black circles represent the regions of interest used for calculating MVs and SDs.

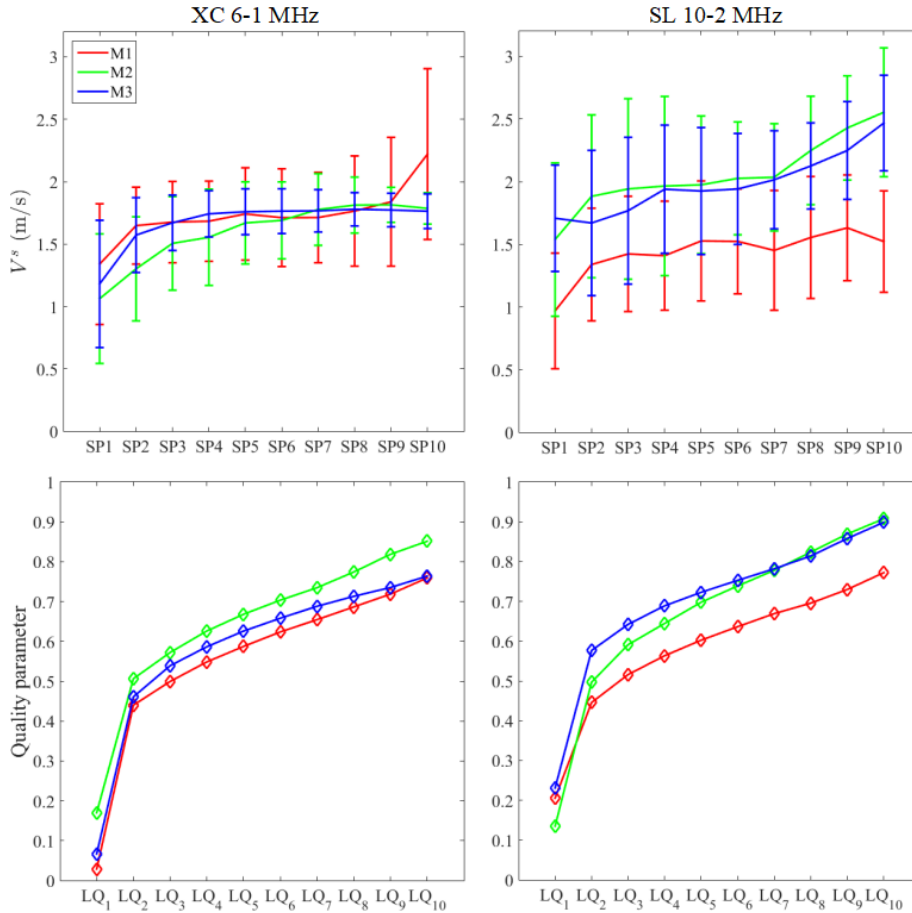


FIGURE 5.10: The first row represents the $MV \pm SD$ of shear velocity values for different sub-population regions of segment 4 obtained with the abdominal probe (left column) and the linear probe (right column) for Volunteer 2; The second row represents the quality quantiles of these regions.

TABLE 5.6: Reproducibility of SSI V^s measurements for Volunteer 2

		Probe XC6-1 MHz				Probe SL10-2 MHz			
		M1	M2	M3	CV	M1	M2	M3	CV
		(m/s)	(m/s)	(m/s)	(%)	(m/s)	(m/s)	(m/s)	(%)
Segment 4	MV	1.78	1.72	1.63	4.68	2.06	2.02	2.20	4.31
	SD	0.18	0.09	0.04		0.46	0.48	0.35	
Segment 5	MV	1.73	1.65	1.70	2.37				
	SD	0.11	0.08	0.09					

5.3.2.2 MRE liver measurements

Figure 5.11 presents the acquired MR phase images and the computed q-field for Volunteer 2 along three orthogonal encoding directions for different excitation frequencies. As for Volunteer 1, it is difficult to observe the regular wave propagation patterns because of the complex *in vivo* conditions. For Volunteer 2, the excitation source was placed close to the right boundary of the liver. We can clearly observe the phase opposition at the near source position for the 85 and 105 Hz data sets as pointed out by the green arrows in

Figure 5.11. The other three frequency data sets were acquired on a different day and the source was thus repositioned. In this new configuration, the phase opposition patterns were not as obvious as in the previous one. In our study, the position of source depends on the liver position during full inspiration observed from the survey scan. The liver position during full inspiration usually varies with individuals and even for a same person the liver position might shift from day to day in the feet-to-head axis. The standardization and reproducibility of the source position is thus a challenge for our excitation system.

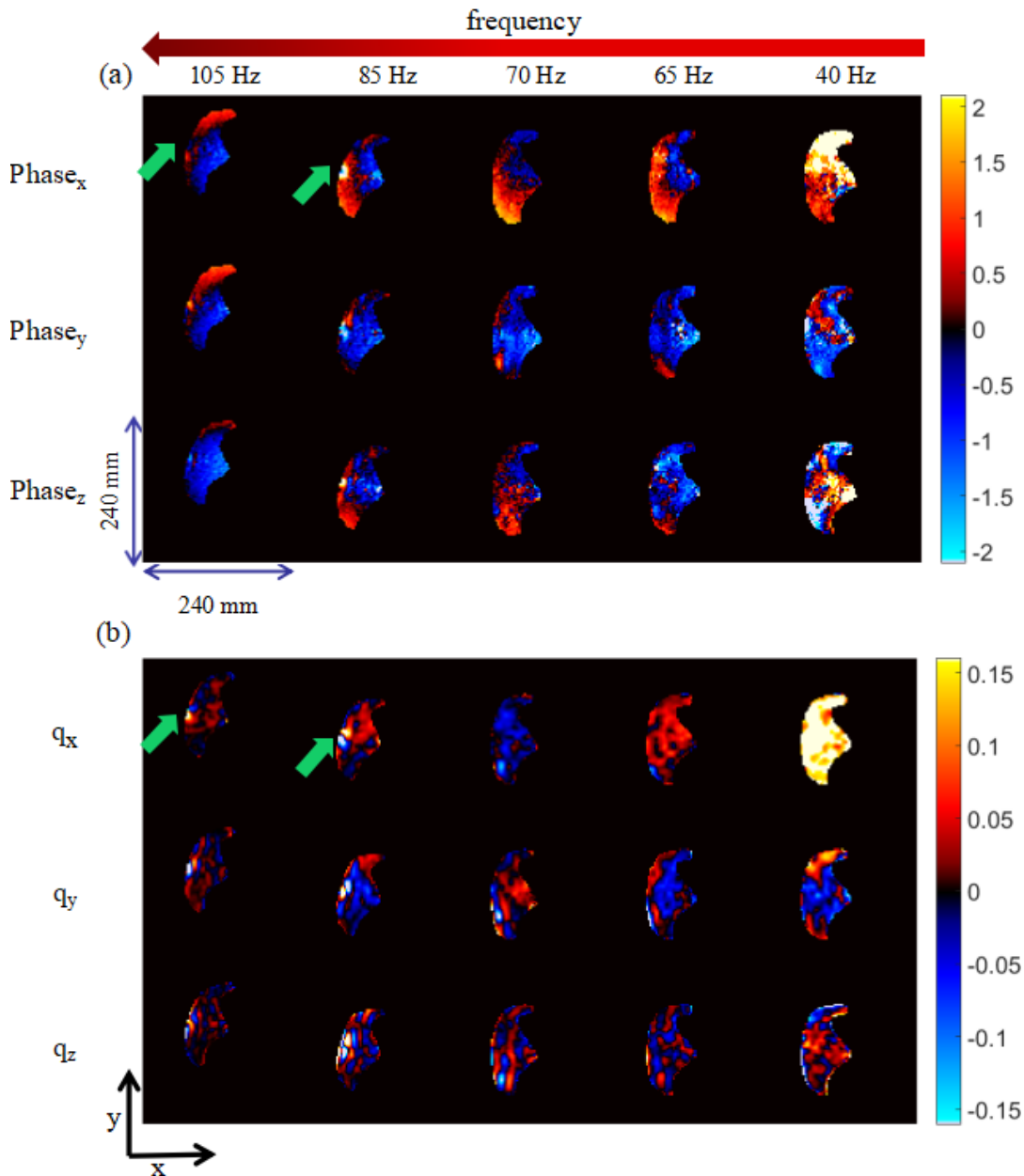


FIGURE 5.11: (a) Acquired MR phase images and (b) Computed q -field along three encoding directions at one time point for Volunteer 2. The green arrows indicate the source position.

Figure 5.12 presents the obtained shear velocity and magnitude of shear complex modulus maps together with the associated quality maps. The quality parameter distribution corresponds well to the source position for the 85 and 105 Hz data sets. The overall quality level tends to decrease when the excitation frequency increases. This decreasing trend is more significant between 40 and 65 Hz data sets. As described in Chapter 3, the quality parameter mainly depends on the wave amplitude and the SNR level. The SNR level in fact tends to increase slightly with the excitation frequency. In this context, the decreasing quality parameters for higher excitation frequency data sets should be mainly due to the viscosity-related attenuation which increases with the excitation frequency. In addition, V^s and $|G^*|$ values present similar increasing trend with the excitation frequency. The reasons for this phenomena can be twofold. First, inappropriate λ/a conditions for MRE reconstruction can lead to this phenomena as shown by the simulation and *in vitro* phantom data in Chapters 3 and 4. Second, there may exist non negligible shear wave dispersion for the liver tissue under investigation as demonstrated by Deffieux in his thesis (Deffieux, 2008).

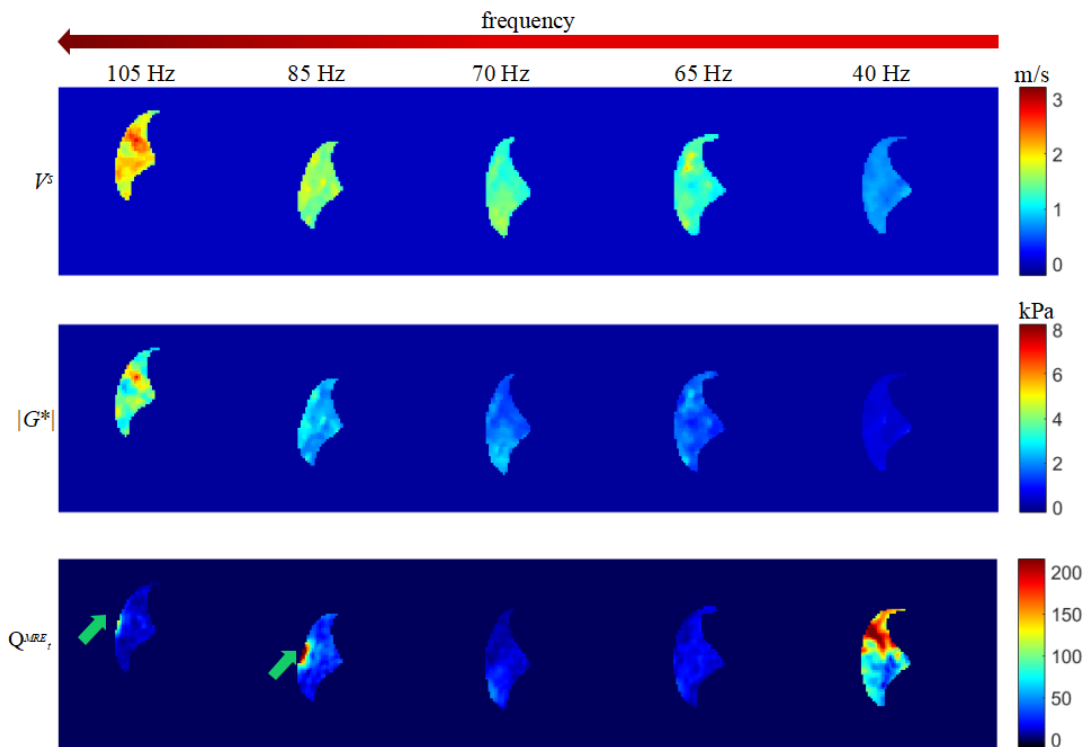


FIGURE 5.12: V^s , $|G^*|$ and associated Q_t maps for Volunteer 2. The green arrows indicate the source position.

Figure 5.13 represents the quality analysis of the V^s and $|G^*|$ values over the $\text{ROI}_{\text{liver}}$ of Volunteer 2. The voxel-wise V^s -quality parameter and $|G^*|$ -quality parameter clusters (Figure 5.13 (a)-(b)) show that V^s and $|G^*|$ converge towards different values for the 40 and 85 Hz data sets when quality parameter Q^{MRE}_t is high enough. For the other three excitation frequencies, quality parameters are not sufficient enough to reach the convergence. Figure 5.13 (c)-(e) further illustrate the evolution of the V^s and $|G^*|$ measurements with

the increasing Q_t^{MRE} intervals. For the 40 Hz data set, a Q_t^{MRE} *threshold* value of 60 also seems to be pertinent to guarantee the measurement convergence as shown for Volunteer 1. Thus 60 was applied for the computation of MVs and SDs of the MRE measurements of the 40 Hz data set. For the other excitation frequency data sets, we did not set a specific quality threshold value. MVs and SDs of V^s and $|G^*|$ were calculated using the 10% voxels that have the best quality parameters on each defined region of interest.

5.3.2.3 SSI and MRE measurement comparison

Table 5.7 and 5.8 summary the MRE and SSI measurements over different regions of interest for Volunteer 2. The SSI measurements of different probes do not agree with each other. The mean value obtained with the SL10-2 probe is significantly higher than that obtained with the XC6-1 probe. This discrepancy is mainly due to the shear wave dispersion induced by the viscosity as described in Chapter 2. The measurements between different segments agree well with each other, supporting the hypothesis of liver homogeneity.

For MRE measurements, the V^s and $|G^*|$ values calculated on different liver regions are highly consistent for the 40 Hz data set, which confirms the hypothesis of liver homogeneity as well as the pertinence of the Q_t^{MRE} *threshold* value. For the other data sets, the 10% best quality parameter range is significantly different among different liver regions and hence the measurement consistency between these regions is degraded. The MVs of V^s and $|G^*|$ calculated over the ROI_{liver} for the 40 and 85 Hz data sets can be considered as valid because the corresponding quality parameters lie within the ranges of convergence shown in Figure 5.13 (a)-(b). The frequency dependence of the V^s and $|G^*|$ measurements in viscoelastic media makes it difficult to compare the SSI broad frequency bandwidth measurements with the MRE simple frequency measurements. In the case of Volunteer 2, the SSI measurements obtained with the XC6-1 probe agree well with the converged MRE measurements at 85 Hz. This might be explained by the fact that the central shear wave frequency generated by the XC6-1 probe is around 85 Hz and hence the obtained shear group velocity is closer to the shear phase velocity corresponding to 85 Hz. However, this correspondence is not generalized because the central shear wave frequency for SSI measurements changes with the probes as well as the imaged objects. In the clinical context, livers often present viscoelastic behavior as the case of Volunteer 2 and hence there exists a non negligible shear wave dispersion effect, especially in advanced fibrosis stages as shown before (Yeh et al., 2015). In this context, frequency specific measurement comparison is essential for cross-validating the measurement of the two modalities.

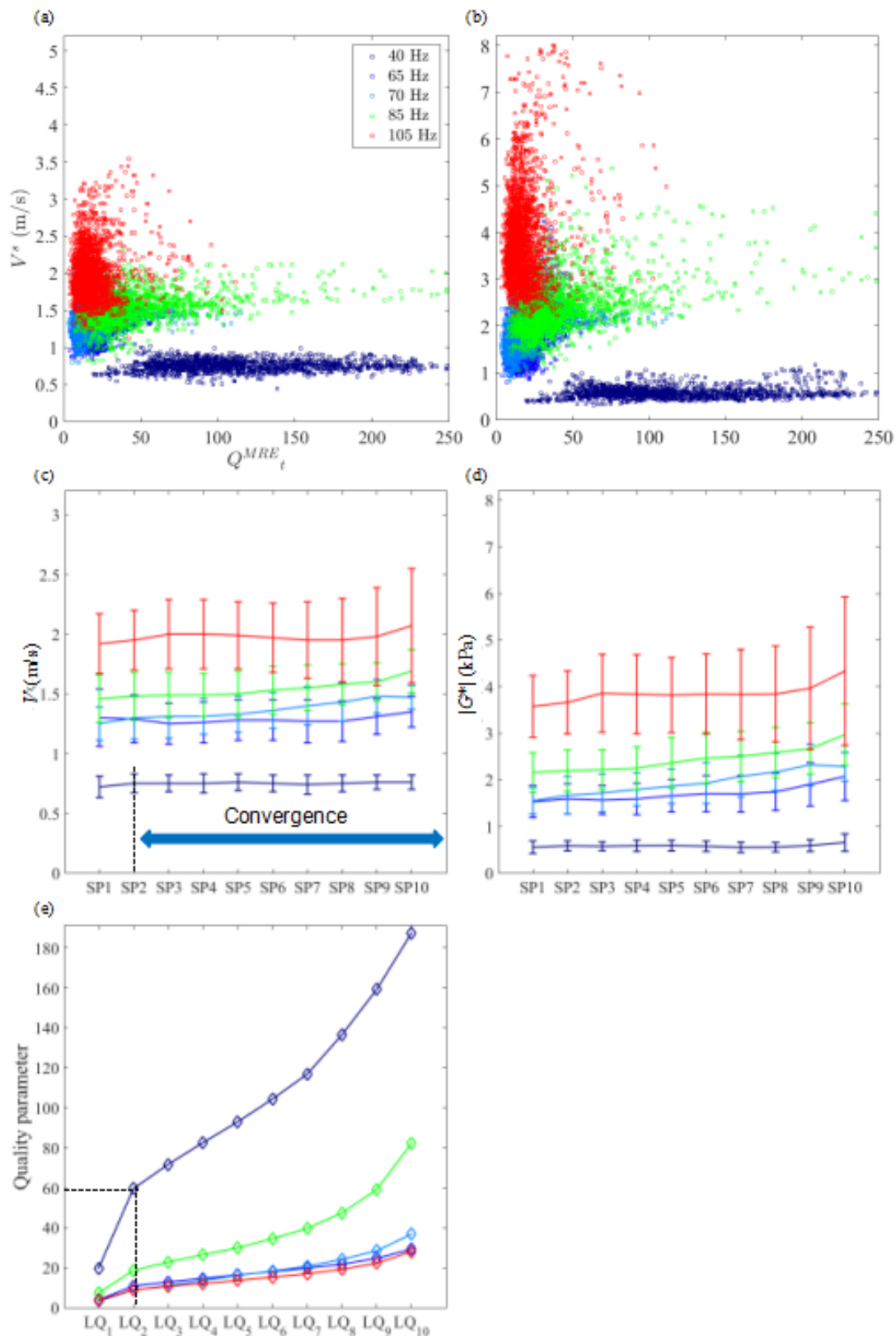


FIGURE 5.13: (a), (b) present the voxel-wise V^s , $|G^*|$ values over the ROI_{liver} of Volunteer 2 as a function of the corresponding quality parameters; (c), (d) present the MV \pm SD of V^s , $|G^*|$ values calculated over different sub-population regions of the ROI_{liver} ; (e) presents the quality quantiles of these sub-population regions.

TABLE 5.7: SSI and MRE V^s measurements for Volunteer 2

	SSI				MRE									
	Convex probe		Linear probe		40 Hz		65 Hz		70 Hz		85 Hz		105 Hz	
	MV	SD	MV	SD	MV	SD	MV	SD	MV	SD	MV	SD	MV	SD
	(m/s)	(m/s)	(m/s)	(m/s)	(m/s)	(m/s)	(m/s)	(m/s)	(m/s)	(m/s)	(m/s)	(m/s)	(m/s)	(m/s)
Segment 4	1.71	0.10	2.09	0.43	0.76	0.06	1.37	0.15	1.47	0.22	1.60	0.12	2.26	0.38
Segment 6	1.69	0.09			0.76	0.08	1.26	0.12	1.43	0.08	1.77	0.18	2.09	0.51
Whole liver					0.75	0.07	1.35	0.13	1.47	0.10	1.69	0.18	2.07	0.48

TABLE 5.8: SSI and MRE $|G^*|$ measurements for Volunteer 2

	SSI				MRE									
	Convex probe		Linear probe		40 Hz		65 Hz		70 Hz		85 Hz		105 Hz	
	MV	SD	MV	SD	MV	SD	MV	SD	MV	SD	MV	SD	MV	SD
	(kPa)	(kPa)	(kPa)	(kPa)	(kPa)	(kPa)	(kPa)	(kPa)	(kPa)	(kPa)	(kPa)	(kPa)	(kPa)	(kPa)
Segment 4	2.95	0.31	4.57	1.81	0.61	0.15	2.56	0.83	2.48	0.76	2.74	0.44	5.00	1.20
Segment 6	2.87	0.31			0.58	0.11	1.77	0.29	2.15	0.28	3.25	0.70	4.37	1.68
Whole liver					0.58	0.12	2.07	0.51	2.28	0.31	2.97	0.66	4.33	1.60

5.4 Conclusions

In our study, we have enrolled two representative healthy volunteers. One volunteer was very lean and had extremely favorable clinical conditions (low BMI, thin SLT) and the other one had less favorable clinical conditions (borderline BMI and SLT) for ultrasound imaging. The SSI measurements are evidently influenced by the clinical conditions. The overall SSI measurement accuracy, precision and reproducibility are better for the volunteer with the most favorable clinical conditions. Although *Chami et al* demonstrated that the high frequency linear probe exhibited better performance than the convex one for unfavorable clinical conditions (*Chami et al., 2016*), this was not the case in our study. This may be due to the fact that we studied the liver segment by segment, whereas *Chami et al* only took one representative measurement for the whole liver in the segment that was most accessible with the given probe. In addition, we found that the segment 4 is always an appropriate region to characterize whatever the chosen probe and the clinical conditions. On the contrary, MRE measurements are less influenced by unfavorable clinical conditions. The high SLT may attenuate the wave amplitude. However this loss can be compensated by choosing lower excitation frequencies and higher levels of source vibration amplitude. One has also to be aware that every patient has different anatomy and respiration patterns which complicates the choice of the source position.

Quality-guided MRE and SSI measurements for livers of these two healthy volunteers have been obtained by incorporating the deduced quality optimization strategies for these two modalities. First, we demonstrated the effectiveness of the proposed quality parameter thresholds for both modalities

to eliminate the unreliable results and hence guarantee the measurement validity. Second, the good agreement between SSI or MRE measurements for different liver segments support the hypothesis of homogeneity for healthy liver. In addition, the SSI measurement comparison between different probes as well as the MRE converged measurement comparison between different excitation frequencies can help to estimate whether the liver tissue under investigation can be considered as quasi-elastic. We found that when the liver is quasi-elastic, the quality-guided shear velocity measurements of the two modalities agree well with each other and hence are interchangeable. This has to be further verified on more healthy cases. In the case of viscoelastic media, both MRE and SSI measurements are frequency dependent. The theoretical difference between the shear group velocity measured by SSI and the shear phase velocity measured by MRE will introduce an important measurement bias between these two modalities. In this case, frequency specific measurements are essential for cross-validating the two modalities.

Conclusions and perspectives

The goal of this work was not to perform a competitive study between MRE and SSI since they both have advantages and disadvantages. MRE can provide viscoelastic properties of large 3D volumes of tissue. MRE is not vulnerable to unfavorable clinical conditions. It can be applicable to patients with obesity, ascites, or narrow intercostal spaces. However, MRE is expensive and has low temporal resolution. On the contrary, SSI is an inexpensive and real-time imaging modality. However, only 2D images in limited local regions can be obtained. Besides, SSI is easily influenced by unfavorable clinical conditions. At this stage, it only provides the measurement of the elastic moduli, although assessment of viscosity should be available in the near future. In this context, MRE and SSI are complementary to each other. The combination of the two modalities will promote the standardization of elastography techniques in clinical applications and ultimately improve the patient care. So the purpose of this work was to establish the conditions for an unbiased comparison between the two modalities and cross-validate the measurements of these two modalities. For achieving this purpose, fundamental studies including methodological developments and experimental comparisons were performed in this work to investigate the validity of MRE and SSI measurements as well as their interchangeability.

First, we have carried out a thorough methodological comparison between MRE and SSI. The two modalities differ from each other in all three elementary steps of elastography. Shear waves generated to excite the tissue differ in their frequency characteristics for the two modalities. Different physical quantities are thus measured by the two modalities, which leads to a potential theoretical bias between MRE and SSI measurements for viscoelastic media. The acquisition and reconstruction processes of each modality determine modality specific uncertainties, which influence the measurement validity. Quality-guided measurements are thus crucial for the validity and interchangeability of the two modalities. In addition, the shear velocity should be estimated for the measurement comparison of the two modalities. Shear modulus or Young's modulus derived from the shear velocity are based on different reconstruction models, which may bring additional measurement biases related to the reconstruction model, squaring and scaling effects. In this frame, the shear velocity parameter should provide a more robust estimation as well as a more pertinent metric for the comparison of the two modalities.

Through a simulation study based on the elastic Green function, we have systematically investigated the influence of acquisition and reconstruction

conditions on the performance of a q-based AIDE method. By using a voxel-wise evaluation criterion, we showed that appropriate spatial sampling of the discrete and noisy displacement fields could improve simultaneously the reconstruction accuracy and precision. This appropriate spatial sampling range can be deduced from *in silico* abaci computed with the study-specific acquisition parameters and reconstruction processes. In addition, we have demonstrated that the interpolation or decimation are effective preprocessing procedures to regulate poorly-defined spatial sampling rates to favorable ranges so as to improve the reconstruction quality. Besides, we have thoroughly compared different shear velocity averaging strategies and identified the quality weighting strategies based on the q-field, the curl of the displacement field \mathbf{u} , and the least square methods as effective strategies to combine the shear velocity measurements along different encoding directions and obtain a more accurate and precise estimation. However, q-field quality based methods are more generally appropriate than least square methods given the potential differences in SNR levels and motion sensitizing levels in the different encoding directions. Finally, we have proposed an effective q-field quality parameter to evaluate the reconstruction quality of different quality weighted shear velocities. All types of shear velocity values converge when the q-field quality parameter is high enough. The q-field quality parameter and the spatial sampling rate of the displacement field should be both optimized in order to more efficiently obtain accurate and precise reconstruction results. In future studies, the established simulation framework will be extended to viscoelastic and anisotropic media, which are closer to the nature of human soft tissue than quasi-elastic and isotropic media, in order to investigate the validity conditions of the q-based AIDE method on reconstructing viscosity and anisotropic mechanical properties.

In vitro and *in vivo* experiments performed in this work validated the proposed strategies for guaranteeing the validity of MRE and SSI measurements and also for minimizing the measurement biases between MRE and SSI. The appropriate spatial sampling range for MRE deduced from *in silico* abaci was proven to be effective to improve the accuracy and precision of real MRE measurement across a large excitation frequency range from tens of Hertz to thousands of Hertz, and different levels of spatial resolution from hundreds of micrometers to several millimeters. Resampling was demonstrated as an effective preprocessing to fulfill appropriate spatial sampling range and thus improve the reconstruction quality. For SSI, the quality parameter provided by the manufacturer was found to be pertinent to eliminate unreliable measurements. The SSI measurement comparison between different probes as well as the MRE converged measurement comparison between different excitation frequencies can serve as a test to verify whether the tissue under investigation can be considered as quasi-elastic. We found that when the tissue is quasi-elastic, the quality-guided MRE and SSI measurements obtained by incorporating the proposed optimization strategies agree well with each other and hence are interchangeable. However, in the case of viscoelastic

media, both MRE and SSI measurements are frequency dependent. The theoretical difference between the shear group velocity measured by SSI and the shear phase velocity measured by MRE will introduce an important measurement bias between these two modalities. In this context, frequency specific measurement comparison is essential for cross-validating the measurements of the two modalities.

The upcoming experimental work will consist of two parts. First, the *in vitro* experiments will be extended to viscoelastic, anisotropic and heterogeneous media in order to demonstrate the validity conditions of MRE deduced from an extensive simulation study and compare the quality-guided MRE and SSI measurements in more realistic media. For viscoelastic media, the shear wave spectroscopy developed by Deffieux in his thesis (Deffieux, 2008) will be exploited to deduce the frequency specific SSI measurements. Second, the *in vivo* frequency specific liver stiffness measurement comparison between MRE and SSI will be carried out on patients with different fibrosis stages in the context of a clinical protocol. In addition, deep inspiration has been shown to increase liver stiffness measurements compared with resting expiratory position (Karlak et al., 2011). Thus the potential influence of different breath-hold instants for MRE and SSI measurements will also be an important topic for discussion.

Publication List

1. Article

JL.Yue, M.Tardieu, F.Julea, T.Boucneau, R.Sinkus, C.Pellot-Barakat and X.Maître. Acquisition and reconstruction conditions *in silico* for accurate and precise magnetic resonance elastography. In: *Physics in Medicine and Biology*, 2017

2. Communication

JL.Yue, F.Julea, T.Boucneau, C.Pellot-Barakat and X.Maître. Magnetic Resonance and Ultrasound Shear Wave Elastography: towards an unbiased comparison. In: *Proceedings of Recherche en Imagerie et Technologies pour la Santé (RITS)*, 2017, Lyon, France

F.Julea, JL.Yue, T.Boucneau, M.Tardieu, B.Larrat, C.Pellot-Barakat and X.Maître. Optimal spatial resolution for accuracy and precision in simulated and experimental micro-MRE at 11.7 T. In: *Proceedings of the 25th Meeting of the International Society of Magnetic Resonance in Medicine (ISMRM)*, 2017, Hawai'i, USA

HC. Wang, C.Sébrié, G.Willoquet, JL.Yue, F.Julea, RM.Dubuisson, S.Judé, A.Maurin and X.Maître. Magnetic Resonance Elastography of Emphysematous Rat Lung *in vivo*. In: *Proceedings of the 25th Meeting of the International Society of Magnetic Resonance in Medicine (ISMRM)*, 2017, Hawai'i, USA

JL.Yue, M.Tardieu, F.Julea, T.Boucneau, C.Pellot-Barakat and X.Maître. Discretization, accuracy, and precision in Magnetic Resonance Elastography reconstruction. In: *Proceedings of the 33th Meeting of the European Society of Magnetic Resonance in Medicine and Biology (ESMRMB)*, 2016, Vienna, Austria

L.Chami, JL.Yue, O.Lucidarme, M.Lefort, Muriel and C.Pellot-Barakat. Feasibility of liver shear wave elastography with different transducers. In: *International Ultrasonics (IUS)*, 2016, Tours, France

JL.Yue, M.Tardieu, F.Julea, C.Pellot-Barakat and X.Maître. MR and Ultrasound Elastography: Phantom comparison study. In: *Proceedings of the 14th Meeting of International Tissue Elasticity Conference (ITEC)*, 2015, Verona, Italy

Bibliography

- Aboumarzouk, Omar M et al. (2012). "Diagnostic accuracy of transrectal elastosonography (TRES) imaging for the diagnosis of prostate cancer: a systematic review and meta-analysis". In: *BJU international* 110.10, pp. 1414–1423.
- Akhtar, Riaz et al. (2011). "Characterizing the elastic properties of tissues". In: *Materials Today* 14.3, pp. 96–105.
- Aki, Keiiti and Paul G Richards (2002). *Quantitative seismology*. Vol. 1.
- Arani, Arvin et al. (2013). "Incorporating endorectal MR elastography into multi-parametric MRI for prostate cancer imaging: Initial feasibility in volunteers". In: *J. Magn. Reson. Imaging* 38.5, pp. 1251–1260.
- Arunachalam, Shivaram P et al. (2016). "Quantitative 3D magnetic resonance elastography: Comparison with dynamic mechanical analysis". In: *Magnetic resonance in medicine*.
- Asbach, Patrick et al. (2008). "Assessment of liver viscoelasticity using multifrequency MR elastography". In: *Magnetic Resonance in Medicine* 60.2, pp. 373–379.
- Athanasiou, Alexandra et al. (2010). "Breast lesions: quantitative elastography with supersonic shear imaging—preliminary results". In: *Radiology* 256.1, pp. 297–303.
- Baghani, Ali, Septimiu Salcudean, and Robert Rohling (2009). "Theoretical limitations of the elastic wave equation inversion for tissue elastography". In: *The Journal of the Acoustical Society of America* 126.3, pp. 1541–1551.
- Barr, Richard G and Amanda E Lackey (2011). "The utility of the "bull's-eye" artifact on breast elasticity imaging in reducing breast lesion biopsy rate". In: *Ultrasound quarterly* 27.3, pp. 151–155.
- Barr, Richard G et al. (2012). "Evaluation of breast lesions using sonographic elasticity imaging". In: *Journal of Ultrasound in Medicine* 31.2, pp. 281–287.
- Bavu, Éric et al. (2011). "Noninvasive in vivo liver fibrosis evaluation using supersonic shear imaging: a clinical study on 113 hepatitis C virus patients". In: *Ultrasound in medicine & biology* 37.9, pp. 1361–1373.
- Bensamoun, Sabine F et al. (2008). "Measurement of liver stiffness with two imaging techniques: magnetic resonance elastography and ultrasound elastometry". In: *Journal of Magnetic Resonance Imaging* 28.5, pp. 1287–1292.
- Bercoff, J et al. (2003). "In vivo breast tumor detection using transient elastography". In: *Ultrasound in medicine & biology* 29.10, pp. 1387–1396.
- Bercoff, Jeremy (2004). "L'imagerie échographique ultrarapide et son application à l'étude de la viscoélasticité du corps humain". PhD thesis. ESPCI ParisTECH.

- Bercoff, Jérémy, Mickael Tanter, and Mathias Fink (2004). "Supersonic shear imaging: a new technique for soft tissue elasticity mapping". In: *IEEE transactions on ultrasonics, ferroelectrics, and frequency control* 51.4, pp. 396–409.
- Berg, Wendie A et al. (2012). "Shear-wave elastography improves the specificity of breast US: the BE1 multinational study of 939 masses". In: *Radiology* 262.2, pp. 435–449.
- Bieri, O et al. (2006). "Balanced alternating steady-state elastography". In: *Magnetic resonance in medicine* 55.2, pp. 233–241.
- Bohte, Anneloes E et al. (2014). "Non-invasive evaluation of liver fibrosis: a comparison of ultrasound-based transient elastography and MR elastography in patients with viral hepatitis B and C". In: *European radiology* 24.3, p. 638.
- Bojunga, Jörg et al. (2010). "Real-time elastography for the differentiation of benign and malignant thyroid nodules: a meta-analysis". In: *Thyroid* 20.10, pp. 1145–1150.
- Braun, Juergen, Karl Braun, and Ingolf Sack (2003). "Electromagnetic actuator for generating variably oriented shear waves in MR elastography". In: *Magnetic resonance in medicine* 50.1, pp. 220–222.
- Brock, Marko et al. (2012). "The impact of real-time elastography guiding a systematic prostate biopsy to improve cancer detection rate: a prospective study of 353 patients". In: *The Journal of urology* 187.6, pp. 2039–2043.
- Brun, Rene and Fons Rademakers (1997). "ROOT—an object oriented data analysis framework". In: *Nuclear Instruments and Methods in Physics Research Section A: Accelerators, Spectrometers, Detectors and Associated Equipment* 389.1-2, pp. 81–86.
- Brusseau, Elisabeth et al. (2008). "2-D locally regularized tissue strain estimation from radio-frequency ultrasound images: Theoretical developments and results on experimental data". In: *IEEE Transactions on Medical Imaging* 27.2, pp. 145–160.
- Carr, Herman Y and Edward M Purcell (1954). "Effects of diffusion on free precession in nuclear magnetic resonance experiments". In: *Physical review* 94.3, p. 630.
- Catheline, Stefan (1998). "Interférométrie-Speckle ultrasonore: Application à la mesure d'élasticité". PhD thesis. Université Paris-Diderot-Paris VII.
- Chami, Linda et al. (2016). "Feasibility of liver shear wave elastography with different transducers". In: *Ultrasonics Symposium (IUS), 2016 IEEE International*. IEEE, pp. 1–4.
- Chan, QCC et al. (2006). "Needle shear wave driver for magnetic resonance elastography". In: *Magnetic resonance in medicine* 55.5, pp. 1175–1179.
- Chen, Shigao, Mostafa Fatemi, and James F Greenleaf (2004). "Quantifying elasticity and viscosity from measurement of shear wave speed dispersion". In: *The Journal of the Acoustical Society of America* 115.6, pp. 2781–2785.
- Cho, Nariya et al. (2011). "Aliasing artifact depicted on ultrasound (US)-elastography for breast cystic lesions mimicking solid masses". In: *Acta Radiologica* 52.1, pp. 3–7.

- Chon, Young Eun et al. (2012). "Performance of transient elastography for the staging of liver fibrosis in patients with chronic hepatitis B: a meta-analysis". In: *PloS one* 7.9, e44930.
- Corbin, Nadège et al. (2015). "Interventional MR elastography for MRI-guided percutaneous procedures". In: *Magnetic Resonance in Medicine*.
- Correas, JM et al. (2011). "Trans-rectal quantitative shear wave elastography: application to prostate cancer—a feasibility study". In: *Proceedings of the European Congress of Radiology*. Vol. 10.
- Cosgrove, D et al. (2013). "EFSUMB guidelines and recommendations on the clinical use of ultrasound elastography. Part 2: Clinical applications". In: *Ultraschall in der Medizin-European Journal of Ultrasound* 34.03, pp. 238–253.
- Curiel, L et al. (2005). "Elastography for the follow-up of high-intensity focused ultrasound prostate cancer treatment: initial comparison with MRI". In: *Ultrasound in medicine & biology* 31.11, pp. 1461–1468.
- De Zordo, T et al. (2010). "Real-time sonoelastography: findings in patients with symptomatic achilles tendons and comparison to healthy volunteers". In: *Ultraschall in der Medizin-European Journal of Ultrasound* 31.04, pp. 394–400.
- Deffieux, Thomas (2008). "Palpation par force de radiation ultrasonore et échographie ultrarapide: Applications à la caractérisation tissulaire in vivo." PhD thesis. Université Paris-Diderot-Paris VII.
- Deffieux, Thomas et al. (2015). "Investigating liver stiffness and viscosity for fibrosis, steatosis and activity staging using shear wave elastography". In: *Journal of hepatology* 62.2, pp. 317–324.
- Doyley, Marvin M et al. (2001). "A freehand elastographic imaging approach for clinical breast imaging: system development and performance evaluation". In: *Ultrasound in medicine & biology* 27.10, pp. 1347–1357.
- Fatemi, Mostafa and James F Greenleaf (1999). "Vibro-acoustography: An imaging modality based on ultrasound-stimulated acoustic emission". In: *Proceedings of the National Academy of Sciences* 96.12, pp. 6603–6608.
- Fehlner, Andreas et al. (2015). "Higher-resolution MR elastography reveals early mechanical signatures of neuroinflammation in patients with clinically isolated syndrome". In: *Journal of Magnetic Resonance Imaging*.
- Ferraioli, Giovanna et al. (2012). "Accuracy of real-time shear wave elastography for assessing liver fibrosis in chronic hepatitis C: A pilot study". In: *Hepatology* 56.6, pp. 2125–2133.
- Fowlkes, JB et al. (1995). "Magnetic-resonance imaging techniques for detection of elasticity variation". In: *Medical physics* 22.11, pp. 1771–1778.
- Garteiser, P et al. (2011). "Physical boundary conditions reconstruction: a novel method to determine viscoelastic parameters from magnetic resonance elastography data". In: *Proceedings of the International Society for Magnetic Resonance in Medicine*.
- Garteiser, Philippe et al. (2013). "Rapid acquisition of multifrequency, multislice and multidirectional MR elastography data with a fractionally encoded gradient echo sequence". In: *NMR Biomed.* 26.10, pp. 1326–1335.

- Gennisson, Jean-Luc (2003). "Le palpeur acoustique: un nouvel outils d'investigation des tissus biologiques". PhD thesis. Université Pierre et Marie Curie-Paris VI.
- Golub, Gene H and Charles F Van Loan (1980). "An analysis of the total least squares problem". In: *SIAM Journal on Numerical Analysis* 17.6, pp. 883–893.
- Hall, Timothy J, Yanning Zhu, and Candace S Spalding (2003). "In vivo real-time freehand palpation imaging". In: *Ultrasound in medicine & biology* 29.3, pp. 427–435.
- Hall, Timothy J et al. (2013). "RSNA/QIBA: Shear wave speed as a biomarker for liver fibrosis staging". In: *Ultrasonics Symposium (IUS), 2013 IEEE International*. IEEE, pp. 397–400.
- Hardy, Peter A et al. (2005). "Imaging articular cartilage under compression—cartilage elastography". In: *Magnetic resonance in medicine* 53.5, pp. 1065–1073.
- Hiltawsky, Karsten Mark et al. (2001). "Freehand ultrasound elastography of breast lesions: clinical results". In: *Ultrasound in medicine & biology* 27.11, pp. 1461–1469.
- Hirsch, Sebastian et al. (2014). "MR Elastography of the Liver and the Spleen Using a Piezoelectric Driver, Single-Shot Wave-Field Acquisition, and Multifrequency Dual Parameter Reconstruction". In: *Magnetic resonance in medicine* 71.1, pp. 267–277.
- Huang, Zeping et al. (2014). "Normal liver stiffness in healthy adults assessed by real-time shear wave elastography and factors that influence this method". In: *Ultrasound in medicine & biology* 40.11, pp. 2549–2555.
- Huwart, Laurent et al. (2006). "Liver fibrosis: non-invasive assessment with MR elastography". In: *NMR in Biomedicine* 19.2, pp. 173–179.
- Huwart, Laurent et al. (2007). "Liver fibrosis: noninvasive assessment with MR elastography versus aspartate aminotransferase-to-platelet ratio index". In: *Radiology* 245.2, pp. 458–466.
- Huwart, Laurent et al. (2008a). "Magnetic resonance elastography for the noninvasive staging of liver fibrosis". In: *Gastroenterology* 135.1, pp. 32–40.
- Huwart, Laurent et al. (2008b). "MR elastography of liver fibrosis: preliminary results comparing spin-echo and echo-planar imaging". In: *European radiology* 18.11, pp. 2535–2541.
- Itoh, Ako et al. (2006). "Breast disease: clinical application of US elastography for diagnosis". In: *Radiology* 239.2, pp. 341–350.
- Karlas, Thomas et al. (2011). "Acoustic radiation force impulse imaging (ARFI) for non-invasive detection of liver fibrosis: examination standards and evaluation of interlobe differences in healthy subjects and chronic liver disease". In: *Scandinavian journal of gastroenterology* 46.12, pp. 1458–1467.
- Klatt, Dieter et al. (2007). "Noninvasive assessment of the rheological behavior of human organs using multifrequency MR elastography: a study of brain and liver viscoelasticity". In: *Physics in medicine and biology* 52.24, p. 7281.

- Klauser, Andrea S et al. (2013). "Achilles tendon assessed with sonoelastography: histologic agreement". In: *Radiology* 267.3, pp. 837–842.
- Krouskop, TA, DR Dougherty, FS Vinson, et al. (1987). "A pulsed Doppler ultrasonic system for making noninvasive measurements of the mechanical properties of soft tissue". In: *J Rehabil Res Dev* 24.2, pp. 1–8.
- Larrat, Benoît et al. (2009). "MR-guided transcranial brain HIFU in small animal models". In: *Physics in medicine and biology* 55.2, p. 365.
- Latorre Ossa, Heldmuth (2012). "In vivo monitoring of elastic changes during cancer development and therapeutic treatment". PhD thesis. Paris 7.
- Lerner, Robert M, SR Huang, and Kevin J Parker (1990). "Sonoelasticity" images derived from ultrasound signals in mechanically vibrated tissues". In: *Ultrasound in medicine & biology* 16.3, pp. 231–239.
- Leung, Vivian Yee-fong et al. (2013). "Quantitative elastography of liver fibrosis and spleen stiffness in chronic hepatitis B carriers: comparison of shear-wave elastography and transient elastography with liver biopsy correlation". In: *Radiology* 269.3, pp. 910–918.
- Liver, European Association for Study of et al. (2014). "EASL Clinical Practice Guidelines: management of hepatitis C virus infection." In: *Journal of Hepatology* 60.2, p. 392.
- Lyshchik, Andrej et al. (2005). "Thyroid gland tumor diagnosis at US elastography". In: *Radiology* 237.1, pp. 202–211.
- Maître, X et al. (2011). "Whole brain MRE with guided pressure waves". In: *Proceedings of the 19th Meeting of the International Society of Magnetic Resonance in Medicine (Montréal)*. Vol. 2560.
- Manduca, Armando et al. (1996). "Image processing for magnetic-resonance elastography". In: *Medical Imaging 1996*. International Society for Optics and Photonics, pp. 616–623.
- Manduca, Armando et al. (2001). "Magnetic resonance elastography: non-invasive mapping of tissue elasticity". In: *Medical image analysis* 5.4, pp. 237–254.
- Manduca, Armando et al. (2003). "Spatio-temporal directional filtering for improved inversion of MR elastography images". In: *Medical image analysis* 7.4, pp. 465–473.
- Mariappan, Yogesh K, Kevin J Glaser, and Richard L Ehman (2010). "Magnetic resonance elastography: a review". In: *Clinical anatomy* 23.5, pp. 497–511.
- Mariappan, Yogesh K et al. (2009). "High-frequency mode conversion technique for stiff lesion detection with magnetic resonance elastography (MRE)". In: *Magnetic resonance in medicine* 62.6, pp. 1457–1465.
- McGarry, MDJ et al. (2011). "An octahedral shear strain-based measure of SNR for 3D MR elastography". In: *Physics in medicine and biology* 56.13, N153.
- McGee, Kieran Patrick et al. (2011). "Calculation of shear stiffness in noise dominated magnetic resonance elastography data based on principal frequency estimation". In: *Physics in medicine and biology* 56.14, p. 4291.

- McGrath, Deirdre M et al. (2016). "Evaluation of wave delivery methodology for brain MRE: Insights from computational simulations". In: *Magnetic Resonance in Medicine*.
- Muthupillai, R et al. (1995). "Magnetic resonance elastography by direct visualization of propagating acoustic strain waves". In: *Science* 269.5232, pp. 1854–1857.
- Nightingale, Kathryn, Rex Bentley, and Gregg Trahey (2002). "Observations of tissue response to acoustic radiation force: opportunities for imaging". In: *Ultrasonic imaging* 24.3, pp. 129–138.
- O'Donnell, Matthew et al. (1994). "Internal displacement and strain imaging using ultrasonic speckle tracking". In: *IEEE transactions on ultrasonics, ferroelectrics, and frequency control* 41.3, pp. 314–325.
- Okamoto, RJ, EH Clayton, and PV Bayly (2011). "Viscoelastic properties of soft gels: comparison of magnetic resonance elastography and dynamic shear testing in the shear wave regime". In: *Physics in medicine and biology* 56.19, p. 6379.
- Oliphant, Travis E et al. (2001). "Complex-valued stiffness reconstruction for magnetic resonance elastography by algebraic inversion of the differential equation". In: *Magnetic resonance in Medicine* 45.2, pp. 299–310.
- Ophir, Jonathan et al. (1991). "Elastography: a quantitative method for imaging the elasticity of biological tissues". In: *Ultrasonic imaging* 13.2, pp. 111–134.
- Othman, Shadi F et al. (2005). "Microscopic magnetic resonance elastography (μ MRE)". In: *Magnetic resonance in medicine* 54.3, pp. 605–615.
- Oudry, Jennifer et al. (2009a). "Cross-validation of magnetic resonance elastography and ultrasound-based transient elastography: A preliminary phantom study". In: *J. Magn. Reson. Imaging* 30.5, pp. 1145–1150.
- Oudry, Jennifer et al. (2009b). "Ultrasound-based transient elastography compared to magnetic resonance elastography in soft tissue-mimicking gels". In: *Physics in medicine and biology* 54.22, p. 6979.
- Oudry, Jennifer et al. (2014). "Comparison of four different techniques to evaluate the elastic properties of phantom in elastography: is there a gold standard?" In: *Physics in medicine and biology* 59.19, p. 5775.
- Palmeri, Mark L and Kathryn R Nightingale (2011). "Acoustic radiation force-based elasticity imaging methods". In: *Interface Focus*, rfs20110023.
- Papazoglou, S et al. (2008). "Algebraic Helmholtz inversion in planar magnetic resonance elastography". In: *Physics in medicine and biology* 53.12, p. 3147.
- Parker, Kevin J, Marvin M Doyley, and Deborah J Rubens (2010). "Imaging the elastic properties of tissue: the 20 year perspective". In: *Physics in medicine and biology* 56.1, R1.
- Plewes, DB et al. (1995). "Visualizing tissue compliance with MR imaging". In: *Journal of Magnetic Resonance Imaging* 5.6, pp. 733–738.
- Ringleb, Stacie I et al. (2007). "Applications of magnetic resonance elastography to healthy and pathologic skeletal muscle". In: *Journal of Magnetic Resonance Imaging* 25.2, pp. 301–309.

- Romano, Anthony et al. (2014). "In vivo waveguide elastography: effects of neurodegeneration in patients with amyotrophic lateral sclerosis". In: *Magnetic resonance in medicine* 72.6, pp. 1755–1761.
- Rossmann, Philip J, Raja Muthupillai, and Richard L Ehman (1999). *Driver device for MR elastography*. US Patent 5,952,828.
- Rouvière, Olivier et al. (2011). "Magnetic resonance elastography of the kidneys: feasibility and reproducibility in young healthy adults". In: *Journal of Magnetic Resonance Imaging* 34.4, pp. 880–886.
- Rump, Jens et al. (2007). "Fractional encoding of harmonic motions in MR elastography". In: *Magn. Reson. Med.* 57.2, pp. 388–395.
- Sahebjavaher, Ramin S et al. (2015). "MR elastography of prostate cancer: quantitative comparison with histopathology and repeatability of methods". In: *NMR Biomed.* 28.1, pp. 124–139.
- Salameh, N et al. (2009). "Early detection of steatohepatitis in fatty rat liver by using MR elastography." In: *Radiology* 253.1, pp. 90–97.
- Salomon, Georg et al. (2008). "Evaluation of prostate cancer detection with ultrasound real-time elastography: a comparison with step section pathological analysis after radical prostatectomy". In: *European urology* 54.6, pp. 1354–1362.
- Sandrin, Laurent et al. (2002). "Shear modulus imaging with 2-D transient elastography". In: *IEEE transactions on ultrasonics, ferroelectrics, and frequency control* 49.4, pp. 426–435.
- Sandrin, Laurent et al. (2003). "Transient elastography: a new noninvasive method for assessment of hepatic fibrosis". In: *Ultrasound in medicine & biology* 29.12, pp. 1705–1713.
- Sarvazyan, Armen P et al. (1998). "Shear wave elasticity imaging: a new ultrasonic technology of medical diagnostics". In: *Ultrasound in medicine & biology* 24.9, pp. 1419–1435.
- Sato, Takuso et al. (1985). "Nonlinear parameter tomography system using counterpropagating probe and pump waves". In: *Ultrasonic Imaging* 7.1, pp. 49–59.
- Sebag, F et al. (2010). "Shear wave elastography: a new ultrasound imaging mode for the differential diagnosis of benign and malignant thyroid nodules". In: *The Journal of Clinical Endocrinology & Metabolism* 95.12, pp. 5281–5288.
- Shattuck, David P et al. (1984). "Explososcan: A parallel processing technique for high speed ultrasound imaging with linear phased arrays". In: *The Journal of the Acoustical Society of America* 75.4, pp. 1273–1282.
- Shiina, Tsuyoshi et al. (2002). "Real time tissue elasticity imaging using the combined autocorrelation method". In: *Journal of Medical Ultrasonics* 29.3, pp. 119–128.
- Silva, G (2003). "Image formation in vibro-acoustography". In: *Mayo Clinic*.
- Singh, Siddharth et al. (2016). "Magnetic resonance elastography for staging liver fibrosis in non-alcoholic fatty liver disease: a diagnostic accuracy systematic review and individual participant data pooled analysis". In: *European radiology* 26.5, pp. 1431–1440.

- Sinkus, R et al. (2000). "High-resolution tensor MR elastography for breast tumour detection". In: *Phys. Med. Biol.* 45.6, p. 1649.
- Sinkus, Ralph et al. (2005). "Viscoelastic shear properties of in vivo breast lesions measured by MR elastography". In: *Magnetic resonance imaging* 23.2, pp. 159–165.
- Sinkus, Ralph et al. (2007). "MR elastography of breast lesions: understanding the solid/liquid duality can improve the specificity of contrast-enhanced MR mammography". In: *Magnetic Resonance in Medicine* 58.6, pp. 1135–1144.
- Souchon, Rémi et al. (2003). "Visualisation of HIFU lesions using elastography of the human prostate in vivo: preliminary results". In: *Ultrasound in medicine & biology* 29.7, pp. 1007–1015.
- Stebbing, Justin et al. (2010). "A meta-analysis of transient elastography for the detection of hepatic fibrosis". In: *Journal of clinical gastroenterology* 44.3, pp. 214–219.
- Talwalkar, Jayant A et al. (2007). "Ultrasound-based transient elastography for the detection of hepatic fibrosis: systematic review and meta-analysis". In: *Clinical gastroenterology and hepatology* 5.10, pp. 1214–1220.
- Tang, An et al. (2015). "Ultrasound elastography and MR elastography for assessing liver fibrosis: part 2, diagnostic performance, confounders, and future directions". In: *American journal of roentgenology* 205.1, pp. 33–40.
- Tardieu, Marion (2014). "Élastographie par résonance magnétique et onde de pression guidée". PhD thesis. Université Paris Sud-Paris XI.
- Tse, Zion Tsz Ho et al. (2011). "Piezoelectric actuator design for MR elastography: implementation and vibration issues". In: *The International Journal of Medical Robotics and Computer Assisted Surgery* 7.3, pp. 353–360.
- Tse, ZTH et al. (2009). "Magnetic resonance elastography hardware design: a survey". In: *Proceedings of the Institution of Mechanical Engineers, Part H: Journal of Engineering in Medicine* 223.4, pp. 497–514.
- Uffmann, Kai et al. (2002). "Design of an MR-compatible piezoelectric actuator for MR elastography". In: *Concepts in Magnetic Resonance Part A* 15.4, pp. 239–254.
- Uffmann, Kai et al. (2004). "In vivo elasticity measurements of extremity skeletal muscle with MR elastography". In: *NMR in Biomedicine* 17.4, pp. 181–190.
- Urban, M, J Chen, and R Ehman (2017). "Comparison Of Shear Velocity Dispersion in Viscoelastic Phantoms Measured by UltrasoundBased Shear Wave Elastography and Magnetic Resonance Elastography". In: *2017 IEEE International Ultrasonics Symposium (IUS)*.
- Van Houten, Elijah EW et al. (2001). "Three-dimensional subzone-based reconstruction algorithm for MR elastography". In: *Magnetic Resonance in Medicine* 45.5, pp. 827–837.
- Varbobitis, Ioannis C et al. (2016). "Reliability and applicability of two-dimensional shear-wave elastography for the evaluation of liver stiffness". In: *European journal of gastroenterology & hepatology* 28.10, pp. 1204–1209.
- Varghese, Tomy and Jonathan Ophir (1997). "A theoretical framework for performance characterization of elastography: The strain filter". In: *IEEE*

- Transactions on Ultrasonics, Ferroelectrics, and Frequency Control* 44.1, pp. 164–172.
- Venkatesh, SK et al. (2011). “Comparison of liver stiffness with MRE and fibrosis quantification with Fibro-C index in chronic hepatitis B patients”. In: *Proceedings of the 19th Annual Meeting of ISMRM*, p. 2934.
- Venkatesh, Sudhakar K, Meng Yin, and Richard L Ehman (2013). “Magnetic resonance elastography of liver: clinical applications”. In: *Journal of computer assisted tomography* 37.6, p. 887.
- Walker, WF et al. (1991). “Real-time imaging of tissue vibration using a two-dimensional speckle tracking system”. In: *Ultrasonics Symposium*. Vol. 2. 1, pp. 873–873.
- Walz, Jochen et al. (2011). “Identification of the prostate cancer index lesion by real-time elastography: considerations for focal therapy of prostate cancer”. In: *World journal of urology* 29.5, pp. 589–594.
- Wojcinski, S et al. (2010). “Multicenter study of ultrasound real-time tissue elastography in 779 cases for the assessment of breast lesions: improved diagnostic performance by combining the BI-RADS®-US classification system with sonoelastography”. In: *Ultraschall in der Medizin-European Journal of Ultrasound* 31.05, pp. 484–491.
- Xie, Hua et al. (2012). “A phantom study to cross-validate multimodality shear wave elastography techniques”. In: *Ultrasonics Symposium (IUS), 2012 IEEE International*. IEEE, pp. 1858–1861.
- Yasar, Temel K, Thomas J Royston, and Richard L Magin (2013). “Wideband MR elastography for viscoelasticity model identification”. In: *Magnetic resonance in medicine* 70.2, pp. 479–489.
- Yeh, Chia-Lun et al. (2015). “Shear-wave elasticity imaging of a liver fibrosis mouse model using high-frequency ultrasound”. In: *IEEE transactions on ultrasonics, ferroelectrics, and frequency control* 62.7, pp. 1295–1307.
- Yin, Meng and Sudhakar K Venkatesh (2017). “Ultrasound or MR elastography of liver: which one shall I use?” In: *Abdominal Radiology*, pp. 1–6.
- Yin, Meng et al. (2007). “Assessment of hepatic fibrosis with magnetic resonance elastography”. In: *Clinical Gastroenterology and Hepatology* 5.10, pp. 1207–1213.
- Yin, Meng et al. (2015). “Hepatic MR elastography: clinical performance in a series of 1377 consecutive examinations”. In: *Radiology* 278.1, pp. 114–124.
- Yoon, Jeong Hee et al. (2013). “Staging of hepatic fibrosis: comparison of magnetic resonance elastography and shear wave elastography in the same individuals”. In: *Korean Journal of Radiology* 14.2, pp. 202–212.
- Zhang, Jiming et al. (2015). “Short-Term Repeatability of Magnetic Resonance Elastography at 3.0 T: Effects of Motion-Encoding Gradient Direction, Slice Position, and Meal Ingestion”. In: *Journal of Magnetic Resonance Imaging*.

Titre : L'élastographie par résonance magnétique et l'élastographie ultrasonore par ondes de cisaillement supersonic: simulation, comparaison expérimentale et l'application pour la caractérisation du foie

Mots clés : élastographie, IRM, ultrason, simulation, reconstruction

Résumé : L'élastographie est une modalité d'imagerie médicale émergente qui permet de mesurer les propriétés mécaniques des tissus mous humains. Ces mesures peuvent servir de biomarqueurs pour l'amélioration de la prise en charge des maladies, du diagnostic précoce et de l'évaluation de la sévérité, au suivi de la réponse au traitement. Parmi les différentes approches de l'élastographie, l'élastographie par Résonance Magnétique (ERM) et l'élastographie ultrasonore par ondes de cisaillement (Supersonic Shear Imaging (SSI)) suscitent des intérêts particuliers. Ces deux modalités ont été largement étudiées pour des applications cliniques multiples. Toutefois, chaque modalité repose sur des conditions d'acquisition et de reconstruction différentes et caractérisées par leur propres limites qui peuvent induire des biais de mesure intra-et inter-modalité et donc entraver l'interchangeabilité des deux modalités pour des applications cliniques.

Dans un premier temps, ma thèse a porté sur l'identification des biais de mesure entre ERM et SSI. Grâce à une comparaison méthodologique approfondie des deux modalités, nous avons identifié les différentes caractéristiques de fréquence des ondes de cisaillement générées par les deux modalités et les contraintes spécifiques de reconstruction, en particulier en ERM, comme les principales sources de biais de mesure entre les deux modalités. Dans un deuxième temps, une étude de simulation a été effectuée afin de caractériser l'influence des conditions d'acquisition et de reconstruction sur l'exactitude et la précision des mesures d'ERM. Nous avons établi des abaci *in silico* pour identifier le nombre de voxels par longueur d'onde idéal (rapport λ/a) pour obtenir des mesures ERM exactes et précises. En outre,

nous avons montré que le rééchantillonnage pouvait s'avérer efficace afin de répondre aux critères de λ/a favorable lorsque le nombre de voxels par longueur d'onde initial était mal défini. Les résultats finaux, qui sont généralement calculés à partir des trois directions d'encodage, peuvent être améliorés grâce à des stratégies de pondération appropriées qui reposent sur le champ rotationnel du déplacement de l'onde de cisaillement. Pour la modalité SSI, nous avons utilisé le paramètre de qualité fourni par le fabricant afin d'éliminer raisonnablement des résultats peu fiables et améliorer encore la qualité des mesures.

Ensuite nous avons intégré les stratégies d'optimisation proposées dans chaque modalité pour effectuer des études de comparaison expérimentales impartiales entre ces deux modalités. Des études *in vitro* ont été effectuées sur des fantômes commerciaux calibrés et aussi des fantômes à la base de l'alcool polyvinylique. Des résultats expérimentaux confirment bien ceux de la simulation. Des mesures SSI et ERM sont en bon accord quand des biais reliés à la théorie, l'expérimentation et la reconstruction sont minimisés. Des études *in vivo* ont été ensuite effectuées sur le foie de deux volontaires sains. On a constaté que lorsque le foie est quasi-élastique, des mesures SSI et ERM avec la qualité optimisée concordent bien les uns et les autres, ils sont donc interchangeables. Dans le cas du tissu hépatique viscoélastique, des mesures SSI et ERM dépendent de la fréquence. Dans ce contexte, des mesures ERM et SSI pour la même fréquence spécifique sont nécessaires pour réaliser une comparaison impartiale entre des deux modalités.

Title : Magnetic Resonance Elastography and Supersonic Shear Imaging: simulation, experimental comparison and application to the characterization of the liver

Keywords : elastography, MRI, ultrasound, simulation, reconstruction

Abstract : Elastography is an emerging medical imaging modality which permits to measure the mechanical properties of human soft tissue. The measured mechanical properties can serve as potential biomarkers for improving the management of diseases, from early diagnosis, to severity evaluation and therapy response monitoring. Among different approaches, Magnetic Resonance Elastography (MRE) and Supersonic Shear Imaging (SSI) have shown particular interests. The two modalities have been widely investigated for multiple clinical applications. However, each modality is challenged by specific acquisition and reconstruction conditions which may induce intra- and inter-modality measurement biases and hence impede the interchangeability of the two modalities.

The first part of my thesis focused on identifying the measurement biases between MRE and SSI. Through a thorough methodological comparison study, we recognized different frequency characteristics of generated shear waves for the two modalities and modality specific reconstruction validity issues as the main sources for the measurement biases between the two modalities. Then through a dedicated simulation study, we established an *in silico* abaci to identify the favorable range of number of voxels per wavelength which leads to accurate and precise MRE. Moreover, resampling was proven effective to regulate poorly defined number of voxels per wavelength to the favorable range.

The overall outcome, which is usually computed from the three acquired motion-encoded directions, may further be improved by appropriate weighting strategies that are based on curl of shear displacement field. For SSI, we referred to the quality parameter provided by the manufacturer to reasonably eliminate unreliable results so as to further improve the measurement quality.

After establishing the potential measurement biases between MRE and SSI, we incorporated the proposed quality optimization strategies into both modalities in order to perform unbiased experimental comparison studies between the two modalities. First, *in vitro* studies were carried out on commercial calibrated phantoms as well as home-made polyvinyl alcohol phantoms. Experimental results corroborate well the simulation findings. MRE and SSI measurements agree well with each other when theory, experiment, and reconstruction biases are minimized. *In vivo* studies were then performed on the livers of two healthy volunteers. We found that when the liver is quasi-elastic, the quality-guided MRE and SSI measurements agree well with each other and hence are interchangeable. In case of viscoelastic liver tissue, both MRE and SSI measurements are frequency dependent. Thus frequency-specific measurements are essential for cross-validating the measurements of these two modalities.

